Primož Skerbiš, BSc

Investigation of transient CFD simulation methods for commercial application in the aerodynamic development process of the automotive industry

MASTER'S THESIS

to achieve the university degree of

Diplom-Ingenieur

Master's degree programme: Mechanical Engineering

submitted to

Graz University of Technology

Supervisor

Ao. Univ.-Prof. Dipl.-Ing. Dr.techn. Helfried Steiner

Institute of Fluid Mechanics and Heat Transfer

Graz, February 2019

AFFIDAVIT

I declare that I have authored this thesis independently, that I have not used other than the declared sources/resources, and that I have explicitly indicated all material that has been quoted either literally or from the content of the sources used. The text document uploaded to TUGRAZonline is identical to the present master‘s thesis.

Date

Signature

Acknowledgments

I would like to give special thanks to my family, who have supported me throughout my studies.

Secondly, I would like to express my sincere gratitude to my advisor, Prof. Helfried Steiner, for his continuous support of my master thesis.

Abstract

The present thesis investigates the scope and limits of transient CFD simulations for use as design a tool in the development process of the automotive industry. The flow around the Ahmed body was chosen as a well-known test case in aerodynamics investigation. As suggested by a literature review the configuration with $25°$ slant angle was considered in particular. This represents the most challenging test case for numerical simulations, mainly due to the partial flow reattachment that occurs on the rear slant. Current practice has shown that different turbulence models either predict entirely separated flow or the fully attached flow over the slant. The prediction of this particular flow region served as a good indicator for the quality of the present simulations. The numerical data were validated against the experimental data measured in the wind tunnel of the Graz University of Technology at the Institute of Fluid Mechanics and Heat Transfer. The experimental validation data include the measurements of the velocity profiles in the wake region and the pressure distribution over the slant.

The tested steady RANS approaches used K-ε Realizble (RKE) and K-ω SST turbulence models. SAS, IDDES, and LES were the tested transient approaches. Six different structured mesh configurations were used providing different levels of spatial resolution and near–wall treatment. Both of the RANS models produced good agreement regarding the predicted lift and drag coefficient. The applied near-wall modeling plays an important role, especially with the K-ω SST turbulence model, which yielded completely different results, using alternatively the wall-resolved or wall-function based boundary conditions. This behavior is directly translated into the SAS approach, which was developed as a partially scale-resolving transient extension to the K-ω SST model. SAS offered no significant improvement despite the marked increase in the computational costs. The transient hybrid approach IDDES could predict the flow reattachment on the slant, but it still markedly overpredicted the drag and lift coefficients. Despite being under-resolved, the LES generally provided the best description of the flow field. For better quantitative accuracy the use of a significantly refined LES-grids is indispensable though. This further refinement is however strongly limited due to high computational costs.

Kurzfassung

Die vorliegende Arbeit untersucht des Potenzial und die Grenzen transienter CFD Simulationen als Auslegungswerkzeug im Entwicklungsprozess der Automobilindustrie. Die Strömung um den so genannten Ahmed-Körper wurde als ein bekannter Testfall für aerodynamische Untersuchungen gewählt. Basierend auf einer Literature Studie, wurde insbesondere eine Ausführung betrachtet, deren Heckschräge um 25° relativ zur Horizontalen geneigt ist. Diese Konfiguration repräsentiert den herausfordersten Testfall für numerischen Simulationen, hauptsächlich aufgrund des teilweisen Wiederanlegens der abgelösten Strömung im unteren Bereich der Heckschräge. Die aktuelle Praxis hat gezeigt, dass die verschiedenen Turbulenzmodelle hier oftmals entweder eine vollständig abgelöste Strömung, oder eine vollständig anliegende Strömung entlang der gesamten Heckschräge vorhersagen. Die Vorhersagegenauigkeit in diesem kritischen Bereich ist daher ein guter Indikator für die Qualität der vorligenden Simulationen. Die numerischen Daten wurden mit den im Windkanal der TU Graz am Institut für Strömungslehre und Wärmeübertragung gemessenen experimentellen Daten validiert. Das Validierungsdaten beinhalten Messungen der Geschwindigkeitsprofile im Nachlaufbereich und der Druckverteilung entlang der Heckschräge.

Die vorliegend getesteten stationären RANS Konzepte verwendeten das K-ε Realizable (RKE) und das K-ω-SST-Turbulenzmodell. SAS, IDDES und LES waren die getesteten transienten Ansätze. Sechs verschiedene strukturierte Rechennetzkonfigurationen, welche unterschiedlich feine räumliche Auflösungen, bzw. Methoden zur Wandbehandlung ermöglichen, wurden verwendet. Beide getesteten stationären RANS-Modelle lieferten eine gute Übereinstimmung in den vorhergesagten Auftriebs- und Widerstandsbeiwerten. Die jeweils verwendete Modellierungen des wand-nahen Bereichs erwies sich dabei als wichtiger Faktor, insbesondere beim Einsatz des K-ω-SST Modells. Dieses lieferte bei vollständiger Wandauflösung, bzw. alternativ, mit der Verwendung einer Wandfunktion völlig unterschiedliche Ergebnisse. Dieses Verhalten überträgt sich direkt in die transiente SAS Methode, welche als eine instationäre teilweise skalen-auflösende Erweiterung des K-ω-SST Modells konzipiert wurde. Die SAS Methode bietet keine wesentliche Verbesserung trotz einer signifikanten Erhöhung des Rechenaufwands. Der transiente hybride IDDES Methode konnte das Wiederanlegung der Strömung an der Heckschräge zwar vorhersagen, überschätzte aber dennoch die Widerstands- und Auftriebskoeffizienten beträchtlich. Obwohl die für die vorliegende LES verwendeten Rechnengitter nicht die hierfür erforderliche räumliche Auflösung gewährleisten, liefert diese Methode generell die realistischeste Beschreibung des Strömungsfeldes. Zur Verbesserung des quantativen Vorhersagegenauigkeit von LES ist allerdings eine maßgebliche Verfeinerung des Rechnungsgitters erforderlich, was aber den Rechenaufwand für LES immens erhöht.

Table of Contents

List of symbols

Latin letters

Nomenclature	Description	Dimension
A_0, A_S	modeling constants (RKE turbulence model)	[-]
A_i	normal face vector	[-]
a_1	modeling constant (in SST)	[-]
C_1, C_2	modeling constants (RKE turbulence model)	[-]
c_i	vector from the cell centroid of the adjacent cell	[-]
$C_{1\epsilon}$, $C_{3\epsilon}$	modeling constants (RKE turbulence model)	[-]
C_{DES}	empirical constant of DES (in IDDES)	[-]
C_k	Kolmogorov constant	[-]
C_μ	Modeling constants (RKE turbulence model)	[-]
c_f	skin friction coefficient	[-]
D_ω	cross-diffusion term (in SST)	[N/m^4]
d_W	wall distance	[m]
$\widetilde{f_d}$	empirical blending function (in IDDES)	[-]
$\mathrm{f_e}$	elevating function in IDDES	[-]
f	relaxation function	[-]
f_i	vector from the cell centroid to the each of the faces	[-]
F_1, F_2	blending functions (in SST)	[-]
G_b	production term of TKE (due to buoyancy)	[N/m^2s]
G_k	production of turbulence energy (k)	[N/m^2s]
g	gravitational acceleration	[m/s^s]
$G(x, x')$	LES filter function	[-]
h_{max}	maximum length scale	[m]

k_P	turbulence energy from the wall to the cell centroid	$[m^2/s^2]$
L_0	reference length	[m]
L_{vK}	Von Kármán length scale	[m]
l_0, ℓ	integral length scale	[m]
L	the length scale of the modeled turbulence	[m]
l_η	turbulence length scale	[m]
Ma	Mach number	[-]
N_f	number of nodes	[-]
n	unit orthogonal vector	[-]
P_k	mean production term of the turbulence energy	[N/m^2s]
$\bar{p}$	averaged pressure	[Pa]
p_i'	pressure fluctuation	[Pa]
p	pressure	[Pa]
S_{CV}	surface enclosing of control volume	[-]
S_c	Sutherland's constant	[K]
S_{ij}	shear strain rate tensor	[1/s]
S_k,S_ϵ, S_ω	source terms (in RKE, SST)	[N/m^2s]
S	scalar invariant of strain tensor	[1/s]
T^*	dimensionless temperature	[-]
t^*	dimensionless time	[-]
t_0	reference time	[s]
T	temperature	[K]
t,T	time	[s]
$\overline{u}'$	quasi-periodic coherent fluctuation	[m/s]
$\langle\bar{u}\rangle$	ensemble average velocity	[m/s]
U'	first velocity derivative	[m/s]
U''	second velocity derivative	[m/s]

u''	random velocity fluctuation	[m/s]
$\bar{u}$	averaged velocity	[m/s]
u_i'	velocity fluctuation	[m/s]
u_i	velocity in index notation	[m/s]
u_i^*	dimensionless velocity	[-]
u_i^C	coherent velocity fluctuation (stresses)	[m/s]
u_j^S	stochastic velocity fluctuation (stresses)	[m/s]
$u_{x,y,z}$	velocity in Cartesian coordinate system	[m/s]
u_τ	wall friction velocity	[m/s]
u	general velocity	[m/s]
$\vec{v}$	velocity vector	[m/s]
v_η	velocity turbulent length scale	[m/s]
x_i^*	dimensionless length	[-]
X,x	Cartesian coordinate	[-]
Y_M , Y_ω, Y_k	dissipation terms (in RKE and SST turbulence model)	[N/m^2s]
y^*	dimensionless wall distance	[-]
y_P	distance from the wall to the cell centroid	[m]
Y,y	Cartesian coordinate	[-]
Z,z	Cartesian coordinate	[-]
∞	infinity	[-]

Greek letters

Nomenclature	Description	Dimension
$\beta_{i,1}$, $\beta_{i,2}$	model constant (in SST)	[-]
Γ_k	effective diffusivity of k	[Ns/m^2]
Γ_ω	effective diffusivity of ω	[Ns/m^2]
Δ	LES length scale	[m]

δ_{ij}	Kronecker delta function	[-]
ε	dissipation rate	$[m^2/s^3]$
ϕ	conserved quantity	[-]
$\widetilde{\Phi}$	filtered quantity (in LES)	[-]
φ	gradient of a scalar	[-]
κ	wave number	[-]
μ	molecular viscosity	[Ns/m^2]
μ_t	turbulent dynamic viscosity	[Ns/m^2]
ν	kinematic viscosity	$[m^2/s]$
ρ	density	[kg/m^3]
ρ^*	dimensionless density	[-]
ρ_0	reference density	[kg/m^3]
ρ_W	density on the wall	[kg/m^3]
σ_k, σ_ϵ	turbulent Prandtl numbers (k and ε in RKE)	[-]
$\sigma_{k,1}$, $\sigma_{k,2}$	turbulent Prandtl numbers (k in SST)	[-]
$\sigma_{\omega,1}$	turbulent Prandtl number (ω in SST)	[-]
σ_{ij}	molecular viscosity strain tensor (in LES)	[1/s]
τ_η	turbulence timescale	[s]
τ_{ij}	Reynolds stress tensor	[Pa]
τ_w	wall shear stress	[Pa]
ω	specific dissipation rate	[1/s]
∇	vector differential operator	[-]
∂	partial derivation	[-]

Abbreviations

ASM	algebraic stress model
CAD	computer-aided design

CFD	computational fluid dynamics
c_D	drag coefficient
c_L	lift coefficient
$c_{D,B}, c_{D,F}, c_{D,S}, c_{D,R}, c_{D,SI}, c_{D,U}$	drag coefficient contribution from the subsurfaces base, front, slant, roof, sides, underbody
$c_{L,B}, c_{L,F}, c_{l,S}, c_{L,R}, c_{L,SI}, c_{L,U}$	lift coefficient contribution from the subsurfaces base, front, slant, roof, sides, underbody
Cp	pressure coefficient
CFL	Courant–Friedrichs–Lewy condition
CPU	central processing unit
CV	Control volume
EASM	explicit algebraic stress model
EARSM	Explicit algebraic Reynolds Stress model
DDES	delayed detached-eddy simulation
DES	detached-eddy simulation
DNS	direct numerical simulation
EVM	eddy-viscosity model
IDDES	improved delayed detached-eddy simulation
K-H	Kelvin−Helmholtz
LBM	lattice Boltzmann method
LDA	laser doppler anemometry
LES	large-eddy simulation
LN, ln	natural logarithm
NACA	National Advisory Committee for Aeronautics
PANS	partially averaged Navier−Stokes equations
RANS	Reynolds-averaged Navier−Stokes equations
Re	Reynolds number
URANS	Unsteady Reynolds-averaged Navier−Stokes equations
PIV	particle image velocimetry

RKE	realizable K-ε model
RSM	Reynolds stress model
S-A	Spalart−Allmaras model
SST	K-ω shear- stress transport model
SMC	second-moment closures
SAS	scale-adaptive simulation
TKE	turbulent kinetic energy
VLES	very-large-eddy simulation
OS	open source

1 Introduction

1.1. Motivation and background

Increasing the efficiency of the automotive design is one of the most critical areas in the automotive industry. Companies are forced to invest regularly in new technologies to maintain competitiveness. Fuel consumption and the reduction of undesirable exhaust emissions has become a crucial optimization factor. This can be achieved by the reduction of the rolling resistance, inertia resistance, and aerodynamic resistance. For example, the passenger car, which travels at approx. 80 km/h must overcome the aerodynamic resistance, which is higher than the resistance of the tires and the transmission together[1]. Since the majority of cars are driven by internal combustion engines, which run on fossil fuels, this directly affects fuel consumption. The same holds true for electric cars, which are becoming increasingly present on the market. Aerodynamics optimization has the potential to increase the efficiency of the vehicle and improve the overall range of the car. Figure 1 shows the effect of aerodynamic resistance on fuel consumption. A car with a mass of 1060 kg and a frontal area of around 1.77m^2 will improve the fuel efficiency by about 23% at the reduction of the drag from 0.5 to 0.3 and running at a speed of 96 km/h[1].

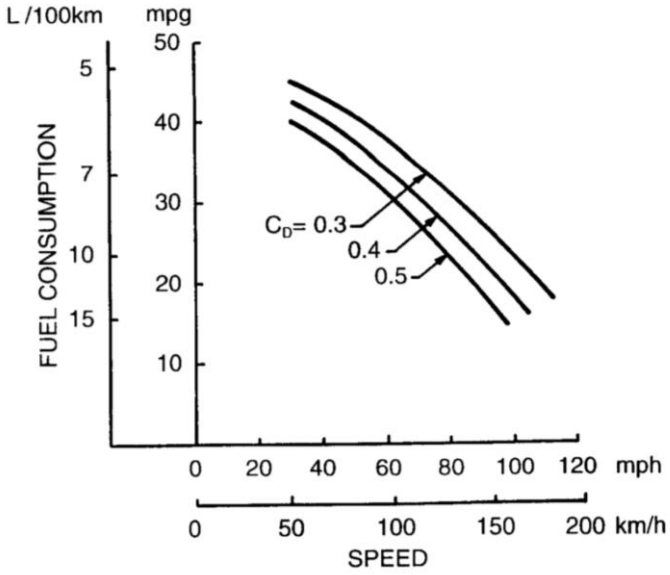

Figure 1: Effect of the reduction of aerodynamic drag on the fuel consumption of a passenger car at different speeds [1].

Not just in the commercial car industry but also in motorsport teams, the aerodynamics remains the most substantial discriminating factor between competitors The possible speed of a racing car depends on the low drag and high downforce, which allow the driver sharp cornering, accelerating and braking. According to some authors [2], the most critical parameters are tires, engine, aerodynamics and weight. The weight of a Formula 1 (F1) car is regulated to approx. 700 kg. Tires are also usually strongly regulated, permitting only one supplier in F1 (currently Pirelli). Although the aerodynamics have to meet a lot of regulations, these, along with the restrictions, are not so strict and offer much more freedom in design. The importance of aerodynamics for F1 is illustrated in the table below, which shows the effect of a change by 10% on the critical performance parameters, such as maximum speed and lap time around a typical F1 circuit. It shows that a combined optimization of drag and downforce affects the lap time more than a 10% increase in engine power. The findings from motorsport also

reflect on commercial vehicles. The need for a low drag is mainly motivated by the desire to reduce fuel consumption. However, there are also other issues that play an important role, such as the stability of the vehicle at high speeds. In the typical design process, the car manufacturers have to take account of different parameters to ensure excellent performance of the vehicle, not just considering economic aspects, but also safety issues. Most apparent is the crosswind effect, arising from aerodynamic yawing moments and side forces.

Aerodynamic Configuration	Laptime (s)	Delta Laptime (s)	Maximum Speed (Km/h)
Reference	83.59	-	295.0
Reference +10% Downforce	82.88	-0.71	295.0
Reference -10% Drag	82.91	-0.68	303.8
Reference +10% Power	82.36	-1.23	304.3
Reference + 10% Tyre Grip	80.50	-3.09	295.1
Reference +10% Weight	85.62	+2.03	293.7

Figure 2: Lap time changes of different performance parameters as the consequence of the 10% changes for a F1 vehicle running on a typical Formula 1 track [2].

In the passenger car, the aerodynamic resistance consists of two sources. The air that flows over the exterior of the vehicle body and flows through the interior (e.g. underhood space, cooling system). The external flow represents more the 90% of resistance. The resistance is the consequence of the normal pressure and the shear stresses, which act on the body of the car. They are known as the pressure drag and skin friction (viscous) drag [1].

There are many different ways to determine the aerodynamic forces on a vehicle. One of them is wind tunnel testing, where the length scale of full-scale models is crucial for understanding representative data on the vehicle. Many wind tunnels in the industry are capable of testing the full-scale models, however, they are costly. Downscaled models are much more convenient and allow fast shape modifications. They are more common and are widely used in the development of a new product.

Over the last decades, the area of computational fluid dynamics (CFD) has grown tremendously, allowing the industry to use CFD in the more complex flow. Each method alone cannot provide reliable results, so the integration of both methods is the most usual practice in the industry. Numerical results are validated against the experimental data. Much testing and data validation must be completed in order to obtain accurate results. The virtual CFD model can be developed and optimized much faster than the conventional models in the wind tunnels. Moreover, CFD offers deep insight into the fluid flow, which would not be possible with the conventional measuring techniques. The complex three-dimensional flows surrounding the vehicle must be reproduced with sufficient accuracy in both numerical and wind tunnel testings.

Although the CFD offers significant potential, there are also limitations. The Navier−Stokes equations cannot be solved analytically. The equation needs to be discretized. The grid resolution necessary to capture even the smallest dynamic features of the turbulent flow is not achievable/obtainable with

today's computational resources, except for the flows around strongly simplified generic shapes at low Reynolds numbers. These limitations encourage the development of different turbulence models. There is a variety of models on the market. It is up to the user to decide on their suitability and their limitations in order to implement them correctly so that they can provide accurate results.

A steady calculation is preferable in the industry because it can often give fair results in a short computational time. The turbulent flow is naturally time-dependent and especially three-dimensional. The simplification to model all the time-dependent turbulent fluctuations in terms of statistical averages can lead to severe shortcomings, especially in correctly predicting flow around a blunt object. Transient simulations are increasing in popularity as the computational resources become more available. Hanjalic [6] predicted in 2005 the increased use of the LES and hybrid methods till 2020. LES has a prospect to at some point establish itself as the future industrial standard, threatening to eliminate RANS, which still is and will remain widely used in the industry.

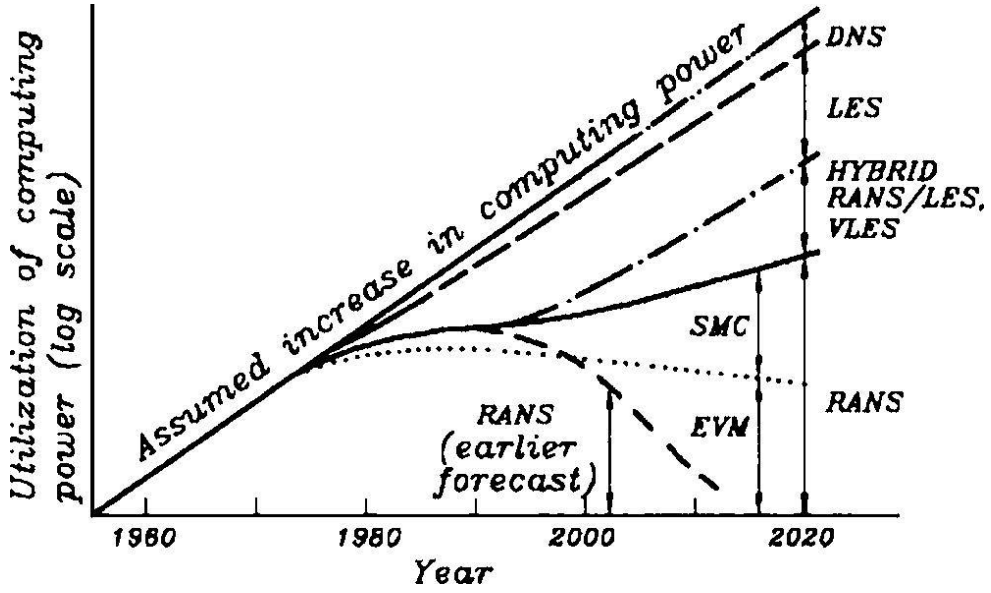

Figure 3: Assumed increase in computing power and different turbulence models[6].

1.2. Objectives

The primary purpose of this thesis is to investigate the accuracy of steady and unsteady computational approaches in automotive external aerodynamics. The air flow around an Ahmed body was considered as a well-suited test configuration due to the high amount of experimental and computational data available in the literature. More specifically, the objectives are:

- To investigate the physical phenomena and formation of the vortical structures emerging from the back end of the vehicle
- To evaluate the performance of the steady and unsteady numerical method in the flow around the test body (Ahmed body) using the commercial software ANSYS Fluent
- To assess the numerical results (steady and unsteady) against the experimental data
- To develop guidelines for the transient simulation in external aerodynamics, following from the obtained results

1.3.Organization of thesis

Chapter 1: indicates the motivations for this thesis and necessary information about the structure and goal of the thesis

Chapter 2: gives a literature review, with the main focus on previous numerical studies and a comparison between the steady and unsteady methods, starting from simple to more complex geometries

Chapter 3: discusses some basic features of the bluff body aerodynamics and discusses the test case considered in the present study

Chapter 4: provides information on the theoretical background of the numerics and finite volume method used in the computation, as well as some elementary turbulence modeling concepts.

Chapter 5: describes the turbulence properties and the most common turbulence modeling approaches as well as the different near-wall treatments for turbulent flows

Chapter 6: contains the numerical setup. First, the model of the body is presented, followed by the mesh generation process and boundary conditions

Chapter7: validates the obtained numerical results for the velocity and pressure against the experimental data as well as other numerical results

Chapters 8, 9 and 10: give conclusions and provide some guidelines for transient simulations as well as recommendations for future work, finally followed by the bibliography.

2 Literature review

2.1 Steady and unsteady CFD methods

Much work on unsteady numerical simulation has been done in the last decades. Both the academia and industry share a great interest in this area. An overview of different studies of researchers from the academic and automotive industry shall be given in the present chapter. The literature survey covers only those studies with close relevance to the work done in this thesis. It starts with transient simulations of simple shapes, then advances from the generic car shapes on to more car-like geometries, finally coming to some real car configurations.

A wide range of variety of industrial applications currently uses CFD. Despite the significant progress made, turbulence modeling remains one of the biggest weaknesses. The challenge is not only to capture all the main features of turbulent flows but also to do this cost-efficiently in order to make applications feasible for industrial use. Basic strategies for computing turbulent flows can be classified into three major categories according to Spalart[3]: direct numerical simulations (DNS); large-eddy simulations (LES) and Reynolds-averaged Navier−Stokes (RANS). RANS can be used for calculating steady and transient case simulations, while LES and DNS simulations are transients by definition. Meanwhile, more recently the lattice Boltzmann method (LBM) has been increasingly used, which basically minimizes the Navier−Stokes equations to a molecular level.

2.2 Transient CFD investigation of simple geometrical shapes

Although more complex unsteady methods offer a more comprehensive description of turbulent motion, the steady RANS approach remains the most economical concept of turbulence modeling. In particular, steady RANS seem to be a good choice for use on the attached boundary layer flows, where they can reproduce the first-order statistics of the turbulent boundary layer reasonably well. A representative test to measure the performance of turbulent models for such conditions is that of the flow along the flat plate [4], whereby a boundary layer develops against an increasingly adverse pressure gradient, as illustrated in Figure 4. The influence of the adverse pressure gradient here is still not sufficiently large for separation to occur.

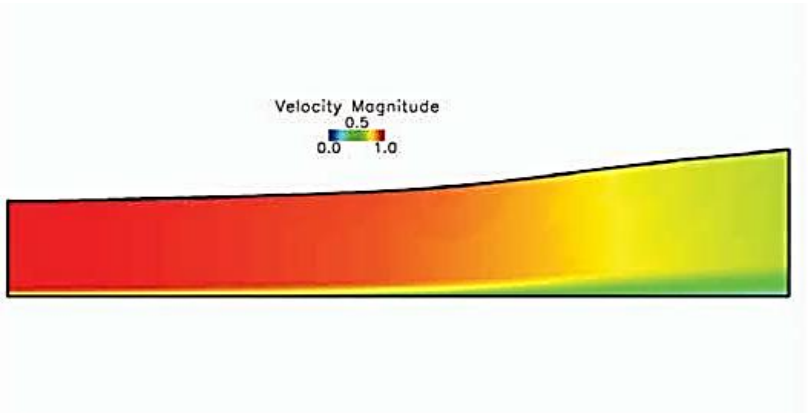

a)

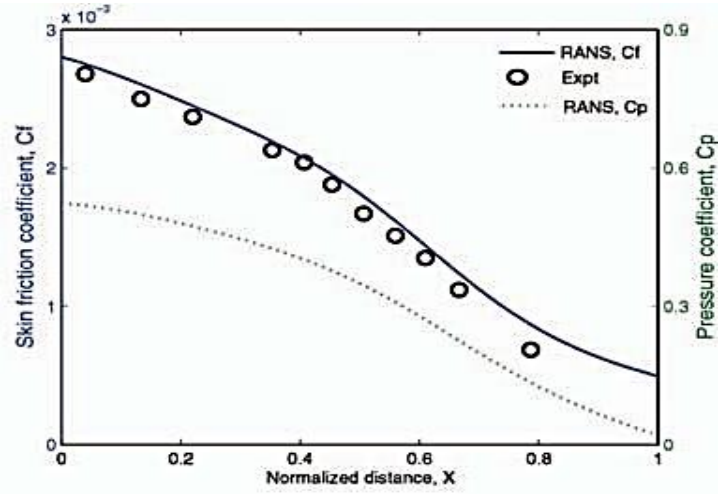

b)

Figure 4: Steady RANS predictions for boundary layer: a) Contours of velocity magnitude b) Skin friction and pressure coefficient [4].

The weakness of the steady RANS models is already revealed when trying to simulate separated flow over smooth 2D or 3D geometries. Mildly separated flow can be realized downstream of a curved solid hump embedded in a turbulent boundary layer, as presented in Figure 5. The flow is separated due to the adverse pressure gradient, resulting from the expansion of the cross section after the hump. The simulation was done using the steady RANS model of Spalart and Allmaras[4]. The model correctly predicted the separation location but overestimated the separation length.

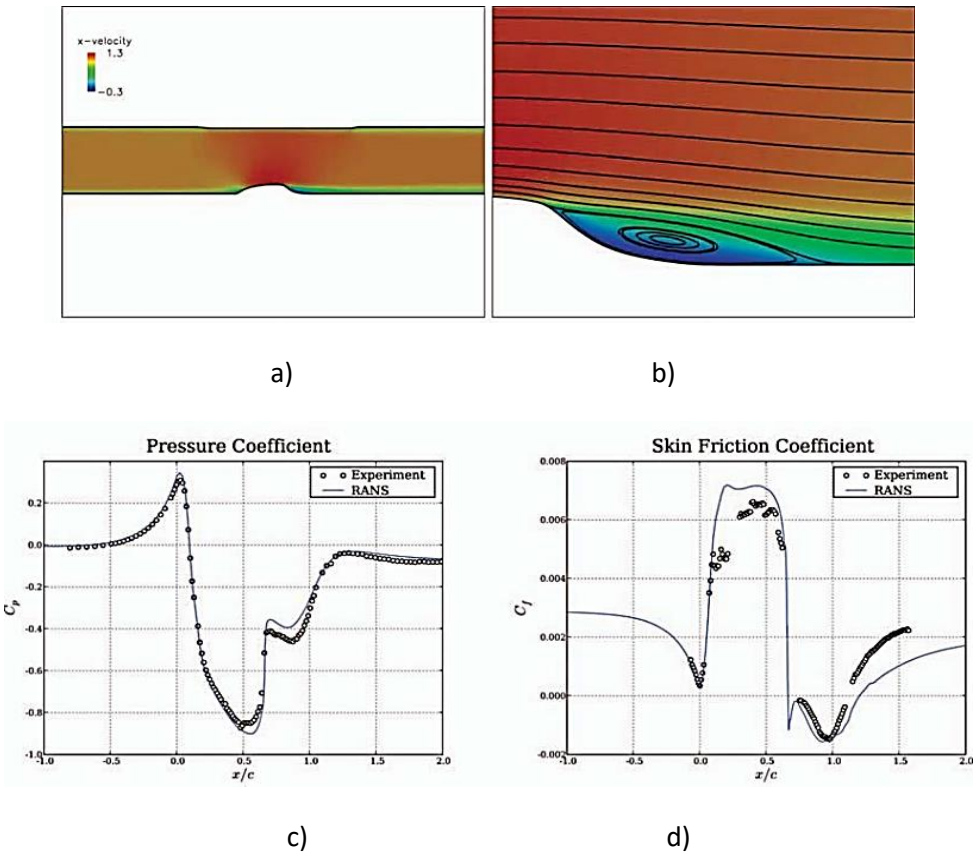

Figure 5: Steady RANS results for a flow over a hump: a)velocity contours; b)streamlines; c) pressure coefficient d) skin friction coefficient [4].

Massively separated flows become a special challenge for steady calculation, due to the highly unsteady nature of the emerging vortical structures impeding the convergence to a steady solution. A typical example is a flow around a bluff body (e.g. a triangular cylinder). In such cases, a strong unsteadiness of non-turbulent origin is present. It can be categorized as follows[7]:

- Externally enforced unsteadiness (moving geometry or time-varying boundary conditions)
- Unsteadiness of non-turbulent nature (a consequence of the hydrodynamic instabilities, e.g. vortex shedding behind a bluff body)

Figure 6 is split into halves and shows the internal flow around a triangular cylinder. The upper half represents the unsteady temporally averaged, and the lower half shows the steady solution computed by steady RANS. The unsteady computation causes the wake to fill more rapidly after separation, which results in a much shorter separation bubble than that in steady RANS solution. This directly translates into different velocity profiles in the wake.

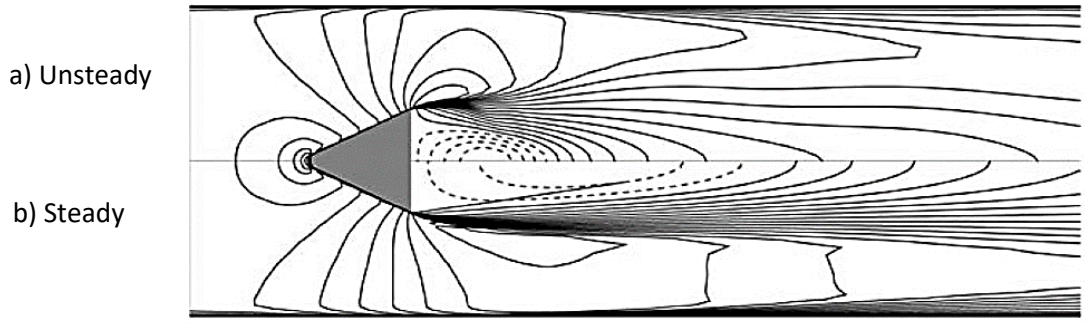

Figure 6: Unsteady(a) and steady(b) velocity contours [7].

The velocity profiles computed by the unsteady RANS are in much better agreement with the experiment than the profiles of the steady RANS. The same is observed in the velocity distribution along the centerline. This clearly shows the need to include the deterministic vortex shedding into the computation and use a turbulence model to represent the statistics of the stochastic component of motion.

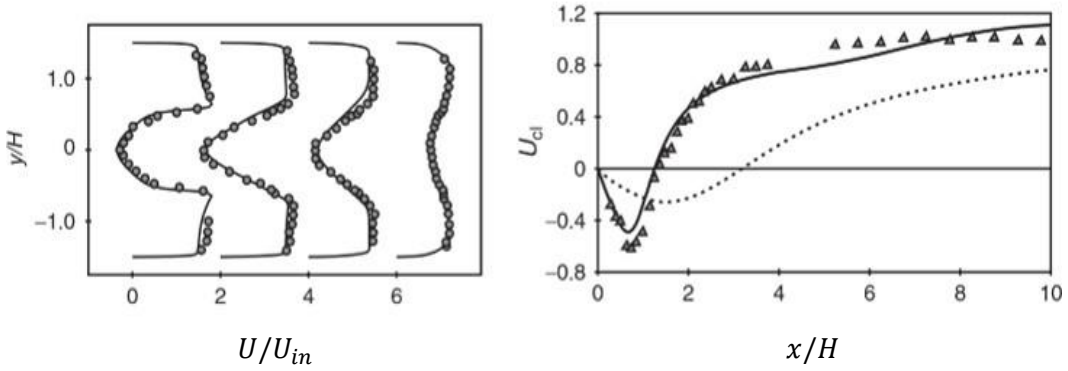

Figure 7: Velocity profiles in the wake and along the centerline: Unsteady RANS(——), Steady RANS(----), Experiment(Δ,○)[7].

It has become common to use the terminology “unsteady RANS” − or URANS − whenever a time-dependent formulation of the RANS equations is solved. Perzon et al. [5] investigated the potential use of the transient CFD simulations for vehicle aerodynamics. The surface-mounted cube was used as a test case. The simple shape of the object allowed the use of the block-structured grid, which was created in the commercial software ICEM. The purpose was to test different modeling approaches. The first one was the transient RANS with the k-ε turbulence model and the second one was LES with the Smagorinsky subgrid scale model. The boundary condition settings were taken from the experiments. Solver was the code StarCD. In a comparsion of the streamwise velocity profile,it was observed that the LES offers better agreement in the wake region than the URANS, which overpredictes the separation. This is most likely triggered by an upstream error. A similar numerical study was performed by Iaccarino et al.[8] on the unsteady separated flow around a square cylinder and wall-mounted cube. Unsteady and steady RANS calculations were compared against the LES calculation and experimental data, which had been previously published. The requirements of LES and RANS are quite different. LES typically requires higher spatial and temporal resolution, therefore it is also computationally much more expensive. The still open question remains as to what extent is RANS able to predict highly unsteady flow. There exist some previous studies on this topic, which tried to numerically predict the flow around the cube and they showed poor agreements between steady-state RANS and experimental data, while the coherent vortex shedding occurs in the flow (e.g. the study by Perzon[5]). This shortcoming strongly suggests the unsteady RANS calculation. In [8] a commercial computational fluid

dynamic code, Fluent 5.5, was used for the simulations. RANS and URANS calculations were carried out in two- and three-dimensional simulations using the $v^2 - f$ turbulence model. The flow around the square cylinder was analyzed first, where the primary interest was the length of the recirculation zone and the surface loads. As expected, the steady RANS results were very inaccurate, while the transient URANS results were better. They captured the size of the separation bubble and overall drag fairly well. The agreement with the LES and URANS results from the literature was good. The most salient feature is exemplarily shown by the streamlines and velocity contours in Figure 8. The vortex core position is predicted at the same position in all simulations. While the steady RANS calculation shows a large recirculation zone a recirculation zone extending downstream for a 3.3 h separation length obtained with LES, and which measures approximately h=1.6, the unsteady RANS is clearly superior over the steady RANS, predicting a seperation length of 1.9 h.

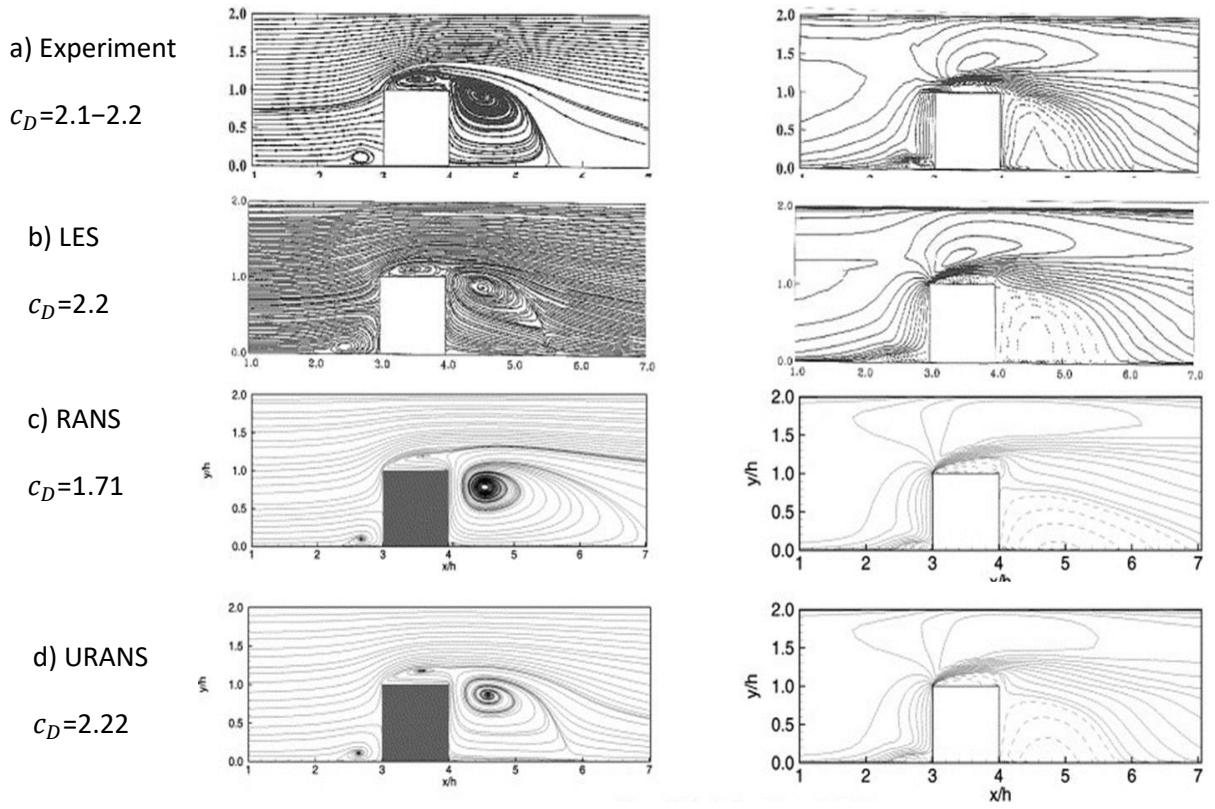

Figure 8: Streamlines and stream-wise velocity contours (top to bottom): Experiment, LES, URANS, RANS [8], Re= 40,000.

Well-known typical deficiencies of the RANS models are overprediction of turbulent kinetic energy and the incapability to account for the phase lag between stress and strain rates. As such, RANS applying linear eddy-viscosity models generally fail in flows where the production of normal stresses plays an important role. In unsteady flows, this mainly leads to suppressed fluctuations, instabilities and eventually to a steady solution or an incorrect transient solution. The latter predicts only the strongest − however time-smoothed − coherent structures. In such cases, second-order closures offer a clear advantage in the prediction of TKE and stress anisotropy.

In order to further examine the potential use and limitations of the URANS approach against the LES, Palkin et al. [9] performed a detailed study of two unsteady RANS closure levels, the linear eddy-viscosity model (LEVM), and the complex Reynolds stress model (RSM) in a separated flow over a bluff body (circular cylinder) at two different Reynolds numbers ($Re = 3.9 \times 10^3$ and $Re = 1.4 \times 10^5$). It has been found that the URANS overpredicts the drag coefficient but accurately predicts the shedding frequency. The mean drag coefficient is poorly predicted by the EVM at the small Reynolds number

(most likely because of the too short recirculation bubble). Better agreement was achieved at a higher Reynolds number where the RSM closely resembles the LES results. The linear eddy viscosity model overpredicts the size of the recirculation bubble by 24%.

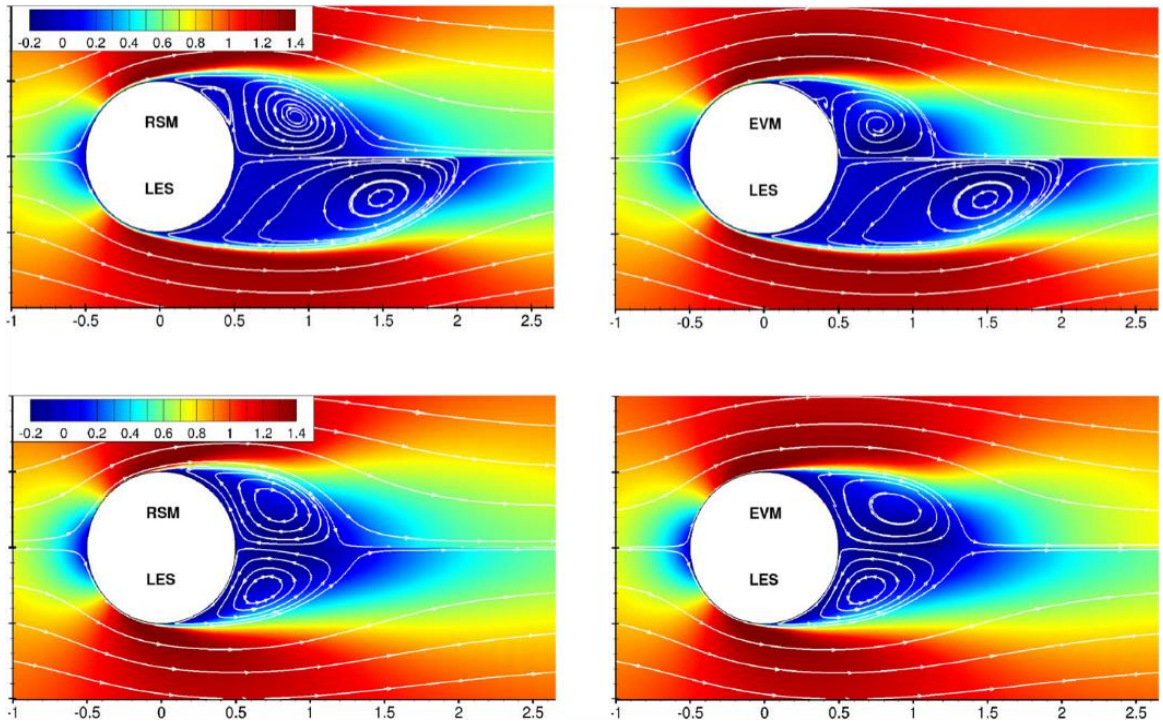

Figure 9: Streamline and velocity contour results for the flow past circular cylinder for Re = 3.9×10³ (top) and 1.4×10⁵ (bottom) [9].

The Reynolds number dependency could be explained using the Reynolds-averaged momentum equation and triple decomposition, rewriting the Reynolds stresses as [9],

$$\overline{U_i U_j} - \overline{U}_i \overline{U}_j = \overline{u_i^C u_j^C} + \left(\overline{u_i^C u_j^S} + \overline{u_i^S u_j^C}\right) + \overline{u_i^S u_j^S} \qquad 1.1$$

The three components represent the coherent, mixed and stochastic stresses. URANS resolve the first term on the right-hand side of the equation and models the last term. The correct combination of resolved and modeled energy plays a vital role in predicting turbulence. Stochastic and coherent fluctuations are related through the mixed terms (cross stresses). Turbulence models used in RANS provide only the stochastic stresses, while the coherent stresses are calculated from the time-dependent solution.

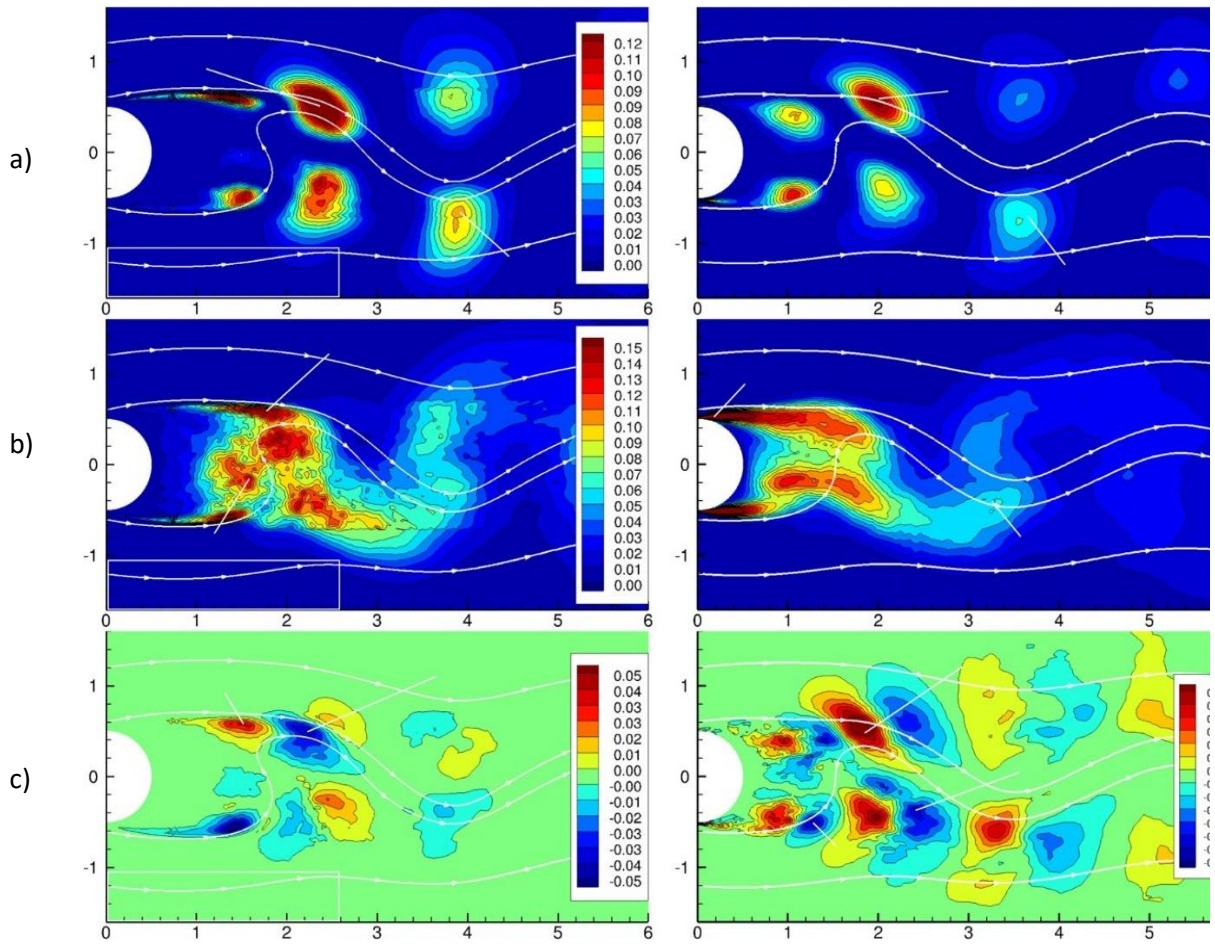

Figure 10: a) coherent($\widetilde{u^c u^c}$) b) mixed ($\widetilde{u^c u^s}$) c) stochastic ($\widetilde{u^c u^s}$) stresses by LES for Re = 3.9×10^3(left) and Re = $1.4 \times 10^5(right)$ [9].

URANS cannot calculate mixed stresses since it resolves no stochastic fluctuations. In order to evaluate the stresses, the authors made a comparison between a LES and URANS simulation of the same flow. The LES terms were analogously decomposed into three the ensemble averaged components following equation 1.1, so that they can be compared directly against each other (see Figure 10). They estimated the relative role of the mixed stress for the two different Re numbers. Results show that the mixed stresses reach up to 30% of the value of stochastic stress at the same location. Their contribution is significant for the low Re numbers and decreases with the high Re numbers.

The comparison of the flow around the surface-mounted [8] cube and also the flow around the circular cylinder[9] shows a significant difference between the predicted lengths of the separation bubble. Palkin et al.[9] named the accurate prediction of the turbulence transition in the initial shear layer as the most likely cause for such results. RANS methods predicted the transition to turbulence much earlier, just after the separation point for the small Reynolds number, compared to the LES, which shows the point of the transition at approx. x/D = 0.45. Early transition triggers the generation of vortices due to the Kelvin–Helmholtz (KH) instabilities in the shear layer. The vortex has more time to grow and to gather energy from the primary field. The formation of such vortical structures in the near-wall region is clearly seen in Figure 11. The intense mixing between the boundary layer and the KH vortices results in the separation and rettachmments near the wall, that can only be detected by the transient, more complex RANS closures or LES. The linear eddy-viscosity model completely fails to predict the very fine near-wall turbulence structures here.

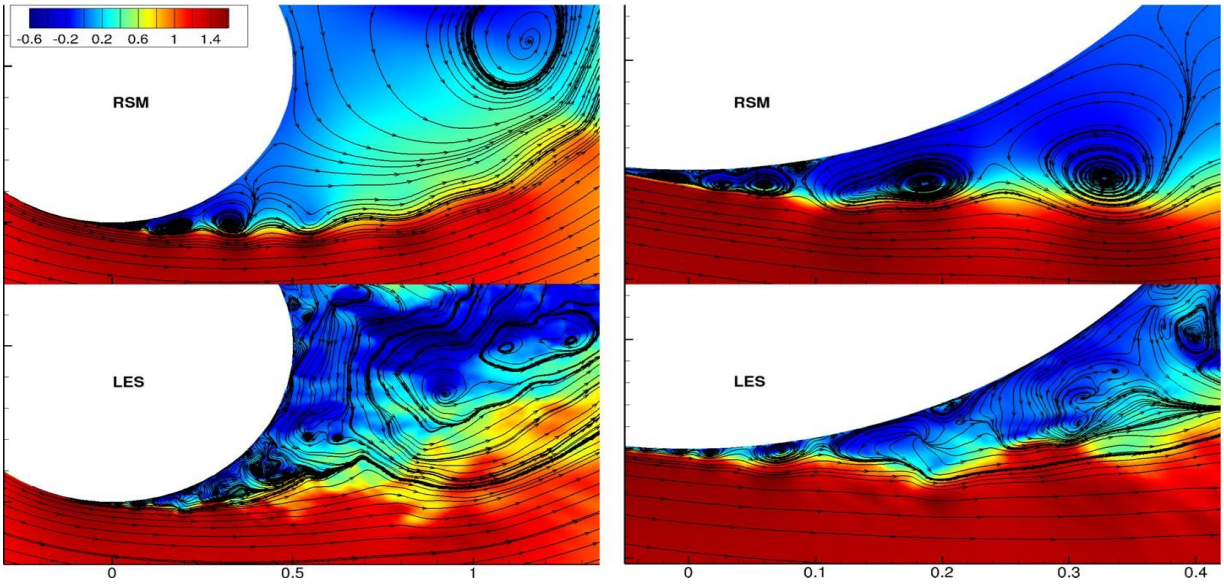

Figure 11: Instantaneous streamlines and velocity contours comparison between the LES and RSM turbulence model [9].

This clearly shows the need to resolve at least some of the near-wall vortical structures, particularly around the separation and reattachment points, to be able to more accurately predict the flow patterns further downstream in the wake region. The transition affects the total turbulent kinetic energy. Figure 12 shows the development of the total turbulent kinetic energy in the boundary layer. Both RANS models failed and overestimated TKE. The growth of the turbulence appears premature compared to the LES. If we carefully follow the TKE profiles in Figure 12 it can be seen there is practically no difference in the prediction of the total TKE between EVM and RSM until x=0.0 x/D. From this point on, the modeled part of the TKE starts to influence the solution. LES still shows no sign of turbulence transition, which happens further downstream.

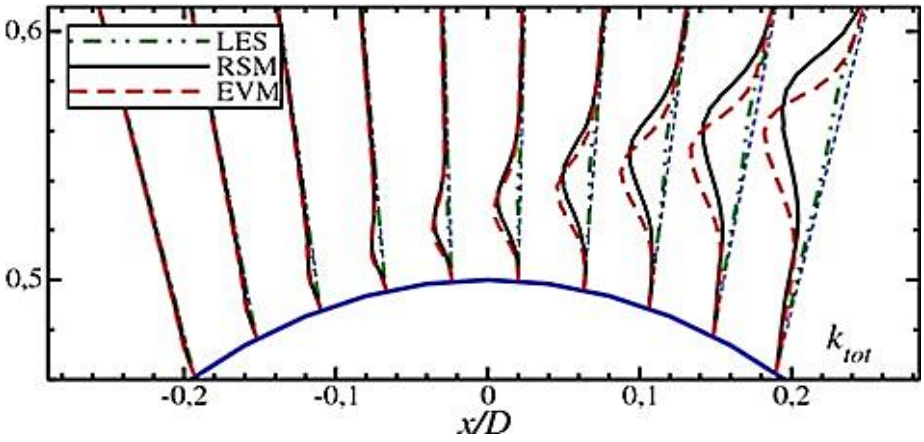

Figure 12: Total TKE in the shear layer at Re = 3.9×10^3 for three different turbulence models: LES, RSM, EVM on the different x positions normalized by the diameter(D) of the cylinder[9].

In order to explain in more detail the cause of the early turbulence transition for RANS-based computations in the flow around the cylinder, we need to have a closer look at the non-dimensionalized momentum equation, in the wall-normal direction y [9]:

$$\underbrace{\overline{U}\frac{\partial \overline{V}}{\partial x}+\overline{V}\frac{\partial \overline{V}}{\partial y}}_{1}=\underbrace{-\frac{\partial \overline{P}}{\partial y}}_{2}+\underbrace{\frac{1}{Re}\frac{\partial^2 \overline{V}}{\partial x^2}+\frac{1}{Re}\frac{\partial^2 \overline{V}}{\partial y^2}}_{3}\underbrace{-\frac{\partial \overline{uv}}{\partial x}-\frac{\partial \overline{vv}}{\partial y}}_{4} \quad 1.2$$

The left-hand side represents the change of the momentum described by the convection term (1). The right-hand side of the equation contains the pressure term (2), viscous term (3) and turbulent stresses (4). Modeling assumptions in both RANS closures cause the overestimation of the $\overline{uv}$ and $\overline{vv}$ stresses. The overpredicted stresses are compensated by the convection and pressure terms in Equation 1.2. As shown in Figure 13 the LES predicts significantly lower turbulence stresses for the low Re number. No compensation is needed through the pressure and convection term, which results in less intense turbulent mixing and a longer separation bubble at low Re compared to the unsteady RANS. A closer agreement between LES and RSM is observed at the higher Reynolds number.

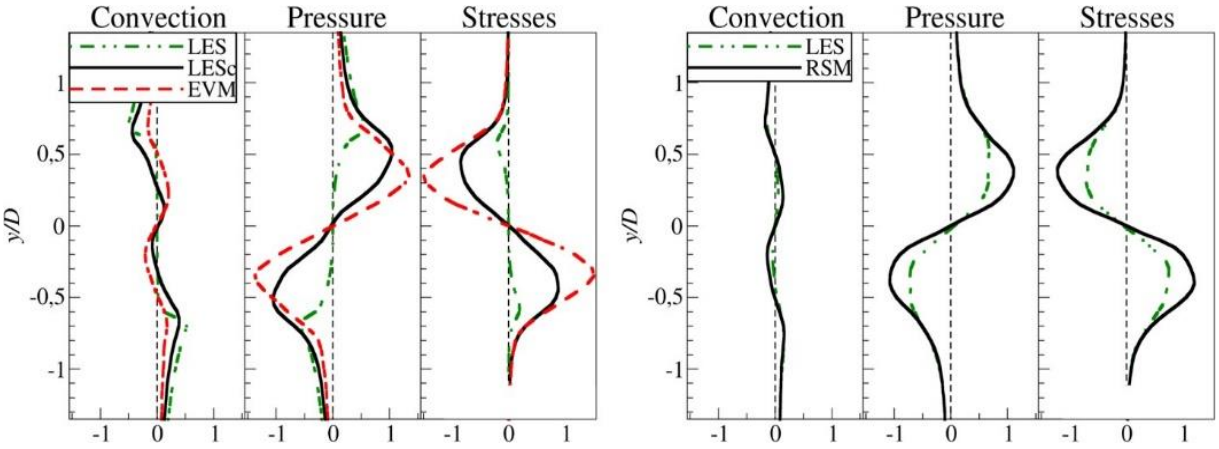

Figure 13: Contribution of the convection pressure and stress components of the V-momentum equation LES for: Re = 3.9×10^3(left) and Re = $1.4 \times 10^5(right)$, position: x = 1.06 D (left) and x=1.0 D(right) on the different y positions normalized by the diameter(D) of the cylinder [9].

Spalart[13] visualized the resolved dynamic structures using transient and steady approaches for a similar flow around the circular cylinder. URANS tendency to overpredict the drag coefficient was noted in this case. Figure 14 shows the resolved vortical structures in the wake of the cylinder. The first subfigure illustrates the standard RANS results, the second subfigure displays 2D URANS, and the third 3D URANS results. The last two upcoming subfigures show DES using different turbulence models for the wall boundary layer. It can be seen that the URANS tend to suppress the three-dimensional flow, but not entirely. Two large quasi-two-dimensional rollers characterize the 2D URANS. The steady RANS case shows no vorticity at all. The DES case evidently provides better resolution, producing much finer structures than URANS. The shown isosurfaces of instantaneous vorticity are visualized using lambda criterion. Unlike DES, URANS/RANS would not produce any finer eddies with grid refinement.

a) Steady-SST RANS

c_D=0.78

b)SST 2D URANS

c_D=1.73

c)SST 3D URANS

c_D=1.24

d) S−A-DES(coarse grid)

c_D=1.26

e) S−A-DES(fine grid)

c_D=1.26

f) SST-DES(fine grid)

c_D=1.28

Figure 14: Flow around a circular cylinder with visualized isosurfaces of vorticity[13] Re=5×10^4.

RANS models basically do not have a dependency on the numerical grid. On the other hand, the LES-based simulations contain a length scale related to the numerical grid. The grid size directly determines the size of the smallest resolved fluctuations. In recent years new RANS models have been proposed, which are capable of resolving some part of the turbulent fluctuations but do not have an explicit dependency on the numerical grid. These are the so-called “second generation models” (2G-URANS) models. One of them is the so-called “scale-adaptive simulation” proposed by Menter and Egorov[42] available in ANSYS Fluent. SAS models use two additional transport equations and introduce the Karman length scale as a further relevant length scale. The model shows good results for the generic examples, e.g. flow past a triangular cylinder. The model was also tested on the flow over the periodic hills, and more complex NACA airfoil beyond stall or full aircraft configurations[11,12]. Figure 15 shows mean velocity profiles for the flow over a periodic hill for two different time steps using the SAS

turbulence model. The results are compared to a steady-state RANS computation and are in good agreement with a reference LES, even for the substantially increased time step. Using the SAS approach, URANS gives here considerable improvement as compared to the steady RANS calculation.

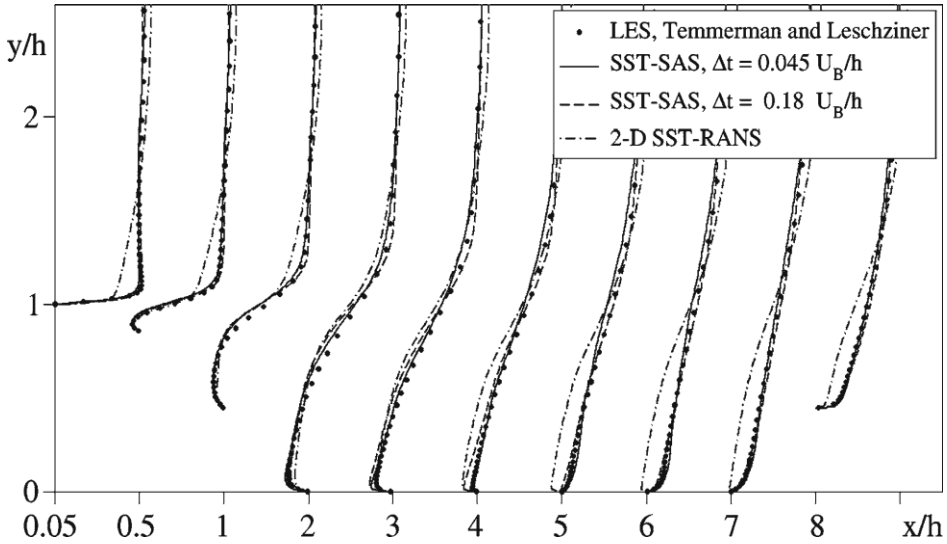

Figure 15: Mean velocity profiles on the flow over the periodic hill for transient SAS and steady SST models[11].

Together with the detached-eddy simulation (DES) the PANS (partially averaged Navier−Stokes) proposed by Girimaji et al.[44] also represents one of the more recent transient approaches. The PANS technique has been used for several different flows, e.g. around pyramids, cylinders and other bluff bodies. Kranjović et al.[14] investigated the potential of the PANS approaches for engineering applications. A surface-mounted cube was chosen as a standard test case. The results were compared to the LES and URANS to display the differences between the methods. Velocity profiles show good agreement with the experiment for the PANS approach using coarse grids. The LES approach still produced the most accurate results on the fine mesh. Regarding the predicted stresses, the PANS show considerably better results than URANS. PANS is not available in ANSYS Fluent.

2.3 Transient CFD simulations of generic bodies and car-like geometries

Simple shapes are a good choice for a first evaluation of the different turbulence modeling approaches. If the model fails to predict the relevant flow patterns around a simple shape, the shortcomings will most likely translate into flows around more complex geometries. In this chapter we will focus mainly on a popular reference body used in car aerodynamics, which is utilized for studying the typically occurring basic flow features, and we evaluate the applied model's potential for use on real car geometries.

The most popular geometry of all is the Ahmed body, introduced by Ahmed et al. [34] in 1984. It has become a standard test case in the automotive industry. Much experimental work has been done to investigate the flow around the body, trying to determine the flow regions that provide a significant contribution to the aerodynamic drag. It was also the subject of many computational studies. In particular, the wake region, which is provided by the flow separation process, seems to be essential for the accuracy of numerical predictions. We forego a detailed description of steady and transient Ahmed body simulation at this point: a more detailed description of previous experimental and numerical (steady and transient) studies on the flow around the Ahmed body will be given in subsection 3.2.1.

The Ahmed body is an elementary shape, which gives a very general insight into the flow structures. The body does not contain many of the geometrical features of real cars, such as the wheels or underbody. The obtained results, therefore, can be just partly translated to the aerodynamic optimization of real cars. A popular more realistic, but still simplified test body is the MIRA. This model was developed in the early 1980s based on the proportions of a family sized car with interchangeable back ends. In addition SUV-type geometries have become increasingly important, as the SUV segment has been gaining popularity in the last years. The consumer appreciates the space in the cabin and a comfortable ride. From the aerodynamical point of view, this means a larger frontal area and high ground clearance.

Forbes et al.[21] carried out a CFD and experimental study of a wake structure and base pressure on a generic SUV model. The study evaluated the accuracy and efficiency of the steady and unsteady CFD methodologies. The authors assessed different RANS, URANS, DES and LBM models using CD-Adapco's Star-CCM, OpenFOAM and Exa's PowerFLOW as flow solver software. Numerical simulation data were compared to experimental data gathered using the PIV method and surface pressure probes. As a result, all the data are presented in horizontal- and vertical-cut planes, positioned in the wake behind the vehicle. Planes are located on a different location on the Y and Z axes and can be seen in Figure 16 Two planes are horizontal and three are vertical.

Length (L)	1.040 m
Width	0.410 m
Height	0.376 m
Wheelbase	0.650 m
Ride height	0.060 m
Wheel diameter	0.160 m
Frontal area (A)	0.139 m^2
Diffuser angle	29.3°

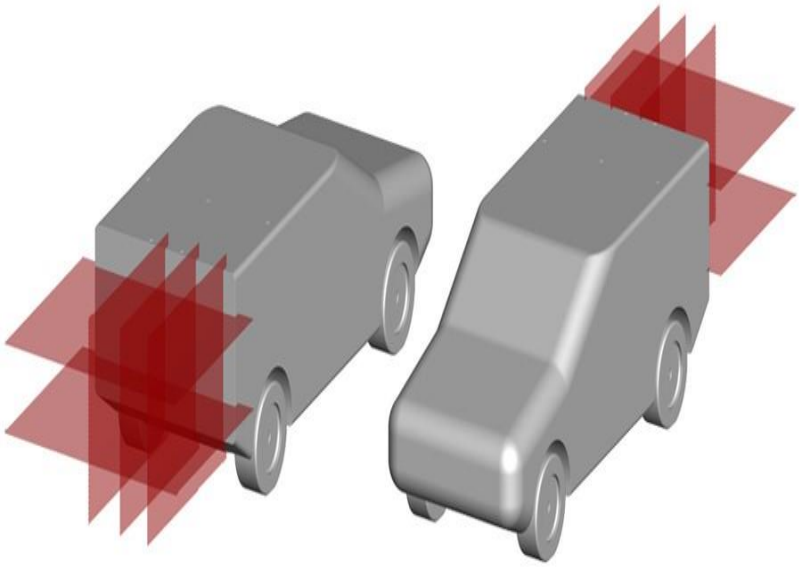

Figure 16: SUV geometry dimensions(left) and CAD model with the cut planes in the wake(right)[21].

The flow behind the vehicle is characterized by large separation at the back end of the vehicle, which represents a big challenge for a steady RANS-based computation. Interesting is the comparison of the velocity contours on the Y= 0.17 mm vertical plane, which is positioned in the outermost part of the vehicle in the wake just behind the rear wheels, which makes the flow even more turbulent. The results comparison between experiment, RANS, DES, and LBM can be seen in Figure 17. OS refers to the open source software (OpenFOAM) and GP to the commercial software package Star CCM. In the experiment a fairly confined low-velocity region is observed, which the steady RANS failed to capture accurately. The approach was particularly inaccurate between z=0.2m and z=0.3m, where the model strongly overpredicted the separation bubble. Better agreement is obtained in the near-ground region at approx z=0.1m. Both open source and the commercial software show very similar results. URANS offered no improvement compared to the steady-state, calculation despite the significant increase in the computational time. The best result is achieved with the DES and lattice-Boltzmann approach,

showing better agreement with the experiment. Interesting is the comparison of the computational costs, where the OpenFOAM software slightly falls behind the commercial packages. The lattice Boltzmann approach is calculated requiring only 20% of the computational time need by DES. Time savings with the steady-state method are significant. URANS costs do not pay off.

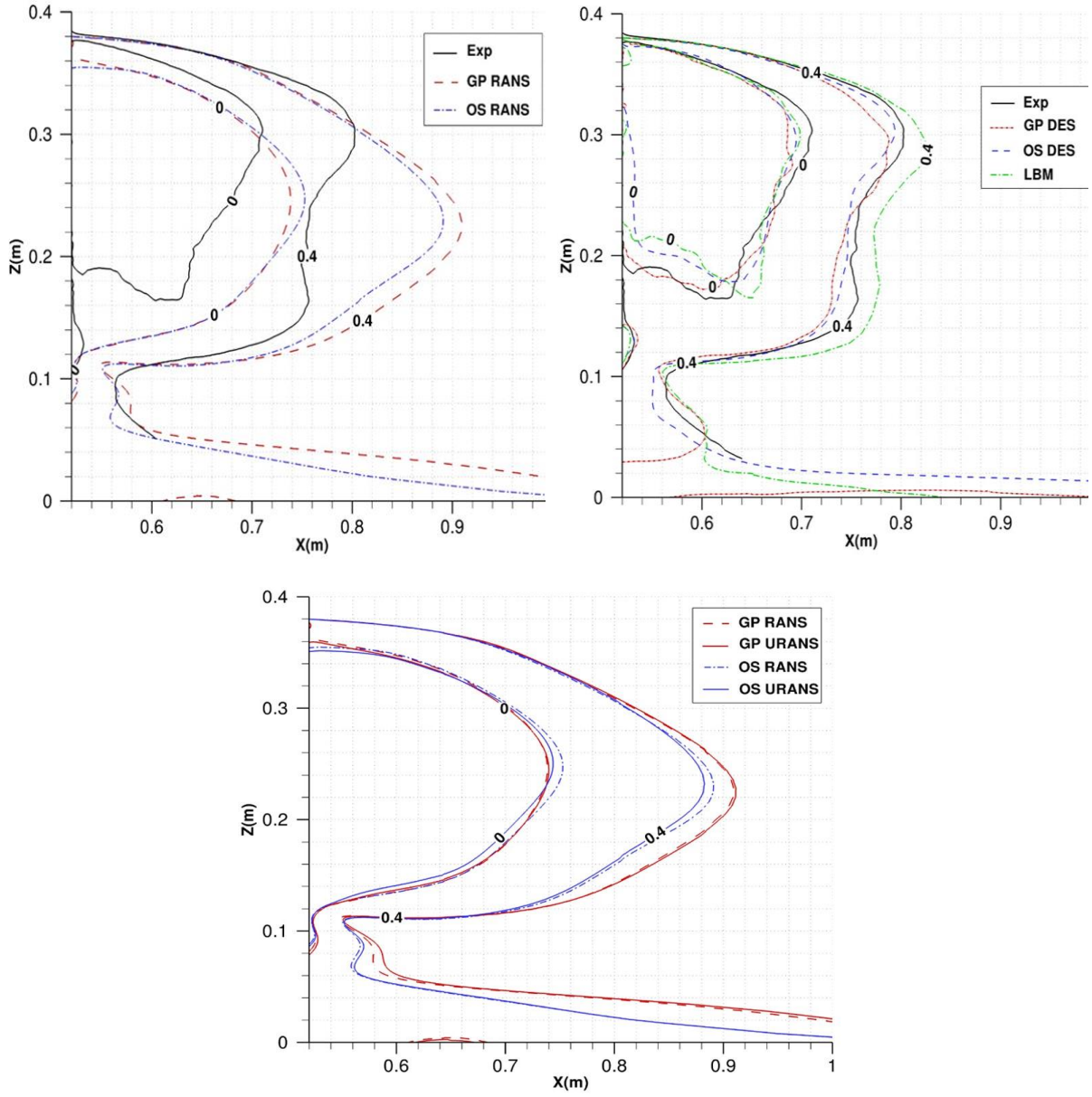

Figure 17: Experiment, RANS, URANS, DES and LBM contour comparison, Y = 0.17 plane behind wheels, normalized u velocity[21].

To close the gap between the simple bodies, basic car models and real production cars, the Institute for Aerodynamics and Fluid Mechanics at the Technical University of Munich, together with partners from the industry, developed a further more realistic car model named the “DriveAer” model. The model can have different rear angle configurations and can contain many features of production cars, such as a side mirror, a detailed underbody and wheels. The increase in the computational power in recent years makes it possible to perform numerical studies on this model vehicle. A comparison between steady and transient simulation was performed by Ashton and Revell [22] from the University

of Manchester. In the steady RANS approach a variety of eddy-viscosity models and second-moment closure were chosen (k-ε, k-ω SST, Spalart−Allmaras, elliptic blending(B)-EVM & elliptic blending(EB)-RSM), and an improved delayed detached-eddy simulation (IDDES) was used for the hybrid approach. The grid contains from 18 M up to 300 M elements for the fine configuration. Regarding the predicted drag coefficient, IDDES provides better results, but the error remains at approx. 3.5% and the pressure coefficient distribution over the rear window was not in good agreement. On the other hand, the RANS simulation could not accurately capture the flow field, even with the Reynolds-stress model. Figure 18 shows the comparison between the SST-RANS and SST-IDDES turbulence model at the back end of the vehicle. No significant difference is observed in the pressure distribution across the rear window. IDDES shows smaller pressure at the upper edge compared to the steady RANS.

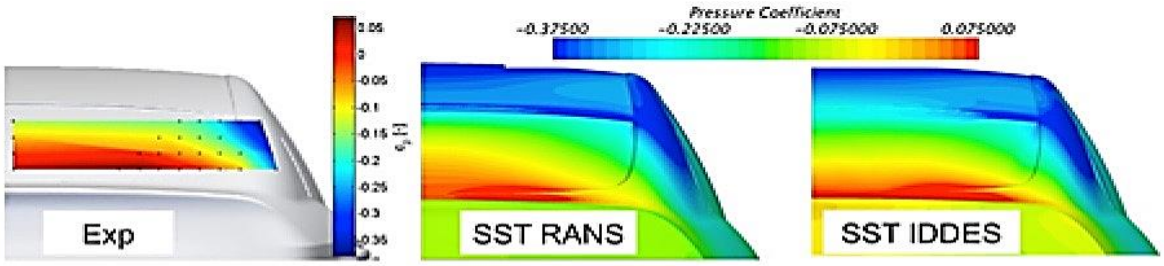

Figure 18: Mean pressure coefficient comparison between the experiment, SST-RANS and SST-IDDES for the estate back configuration [22].

Jakirlić et al.[23] investigated eddy-resolving simulations of the notchback `DrivAer' model. The underbody and wheel rotation play a vital role in the aerodynamic performance. These two crucial features were in the focus of the study. Different configurations were tested, e.g. a detailed and smooth underbody together with rotating and stationary wheels. The computation was done using VLES(very-large-eddy simulation), RANS and URANS. RANS-based approaches used the k-ζ-f turbulence model. It was shown that the RANS/URANS method was not capable of capturing any spectral dynamics of turbulence. VLES appeared as being clearly the superior method in this case.

2.4 Transient CFD simulations of real car geometry

In the previous section, we discussed the differences in steady and transient approaches considering simple shapes and car-like geometries. In this section, we will focus on real, production car geometries. The development of production car aerodynamics usually has its roots in the racing teams departments. The new developments and techniques are then transferred to the production car through the so-called “technology transfer”[24][30]. The car manufacturers usually never publish their aerodynamic research, or, if they do, they rarely provide any detail. Two examples are the publications [26] and [27]. These papers discuss the aerodynamic development of the Audi Q5 and the Range Rover Evoque SUV models. In the case of the Audi car model, the authors used DES for the CFD optimization of the car. The development of the DES approach is described in [28]. The test case Audi A6 car model was simulated using the OpenFOAM software. Special attention was dedicated to the newly developed automatic mesh generation tool. The new method, while still producing a satisfactory, good parallel performance, enables a reduction of the turnaround times to almost 24 hours, starting from the surface mesh and ending with a quasi-steady DES solution. A test case using the Audi A6 used 0.5 hours clock time for mesh generation, 5 minutes for case initialization and 28 hours for the flow simulation on a Linux cluster (192 cores of a 3.3 GHz Xeon and 2 GB RAM per core)

Jakirlić et al. [29] assessed different steady and transient approaches applied to production car geometry. The turbulence models were tested on a full-scale Audi A1 car model. The study compared hybrid RANS/LES as DDES (delayed detached-eddy simulation) with the PANS and VLES approach, as well as steady and unsteady RANS using the k-ζ-f turbulence model. All calculations were done in parallel using the OpenFOAM software tool. The incoming velocity was assumed as 38.8 m/s. Results from all four methods show good agreement with the experiment for the mean pressure coefficient distribution along the upper and lower surface of the vehicle. There is a stagnation point at the nose of the vehicle where the pressure coefficient reaches values of around 1. As the flow continues towards the upper curved front surface it comes to the flow acceleration and the pressure drops. It reaches values around -0.5. This is followed by the second pressure increase over the front window and a step-like decrease over the top surface. The last pressure increase is caused by the flow deceleration in the wake region of the rear window. Pressure coefficient oscillations are noted near the radio antenna. The distribution on the underbody showed fewer variations. There is a pressure drop at the front wheel axis followed by a smooth pressure increase. The small variations most likely come from the spanwise velocity fluctuation and detailed underbody.

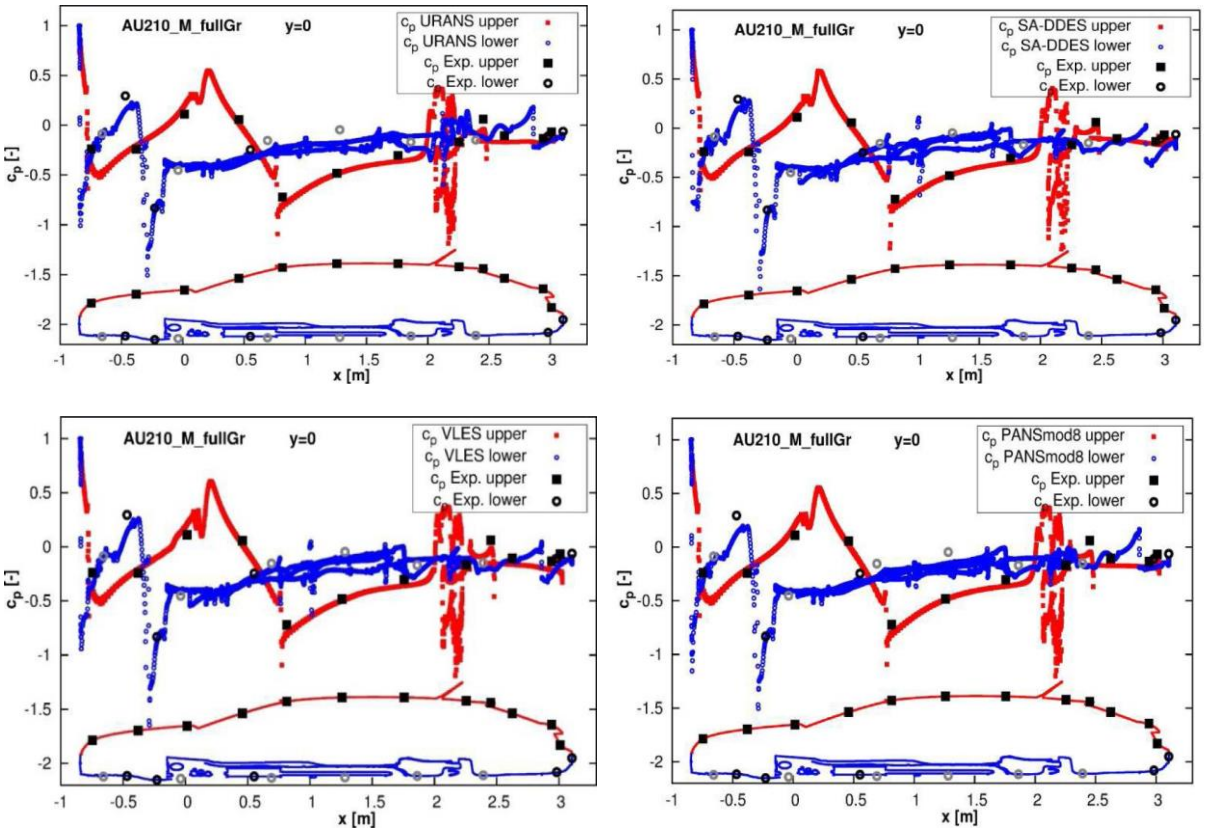

Figure 19: Mean pressure distribution along the upper and lower central vertical plane of the Audi A1 model [29].

3 Bluff body aerodynamics

3.1 Bluff body

Every rigid body that moves through fluid experiences a drag force, which slows its motion. This force consists of the two components viscous (frictional) drag and pressure drag. The viscous drag is the consequence of the tangential viscous shear stresses between the fluid and the wall surface of the body. It is associated with the development of the boundary layer. A parallel flow along a flat plate or streamlined bodies could be considered as a typical example of a viscous-dominated drag. Such streamlined bodies experience mild pressure gradients and the flow remains attached over almost the entire streamwise length.

On the other hand, the pressure drag comes from the turbulent motion in the separated wake flow region emerging on the downstream side of the bluff bodies. As seen from the experiments, the rectangular box produces a drag coefficient of $c_D = 0.9$, which is entirely due to the pressure drag. An even higher value is shown for the vertical flat plate, where viscous forces are practically negligible. [25]

The passenger car is categorized as the bluff body and forms very similar flow features to the rectangular box. Although, with the aerodynamic optimization, there is a trend that progresses to a body of revolution, the flow separation still characterizes the nature of such a body.

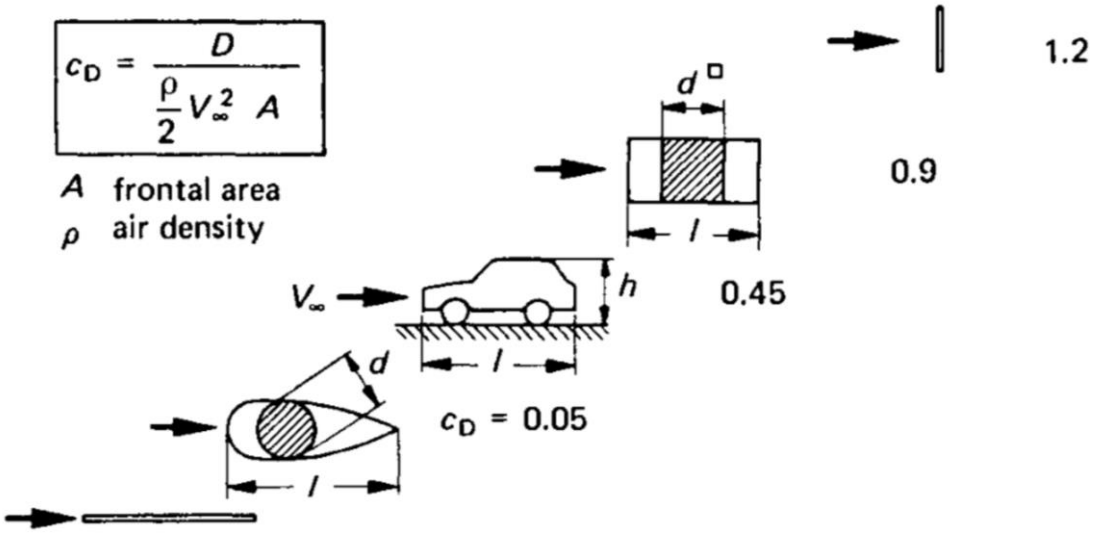

Figure 20: Drag coefficient comparison for different bluff bodies and a car[25].

3.2 Reference bodies in automotive aerodynamics and choice of the test case

The automotive industry uses many different generic as well as more complex car-like models for aerodynamics investigation. Most of these models are small-scale, mainly to reduce the cost of such investigation. The car shapes can be divided into three categories: simple bodies; basic car shapes; and the production (series) cars [36]. The first two categories are often studied in the literature. Investigation of the production cars are very rarely published and mostly kept in secret.

The Ahmed body is probably the most well-known test case. It demonstrates the significance of the rear-end slant angle and its impact on the aerodynamic characteristics. After the measurements in the wind tunnel, Ahmed[34] associated different flow regimes with the slant angle. The peak of the drag was identified at an approximate 30-degree slant angle. This identified a critical slant angle. Several different simplified bodies have been developed by different authors since the Ahmed, such as the NRSSCC SAE model, the Davis model, and the Chrysler model. But none of them have been as well accepted in academic circles as the Ahmed body. Windsor and Howell presented another generic body – the so-called “Rover model”− to accelerate the investigation of shape effects with a more complex body compared to the Ahmed. The body has a different nose design. The geometry is based on the proportions of medium-sized production cars of that time. Interchangeable back-ends make it possible to study flow conditions under different slant angles.

MIRA is the most well-known car-like geometry, which has nowadays been replaced by the more complex DriveAer model [38] to close the gap between the generic car geometry and production car. The model has become popular due to its realistic representation of the flow field, which is very similar to that of production cars. The geometry and experimental data are available to the public in order to allow for verification for CFD simulations. The vehicle was developed with 18 mockup configurations (Fastback, Estate Back, and Notchback)

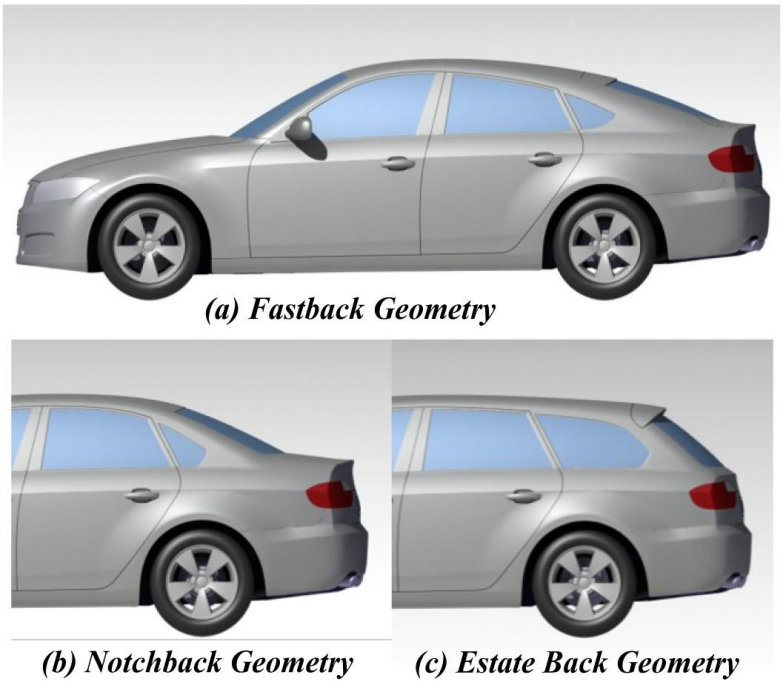

Figure 21: Different rear configurations of DriveAer Model[38].

Physically, car-like bodies produce an incredibly complex flow, which is very difficult to simulate even with today's high-performance computers. Simulation of real driving conditions would have to consider the road, rotation of the wheels, the internal flow throughout the engine and front radiator, as well as the side mirrors, detailed underbody, and many other details for a realistic description[37]. The flow gets even more complicated in a racing application, where the vehicle possesses additional geometry features to improve different aerodynamic characteristics, such as downforce. Even though there has been a significant improvement in computational technology, which makes computational resources more affordable and allows computation of the meshes that exceeds 100 M or even 300 M elements[22], many of the flow features are still not reproduced correctly.

As already seen in the literature review, the simple steady turbulence models struggle to capture the flow correctly even for the simple shapes, e.g., cylinder or cube. Problems arise especially in the prediction of the velocity profiles in the wake or bubble length. The flow around the Ahmed body is far more complex, due to the flow separation, detachment, and reattachment. However, it is still significantly simpler than complex geometries like the DriverAer model. Simpler models require a small computational grid, which means shorter computational time and smaller resources. This is considered as an advantage when many different model parameters or complete turbulence models need to be tested in a short period. The behaviors of the different turbulence models can be quickly evaluated on a simple geometry before switching to a more complex shape. This allows the poorly performing models to be excluded very early on and for the simulation with the models which have already provided good results to be continued. This procedure can reduce the overall time, which is necessary for a comprehensive model assessment. In this context, the Ahmed body is a very suitable test case for the starting point.

3.2.1 The Ahmed body

The Ahmed body is a generic car model, and it has essential aerodynamic characteristics of a car. Ahmed[34] originally proposed the model in the 80s. It was designed to investigate the effect of the different slant angles on the flow characteristics and drag coefficient. The body is basically made up of three parts: a forebody, a midsection, and a rear end. The front part has rounded edges to achieve a separation-free flow over its surface, even though recent experiments confirm some locally confined separation at the front part. The middle section is long enough to exclude any flow interference between the front and rear part of the body. The original dimensions of the Ahmed body as experimentally investigated by Meile et al.[40] can be seen in Figure 22. The body is mounted 50 mm above the ground, it is 1044 mm long, 389 mm wide, and 288 mm high. The front nose has a radius(R) equal to 100 mm.

The model does not have any rotating or fixed wheels, side mirrors or other details that are typical of a car's geometry. The model should still be able to reproduce the typically three-dimensional flow in the front area as well as the flow along the side wall, roof, underbody, and slant. The whole idea behind the Ahmed body was to generate a simplified car model, which could produce the main flow features of a real car.

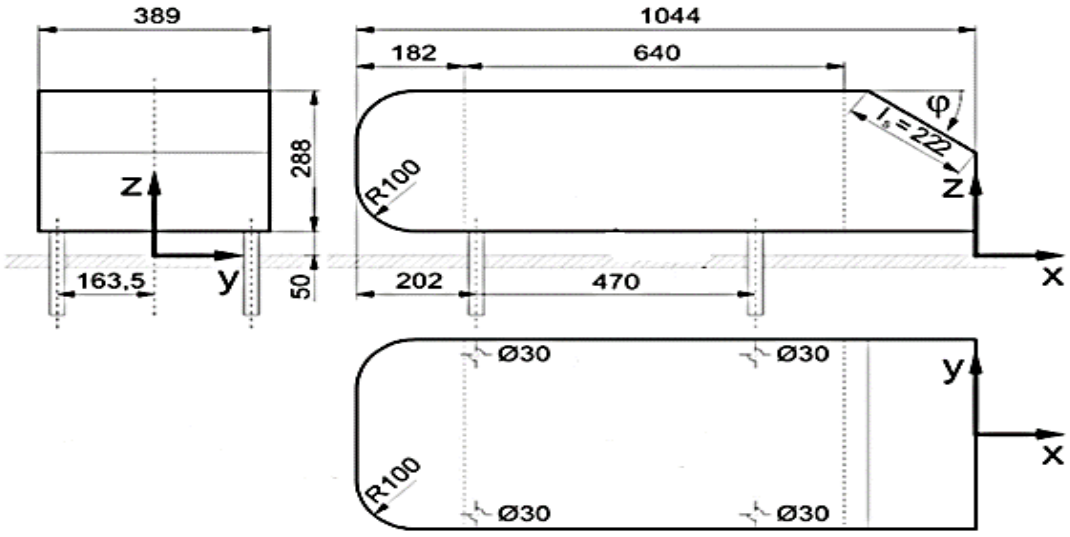

Figure 22: Original Ahmed body dimensions from the experimental study of Meile et al.[40].

3.2.1.1 Experimental investigations

Ahmed [34] investigated several different slant angles from 0 to 40° (0, 5, 12.5 ,20, 30, 40). The model was tested at the imposing 60 m/s free-stream velocity, which corresponds to the Reynolds number of 4.29×10^5 based on the car length. The original experiments were conducted in a subsonic wind tunnel. Pressure taps were positioned only on one half of the body, with approx. 210 pressure taps on the forebody and 83 on the midsection. Only three slant angles(5°, 12.5°, 30°) had pressure taps integrated into the rear slant. Their number varied from 430 to 450 taps, depending on the slant angle. Flow visualization and pressure measurements were carried out on the facility at Braunschweig, the force measurements and wake survey at Göttingen. The level of inflow turbulence intensity was estimated as below 0.5% in both wind tunnels. The measurements were set up exclusively for the zero yaw flow condition. A directional probe with ten holes was used for the wake survey. The probe was mounted on a rigid carriage for easy manipulation at the Cartesian translation. Various oil fog techniques were used for visualization of the flow and vorticity in the rear part. Force and pressure measurements were taken using a strain gauge balance, which was connected to the four cylindrical legs of the body.

Based on the measurement of all the different slant angles φ it was possbile to analyze the drag behavior. The pressure drag contributions of the front part c_k^*, slant c_S^* and base c_B^*, as indicated in Figure 23 are listed together with the total drag coefficient for the selected slant angle in Table 1. The front, base and slant pressure drag coefficent are defined [34]:

$$c_{B,S,K,W}^* = \frac{F_{B,S,K,W}}{\frac{\rho}{2}\, {v_\infty}^2\, A_{proj}} \qquad 3.1$$

where A_{proj} denotes the reference area computed as $A_{proj} = 0.389 \cdot 0.288 = 0.112\, m^2$ and the force is obtained by the experiment using a strain gauge balance. It is clear that the fore-body makes only small contributions to the total drag coefficient and stays nearly constant; a higher value is obtained only for the 30° low drag case. This demonstrates the very weak interference between the front and the rear part of the body as a consequence of the long midsection part. The pressure drag from the slant and base increases as the slant angle increases. For the zero slant angle, all contribution comes from the base area. As the angle φ increases, the vertical base area decreases and the slant area increases. This directly translates into the pressure distribution, in that the slant contribution increases while the base contribution decreases. For example, the change from 5° to 30° implies a decrease of the base pressure drag from 86% to 29%. On the other hand the pressure drag from the slant increases from 5% to 66%. In total, the pressure drag contribution varies between 76% and 85% and the friction drag c_R^* takes values from 24%−15%, dependent on the slant angle. The total pressure drag remains dominant but exhibits a minimum of around $\varphi = 12.5°$ as seen in Figure 23. The literature usually describes the angles 12.5° and 30° as critical angle φ_c. Below $\varphi_c = 12.5°$ the flow remains fully detached while it is fully detached beyond $\varphi_c = 30°$. The latter is indicated by the sudden decrease of the drag coefficient.

Table 1: Drag breakdown for different slant angle configurations [34]

φ	c_w	c_k^*	c_S^*	c_B^*
5°	0.231	0.016	0.010	0.158
12.5°	0.230	0.016	0.037	0.122
30°(High drag)	0.378	0.016	0.213	0.092
30°(Low drag)	0.260	0.019	0.089	0.101

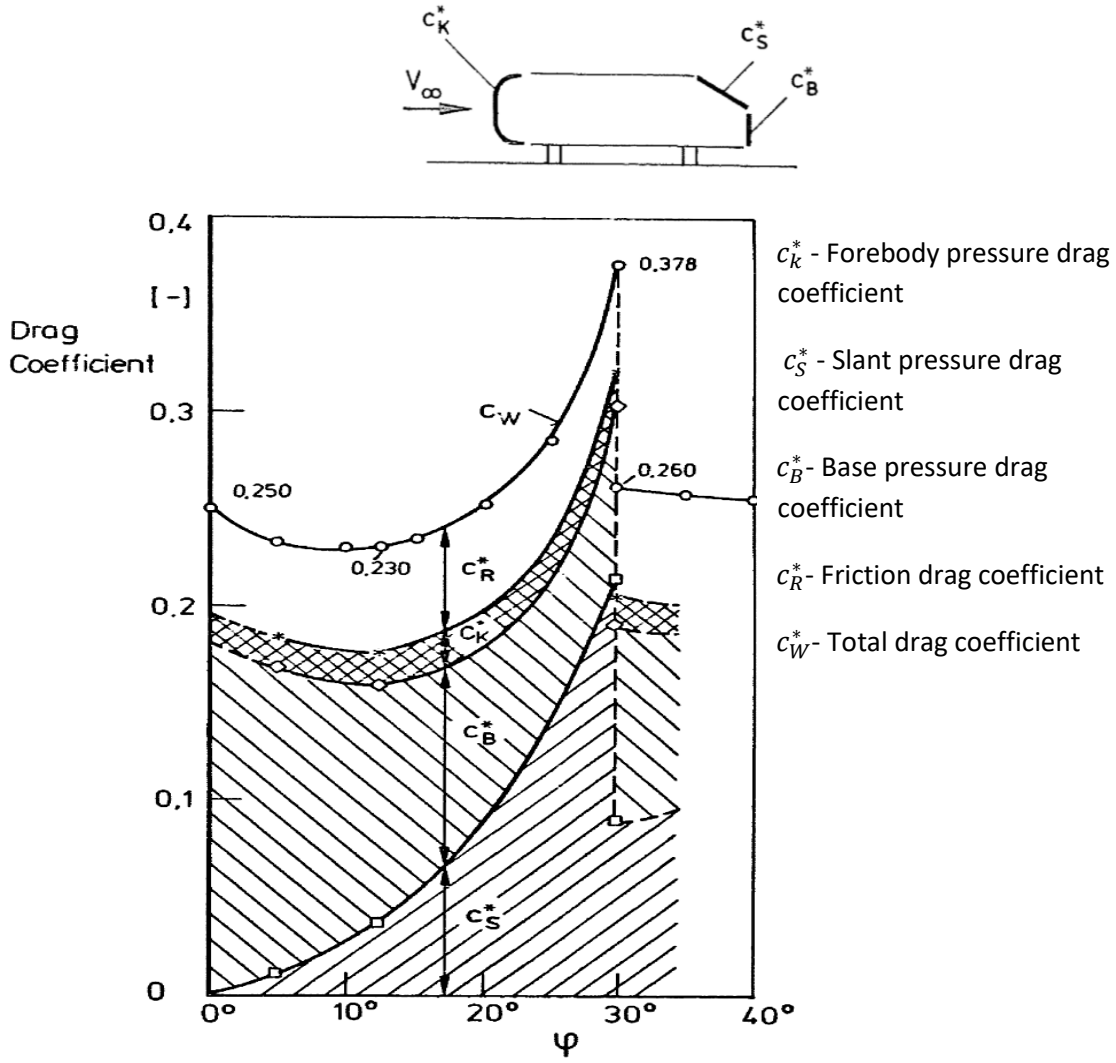

Figure 23: Variations of and drag coefficient c_k^*, c_S^*, c_B^*, c_R^* and c_W^* for selected slant angles [34].

The different drag coefficients observed for the varying slant angles result from the different flow features over the rear part and downstream of the body. At angles less than 12.5°, the flow remains fully attached over the entire slant. The separation occurs only along the lateral sides, as the flow separates along the trailing-edge forming two counter-rotating vortices indicated with the letter C in

Figure 24. The intensity of this vortex depends on the rear slant angle. The two recirculation regions (A and B) are the consequence of the flow coming from the top and bottom edge of the base being located one above the other. These two recirculation regions are being formed by two horseshoe vortices D, which emerge parallel to the base surface, and align themselves with the main flow downstream where they merge with the vortices C. The flow, in this case, is mainly two-dimensional. Some three-dimensional features can be noticed along the side edges due to longitudinal vortices. Ahmed discovered an interaction between the vortex C and A and their dependency on the slant angle. Vortex B is mainly dependent on the flow conditions and the ground gap but is indirectly affected by slant angle through the vortices A and C.

At angles of between 12.5° and 30° the flow separates along the upper edge of the slant forming a closed, elliptic region of the recirculation flow indicated with the letter E. A higher slant angle means stronger C-pillar vortices, which prevent the spreading of the recirculation over the lateral sides. The region between the reattachment line, the lower and side slant edge forms two triangular-like shaped regions of attached flow indicated with F. The locally confined separation region causes a significant pressure drop over the whole surface of the slant, which results in a rise of the pressure drop. The length of the separation bubble and the pressure drag increase with the slant angle. Again the flow coming from the underbody gap and the trailing edge forms the two counter-rotating vortices A and B in the wake, emerging into a large recirculation zone D. The drag coefficient becomes the highest for $\varphi = 30°$, reaching $c_D = 0.378$.

Beyond 30° no reattachment occurs on the slant, the flow remains entirely separated. The pressure along the base begins to increases as a result of the weaker strength of the C-pillar vortices. Once again the flow attains a quasi-two-dimensional characteristics.

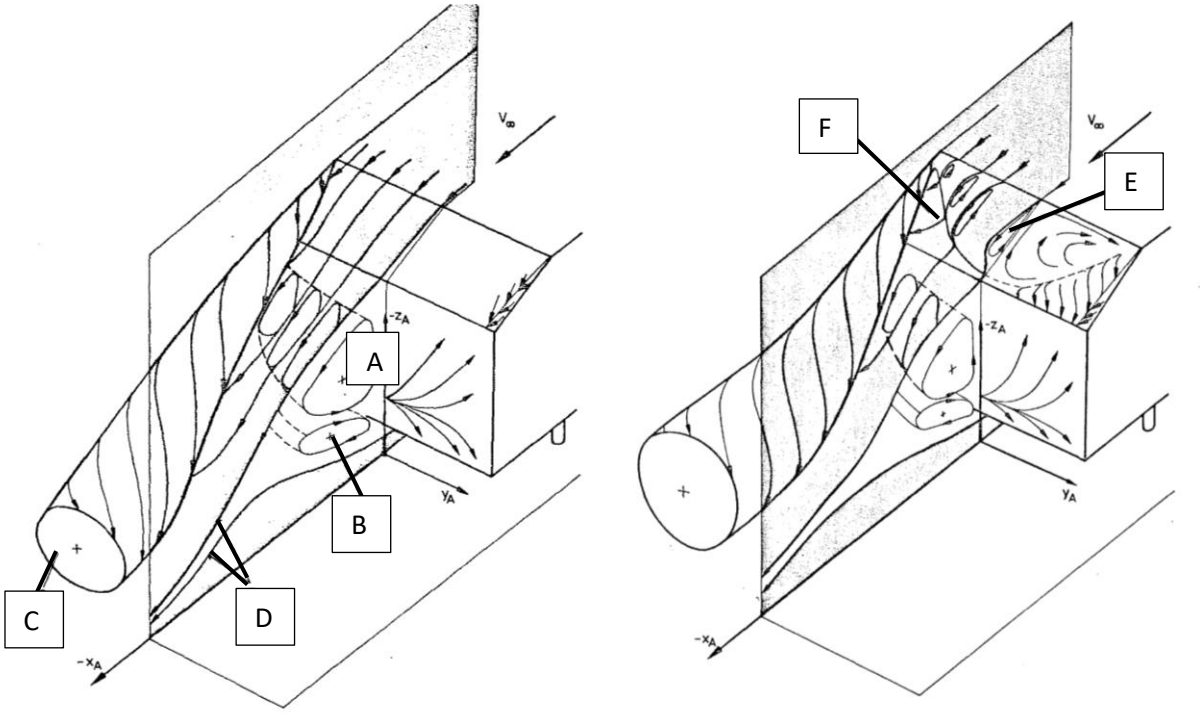

Figure 24: Vortex system in the wake region of Ahmed body for two different slant angles: left(<12.5°) and right (12.5≤ φ ≤30°) [34].

MOVA (models for vehicle aerodynamics) was a project funded by the European Union to develop a framework for the efficient and accurate calculation of the external aerodynamic flow using improved turbulence models. The turbulence models needed to be validated against the experimental data to

assess their accuracy. For this purpose H. Lienhart et al. [39] performed an experimental study of the flow around the Ahmed body to generate a new database. Two different slant angles (25° and 35°) were tested in the ¾ open LSTM low-speed wind tunnel at Erlangen. The measurements were done at 40 m/s airflow velocity. The inlet conditions were measured by a two-component hot-wire system to provide boundary conditions for the numerical simulation. The flow visualization confirmed the early findings by Ahmed regarding the complex three-dimensional flow in the wake. The flow is particularly sensitive to small changes in the slant angle at values of around 30°. The oil streak lines in Figure 25 show attached flow in the case of a 25° angle, while showing full separation at 35°. Laser Doppler anemometry was used for the measurements of all three velocity components in the symmetry plane. These measurements covered part of the downstream wake region as well as part of the upstream region of the model.

Figure 25: Flow visualization on the slant: 25°(left) and 35°(right)[39].

Figure 26 shows the distribution of the mean velocity vectors along the symmetry plane upstream and downstream of the body. The three perpendicular planes in the wake region shows the distribution of the turbulent kinetic energy . They clearly indicate the formation of the of two counter-rotation C-pillar vortices on each side of the slant.

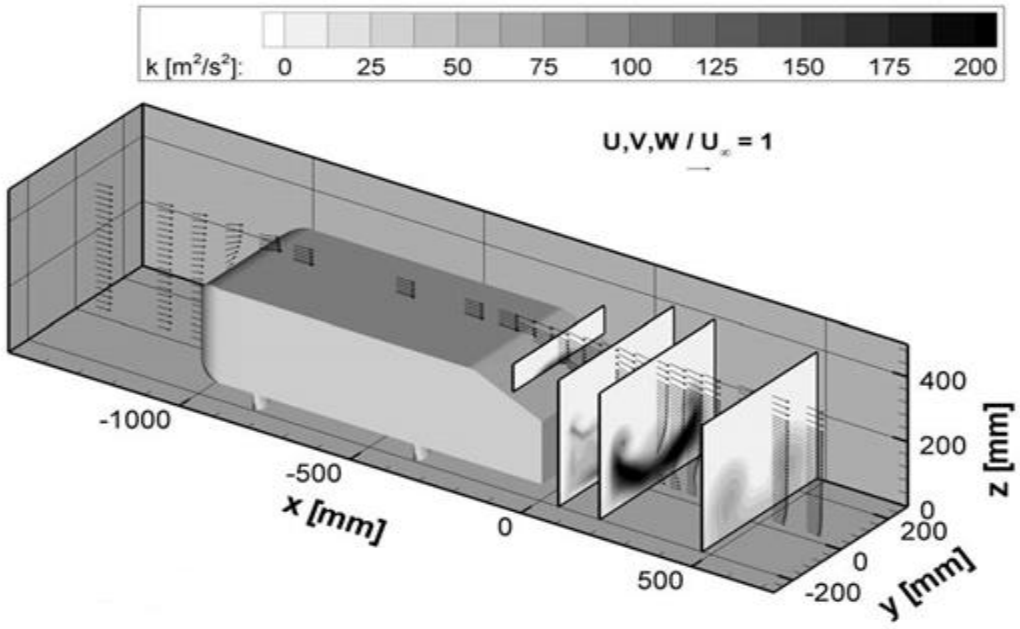

Figure 26: Turbulent kinetic energy and velocity distribution around the Ahmed body(25°)[39].

More recently, Meile et al.[40] performed a further experimental study, considering two Ahmed body configurations (25° and 35°) under symmetrical and yawing inflow conditions. The model was used in its original dimensions (see Figure 22). The test was performed in the low-speed wind tunnel of the Institute of Fluid Mechanics and Heat Transfer at the Graz University of Technology. Maximum inlet speed is limited to 41 m/s. A six-component load balance platform was used for the measurement of the aerodynamic forces. PIV (particle image velocimetry) was used for the analysis of the velocity field in the wake region.

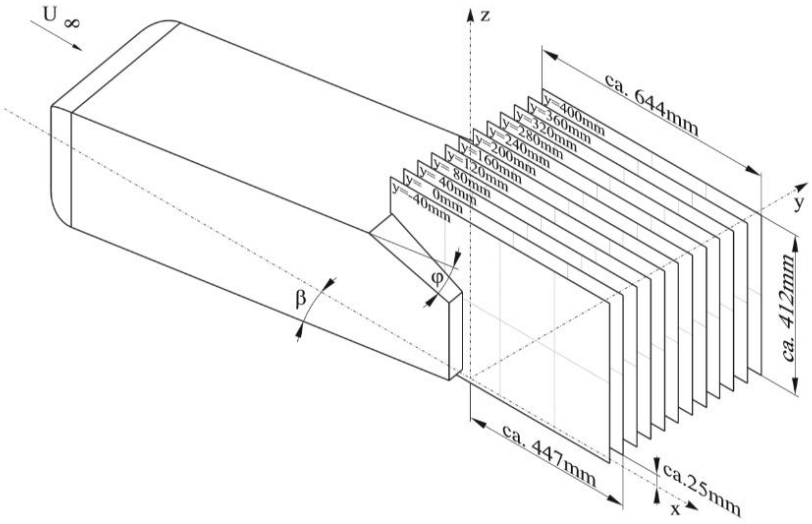

Figure 27: PIV measurement planes[40].

Figure 28 shows a comparison of the velocity profiles measured for the 25° angle on the symmetry plane for zero yaw angle. The data from Meile et al. [40] are compared to the experimental data from Lienhart et al.[39], which were obtained using the LDA method. The comparison shows good overall agreement in the wake region. A minor disagreement appears on the slant in the near-wall region. The authors claimed this might be due to the light reflections in the PIV measurements.

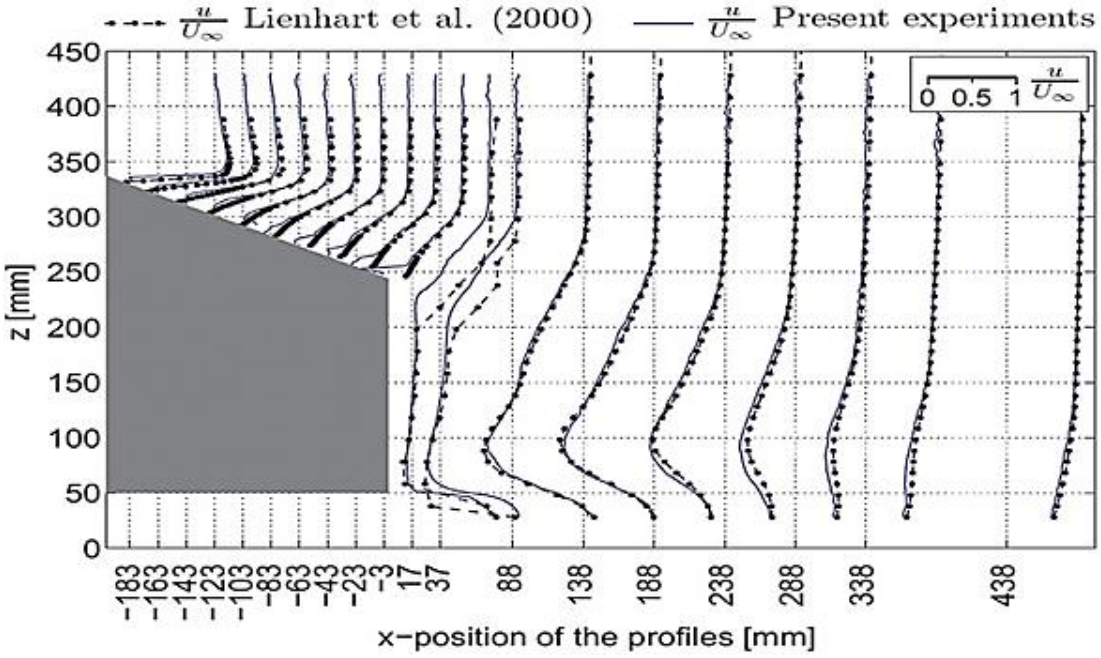

Figure 28: Normalized velocity profiles at different x-positions on the symmetry plane for 25° slant angle U=30 m/s[40].

The most experimental studies focus only on the rear part to investigate the flow beside and near the wake. Very rarely some authors have studied the structure of the flow separation on the front part of the body. Spohn and Gilliéron[41] experimented in a closed water tunnel on a 0.28 scaled Ahmed body with 25° slant angle. The model was tested at inlet velocities 0.1 and 0.3 m/s, which corresponds to $Re = 3 \cdot 10^3$ and $Re = 9 \cdot 10^4$, respectively, based on car length. An electrolytic precipitation technique was used for flow visualization. The results indicate two foci, which are the origin of the two counter-rotating longitudinal vortices. A detailed flow topology can be seen in the Figure 29 The separation starts as the flow reaches the upper curved surface of the front part. This produces two counter-rotating vortices, which arise from the foci F_1 and F_2.

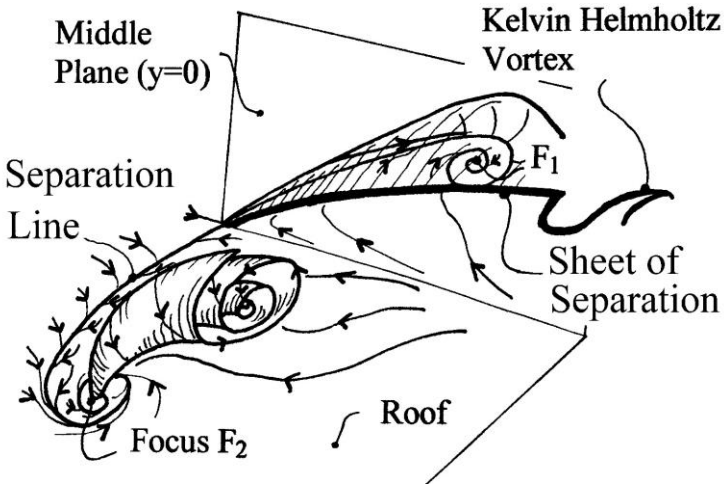

Figure 29: Flow topology on the front part (Roof)[41].

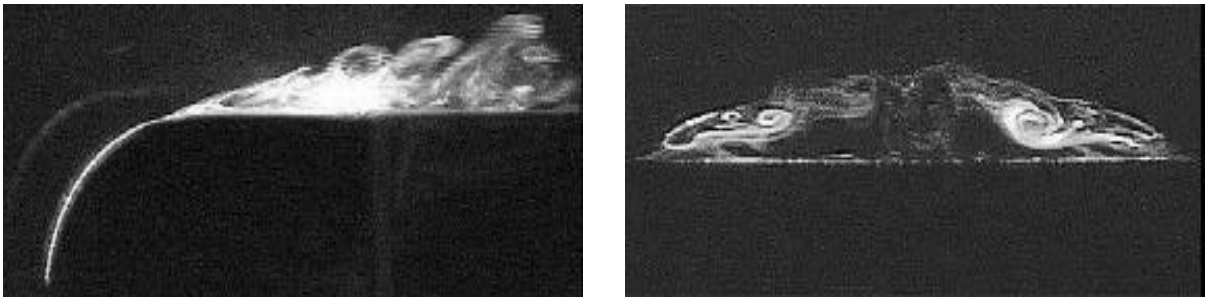

Figure 30: Side(left) and cross-section(right) view of the flow structure in the front separation zone[41].

Vino et al. [45] made a temporally averaged and time-resolved unsteady analysis of the wake. The analysis of the flow in the wake reveals more completed mechanisms than those originally proposed by Ahmed[34]. Time-resolved averaged measurement still shows good agreement with the previous experiments. The unsteady analysis of the instantaneous signals coming from the two pressure taps on the base.Taps were located one above the other so that they can monitor the unsteady pressure history in recirculatory bubbles emerging inside the wake. The vortex shedding is similar to the flow past square cylinder at a Strouhal number of about 0.39. Figure 31 show the streamlines in the wake region of the Ahmed body.

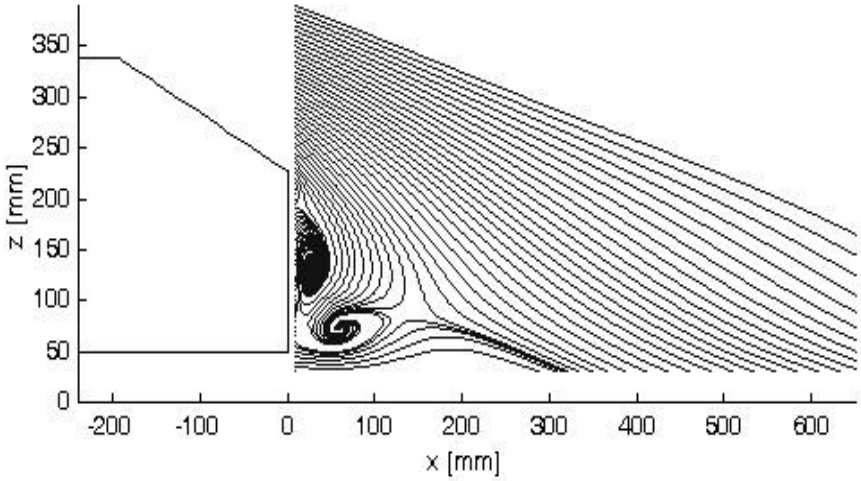

Figure 31: Streamlines visualization on the symmetry plane in the wake region of the Ahmed body [45].

3.2.1.2 Numerical investigation

Guilmineau [18] performed an unsteady numerical simulation of the flow around the Ahmed body for two slant angle configurations (25° and 35°) using a URANS approach. The investigation was done using several different turbulence models: k- ω SST, EASM (explicit algebraic stress model), S-A (Spalart – Allmaras), ASM (algebraic stress model), Reynolds stress transport model-based on isotropization of the production model for the pressure strain correlation ($R_{ij} - \omega$IP), Reynolds stress transport model: ($R_{ij} - \omega$ SSG) of Speziale, Sarkar and Gatski. For the less challenging case $\varphi = 35°$, all turbulence models predict correctly the flow topology. The best results for the drag coefficient was achieved with the EASM turbulence model with an error of less than 3% relative to the experimental value. On the other hand, none of the models were able to correctly predict the flow reattachment on the slant for the φ =25°. All simulations predicted a massive flow separation.

Similar observations were noted by Krastev and Bella [19]. In this paper, the authors tested several URANS turbulence models on a 25° slant angle configuration. Alternative calculations were done using steady-state RANS. The latter was carried out to evaluate which kind of approach could be the best compromise between accuracy and time-saving optimization. All the data were compared to the experimental data from the literature. Not all tested turbulence models were able to capture time-dependent flow behavior. The k-ε models gave satisfactory results regarding the local and global drag coefficients. Results obtained from the Spalart−Allmaras model were overpredicted. Good results were obtained using a modified k-g model. The model was proposed by Kalitzin, where g stands for $g = \frac{1}{\sqrt{\beta^* \omega}}$ (β^* represents modelling constant). The k-ε and k-g model captured a time-dependent behavior of the flow. The flow comparison of the results from the RANS/ URANS was followed by a brief discussion on which of the two could be the best modeling approach for the first stage of the aerodynamics optimization process. The obtained results showed that the max. differences in the drag coefficient computed steady and time-averaged URANS solutions were less than 2%. Velocity profiles were almost the same. The differences appear to be not very sensible in view of the substantial time savings associated with the steady approach. URANS would seem to be not so stable when dealing with

more complex flow configurations. The author therefore suggested using LES or DES as an alternative transient approach rather than URANS.

In a later study, a hybrid RANS−LES approach was tested and evaluated against the transient RANS approach by E.Guilmineau el at. [35]. The authors tested k- ω SST and EARSM (explicit algebraic Reynolds stress model) compared against the DES and IDDES hybrid RANS−LES methods considering an Ahmed body with 25° and 35° slant angle. The RANS parts of the tested hybrid models are based on the k- ω SST turbulence model. The 35° slant angle showed good results for all turbulence models. In the 25° configuration none of the models except for the IDDES were able to correctly predict the flow reattachment. Poor results were achieved with the SST and EARSM models, especially for the lift coefficient, which is strongly underpredicted. In contrast, DES and IDDES overpredicted the drag coefficient. All in all, it could be concluded that IDDES provided the best agreement with the experiment.

Large-eddy simulation can basically provide a more accurate description of the turbulent flow than the hybrid approach. The method directly resolves the larger eddies and models the small, more isotropic structures. Serre et al. [20] simulated the flow around the Ahmed body using different LES subgrid-scale models (near-wall modeled, dynamic-Smagorinsky and wall-resolved spectral-vanishing method) and the hybrid approach DES−SST. Different grids were used with a sizing of 20 to 40×10^6 nodes. The LES has a high demand on the numerical resolution. The near-wall-resolved LES predicted the attached flow over the slant; all other models show detached flow. All simulations satisfactorily describe the recirculation in the wake region of the body. The occurrence of flow reattachment on the slant at the smaller Reynolds number predicted by LES in the flow around the Ahmed body was confirmed by Kranjović and Davidson [15,16**]**. Moreover they additionally studied the flow along the front part, where they confirm the experimental findings of the small separation region at the curved front section of the body. The focus of the study is not only to show the capabilities of the LES but also to highlight the differences between the instantaneous and time-averaged representation of the results when post-processing unsteady numerical simulation. The results show significant differences. According to the authors, the instantaneous flow never takes averaged values, which is however the most common way of showing the unsteady results. The relevance of the time-averaged results for some aerodynamic properties is questionable.

It has become an essential task, especially for the application in industry, to test and adjust different CFD models by comparing the results in a benchmark study. The benchmark test is important for the selection of appropriate turbulence models, testing new programs or grid dependency. Bordei and Popescu [17] present a comprehensive benchmark study of 138 numerical simulations of the flow around the Ahmed body to test the aerodynamic efficiency. The software used in the study was: Fluent, CFX, OpenFOAM, and PowerFLOW. Thirteen different grid resolutions were tested, ranging from 500 k to 23 M cells. The grids were created by the Harpoon meshing software. Turbulence models used were: Spalart−Allmaras; realizable k-ε (RKE); k-ω shear-stress transport (k-ω SST); transition k-kl- ω; transition -SST; Reynolds stress model (RSM); large-eddy simulation (LES); detached-eddy simulation (DES), scale-adapted Simulation (SAS); and v^2-f. The simulations were run in steady as well as the unsteady mode. The Spalart−Allmaras appeared to be an excellent choice for predicting the aerodynamic performance. It yielded the smallest error for the drag coefficient(0.53%) followed by SST-CFX and RKE steady. It produced better results than, for example, the very popular k−ε model or the three equation k-kl- ω model and even the sophisticated RSM model. It is computationally cheap and seems to be a good choice for c_D optimization. The realizable k- ε also produces very good results and the steady RKE took third place in the drag coefficient. It has to be kept in mind that the RKE produces better results than,

for example, than coarse LES , which is computationally much more costly. Unsteady RKE produces worse results for both the lift and drag coefficient. The best value for the lift coefficent is achieved by the transition SST model (0.27%) followed by the k-ω SST (OpenFoam) and an error of 0.7%. Third was $the\ v^2$- f turbulence model with an error of 1.3%. LES and DES lift coefficient produced an error of 9.22% and 11.59%, respectively.

4 Numerical analysis

This section will focus on a brief introduction to the CFD. Partial differential equations can describe flows and their phenomena. The conservation equations cannot be solved analytically except for limited cases. Approximate solutions can be obtained using numerical methods, where a discretization method approximates the differential equation by a system of algebraic equations. The quality of the numerical methods depends on the quality of the discretization used.

4.1 The basic equations of fluid dynamics (Navier−Stokes equations)

A most accurate approximation of the governing system of partial differential equations and boundary conditions plays a crucial role in every numerical method. In fluid dynamics, the governing system of partial differential equations is the set of the Navier−Stokes equations.

4.1.1 Conservation principles

In fluid mechanics, the conservation laws can be derived by considering a given considered quantity in a control volume. The two considered quantities are the mass and the momentum. The general form of the conservation equation is[48]:

$$\frac{d}{dt}\int_{\Omega_{CM}} \rho\phi \, d\Omega = \frac{\partial}{\partial t}\int_{\Omega_{CV}} \rho\phi \, d\Omega + \int_{S_{CV}} \rho\phi \, (\vec{v}) \cdot \vec{n} \, dS \tag{4.1}$$

where CV represents the control volume fixed in space, S_{CV} the surface enclosing CV, $\vec{n}$ is the unit orthogonal vector to S_{CV}, $\vec{v}$, stands for the fluid velocity. It basically describes the rate of change of the quantity ϕ, which is equal to the change of the quantity inside the control volume plus the net flux through the boundary of the control volume. This term is usually called a “convective term.” For the continuity equation $\phi = 1$,and for the momentum equation $\phi = \vec{v}$(velocity vector).

4.1.2 Continuity equation

The continuity equation can be obtained by writing the balance of mass for a control volume Ω. The physical principle can be described with the following statement: the net mass flow out of the element must be equal to the time rate of decrease of mass inside the element. The statement mathematically represents the following equation[48],

$$\frac{\partial}{\partial t}\int_{\Omega} \rho \, d\Omega + \int_{S} \rho\vec{v} \cdot \vec{n} \, dS = 0 \tag{4.2}$$

After applying the Gauss theorem, we can rewrite the integral formulation into a differential form of this equation, which is more widely known as the continuity equation,

$$\frac{\partial \rho}{\partial t} + \nabla \cdot (\rho v) = 0 \tag{4.3}$$

Using a cartesian coordinate system it can be further rewritten

$$\frac{\partial \rho}{\partial t} + \frac{\partial \rho u_i}{\partial x_i} = \frac{\partial \rho}{\partial t} + \frac{\partial (\rho u_x)}{\partial x} + \frac{\partial (\rho u_y)}{\partial y} + \frac{\partial (\rho u_z)}{\partial z} = 0 \tag{4.4}$$

4.1.3 Momentum equation

The momentum equation represents Newton's second law applied to the moving fluid element. The net force on the body is equal to mass times acceleration. The starting point for the derivation represents the control volume, where we apply the equation[48]:

$$\frac{\partial}{\partial t}\int_{\Omega}\rho\vec{v}\,d\Omega+\int_{S}\rho\,\vec{v}(\vec{v}\cdot\vec{n})\;dS=\sum\vec{f} \tag{4.5}$$

The right-hand side of the equation represents the forces that act on the fluid. They can be either surface forces (shear stresses, surface tension) or body forces (gravity, centrifugal). To be able to solve the equation system we need to make some assumptions. One way is to describe the fluid as Newtonian, which can be applied to many technically relevant actual fluids. We can define the total surface stress tensor in index notation as [48]:

$$T_{ij}=-\left(p+\frac{2}{3}\mu\frac{\partial u_j}{\partial x_j}\right)\delta_{\mathrm{ij}}+2\mu D_{ij} \tag{4.6}$$

$$D_{ij}=\frac{1}{2}\left(\frac{\partial u_i}{\partial x_j}+\frac{\partial u_j}{\partial x_i}\right) \tag{4.7}$$

where δ_{ij} represents the Kronecker delta function ($\delta_{\mathrm{ij}}=1$, if i=j, $\delta_{\mathrm{ij}}=0$, if $i\neq j$). Accordingly the viscous stress tensor can be rewritten as,

$$\tau_{\mathrm{ij}}=2\mu D_{ij}-\frac{2}{3}\mu\delta_{ij}div\;v \tag{4.8}$$

The equation simplifies for the incompressible flows ($\partial u_j\backslash\partial x_j=0$). After introducing the surface and body forces into the conservation equation,

$$\frac{\partial}{\partial t}\int_{\Omega}\rho\vec{v}\,d\Omega+\int_{S}\rho\,\vec{v}(\vec{v}\cdot\vec{n})\;dS=\int_{S}\underline{T}\cdot\vec{n}\,dS+\int_{\Omega}\rho\vec{b}\,d\Omega \tag{4.9}$$

The equation contains volume and surface integrals. This can be simplified using the Gauss divergence theorem and rewritten in vector notation as,

$$\frac{\partial(\rho\vec{v})}{\partial t}+\nabla\cdot(\rho\vec{v}\vec{v})=\nabla\cdot\underline{\mathrm{T}}+\rho\vec{\mathrm{b}} \tag{4.10}$$

If we assume the gravity as the only body force and we can rewrite 4.10 in index notation

$$\frac{\partial(\rho u_i)}{\partial t}+\frac{\partial}{\partial x_j}\left(\rho\mathrm{u_j}\mathrm{u_i}\right)=\frac{\partial\tau_{ij}}{\partial x_j}-\frac{\partial p}{\partial x_i}+\rho\mathrm{g_i} \tag{4.11}$$

where $\mathrm{g_i}$ corresponds to the gravitational acceleration in the direction $\mathrm{x_i}$.

4.1.4 Dimensionless form of equations

In automotive aerodynamics, the experimental studies are often carried out on a small prototype, and the results are provided in the dimensionless form. Reducing the number of parameters which determine the solution is a useful technique, allowing for a scaling of the solution to the real conditions. An order of magnitude analysis indicates the importance of different terms. Some of them may be neglected depending on the physics of the flow and reduce the computational effort. The procedure

begins with the selection of the appropriate scales for the normalization. In the case of Navier−Stokes equations, we usually use a reference velocity v_0, reference length L_0, reference time t_0, reference pressure $\rho_0 v_0^2$ The variables are defined as[48]:

$$t^* = \frac{t}{t_0} \qquad x_i^* = \frac{x_i}{L_0} \qquad u_i^* = \frac{u_i}{v_0} \qquad p^* = \frac{p}{\rho_0 v_0^2} \tag{4.12}$$

Applying the normalized variables in the continuity and momentum equation, we obtain for the constant density flow $\rho = \rho_0 = const.$,

$$\frac{\partial u_i^*}{\partial x_i^*} = 0 \tag{4.13}$$

$$St\frac{\partial (u_i^*)}{\partial t^*} + \frac{\partial}{\partial x_j^*}\left(\mathrm{u_j^* u_i^*}\right) = +\frac{1}{Re}\frac{\partial^2 u_i^*}{\partial x_j^{*2}} - \frac{\partial p^*}{\partial x_i^*} + \frac{1}{Fr^2}\,\gamma_\mathrm{i} \tag{4.14}$$

In the equation above we define the Strouhal, Reynolds, Froude number and γ_i denotes the normalized gravitational vector.

$$St = \frac{L_o}{v_o t_o} \qquad Re = \frac{\rho v_o L_0}{\mu} \qquad Fr = \frac{v_0}{\sqrt{L_0 g}} \qquad \gamma_\mathrm{i} = \frac{g_i}{g} \tag{4.15}$$

The most commonly used formulation in external aerodynamics depends only on the Reynolds number, as Fr >> 1 and St=1 (time scale is assumed as $\mathrm{t_0} = \frac{L_0}{v_0}$).

4.2 Numerical discretization

4.2.1 Finite volume method

Discretization methods are used to approximate the system of differential equations of fluid flow at discrete locations in time and space. The most common approach in CFD is the finite volume method. This method is applied on most commercial CFD software including ANSYS Fluent. In this method, the computation domain is subdivided into smaller volumes or cells. The conservation laws are expressed for the centroid of each cell. The flow variables are calculated at this point. They are interpolated to the control volume surface to approximate the surface fluxes. Fluent manages this using upwind schemes. There are several different upwind schemes available (first order, second order, Quick ...)[48,49,51].

After applying a balance equation to each cell of the domain, we obtain a system of algebraic equations that needs to be solved. This is done numerically in an iterative manner. The advantage of a Finite Volume Scheme is that it is a conservative regardless of the applied face-value interpolation and grid type. As such a scheme is not sensitive to the combination of different grid elements in the case of unstructured grids, like triangles and quads in 2D, or hexahedra and tetrahedron in 3D. This an advantage, especially when handling complex geometries.

4.2.1.1 Spatial discretization

Third–order MUSCL scheme

This represents the combination of central differencing and second-order upwind schemes,

$$\varphi = \Theta\varphi_{f,CD} + (1-\Theta)\varphi_{f,SOU} \quad 4.16$$

This is more accurate than the second-order upwind scheme and provides less numerical diffusion in complex flows. In contrast to the Quick scheme, it can be used on structured and unstructured meshes and for all transport equations [51].

Bounded central differencing scheme (BCDS)

This scheme is not as accurate as the central differencing scheme but it is the default option for the LES approach in ANSYS FLUENT. Central differencing schemes provide lower numerical diffusion, but have problems with physical oscillations. The method is based on the normalized variable diagram (NVD) and the convection boundedness criterion (CBC)[51].

4.2.1.2 Temporal discretization

Bounded second-order implicit

Basic flow equations require discretization in space and time when considering unsteady flow problems. The spatial discretization remains identical to the steady formulation. Every transient term needs to be integrated over Δt. In the case of bounded second-order implicit scheme, the variable is described as, [51]

$$\frac{\partial\varphi}{\partial t} = \frac{\varphi_{n+\frac{1}{2}} - \varphi_{n-\frac{1}{2}}}{dt} \quad 4.17$$

$$\varphi_{n+\frac{1}{2}} = \varphi_n + \frac{1}{2}\,\beta_{n+\frac{1}{2}}(\varphi_n - \varphi_{n-1}) \quad 4.18$$

$$\varphi_{n-\frac{1}{2}} = \varphi_{n-1} + \frac{1}{2}\,\beta_{n-\frac{1}{2}}(\varphi_{n-1} - \varphi_{n-2}) \quad 4.19$$

4.2.1.3 Evaluation of gradients and derivatives

Scalar values at the cell faces, velocity derivatives and subsequent diffusion terms are calculated using gradients. In ANSYS Fluent the gradient can be computed by the Green-Gauss cell-based, Green-Gauss node-based or the least square cell-based technique[51].

Green-Gauss node-based

This is known as a very accurate but also expensive method. It gives particularly good results on unstructured meshes. The gradient is approximated by the arithmetic average of nodal values on the face[51]:

$$\bar{\varphi}_f = \frac{1}{N_f}\sum_{n}^{N_f}\bar{\varphi}_n \qquad 4.20$$

Least square cell-based

This provides similarly accurate results as the node-based method on the unstructured meshes but it less expensive to compute then the Gauss node method. It is the default option in ANSYS Fluent. [51] The method assumes a linear solution between the cell centroid of the two cells c_0 and c_i along the vector δr_i,

$$(\nabla\varphi)\cdot\Delta r_i = \left(\varphi_{c_i} - \varphi_{c_0}\right) \qquad 4.21$$

4.3 The computational domain

The definition of the computational domain plays an essential role for the accuracy of the numerical simulation of road vehicles. Giving a general recommendation for the domain size is difficult. They are usually based on the wind tunnel experiments in the industry, an expert aero-dynamist or simply by trial-and-error. The domain should be as representative as possible to reproduce the wind tunnel experiment accurately, but at the same computationally affordable. A vast domain could result in an increased number of cells, which leads to a lengthy computational time.

The flow field downstream of the car and generic bodies (wake flow region) is of primary interest for correctly predicting the aerodynamic coefficients. In the case of the Ahmed body the wake flow is dominated by two counter-rotating vortices, which spread far downstream towards the exit of the domain. Different experiments, e.g. Lienhart et al. [39] (see Fig. 26) still show high levels of TKE at around half a meter downstream the Ahmed body, but the turbulence is probably present long further downstream before it completely dissipates. It is desired to have a mostly recovered flow regime before the flow reaches the end of the domain. Downstream domain lengths may extend from 3 streamwise lengths L of the body up to 17 L, depending on the case. The upstream flow should have a fully developed boundary layer before reaching the vehicle [30]. The blockage ratio usually determines the lateral boundaries and height. This represents the ratio of the frontal area of the vehicle to the cross-sectional area of the wind tunnel. The blockage ratio is equal to zero on the road. Ideally, the blockage ratio should be kept as small as possible in CFD simulations. As a rule of thumb, it is desirable to keep the blockage ratio under 5% [32]. The effect of the blockage ratio and differences between the CFD and measurements were investigated by Perzon [74]. The Fluent [75] guidelines suggest to keep it under approx. 1.5%. Some of the relevant domain sizes used in the literature are in shown in the Table 2 below. The dimensions are represented for each of the coordinate direction x, y, z.

Table 2: Domain sizes

Test case		Domain size			
		X(L-length of the vehicle) total length of the domain in the x-direction		Y(W-width of the vehicle)	Z(H-height of the vehicle)
		Upstream of the model nose	Downstream of the model rear		
Ahmed body					
	Guilmineau[18]	2L	3L	0.9L	1.46L
	Krastev & Bella[19]	1.2L	5L	1.9L	1.4L
	E.Guilmineau el at.[35]	2L	5L	1.79L	1.34L
	Serre et al.[20]	8L		1.86L	1.37
	Stevenson[30] Brondolo[77]	2L	5L	2L	2L
	Meile et al.[62]	14.36L		1.8L	1.46L
Generic SUV model					
	Forbes et al.[21]	15.5L	12.5L	-	-
»DrivAer« Automotive Body					
	Ashton and Revell [22]	4L	6L	11W	8H
Real car model					
	Audi A1 car model				
	Jakirlić et al.[29]	Approx. 17L		Approx. 8.4L	Approx.7.4L

4.4 Grid generation

After choosing the appropriate domain, we need to define a proper mesh point distribution. For simple geometries, e.g. a circular cylinder or surface-mounted cube, it is easy to construct a grid. Such shapes can be meshed using quadrilaterals or triangles in 2D or hexahedra and tetrahedra in 3D. The gridlines are usually aligned with the flow. These grids are structured. In the automotive industry, we deal with far more complex geometries, which do not allow the use of pure hexa elements. Such grids usually contain a mix of quadrilaterals and triangles in 2D, and pyramids, hexahedra and tetrahedra in 3D. These are called unstructured grids. A structured grid is, in general, more accurate, requires less computational time and less memory. On the other hand, the unstructured grid is usually much faster to generate. A brief introduction into different grid topologies will be given in the following subsections.[49]

4.4.1 Structured grid

The ideal mesh element would have a perfect cube shape. The edges of the cube are aligned with the cartesian coordinates where all the edge points are equidistant (Δx=Δy=Δz). The position of any grid point can be easily identified using two indices for a 2D case or three for 3D, e.g. (i,j,k). In this system, each point has four or six neighboring cells, depending on the dimensionality. If we consider point K, with the indices (i,j,k), then the indices of the neighboring cells differ by ± 1 from the corresponding index of K. The connectivity between the neighboring cells simplifies programming. The obtained algebraic system of equations can be solved quickly and efficiently. This type of mesh is the so-called Cartesian grid, which offers the ideal solution regarding accuracy. This mesh could be an option in simple applications, such as a parallel wall or in certain aeroacoustic computation, where higher order schemes are required.[48,49]

The Cartesian grid cannot be applied for many simple external flows in engineering application, e.g. like the NACA wing profile. The body consists of the curved front part, which would be impossible to be meshed with entirely orthogonal elements. In order to fit the geometry, we need the curvilinear grid. These are the so-called body-fitted grids. Such a grid structure may have different topologies, the most common being [49]:

- H-mesh
  The topology can be associated with the letter H. Horizontal and vertical gridlines are curvilinearly approaching the wing profile. Grid refinement can be applied near the leading and trailing edge.

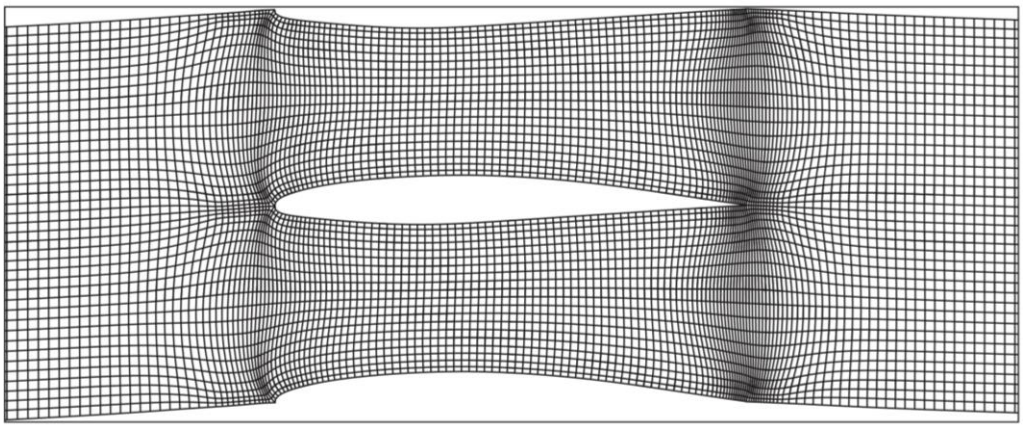

Figure 32: H-type grid around the wing profile[49].

- C-mesh
  The grid around the leading edge can be associated with the letter C. The gridlines are curvilinear on one side of the domain and are straightened out on the other side. The topology is good for the concentration of the gridline in the wake region.

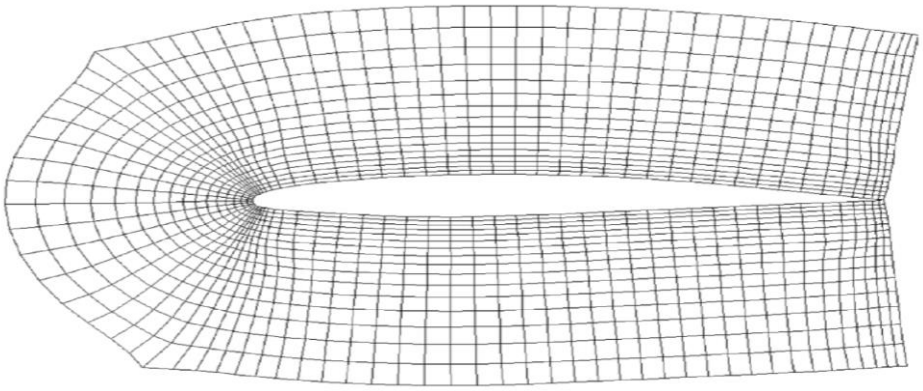

Figure 33:C-type grid around the wing profile[49].

- O-mesh
  The geometrical shape of the obstacle is surrounded by curvilinear gridlines. This configuration allows for an accurate resolution in the near-wall region, especially around the leading and trailing edges, which makes it interesting for accurate description of the boundary layer. It is often used in external aerodynamics applications.

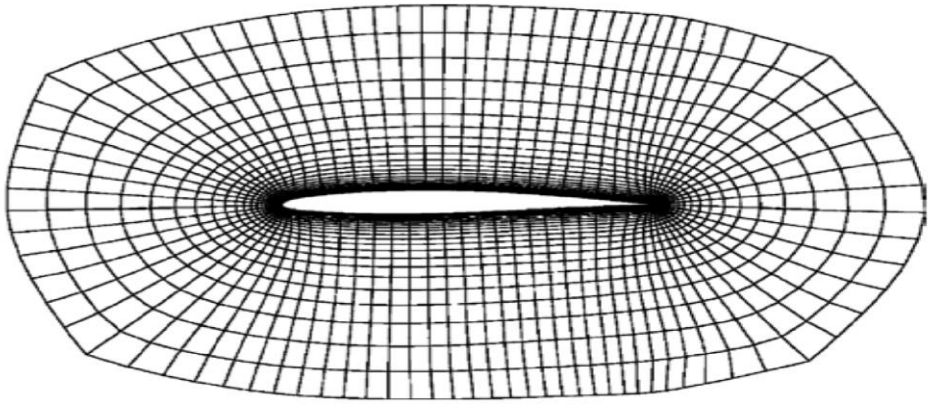

Figure 34: C-type grid around the wing profile[49].

One of the drawbacks of the structured grid is controlling the distribution of the grid points. Adding a point in one region produces unnecessary spacings in other regions, which will affect the mesh of the whole domain. As a consequence, the mesh may contain long and thin cells, which could potentially affect convergence. The problem gets worse for complex 3D geometries. The solution is to define the multi-block grids. Each block represents a subset of the numerical domain with its grid. The disadvantage of such an approach is the enforcement of conservation at the block boundary. On the other hand, the approach allows for an adaption to more complex topologies. One block can be chosen for the near-field of the body and others for the surroundings. This approach is popular in the external aerodynamic flow. Generic bodies in automotive aerodynamics are simple enough and allow the use of the structured grids inside the blocks. An example can be found in Hinterberger et al. [47]. They perform a LES simulation of the Ahmed body with the self-developed finite volume Code LESOC_2. The code was developed at the Karlsruhe University at the Institute for Hydromechanics. It was developed

to solve the incompressible three-dimensional Naviers−Stokes equation on block-structured grids. The computational grid was created by the commercial software ICEM-CFD. The first considered grid had aprox. $8.8 \cdot 10^6$ elements and 93 blocks and the second grid had $18.5 \cdot 10^6$ elements and 214 blocks. Due to the rounded nose on the front, it is necessary to use the O-grid topology in the near-wall region. This allows for a high quality grid resolution particulary when using small grid spacing normal to the wall.

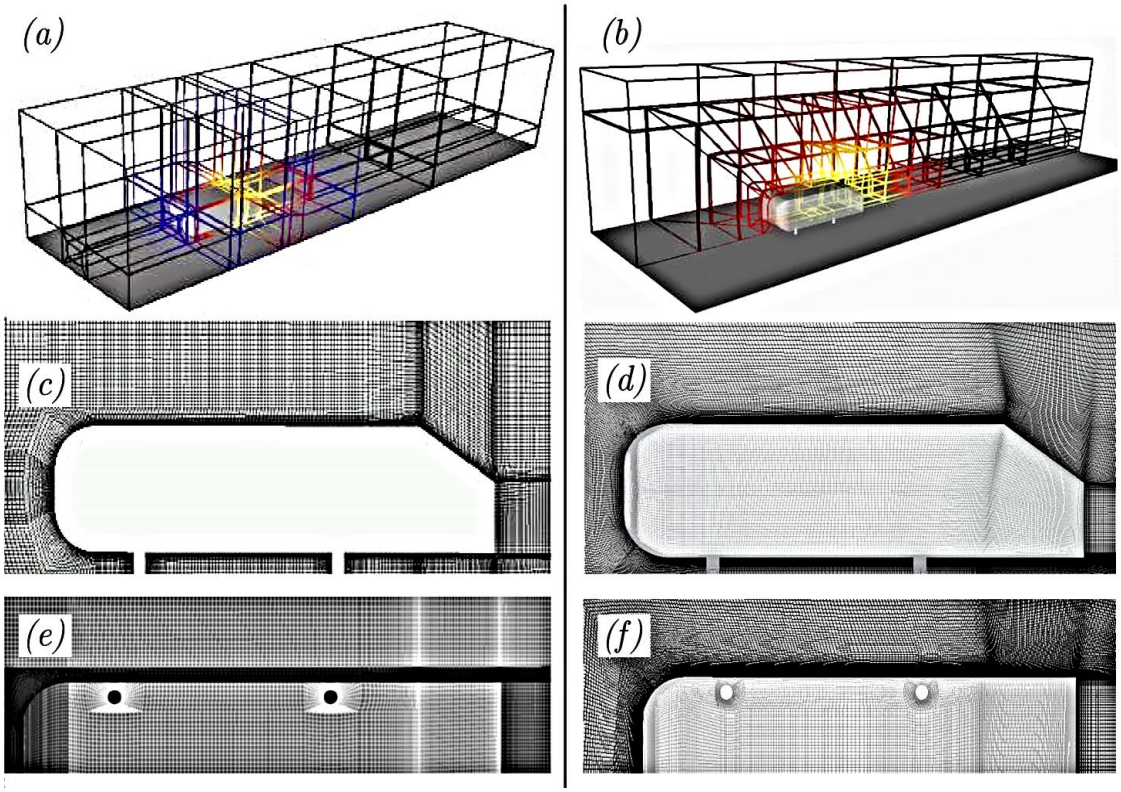

Figure 35: LES grids for Ahmed body: (a,b) block topology; (c,d) side view; (e,f) bottom view; Grid 1: (a,c,e), Grid 2: (b,d,f) [47].

4.4.2 Unstructured grid

The meshing of the unstructured grid is flexible and can be applied to practically any geometry. They have become the standard approach in industrial CFD. Most of the commercial meshing tools have integrated meshing algorithms, which automatically creates a mesh after some primary constraints are given to the program. The unstructured grid allows the grid refinement in a specific region, with no effect on the other parts of the domain. This is very convenient for flexible grid adaption (refinement or coarsening) based on different criteria like, for example, flow gradients. Based on the shape of the elements for the mesh generation, we distinguish: a) triangle/tetrahedra elements; b) hybrid elements (combinations of tetrahedra, pyramids, and prisms); c) quadrilateral and hexahedra[49].

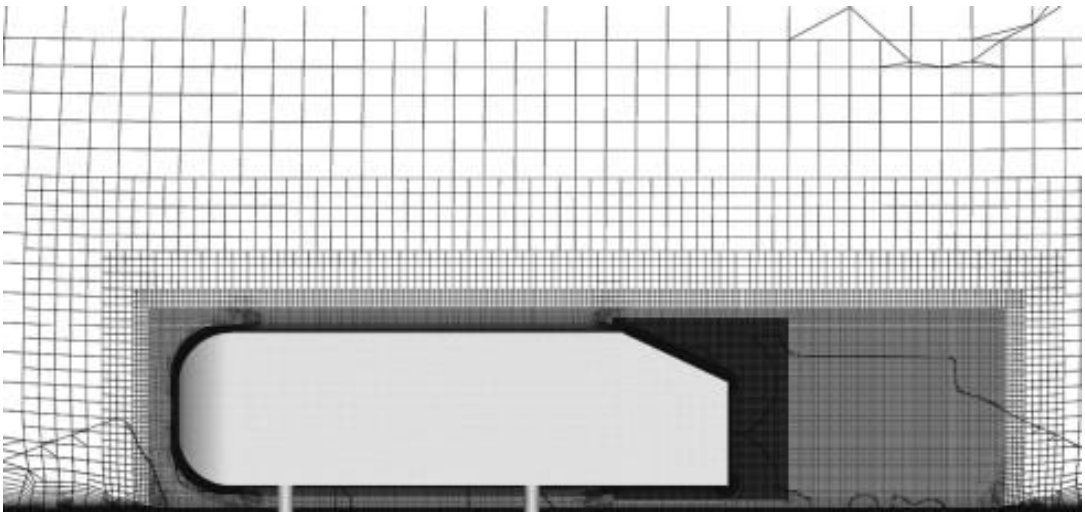

Figure 36: Unstructured mesh around the Ahmed body[47].

4.4.3 Near-wall mesh treatment

The position of the first grid cell above the wall is essential to predict the flow inside the boundary layer accurately. Flow near the wall is mainly affected by the viscous forces. The near wall flow conditions strongly depend on Reynolds number. The thickness of the boundary layer usually varies and is not constant along the body. The near-wall region can be typically divided into several sublayers, as shown in Figure 37. [51]

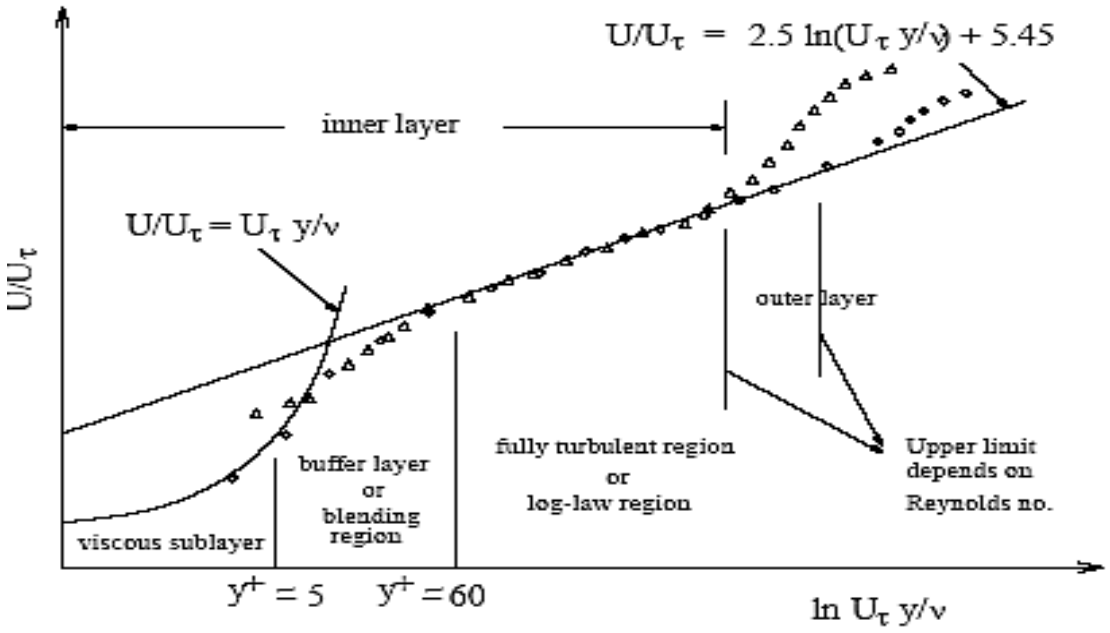

Figure 37: Streamwise velocity in the near-wall region [51].

The viscous sublayer(y^+<5) has practically a laminar flow. Viscous forces are dominant over the inertial forces in the transfer of mass, momentum or heat. The buffer layer(5 <y^+< 60) represents the transitional layer between the viscous region and the fully turbulent region. The next region is the fully turbulent inner layer where the log-law applies. The fully turbulent outer layer depends on the Reynolds number. The accurate prediciction of the flow in this near-wall region is significantly

important for the results of the numerical simulation, particularly for an accurate prediction of the drag coefficient Therefore, the mesh generation in this region should be carefully planned

The choice of the wall boundary condition essentially depends of the wall distance of the first grid point measured in y^+ units. There are different approaches. Some of them use a wall function to describe the near-wall region, others attempt to solve (or model) the flow equations down to the wall. A wall function-based computation usually requires the height of the first cell inside the log-layer, which starts at y^+ values of around 30 and can extend up to 100 or even 200, dependent on the Reynolds number. For the wall-resolved meshes, at least a couple of the cells are needed in the viscous and buffer layers to ensure accurate results. In such cases a wall spacing with a y^+ of the first grid point close to 1 is required. The height estimation can be made according to [52]. If we at first define the y^+ as,

$$y^+ = \frac{\rho_W u_\tau y}{\mu_w} \tag{4.22}$$

where the subscription w of the density and viscosity variable stands for the wall. The $u_\tau = \sqrt{\frac{\tau_w}{\rho}}$ denotes the friction velocity. Assuming the densitiy and viscosity as, $\rho_w = \rho_\infty$ and $\mu_w = \mu_\infty$, the equation above can be rewritten as [52],

$$y^+ = Re\sqrt{\frac{c_f}{2}}\frac{y}{L}, \text{ with } Re = \frac{\rho_\infty U_\infty L}{\mu_\infty}, \tag{4.23}$$

and hence,

$$\frac{y}{L} = \frac{y^+}{Re\sqrt{\frac{c_f}{2}}} \tag{4.24}$$

The wall distance relative to the characteristics length L of the body as the function of the Reynolds number and skin friction coefficient c_f. The latter can be aproximated from the flat plate correlation, using the following equation:

$$c_f \approx \frac{0.455}{ln^2(0.06Re_x)} \tag{4.25}$$

with,

$$Re_x = 0.1 \cdot Re \tag{4.26}$$

4.4.4 Mesh-quality metrics

In the previous section, we discussed some fundamental differences between the structured and unstructured grid generation. The structured grid is numerically more efficient, but this cannot be taken for granted. To ensure and minimize the discretization error, elements have to have a regular shape and fulfill some orientation requirements and others. Some of the mesh quality metrics used for the evaluation of the hexahedra element used in the study will be represented below. The categorization of values is made according to the ICEM-CFD software, which was presently used for the mesh generation.

4.4.4.1 Determinant (3x3x3)

This criterion is very similar to the determinant (2x2x2) stencil. It is based on the computation of the Jacobian matrix. The determinant is defined as the ratio between the smallest and the largest determinant of the Jacobian matrix. The determinant (3x3x3) is more convenient for hexahedral elements. The only difference is that the latter include the edge midpoints of the block in the computation of the Jacobian determinant. The Jacobian determinant is calculated in the natural coordinate system of the element for 27 node positions. This helps to determine how close the elements are to the perfect shape. Perfect shape for a hexahedron is a cube and has the Jacobian of 1, on the other hand, 0 indicates a degenerated element and negative values inverted elements. [53]

4.4.4.2 Orthogonal quality

This describes how close the internal angle is to the ideal angle. In the case of the hexahedron this means an angle of 90°. Orthogonal quality is computed using the normal face vector (A_i) , the vector from the cell centroid of the adjacent cell (c_i) and the vector from the cell centroid toeach of the faces (f_i). In the next step the cosine is computed between each face. The smallest calcuated cosine value between the faces represents the orthogonality of the cell. The orthogonality takes a value from 0−1 (0=worst cells , 1=best cells)[53].

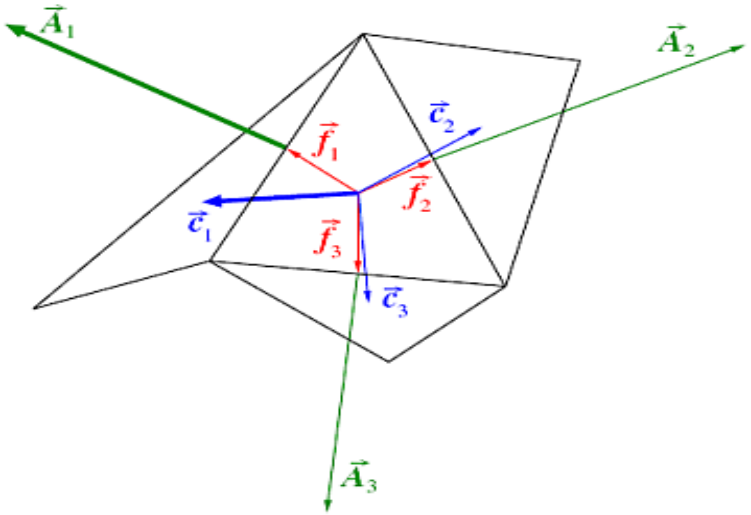

Figure 38: Vector distribution along the cell element[53].

4.4.4.3 Skew

The criterion skew calculates the maximum skewness of an element. The definition is different for two- or three-dimensional elements. An example of the vector distribution used for calculation is shown in Figure 39 for a hexahedron. The quality metric is defined as the worst (max.) normalized angle of all the element's faces, and the vector that starts from the centroid point of the element goes through the center of the face. 1 indicates ideal and 0 the worst skewness [53].

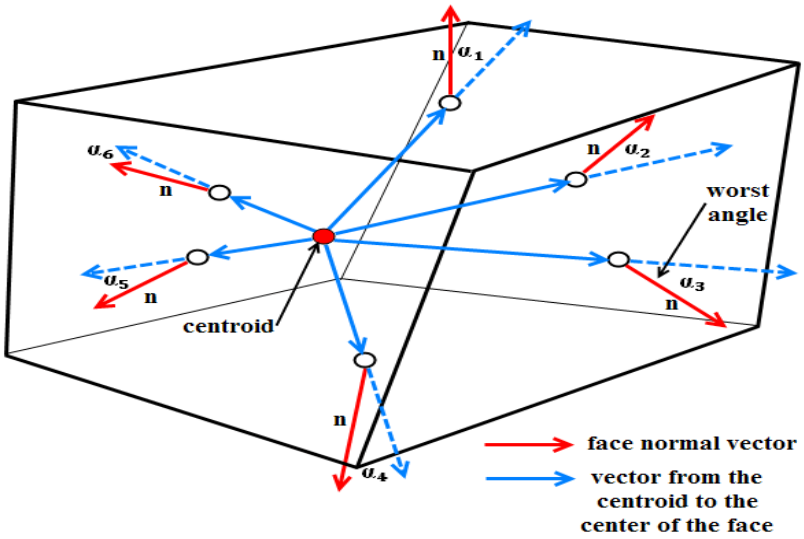

Figure 39: Skew for hexa element[53].

4.4.4.4 Aspect ratio

Different element types have different aspect ratio definitions. For the hexahedron, the aspect ratio is defined as the ratio between the minimum and the maximum element edge. 1 represents the best possible and 0 the worst [53].

$$Aspect\ Ratio = \frac{\min[e, f, j]}{\max[e, f, j]}$$

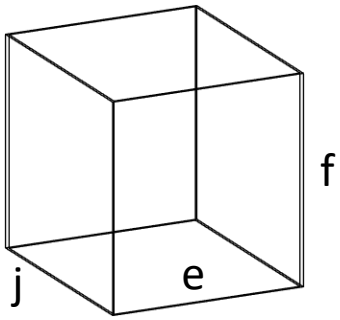

Figure 40: Aspect ratio edge definition.

4.5 Solution method

After the grid generation and discretization, we arrive at a large system of nonlinear algebraic equations that needs to be efficiently solved. In general, we distinguish between the pressure- and density-based solvers. The pressure-based solver is more convenient for low-speed incompressible flows and is often used in ground vehicle aerodynamics. The velocity is calculated from the momentum equation. The pressure field is obtained from the continuity solving a pressure or pressure correction equation, so that the velocity with the pressure correction then satisfies the continuity equation [51,65].

4.5.1 Pressure-based coupled solver

There are two types of pressure-based solvers: segregated and coupled. The first one solves the continuity, momentum (and energy) equation in an uncoupled manner. The method is very robust and uses a minimal amount of memory (each variable needs to be stored once at a time). The disadvantage of this approach is a poor convergence rate in some applications. The pressure based coupled algorithm solves the continuity and momentum equations in a coupled manner. This increases the convergence rate. The disadvantage is the memory increase. The memory requirements are up to two times higher compared to the segregated solver. The procedure for the coupled algorithm is represented in Figure 41. [51]

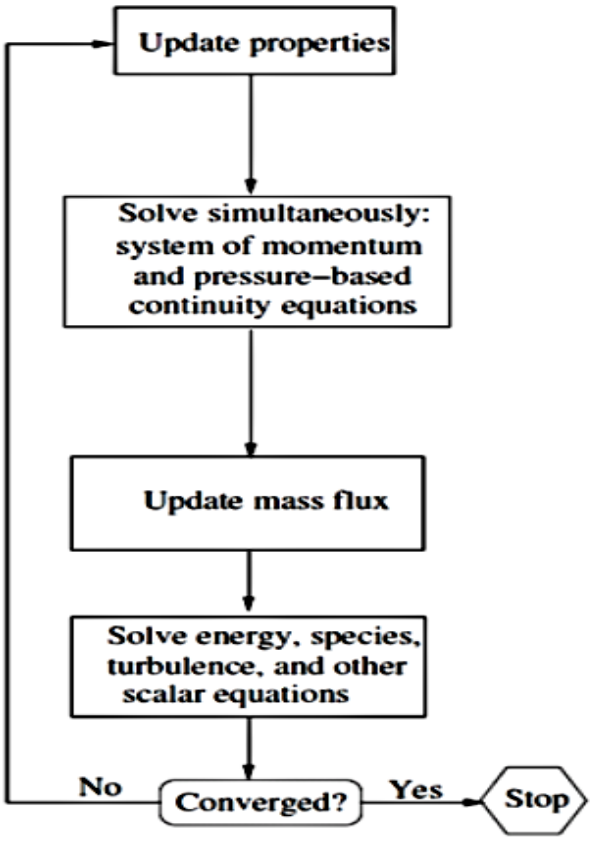

Figure 41: Pressure-based coupled algorithm[51].

5 Turbulence modeling

5.1 Turbulence overview

In general, we distinguish between the laminar and turbulent flows. In engineering applications, we mostly deal with turbulent flows. It is hard to give general definitions. Many authors instead describe turbulence by its characteristic features. Some of them are[54]:

- Irregularity: the motion is irregular and chaotic, but the Navier-Stokes equations can describe it
- Reynolds number: it is strongly affected by the Re numbers, which usually occur at the higher Reynolds number (e.g., for pipe flow $Re \cong 2300$)
- Continuum phenomenon: the size of the turbulent structures is much bigger than the molecular scale, the fluid behaves like a continuum
- Three-dimensional: the motion has a strongly 3D and unsteady character, some of which is suppressed when applying the statistical approach for turbulence modeling (e.g. like RANS)
- Diffusivity: represents an important aspect from the engineering point of view; it increases the transfer of momentum and energy exchange in the boundary layer, increases the resistance in internal flow, or particle mixing in the combustion process
- Dissipation: energy loss due to energy transfer between larger and smaller eddies

The physical process described in the last bullet above is known as the cascade process. The process is based on the transfer of the turbulent kinetic energy between the scales of motion, from larger to smaller eddies. Viscous forces are dominant in smaller scales and cause the dissipation of kinetic energy into heat. The friction forces are present in practically all scales, including the larger ones. However, it is believed that most of the energy that enters the larger eddies (up to 90%) is being dissipated at smallest scales. This was one of the conclusions of the Russan scientist Kolmogorov and is known as the Universal Equilibrium theory. By this theory, the smallest scales of turbulent motion are also known as the Kolmogorov scale. The velocity, time and length scales of such eddies can be described using two quantities: viscosity and dissipation. Viscous forces play a dominant role in the dissipation of the smallest eddies and therefore seem to be the most natural choice. The established quantity for dissipation is denoted by $\epsilon[\frac{m^2}{s^3}]$. This describes the energy transfer per unit time and unit mass. The higher the veloctiy gradients in the system, the higher the turbulence rate and the more kinetic energy is being transformed into thermal energy. The velocity, length and time scale are described by v_η, l_η and τ_η. [54]

$$v_\eta = (\nu\epsilon)^{\frac{1}{4}} \qquad l_\eta = \left(\frac{\nu^3}{\epsilon}\right)^{\frac{1}{4}} \qquad \tau_\eta = \left(\frac{\nu}{\epsilon}\right)^{\frac{1}{4}} \tag{5.1}$$

We can consider a typical boundary layer flow, for example along a moving automobile, to demonstrate how small the Kolmogorov scales are. For a car with the velocity of approx. 100 km/h, the length scales of the smallest eddies moving around the vehicle are approx. $4.6 \cdot 10^{-3}$mm in length. We can compare this to the mean free path length of two molecules ($l_{m_{ff}} \approx 63.5 \cdot 10^{-5}$mm), and we get [50]:

$$\frac{l_\eta}{l_{m_{ff}}} \approx 72 \qquad 5.2$$

This clearly shows how much larger the smallest flow scales are relative to the relevant length scale for the molecular collision.

To get a better insight into turbulence and to better understand the connection with the turbulence models, it is worth discussing different turbulent scales a bit further. A convenient way to study them is based on an analysis of the spectral distribution of energy. A spectral distribution can be represented as a Fourier decomposition dependant on the wave numbers κ. The turbulent kinetic energy k is related to the corresponding spectral densitiy $E(\kappa)$ through the following equation,

$$k = \int_0^\infty E(\kappa) d\kappa. \qquad 5.3$$

As shown in the graphical representation in Figure 42, the spectrum of E can be divided into three regions [54]:

- Energy containing eddies: this region contains the largest and energy-containing eddies, which extract their energy from the mean flow. The characteristic length of the larger eddies ℓ can be expressed by k, ℓ, and ϵ according to Wilcox[50]:

  $$\epsilon \backsim \frac{k^{\frac{3}{2}}}{\ell} \text{ or } k \backsim (\epsilon\ell)^{\frac{2}{3}} \qquad 5.4$$

  Many turbulence models are based on the length scale ℓ. The measure is also known as the integral length scale and is much larger compared to the Kolmogorov length scale. Many authors also use the notation l_0

- Inertial subrange: Kolmogorov discovered that there exists a mid-range between the larger and smaller eddies, which is independent of the large, energy-containing eddies and eddies in the dissipation range. The hypothesis is based on the fully turbulent flow regime. The energy transfer in the region is mainly affected by the inertial forces. The $E(\kappa)$ depends on two quantitites ϵ and κ.

  $$E(\kappa) = C_k \epsilon^{\frac{2}{3}} \kappa^{-\frac{5}{3}} \qquad 5.5$$

  The equation above is more widely known as the Kolmogorov spectrum law or law of -5/3, where the C_k stands for the Kolmogorov constant. It basically says that the flow in a fully turbulent regime, the turbulent energy spectrum should have a slope of -5/3 in the inertial subrange. Many experiments and numerical simulations confirm the existence of this region.

- Viscous range: (sometimes also dissipation range) represents the small isotropic eddies. The flow is mainly characterized by the dissipation of eddies. The turbulent kinetic energy is being transferred here to thermal energy. The eddy size is in the range of the Kolmogorov scale.

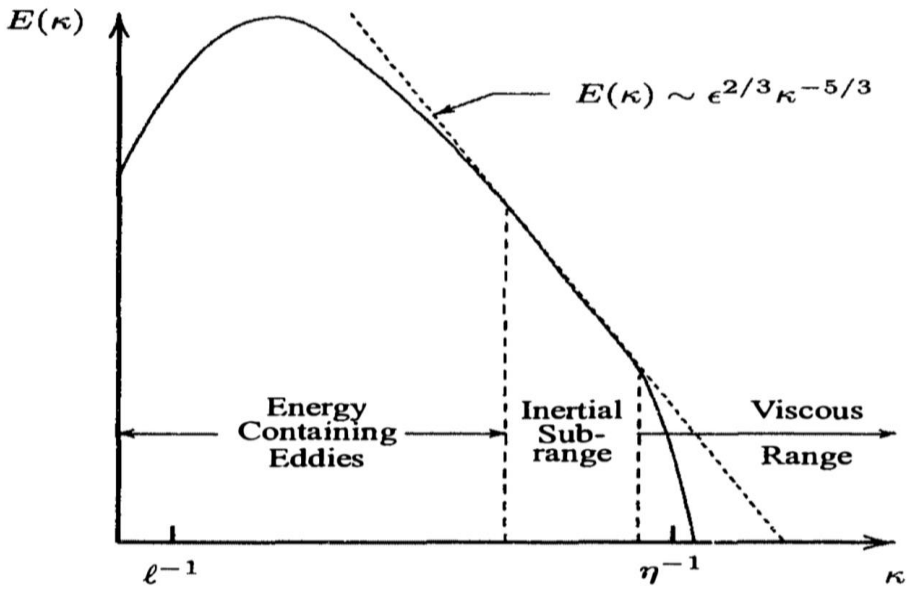

Figure 42: Spectrum of turbulent kinetic energy [50].

5.2 Numerical approaches for turbulence modeling

There are different approaches to solving turbulent flows. A primary classification can be made by distinguishing DNS (direct numerical simulation), LES (large-eddy simulations) and RANS (Reynolds averaged Navier−Stokes equations)[48]. They are all based on solving the non-linear Navier−Stokes equations, which do not allow for a general analytical solution.

DNS represents the most accurate and straightforward approach. The method solves directly the Navier−Stokes equations. There is no averaging or approximation. The only error is the numerical discretization. At a sufficient small grid resolution and time step, such simulation resolves all the relevant scales of turbulence motion in the flow. It provides very detailed flow information, which could be practically identical to those gained in the experiments. This could be useful in some cases (mainly limited to an academic investigation), but normally such an amount of detailed flow information exceeds the engineering needs. More computationally such a simulation requires an enormous amount of computational resources and is mainly limited to study very simple geometries at small Reynolds numbers. The method calculates the whole turbulent kinetic energy spectrum down to the Kolmogorov scale.[48]

LES directly calculates the large eddies and models the smallest ones using the so-called subgrid-scale models. The larger eddies contain much more energy and are more anisotropic. A big part of the turbulence spectrum is still calculated directly. They have a more significant influence on the flow than smaller scales near the dissipation range. The LES is time-dependent and three-dimensional, but it is less expensive than DNS. The reason for this lies in the cells grid size, which can be much larger than the Kolmogorov length. This makes it possible to consider flows with reasonably high Reynolds numbers at very high but still affordable computational costs.[48]

RANS is a statistical approach to turbulence modeling. All the fluctuations are averaged out. The averaging procedure brings about unclosed terms from higher-order statistics, which need to be modeled. The approach is popular in engineering applications, because it is fast and can provide

reasonably accurate results if appropriately validated. The whole turbulence spectrum represented in Figure 43 is modeled using different correlations. It should be considered more like an approximation. It is frequently used in external automotive aerodynamics. In the transient case, the method is called URANS.[48]

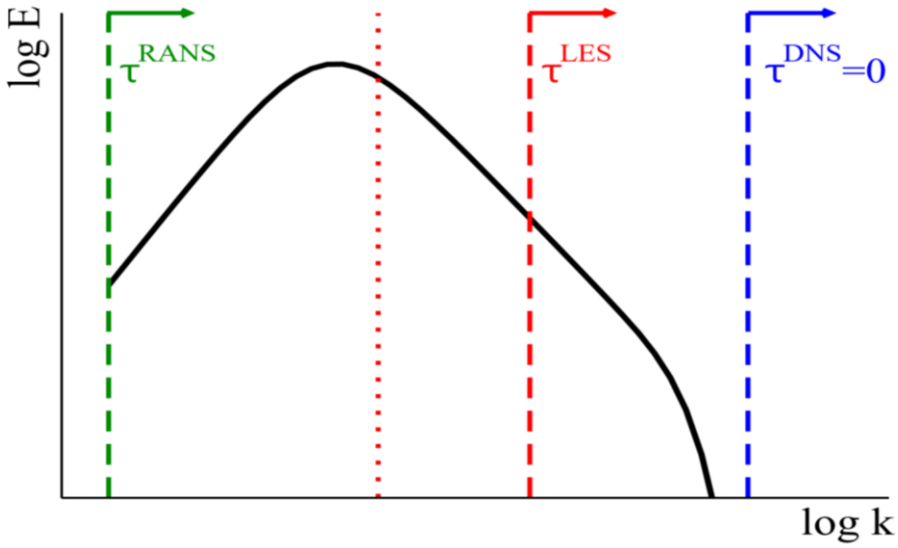

Figure 43: Turbulence energy spectrum and representation of different turbulent modeling strategies: RANS, LES, DNS, dotted red line represents hybrid RANS\LES and VLES approaches, τ stands for modeling term[10].

5.2.1 Choosing the appropriate turbulence model for the Ahmed body test case

The choice of the turbulence model depends on many factors: physics of the flow, required accuracy, computational time, and resources. To choose the right turbulence approach we need to understand the weaknesses and strengths of the different approaches. Each model has its range of applicability. Some of them are suited for internal or external flows, some of them are good in the prediction of the flow separation. It is hard to give general recommendations which model could be the best choice in a particular application. The accuracy should increase as the model gets more complex (at least in theory). RANS involves much more modeling contributions compared to LES, but LES leads to a higher computational cost. Usually, the user has to find the balance between the required accuracy and computational cost [48].

The first choice for the steady RANSapproaches applied to the test case Ahmed body was the realizable K-ε (RKE) and the K-ω SST. The RKE model should give good results in the case of shear layer and recirculation flows. The model was suggested in Fluent's guidelines[75] for handling external flows in automotive aerodynamics. Using this model excellent results on the Ahmed body with 25° slant angle were achieved by Bordei and Popescu[17]. Steady RKE took here third place in the prediction for drag coefficient. It has to be borne in mind that RKE produce here better results than, for example, coarse LES or RSM, which are computationally much more costly. Unsteady RKE produced worse results for both the lift and drag coefficient than the steady RKE. The RKE model gave also satisfactory results regarding the local and global drag coefficients in [19]. The K-ω SST model is more sophisticated than the RKE because it can account for the transport of the shear stresses. In the benchmark study of Bordei

and Popescu [17] the k-ω SST model took second place for the drag coefficient in the steady formulation. It was second for lift coefficient in the OpenFOAM implementation.

Although the steady calculations were shown to produce very good results regarding integral values like the drag and lift coefficients, it does not always succeed and accurately predict other flow features like velocity profiles, pressure distribution or flow patterns. Scale-adaptive simulation (SAS) was the chosen candidate for the transient simulation. It represents the second-generation URANS approach, which allows for the resolving of some part of the turbulent spectrum. SAS took third place in predicting the aerodynamic coefficient (c_D/c_L) in [17].

RANS/URANS methods give no information about the turbulent flow structures and their spectral distribution. This could be especially important when trying to predict the flow-induced noise or vibration. In order to resolve directly at least the significant part of the turbulence spectrum remote from the walls, we apply the detached-eddy simulation (DES). The classical DES model does not have shielding, which prevents the resolved eddies from entering the boundary layer calculated with the RANS. According to the literature survey [35,20], none of the DES or DDES approaches predicted the flow reattachment on the slant. This was possible only with the IDDES (improved delay detached-eddy simulation), which was therefore chosen as the best option in the present study.

LES resolves most part of the turbulence energy spectrum. There are several subgrid-scale models like the Smagorinsky−Lilly model, the dynamic Smagorinsky-Lilly model, the wall-adapting local eddy-viscosity (WALE), WMLES (wall-modeled large-eddy simulation). WALE offers some advantages over the Smagorinsky model. It is capable of reproducing the laminar-turbulent transition and it also provides the possibility of a correct description of asymptotic near-wall behavior for the wall-bounded flows. Dynamic Smagorinsky models have similar advantages as WALE but are computationally more expensive and prone to instability. In addition, they were not able to reproduce the partial reattachment on the slant in the study of[20].Therefore, the WALE model was presently chosen as the most appropriate candidate.

5.2.2 Reynolds-averaged Navier−Stokes equations – RANS

The flow variables can be decomposed in the mean (ensemble-averaged) and fluctuation part. Accordingly, the velocity and pressure can be written as [54]:

$$u_i = \langle u_i \rangle + u_i' \tag{5.6}$$

$$p_i = \langle p \rangle + p_i' \tag{5.7}$$

Ensemble averaging is a general type of statistical averaging, which can be used for statistically stationary or non-stationary flows. In the case of statistically stationary flow and at sufficiently large observation time T, the ensemble-averaged flow variables, e.g $\langle u_i \rangle$, can equivalently computed as the time-averaged defined by [54]:

$$\langle u \rangle = \bar{u} = \frac{1}{2T}\int_{-T}^{T} u dt \tag{5.8}$$

Statistically stationary flows are present in most engineering applications and time-averaging is the most commonly used method of Reynolds averaging. When we deal with the homogeneous turbulence, which is uniform in space, it is convenient to do averaging over the spatial directions. This

is the so-called “spatial averaging”. However, hereafter we will consider only the time-averaging method.

Equation 5.8 represents the mathematical definition for the time-averaged velocity. In the real world, it is impossible to realize the infinite T. In praxis we usually select the observation time that is very long relative to the maximum period of the fluctuations. Averaging the decomposition 5.6 in time again yields, [54]

$$\overline{u_i} = \overline{\overline{u_i}} + \overline{u_i'} = \overline{u_i} + \overline{u_i'} \ . \tag{5.9}$$

Considering the $\overline{\overline{u_i}} = \overline{u_i}$, this implis $\overline{u_i'} = 0$ and $\overline{p'} = 0$. The equation for continuity and momentum can be written in Cartesian coordinates for incompressible flow and without body forces,

$$\frac{\partial u_i}{\partial x_i} = 0 \tag{5.10}$$

$$\rho \frac{\partial u_i}{\partial t} \rho \frac{\partial u_i}{\partial x_i} + \rho \frac{\partial u_i u_j}{\partial x_j} = -\frac{\partial p}{\partial x_i} + \mu \frac{\partial^2 u_i}{\partial x_j \partial x_j} \tag{5.11}$$

Introducing the decompositions 5.6 and 5.7 in the time-averaged continuity and momentum equations gives:

$$\frac{\partial\, \overline{\overline{u} + u_i'}}{\partial x_i} = \frac{\partial \overline{\overline{u_i}}}{\partial x_i} + \frac{\partial\, \overline{u_i'}}{\partial x_i} = \frac{\partial \overline{\overline{u_i}}}{\partial x_i} = \frac{\partial \overline{u_i}}{\partial x_i} \tag{5.12}$$

$$\underbrace{\rho \frac{\partial\, \overline{(\overline{u_i} + u_i')}}{\partial t}}_{1} + \underbrace{\rho \frac{\partial\, \overline{(\overline{u_i} + \overline{u_i'})(\overline{u_j} + \overline{u_j'})}}{\partial x_j}}_{2} = \underbrace{-\frac{\partial\, \overline{(\overline{p} + p_i')}}{\partial x_i}}_{3} + \underbrace{\mu \frac{\partial^2 \overline{(\overline{u_i} + u_i')}}{\partial x_j \partial x_j}}_{4} \tag{5.13}$$

If we now simplify the equation and consider each term starting from left to right,

1) $\rho \frac{\partial\, \overline{(\overline{u_i} + u_i')}}{\partial t} = \rho(\frac{\partial \overline{\overline{u_i}}}{\partial t} + \frac{\partial \overline{u_i'}}{\partial t}) = \rho \frac{\partial \overline{\overline{u_i}}}{\partial t} = \rho \frac{\partial\, \overline{u_i}}{\partial t}$ (5.14)

2) $\frac{\partial\, \overline{(\overline{u_i} + \overline{u_i'})(\overline{u_j} + \overline{u_j'})}}{\partial x_j} = \rho \frac{\partial \overline{\overline{u_i}\,\overline{u_j} + \overline{u_i}\,u_j' + u_i'\,\overline{u_j} + u_i' u_j'}}{\partial x_j} = \rho \left(\frac{\partial \overline{\overline{u_i}\,\overline{u_j}}}{\partial x_j} + \underbrace{\frac{\partial \overline{\overline{u_i}\,u_j'}}{\partial x_j}}_{=0} + \underbrace{\frac{\partial \overline{u_i'\,\overline{u_j}}}{\partial x_j}}_{=0} + \frac{\partial \overline{u_i' u_j'}}{\partial x_j} \right) = \rho(\frac{\partial\, \overline{u_i}\,\overline{u_j}}{\partial x_j} + \frac{\partial\, \overline{u_i' u_j'}}{\partial x_j})$ (5.15)

3) $-\frac{\partial\, \overline{(\bar{p} + p_i')}}{\partial x_i} = \frac{\partial \bar{\bar{p}}}{\partial x_i} + \underbrace{\frac{\partial \bar{p}'}{\partial x_i}}_{=0} = \frac{\partial\, \bar{p}}{\partial x_i}$ (5.16)

4) $\mu \frac{\partial^2 \overline{(\overline{u_i} + u_i')}}{\partial x_j \partial x_j} = \mu \frac{\partial^2 \overline{(\overline{u_i})}}{\partial x_j \partial x_j} + \mu \underbrace{\frac{\partial^2 \overline{(u_i')}}{\partial x_i \partial x_i}}_{=0}$ (5.17)

The time-averaged Navier−Stokes equation, also known as the Reynolds-averaged Navier−Stokes equations are obtained as,

$$\frac{\partial \overline{u_i}}{\partial x_i} = 0 \tag{5.18}$$

$$\rho \frac{\partial \overline{u_i}}{\partial t} + \rho \frac{\partial \overline{u_i}\,\overline{u_j}}{\partial x_j} = -\frac{\partial \overline{p_i}}{\partial x_i} + \frac{\partial}{\partial x_j}\left(\mu \frac{\partial \overline{u_i}}{\partial x_j} - \rho \overline{u_i' u_j'}\right) \tag{5.19}$$

The time-averaged continuity equation is identical to the instantaneous equation, the only difference being the replacement of the instantaneous value with the mean velocity. If we make the same observation for the momentum equation, the difference between the instantaneous and time-averaged value lies in the appearance of the new term $\rho\overline{u_i' u_j'}$ on the right-hand side of the equation. The term is often called "Reynolds stress tensor" and represents the time-averaged momentum transfer due to the turbulence. This is a symmetric tensor ($\overline{u_1' u_2'} = \overline{u_2' u_1'}$) and has six independent components, which are the result of the Reynolds averaging. This additional term is unknown. When considering any three-dimensional flow we have ten unknowns (pressure, velocity components and six components of Reynolds stress tensor) and only four equations (continuity equation and momentum equation for three velocity components). The system of equations is not closed. The closure problem requires some approximations. Correlations are usually modeled by the so-called turbulence models. Some popular approches among them are the Spallart–Allmaras, K-ε, K-ω and RSM models.

All the equations and descriptions for the turbulence models described in the next section are extracted from the Fluent Theory guide [51].

5.2.2.1 Realizable K-ε (RKE)

The model was initially proposed by Shih[31] to improve the weaknesses of the standard k- ε model. It is based on the standard k-ε model with a few modifications. The word "realizable" refers to the satisfaction of a mathematical condition for the Reynolds stresses. It contains an adapted formulation for the turbulent viscosity and modified transport equation for the dissipation rate ε. The fairly prediction of free flows are one of the biggest weaknesses of the standard model. The round-jet anomaly in free flow applications occurs, a mainly, due to poorly modeled dissipation equation. The standard model is not able to predict the spreading rate correctly for symmetric jets. A significantly better performance was shown in channel flows, and boundary layer separated flows. Production of the non-physical turbulent viscosities represents one of the disadvantages of the RKE model. This usually happens when the flow contains stationary and rotating fluid regions[51].

Transport equations:

k:
$$\frac{\partial}{\partial \mathrm{t}}(\rho \mathrm{k}) + \frac{\partial}{\partial \mathrm{x_j}}\left(\rho \mathrm{k u_j}\right) = \frac{\partial}{\partial x_j}\left[\left(\mu + \frac{\mu_t}{\sigma_k}\right) + \frac{\partial k}{\partial x_j}\right] + G_k + G_b - \rho\epsilon - Y_M + S_k \tag{5.20}$$

ε:
$$\frac{\partial}{\partial \mathrm{t}}(\rho \epsilon) + \frac{\partial}{\partial \mathrm{x_j}}\left(\rho \epsilon \mathrm{u_j}\right) = \frac{\partial}{\partial x_j}\left[\left(\mu + \frac{\mu_t}{\sigma_\epsilon}\right)\frac{\partial \epsilon}{\partial x_j}\right] + \rho C_1 S\epsilon - \rho C_2 \frac{\epsilon^2}{k + \sqrt{\nu\epsilon}} + C_{1\epsilon}\frac{\epsilon}{k}\, C_{3\epsilon}\, G_b + S_\epsilon \tag{5.21}$$

where,

$$\mathrm{C_1} = \max\left[0.43, \frac{\eta}{\eta + 5}\right], \eta = S\frac{k}{\epsilon}, \;\; S = \sqrt{2 S_{ij} S_{ij}} \tag{5.22}$$

The individual terms occurring in equations are, G_k (production of turbulent kinetic energy), G_b (turbulence kinetic generation due to buoyancy), Y_M – (dissipation term), S_k,S_ϵ- sources terms and are user-defined.

Turbulent viscosity

The viscosity can be calculated using the following expression,

$$\mu_t = \rho C_\mu \frac{k^2}{\epsilon} \tag{5.23}$$

where the model coefficient C_μ is computed from,

$$C_\mu = \frac{1}{A_0 + A_S \frac{kU^*}{\epsilon}} \ , \tag{5.24}$$

which is different from the constant setting used in the standard k-ε model.

Modeling constants

$C_{1\epsilon} = 1.44$,$C_2 = 1.9$,$C_{3\epsilon}$- model constants

σ_k=1.0,$\sigma_\epsilon = 1.2$- turbulent Prandtl numbers

5.2.2.2 K-ω SST (Shear-stress transport)

In 1994 Menter[61] introduced an improved version of the two-equation eddy viscosity model. It was designed and validated for typical engineering applications. The model primarily uses the standard K-ω in the boundary layer. This makes it usable all the way to the viscous sublayer next to the wall. The model switches to the K-ε in the far field. To join these two approaches together, the model uses a blending function. This approach had already been introduced in the baseline (BSL) K-ω model, but the model fails to account for the transport of turbulence shear stresses. It was not able to correctly predict the flow separation over curved surfaces as a consequence of the overprediction of eddy viscosity. The account of the shear stresses is the main feature of the SST that makes it more accurate than the BSL or standard model. However, in some flows, the model still produces too large turbulence levels [51].

Transport equations :

k:
$$\frac{\partial}{\partial t}(\rho k) + \frac{\partial}{\partial x_i}(\rho k u_i) = \frac{\partial}{\partial x_j}\left(\Gamma_k \frac{\partial k}{\partial x_j}\right) + G_k - Y_k + S_k \tag{5.25}$$

ω:
$$\frac{\partial}{\partial t}(\rho \omega) + \frac{\partial}{\partial x_i}(\rho \omega u_j) = \frac{\partial}{\partial x_j}\left(\Gamma_\omega \frac{\partial \omega}{\partial x_j}\right) + G_\omega - Y_\omega + D_\omega + S_\omega \tag{5.26}$$

Γ_k, Γ_ω model the effective diffusivity as,

$$\Gamma_k = \mu + \frac{\mu_t}{\sigma_k} \tag{5.27}$$

$$\Gamma_{\omega}=\mu+\frac{\mu_t}{\sigma_{\omega}} \quad 5.28$$

σ_k, σ_{ω} denotes the turbulent Prandtl numbers. G_k, Y_k, $S_k$production, dissipation and source term for the turbulence energy, respectively. Analogosly G_{ω}, Y_{ω}, S_{ω} stand for production dissipation and source term of ω, respectively. The term $D_{\omega}$is the cross-diffusion term.

Turbulent viscosity

$$\mu_t=\frac{\rho k}{\omega}\frac{1}{max\left[\frac{1}{\alpha},\frac{SF_2}{a_1\omega}\right]} \quad 5.29$$

the function F_2 can be expressed dependant on the parameter Φ_2 for each wall distance y as,

$$F_2=\tanh(\Phi_2^2)\ ,\Phi_2=max\left[2\frac{\sqrt{k}}{0.09\omega y},\frac{500\mu}{\rho y^2\omega}\right] \quad 5.30$$

Modeling constants

Most of the modeling constants are the same as in the standard BSL model, additional model constants in the SST model are:

$\sigma_{k,1}=1.176$, $\sigma_{\omega,1}=2.0$, $\sigma_{k,2}=1.0$, $\sigma_{\omega,2}=1.168$, $a_1=0.31$, $\beta_{i,1}=0.075$, $\beta_{i,2}=0.0828$

5.2.3 Unsteady Reynolds-averaged Navier–Stokes equations – URANS

In the steady RANS approach, the time-averaging for the Navier−Stokes equations is applied to get the time-averaged mean motion of the flow, which is described by a steady-state solution. This is an adequate choice for statistically steady flows. In many cases, for example, flow around the bluff body, this is inappropriate and can lead to significant error. In such cases the unsteady description of the flow offers advantages over the steady approach. Typically, the flow separation in the wake region triggers the formation of the von Kármán-like vortex street even in a fully turbulent regime. Various experiments have shown the existence of the non-random vorticity, which appears as a spike in the frequency spectrum and is clearly distinguished from broadband. In such cases, an time-averaging over a finite period is more suitable if the time-scale of the non-turbulent vortical structures is still much longer then the averaging period. If not, the time-averaging, e.g. of velocity signals, would produce an overestimation of the turbulent stress as the periodic, coherent non-turbulent fluctuation would be included into the turbulence budget [7,54].

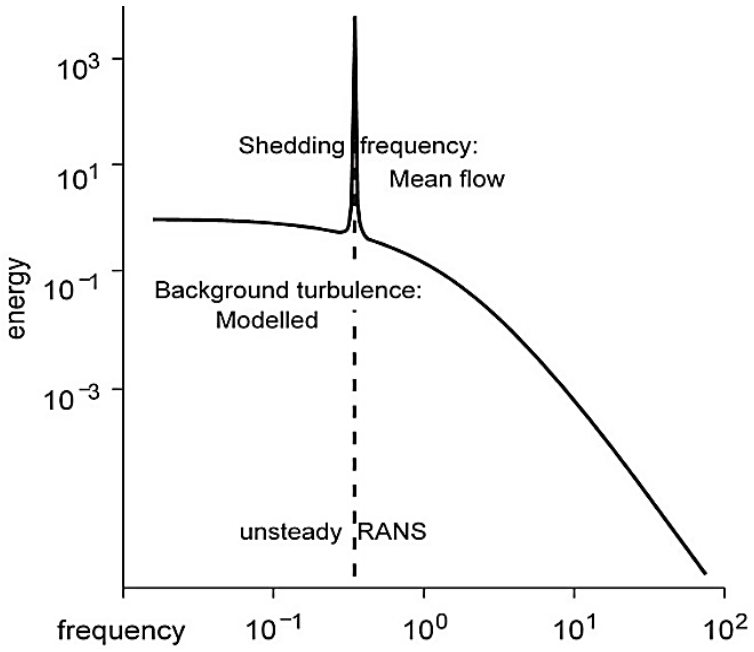

Figure 44: Frequency spectrum of the flow around bluff body (URANS)[7].

As seen in the figure above a vortex shedding translates into a typical low-frequency peak in the energy spectrum. In URANS the non-random turbulent structures are resolved as a part of the mean flow, and the RANS closure resolves the turbulent fluctuations. The velocity vector u can be decomposed into a mean, a quasi-periodic (resolved) coherent fluctuation and random (modeled) fluctuation (triple decomposition) [54] :

$$u = \underbrace{\langle \overline{u} \rangle + \overline{u}'}_{=\overline{u}} + u'' \quad , \tag{5.31}$$

which is represented in Figure 45. Using this decomposition the incompressible URANS equations are written as[54]:

$$\frac{\partial \overline{u_i}}{\partial x_i} = 0 \tag{5.32}$$

$$\frac{\partial \overline{u_i}}{\partial t} + \frac{\partial (\overline{u_i}\,\overline{u_j})}{\partial x_j} = -\frac{1}{\rho}\frac{\partial \overline{p_i}}{\partial x_i} + \frac{\partial \overline{u_i}}{\partial x_j \partial x_j} - \frac{\partial \overline{u_i'' u_j''}}{\partial x_j} \tag{5.33}$$

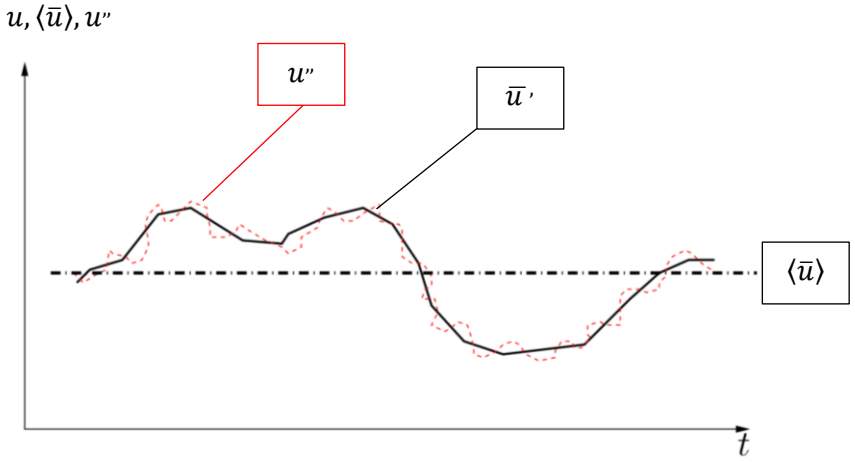

Figure 45: Triple decomposition of an unsteady velocity signal [54].

RANS and URANS models do not explicitly depend on the numerical grid. A higher grid resolution results generally in a higher numerical accuracy, but no new physics is added to the solution. On the other hand, the LES directly depends on the cell size, such that the resolved fluctuation depends on this length scale. These are the so-called second-generation models (2G-URANS), where some part of this spectrum can be resolved. One of the most recent approaches of this type is the scale-adaptive simulation (SAS).

5.2.3.1 Scale-adaptive simulation

Unsteadiness in the flow represents different turbulent time scales. In order to increase the accuracy of URANS computations needs to resolve the large-scale motions. For this, a suitable length scale can be determined using the von Kármán length scale. Menter and Egorov[42,11] developed the SAS method. It is based on the K-KL turbulence model by Rotta. K denotes the turbulent kinetic energy and L the macro length scale of turbulence. It was designed to produce an LES-like flow in the separated flow regions. The model as implemented in Fluent, is a combination of the Rotta approach and the K-ω SST turbulence model. This gives reasonably accurate results in the isotropic turbulence [51].

Transport equations :

k:
$$\frac{\partial}{\partial \mathrm{t}}(\rho \mathrm{k}) + \frac{\partial}{\partial \mathrm{x_i}}(\rho \mathrm{k u_i}) = \mathrm{G_k} - \rho c_\mu k\omega + \frac{\partial}{\partial x_j}\left[\left(\mu + \frac{\mu_t}{\sigma_k}\right)\frac{\partial k}{\partial x_j}\right] \quad 5.34$$

ω:
$$\frac{\partial}{\partial \mathrm{t}}(\rho\omega) + \frac{\partial}{\partial \mathrm{x_i}}(\rho\omega \mathrm{u_i}) = \alpha\frac{\omega}{k}\,G_k - \rho\beta\omega^2 + Q_{SAS} + \frac{\partial}{\partial x_j}\left[\left(\mu + \frac{\mu_t}{\sigma_\omega}\right)\frac{\partial \omega}{\partial x_j}\right] + (1 - F_1)\frac{2\rho}{\sigma_{\omega,2}}\frac{1}{\omega}\frac{\partial k}{\partial x_j}\frac{\partial \omega}{\partial x_j} \quad 5.35$$

The SST-SAS model has an additional source term in the equation for ω compared to the SST model. The Q_{SAS} source term is defined as :

Q_{SAS}: $$Q_{SAS} = max\left[\rho\eta_2\kappa S^2\left(\frac{L}{L_{vK}}\right)^2 - C\cdot\frac{2\rho\, k}{\sigma_\Phi}\, max\left(\frac{1}{\omega^2}\frac{\partial\omega}{\partial x_j}\frac{\partial\omega}{\partial x_j}, \frac{1}{k^2}\frac{\partial k}{\partial x_j}\frac{\partial k}{\partial x_j}\right), 0\right] \quad 5.36$$

$\eta_2 = 3.51$, $\sigma_\Phi = 2/3$ and $C = 2$ are constants. The term in $\rho\eta_2\kappa S^2\left(\frac{L}{L_{vK}}\right)^2$ involves L and L_{vK}, which are the macro and von Kármán length scale, modelled as

$$L = \frac{\sqrt{k}}{c_\mu^{\frac{1}{4}}\,\omega},\ L_{vK} = \kappa\left|\frac{U'}{U''}\right| = \kappa\left|\frac{\frac{\partial U}{\partial y}}{\frac{\partial^2 U}{\partial^2 y}}\right| \quad \text{, respectivetly.} \quad 5.37$$

The first derivative of the velocity can be expressed in terms of a scalar invariant of the strain tensor S_{ij},

$$U' = \sqrt{2\cdot S_{ij}S_{ij}}\,;\, S_{ij} = \frac{1}{2}\left(\frac{\partial U_i}{\partial x_j} + \frac{\partial U_J}{\partial x_i}\right) \quad 5.38$$

The second velocity derivative can be expressed using the Laplacian of the velocity,

$$U'' = \sqrt{\frac{\partial^2 U_i}{\partial {x_k}^2}\,\frac{\partial^2 U_i}{\partial {x_j}^2}} \quad 5.39$$

To control damping of the high wave numbers the model uses the formulation 5.40 which works as a limiter to control the size of the resolved turbulent structures. The size is determined by the Δ as the root of the cell size.

$$L_{vK} = max\left(\kappa\left|\frac{U'}{U''}\right|, C_S\sqrt{\frac{\kappa\eta_2}{\left(\frac{\beta}{C_\mu}\right)-\alpha}}\cdot\Delta\right), \Delta = {\Omega_{CV}}^{\frac{1}{3}} \quad 5.40$$

5.2.4 Detached-eddy simulation

The LES model faces some difficulties trying to simulate wall-bounded flows at the high Reynolds number flows. The problem is the required high mesh resolution, which can significantly increase the computational costs. The solution is to combine the RANS and LES approach into a single-solution strategy. RANS is used for the treatment of the boundary layer and LES for the outer flow. The transition between these two approaches is critical. The turbulence in the boundary layer is completely modeled but when switching to the LES, the modeled energy is supposed to represent the resolved energy which enters in the LES region. The DES consideration of the boundary layer can be based on several different turbulence models. The simplest method is to use a one-equation model, like the Spalart–Allmaras model. A more sophisticated approach is to use two equations or the K-ω SST model [51,10].

Classical DES may have a problem when applied to a fine grid in the streamwise and spanwise direction in addition to a small cell size in y-direction. A critical problem lies in the function (e.g., in the case of DES-SST this is F_{DES}) that is responsible for the switching between RANS/LES. If the grid is too fine, this switch may already occur inside the boundary layer. Then the flow is treated with the LES in a region

where it was not supposed to. This leads to a poorly resolved LES and inaccurate predictions of the flow. To prevent the DES from switching too early to LES, a new improved version has been introduced, called the delayed detached-eddy simulation or DDES. In recent years a further developed approach has been introduced, called: Improved Delayed Detached-Eddy Simulation (IDDES), which is a combination of the various existing DES approaches [51,10].

5.2.4.1 Improved delayed detached-eddy simulation – IDDES

IDDES represents a sufficiently scale resolving method for high Reynolds number flows. The method is a mix between the DDES and wall-modelled LES. The IDDES reduces several shortcomings present in previous methods (associated with the switch between the RANS and LES when the mesh is too fine in the longitudinal direction), which makes the model switch to LES too early, reducing substantially the RANS viscosity. The lack of modeled stresses leads to artificial flow separation, known as grid-induced separation. Although the DDES already provided this improvement, the IDDES includes an additional feature that allows the model to be run in wall-modeled LES (WMLES). The use of the WMLES depends on the turbulent inflow content. If it is present, most of the turbulence is resolved except in the near-wall region, and the model reduces to WMLES. In case of a non-turbulent inflow condition, the model performed as DDES. However, the unsteadiness could alternatively also be triggered by an obstacle (e.g. bluff body), or a backward facing step and not necessarily by the unsteady inlet conditions, which also makes the model switch to WMLES. The switching between both approaches is done using a blending function [55,51]**.**

The ANSYS Fluent implementation of IDDES is based on the BSL/SST RANS model. The modification is done on the k-equation. The ω equation remains untouched [56,51].

Transport equations :

k:
$$\frac{\partial}{\partial \mathrm{t}}(\rho \mathrm{k}) + \nabla \cdot (\rho \bar{U} \mathrm{k}) = \nabla \cdot [(\mu + \sigma_k \mu_t) \nabla k] + P_k - \rho \sqrt{k^3} \, / I_{IDDES} \tag{5.41}$$

ω:
$$\frac{\partial}{\partial \mathrm{t}}(\rho \omega) + \nabla \cdot (\rho \bar{U} \omega) = \nabla \cdot [(\mu + \sigma_\omega \mu_t) \nabla \omega] + 2(1 - F_1) \rho \sigma_{\omega 2} \frac{\nabla k \cdot \nabla \omega}{\omega} + \alpha \frac{\rho}{\mu_t} P_k - \beta \rho \omega^2 \tag{5.42}$$

P_k above can be expressed as

$$P_k = \min(\mu_t S^2, 10 \cdot C_\mu \rho k \omega) \tag{5.43}$$

Turbulent viscosity

$$\mu_\mathrm{t} = \rho \frac{a_1 \cdot \mathrm{k}}{\max(a_1 \cdot \omega, \ \mathrm{F}_2 \ \cdot \mathrm{S})} \tag{5.44}$$

F_1 and F_2 represent the SST blending functions. The I_{IDDES} can be expressed as in equation 5.45 where $\mathrm{I_{IDDES}}$, $\mathrm{I_{RANS}}$ and $\mathrm{I_{LES}}$ stand for the corresponding length scale. $\widetilde{f_d}$, $\mathrm{f_e}$ are the empirical blending function and elevation function, respectively. The IDDES length scale is,

$$\mathrm{I}_{\mathrm{IDDES}} = \widetilde{f_d} \cdot (1 + \mathrm{f_e}) \cdot \mathrm{I}_{\mathrm{RANS}} + \left(1 - \widetilde{f_d}\right) \cdot \mathrm{I}_{\mathrm{LES}} \quad 5.45$$

The length scales in equation 5.45 are defined as

$$\mathrm{I}_{\mathrm{LES}} = C_{DES}\,\Delta \ , \quad 5.46$$

$$\mathrm{I}_{\mathrm{RANS}} = \frac{\sqrt{k}}{C_\mu} \ , \quad 5.47$$

$$\text{with} \quad \mathrm{C}_{\mathrm{DES}} = C_{DES1} \cdot F_1 + C_{DES2} \cdot (1 - F_1) \quad 5.48$$

Moreover, the LES length scale is

$$\Delta = \min\{C_w \max[d_W, h_{max}], h_{max}\} \ , \quad 5.49$$

where the $h_{max} = \max\{h_x, h_y, h_z\}$ represents the maximum edge length of the cell in each direction [55]. Δ combines the local grid scale and the wall distance d_W and $C_w = 0.015$.

5.2.5 Large-eddy simulation – LES

Applying a statistical averaging approach on the momentum and continuity equations is typical for RANS, where all the fluctuating quantities are modeled. However, sometimes it is considered as an advantage, if the turbulent structure is directly calculated, e.g., large-scale components of the velocity field. The best approach to do this is to filter the velocity field. The velocity can be filtered using a box or spectral cutoff filter. The latter is particularly convenient for the user, because it is straightforward. The contributions that are larger than the cutoff wave number are set to zero. The cutoff should take place in the inertial subrange. In both filters there exists a connection between the eddies length scales and the cell size (Δ). Eddies that are larger than Δ are considered as large eddies and eddies that are smaller than Δ are small eddies. These are the eddies that need to be modeled[54,48].

The filtering procedure can be generally defined as[51,76]

$$\widetilde{\Phi}(\vec{x}) = \int_D \Phi(\vec{x'})\ G(\vec{x}, \vec{x'}) dx' \quad 5.50$$

D describes the integration domain and G stands for the filter function. Fluent uses a box-type filter.

$$G_C(\kappa) = \begin{cases} \frac{1}{V} & if\ \vec{x'} \in V \\ 0, otherwise \end{cases} \quad 5.51$$

The filtered Navier−Stokes equations for the calculation of incompressible flows are

Continuity:
$$\frac{\partial\, \widetilde{u_i}}{\partial x_i} = 0 \quad 5.52$$

Momentum:
$$\frac{\partial\, \rho \bar{u}_i}{\partial t} + \frac{\partial}{\partial x_j}\rho\left(\bar{u}_i\, \bar{u}_j\right) = -\frac{\partial\, \bar{p}}{\partial x_i} + \nu \frac{\partial^2\, \bar{u}_i}{\partial x_j \partial x_j} - \frac{\partial\, \tau_{ij}}{\partial x_j} - \frac{\partial}{\partial x_j}\left(\sigma_{ij}\right) \quad 5.53$$

τ_{ij} describes the stresses tensor due to molecular viscosity and is expressesed as,

$$\tau_{ij} = \left[\mu\left(\frac{\partial\,\bar{u}_i}{\partial x_j} + \frac{\partial\,\bar{u}_j}{\partial x_i}\right)\right] - \frac{2}{3}\,\mu\frac{\partial\,\bar{u}_l}{\partial x_i}\,\delta_{ij} \qquad 5.54$$

A new term occurs in the momentum equation and is called the subgrid-scale Reynolds stresses,

$$\tau_{ij} = \rho\overline{u_i u_j} - \bar{u}_i\bar{u}_j \qquad 5.55$$

The equation needs to be closed using a subgrid-scale model. The computation of these unknown stresses in ANSYS Fluent is based on the Boussinesq hypothesis, where the stresses are calculated from

$$\tau_{ij} - \frac{1}{3}\,\tau_{kk}\delta_{ij} = \mu\left(\frac{\partial\,\bar{u}_i}{\partial x_j} + \frac{\partial\bar{u}_j}{\partial x_i}\right) = -2\mu_t\bar{S}_{ij} \qquad 5.56$$

The equation of 5.56 describes the anisotropic part of subgrid-scale stresses, which is modeled, $\tilde{S}_{ij}$ describes the rate of the strain tensor and μ_t the subgrid-scale turbulent viscosity (which needs to be modeled). There are several different models available: the Smagorinsky−Lilly model, the dynamic Smagorinsky−Lilly model, the WALE model, the algebraic wall-modeled LES model (WMLES), and others. The WALE turbulence model was chosen for the present simulations.

5.2.5.1 Wall-adapting local eddy-viscosity (WALE) model

Nicoud and Ducros [57] proposed the WALE model for handling complex geometries using LES on structured and unstructured grids. The model has advantages over the Smagorinsky formulation [51]:

- It can correctly predict the asymptotic wall behavior of the wall-bounded flows. It is designed to produce a zero-eddy viscosity at the wall automatically − no constant adjustment or damping function is needed
- Local rotation and strain rates are included into the spatial operator, allowing a broader spectrum of turbulence to be detact for the TKE dissipation
- It produces zero-eddy viscosity for laminar shear flows. This makes the model capable of correctly reproducing the laminar zones in the domain as well as the laminar-to-turbulent transition process

The turbulent viscosity is computed as [51,57]:

$$\mu_t = \rho L_s^2 \frac{\left(S_{ij}^d S_{ij}^d\right)^{\frac{3}{2}}}{\left(\bar{S}_{ij}\,\bar{S}_{ij}\right)^{\frac{5}{2}} + \left(S_{ij}^d S_{ij}^d\right)^{\frac{5}{4}}} \quad . \qquad 5.57$$

L_S and S_{ij}^d are

$$L_S = \min(\kappa d, C_w V^{\frac{1}{3}}) \quad , \qquad S_{ij}^d = \frac{1}{2}\left(\bar{g}_{ij}^2 + \bar{g}_{ij}^2\right) - \frac{1}{3}\delta_{ij}\bar{g}_{kk}^2 \quad , \qquad \bar{g}_{ij} = \frac{\partial\,\overline{u_i}}{\partial x_j} \qquad 5.58$$

V is the volume of the computational cell, and C_w=0.325 is a WALE model constant.

5.3 Near-wall treatment in turbulent flows

Wall treatments describe a set of different modeling assumptions for each turbulence model. They either model a near-wall behavior or resolve the flow all the way to the wall. The first case is typically in the meshes with a high y^+ value of the first grid point. The inner region of the near-wall layer (viscous and buffer layer) is not resolved. The model uses an empirical formula to bridge the viscosity affected region near the wall to the outer flow. This is the so-called wall function approach. The second case, where we resolve the viscosity-affected boundary layer requires a low y^+ value of the first grid point, usually around 1 or below. The reduction of the mesh size in the wall normal direction increases the computational costs, but it is often well worth it and is practically becoming a standard in today's industrial applications [51].

5.3.1 Wall treatment for the realizable k-ε (RKE)

5.3.1.1 Wall function

In some cases, it is not possible to solve the flow equation all the way to the wall. This is the so-called near-wall modeling approach, where we use a wall function. They can be described by the set of the semi-empirical equations, which try to describe the near-wall behavior. The advantage of this approach is the wall resolution, which can be much coarser compared to the wall-resolved methods. The first grid point is usually located outside the viscous sublayer in the log layer, at a distance up to y^+= 200, depending on the Reynolds number. The primary purpose of the wall function is to reduce the computational costs. The near-wall mesh resolution for the engineering applications at the middle to moderate Reynolds number could exponentially increase for the LES-based computations. Launder and Spalding [66] suggests the following wall function (see equation 5.59), which is the standard method in ANSYS Fluent[51]

$$u^* = \frac{1}{\kappa}\ln(Ey^*) \tag{5.59}$$

The equation 5.59 describes the mean streamwise velocity in the fully turbulent inner wall layer. The non-dimensional velocity can be rewritten as,

$$u^* = \frac{U_P C_\mu^{\frac{1}{4}} k_p^{\frac{1}{2}}}{\frac{\tau_w}{\rho}} \tag{5.60}$$

y^* is the non-dimensional wall distance

$$y^* = \frac{\rho C_\mu^{\frac{1}{4}} k_p^{\frac{1}{2}} y_p}{\mu} \tag{5.61}$$

κ repppresents the von Kármán constant (κ=0.4187), E is an empirical constant (E = 9.793). U_P, k_P and y_P stand for the mean velocity, turbulence kinetic energy and distance from the wall to the cell centroid, respectively.

5.3.1.2 Enhanced wall treatment

The generation of the fine mesh everywhere in the domain may mean too much computational effort. On the other hand, the use of a wall function on a coarse mesh may lead to inaccurate results. The

ideal would be to be able to combine both of the approaches into a single method. Fluent introduced the so-called enhanced wall treatment for the ϵ- equation. It combines the standard two-layer approach with the enhanced wall function. The approach can be used in the k-ϵ turbulence model [51].

Two-layer approach

This divides the computational domain into two regions, the viscosity region near the wall and a fully turbulent region. The boundary between these two regions is determined by the turbulent Reynolds number[51],

$$Re_y = \frac{\rho y \sqrt{k}}{\mu} \tag{5.62}$$

y is the normal wall distance at the cell center

$$y = min\left||\vec{r} - \overrightarrow{,r_w}|\right| \tag{5.63}$$

where r_w stands for the position vector of the wall boundary, and $\vec{r}$ for the position vector of the considered field point. The Reynolds number value for the switch is:

- the outer flow $Re_y > Re_y^*; Re_y^* = 200$
- the viscous region $Re_y < Re_y^*$

In the near-wall region the approach uses a one equation model. The momentum and k equation is the same as in the RKE. The turbulent viscosity and length scales are computed as,

$$\mu_{t,2layer} = \rho C_\mu l_\mu \sqrt{k} \quad , \qquad l_\mu = y\, C_t^* (1 - e^{-\frac{Re_y}{A_\mu}}) \tag{5.64}$$

The two-layer turbulent viscosity and turbulent viscosity from the outer flow (as from the standard k-ϵ model) are combined together forming a viscosity for enhanced wall treatment

$$\mu_{t,enh} = \lambda_\epsilon \mu_t + (1 - \lambda_\epsilon)\mu_{t,2layer} \quad . \tag{5.65}$$

λ_ϵ represents a blending function,

$$\lambda_\epsilon = \frac{1}{2}\left[1 + tanh\left[\frac{Re_y - Re_y^*}{A}\right]\right] \tag{5.66}$$

$$A = \frac{\left|\Delta Re_y\right|}{artanh(0.98)} \tag{5.67}$$

The working width of the blending function is determined by the constant A. The main reason for using the blending function is to avoid a convergence problem when the values of the turbulent viscosity in the inner and outer region do not match on the boundary.

The turbulent dissipation rate ε in the viscous near-wall region is,

$$\varepsilon = \frac{k^{\frac{3}{2}}}{l_\epsilon} \tag{5.68}$$

$$l_\varepsilon = y\, C_t^*(1 - e^{-\frac{Re_y}{A_\epsilon}}) \tag{5.69}$$

A similar procedure as used for combining the turbulent viscosity into one single equation is being applied on the ϵ. This helps to avoid errors and ensure a smooth transition between the inner and outer region for the dissipation value ε computed, from the transport equation. Constants are $C_t^* = \kappa C_\mu^{\frac{3}{4}}$, A_μ=70, A_ϵ=2C_t^*.

5.3.2 Wall treatment for the k-ω SST

Automatic near-wall treatment

The wall function approach is not the preferable method here, especially when considering wall-bounded flows, it is more convenient to integrate, for example, ω down to the wall without the need of the two-layer method. The ω-based models are described using an analytical expression, which describes the viscous sublayer and the logarithmic region in the boundary layer. This makes it suitable for describing the inner region using automatic near-wall treatment. The idea behind this is to automatically shift between the formulation of the viscous sublayer and wall function based on the grid density. The model has an integrated blending function, which depends on the y^+. The expressions for ω in the viscous and logarithmic layer are [59,60,61,51].

$$\omega_{vis} = \frac{6\nu}{0.075y^2} \quad , \quad \omega_{log} = \frac{1}{0.3\kappa}\frac{u_\tau}{y} \tag{5.70}$$

The above equations can be written as a function of y^+,

$$\omega_1(y^+) = \left(\omega_{vis}^2(y^+) + \omega_{log}^2(y^+)\right)^{0.5} \tag{5.71}$$

For the friction velocity ($u_\tau = \tau_w/\rho$), we assume similar,

$$u_\tau = \left[(u_\tau^{Vis})^4 + (u_\tau^{log})^4\right]^{0.25} \tag{5.72}$$

where,

$$u_{\tau,vis} = \frac{U_1}{y^+}\ , u_\tau^{log} = \frac{U_1}{\frac{1}{\kappa}\ln(y^+)+C} \tag{5.73}$$

and U_1 is the velocity in the first grid point.

5.3.3 Wall treatment for the LES

The LES method has a certain advantage over the RKE and SST near wall treatment, because it uses less complex calculations for handling wall-bounded flows, and there are less modeling assumptions. However, this requires an increase in the grid resolution. In the case of a fine enough grid, which is able to resolve the viscous sublayer, we define the laminar profile as [51],

$$\frac{\bar{u}}{u_\tau} = \frac{\rho u_\tau y}{\mu} \tag{5.74}$$

Coarse mesh does not allow for the resolution of the viscous sublayer. In such cases, it is assumed that the cell faces lie in the logarithmic region (law of the wall), where [51]

$$\frac{\bar{u}}{u_\tau} = \frac{1}{\kappa} lnE\left(\frac{\rho u_\tau y}{\mu}\right) \qquad 5.75$$

applies.

6 Numerical simulation

The primary purpose of this section is to describe the numerical setup used for the steady and transient simulations.

6.1 Geometry and computational domain

The geometrical dimensions of the Ahmed body generated for the CFD simulations correspond to the original dimensions from Ahmed's publication [34], which were also used in the experiment by Meile et al.[40]. The model is 1044 mm long, 288 mm high and 389 mm wide. The supporting struts hold the body 50 mm above the stationary ground. They are cylindrical and have a diameter of 30 mm. The version with the most challenging slant angle (25°) for numerical simulation has been chosen.

An appropriate definition of the computational domain is necessary for an accurate computation of the flow field. The choice of the domain was already discussed in a previous section. When choosing the domain size, we took into account some available recommendations. We chose three different domain sizes to be tested based on the literature review. This is a necessary step to exclude any possible error, resulting from a poorly determined domain size from the calculation.

6.1.1 Domain 1

The computational domain has been reconstructed according to the wind tunnel experiments of Meile et al.[62]. It is 15 m in length, 1.87 m wide and 1.4 m high. The domain is particularly long in the upstream and downstream direction to prevent any perturbation from the inlet or outlet from affecting the flow. Blockage ratio is equal to 4.27%.

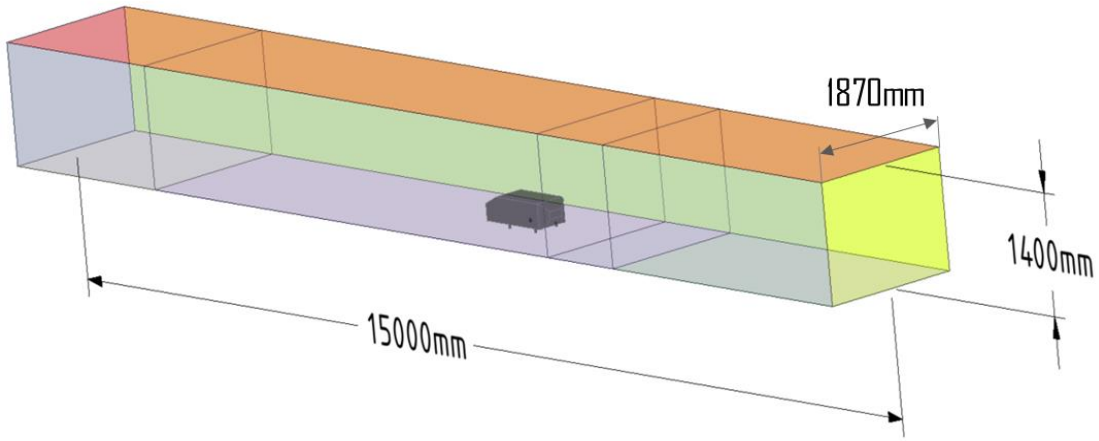

Figure 46: Domain 1(1500x1870x1400 mm).

6.1.2 Domain 2

This domain size is recommended by Stevenson [30] in a previous study on the same Ahmed body geometry. The length of the vehicle, L, is chosen as the characteristic length (model length is equal to 1044 mm). It has a total length of 8352 mm, and is 2088 mm in width and height. This domain is shorter in the upstream and downstream directions compared to Domain 1, but it still fulfills Fluent's guidelines [75], which suggest having five car lengths of space behind the vehicle. The blockage ratio is equal to 2.57%.

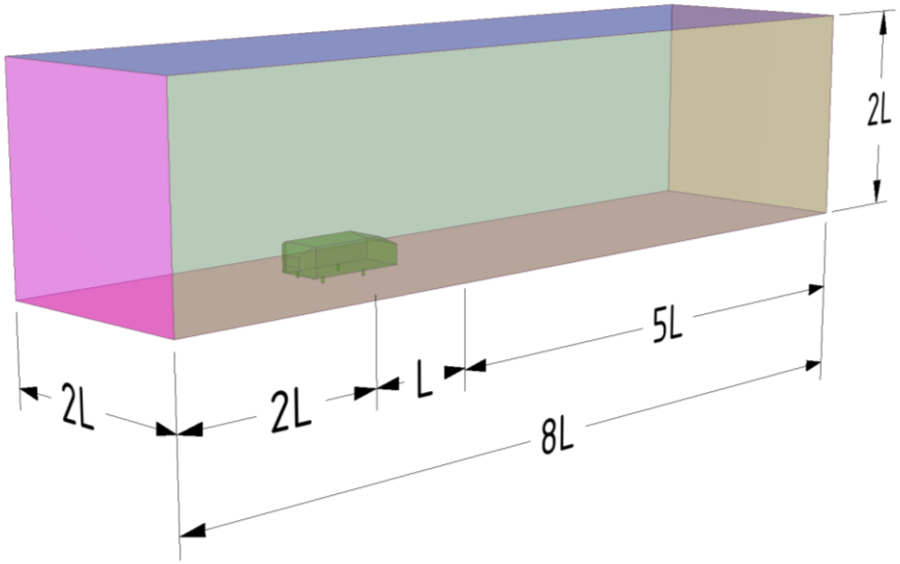

Figure 47: Domain 2 (8L x 2L x 2L).

6.1.3 Domain 3

This has the same stream- and spanwise dimensions as Domain 2, but with the vertical height extended by two additional car lengths L. The purpose of this was to eliminate the possible risk of artificial acceleration of the flow above the vehicle in Domain 2. The blockage ratio is equal to 1.28%.

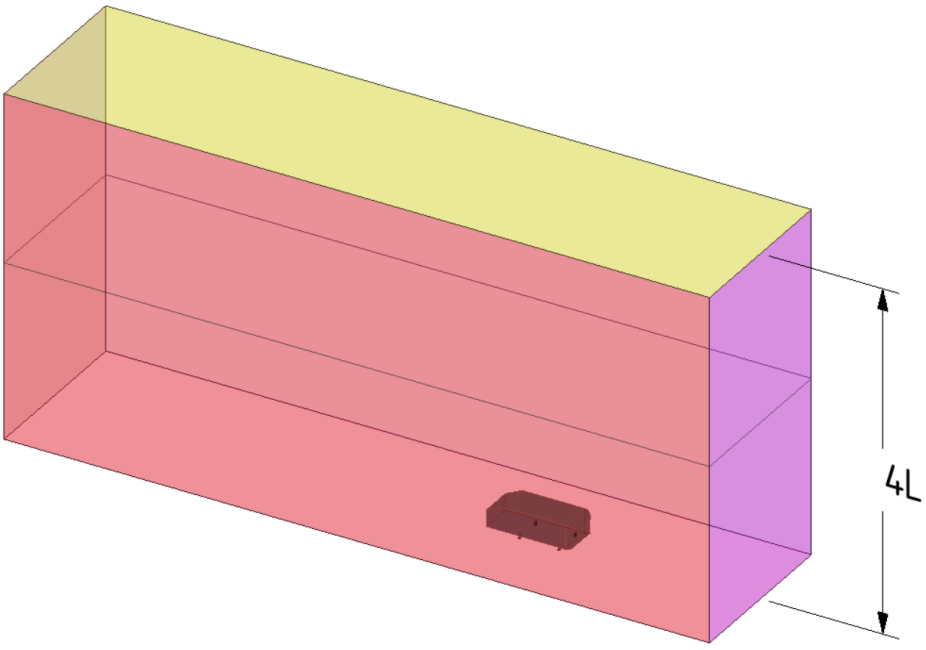

Figure 48: Domain 3(8L x 2L x 4L).

6.2 Meshing strategy

6.2.1 Unstructured mesh

Unstructured meshing has been made by the ANSYS default mesher. This software is very robust and easy to use. A high level of automatization allows quick mesh generation, which makes it a desirable tool in the first stages of the mesh generation process before alternatively switching to a more complex grid generator.

A tetra-dominant mesh was created for volume and the surfaces of the body and domain. The approach is based on a fully automated patch conforming to the tetra mesh method, using the Delaunay (the mathematical process of connecting the discrete points in space using triangles, such that no point lies inside any triangle). The patch-conforming mesh follows each patch of the geometry within minimal tolerance. Geometry should be clean and "water-tight" to be able to produce a good-quality mesh[33]. The method supports the creation of an inflation layer. The height of the first layer has been calculated according to the procedure shown in section 4.4.3 to ensure a y^+ value of the first grid point of around 1. Face-sizing functions have been applied to the surface of the body to control the surface element size. Local refinement of the mesh in the region of interest has been done using the body-of-influence method. In this method, internal boxes are created around the body and in the wake region with the intention of controlling the mesh size within this region. The geometry of the boxes was created in the preprocessing tool. Such a body works as the source of another body (body of influence). Boxes have been created in the wider surrounding of the vehicle. The guidelines [75] recommend the inner box should extend about half of the body length in the front of the car and sides, and a car length in the wake region. If possible, in the praxis it is better to define more boxes to ensure a better transition between the cell sizes. Inside the inner boxes, we additionally define further refinement boxes in the wake region and underbody, which can be seen in Figure 49 The dimensions for the wake refinement box have been taken from [37](L − vehicle length, H − vehicle height).

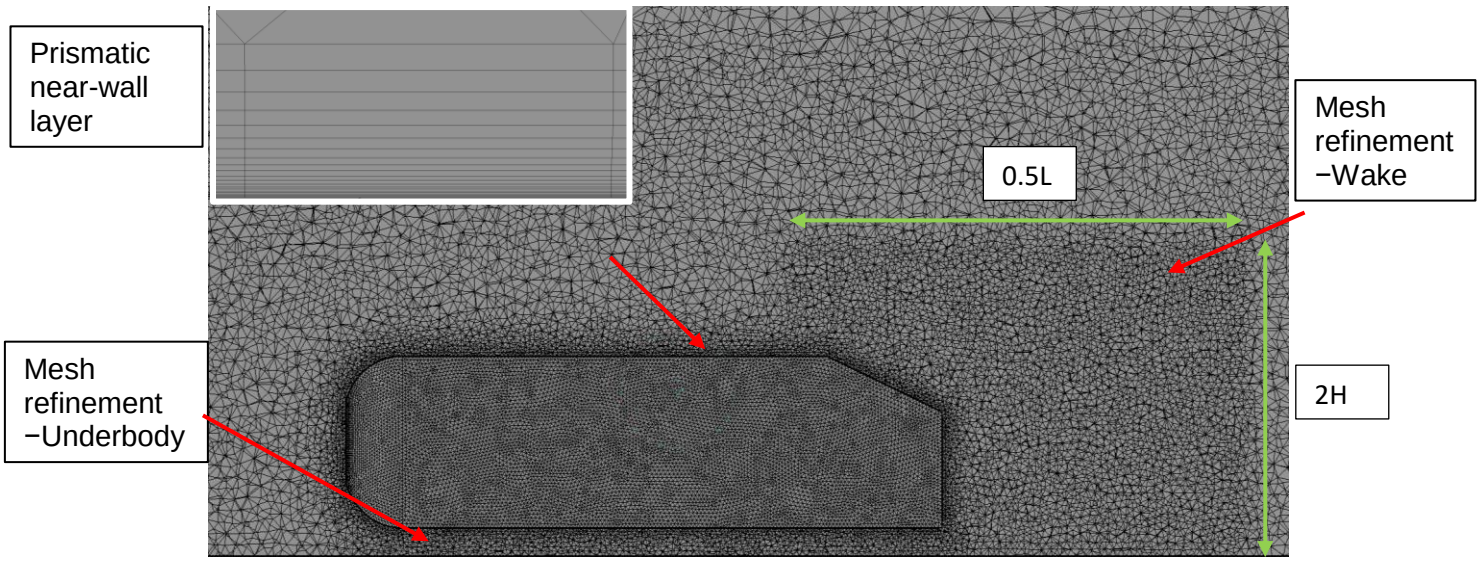

Figure 49: Unstructured mesh of Ahmed body with different refinement boxes.

There were some disadvantages of using an unstructured mesh:

- Such a mesh results in a poor quality of transition from the prismatic near-wall layer to the outer unstructured (tetrahedral) grid

- Secondly, the user has very limited control of the mesh parameters (orthogonality, skewness…)
- The strategy tends to produce a large number of cells (which could result in a long CPU time)

6.2.2 Structured mesh

The simple geometry of the Ahmed allows the structured meshing strategy to be used. Section 4.4 discusses the advantages of this approach. The advantages are numerical as well as computational. For example, the mesh can maintain orthogonal grids in the normal wall direction. This is important at high Reynolds numbers, when the mesh requirements for the spacing in the wall normal direction drastically increase.

The structured grid was generated in the ANSYS ICEM CFD mesh tool, which is a standard tool used for CAD and mesh generation in many engineering applications. The program is designed for application in computational fluid dynamics as well as structural mechanics. It has a handy geometry module, which allows quick surface, point or curve modifications. The grid generation tool offers different kinds of mesh types generation, from multiblock structured to unstructured, tetrahedral and hybrid meshes [53].

The multiblock hexa-mesh approach was found to be the most suitable for the Ahmed body test case. The workflow of the mesh generation can be represented using the following steps[53]:

1. Geometry import
2. Block definition (split, merge, O-grid, vertex movements…)
3. Block quality check
4. Setting mesh parameters (element size, expansion ratio…)
5. Pre-mesh generation
6. Pre-mesh quality check
7. Mesh generation
8. Write the output file

After the geometry import, the first step in grid generation is to choose the topology. This means how many grid blocks are necessary for the geometry and how these blocks should be ordered in relation to each other. ICEM CFD recommends two basic strategies: top-down and bottom-up. The bottom-up approach starts building the mesh from the surface of the 3D model. The blocking face is created for each 2D face of the geometry. In the next step, the approach creates the volume mesh. This procedure has some disadvantages, and it does not always necessarily create a hex-mesh. We decided to use a top-down strategy. This method creates the blocks from the 3D bounding box around the geometry. The blocks are then reformed using split, merge and other procedures, so that they fit to the geometry as well as possible.[53]

Structured meshes can have a different grid topology, e.g. O, C, H. The lines surrounding the geometry in the Figure 50 have a topology that can be associated with the letter »O«. This method is very suitable for external aerodynamics because it allows an accurate point distribution. The main advantage of the O-grid topology is the capturing of the near-wall region. However, there may be some poor-quality mesh regions at different edges, which have to be solved by individually moving the block vertices to the desired positions. ICEM has implemented an automatic O-grid generation. The O-grid tool orthogonally offsets the boundary faces, which results in twice as many vertices [53]. It is appropriate

to adjust all the blocking and vertices to ideal locations before using the O-grid functions. The O-grid is essential because of the definition of the boundary layer in this region, particularly when considering turbulence models which solves the flow equations all the way to the wall boundary. Figure 51 shows the O-grid around the legs and the side of the Ahmed body. A separate O-grid has been created around the legs (supporting struts).

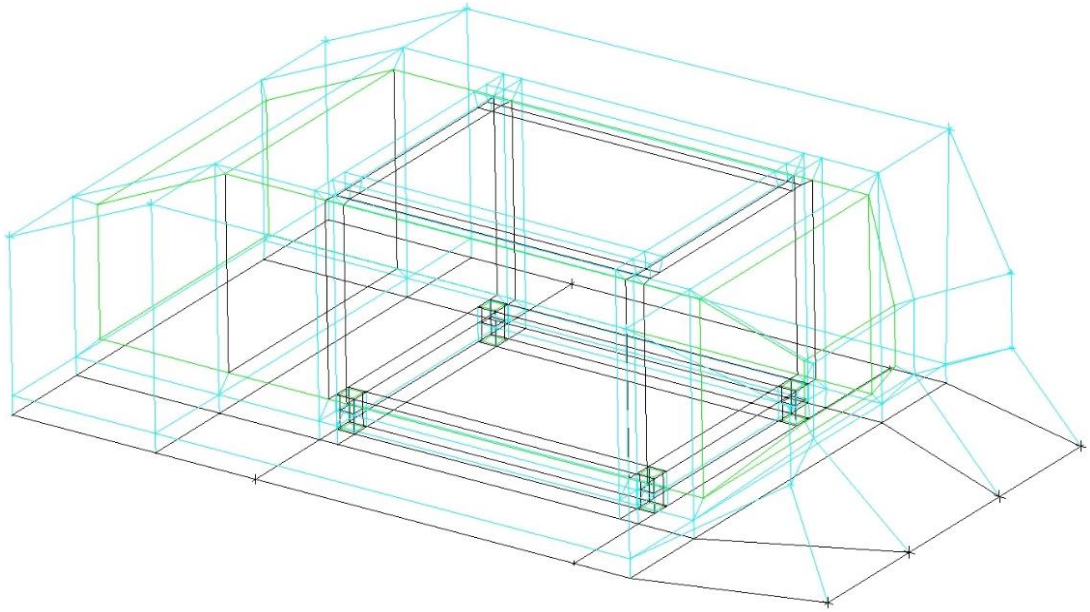

Figure 50: Blocking topology around the Ahmed body.

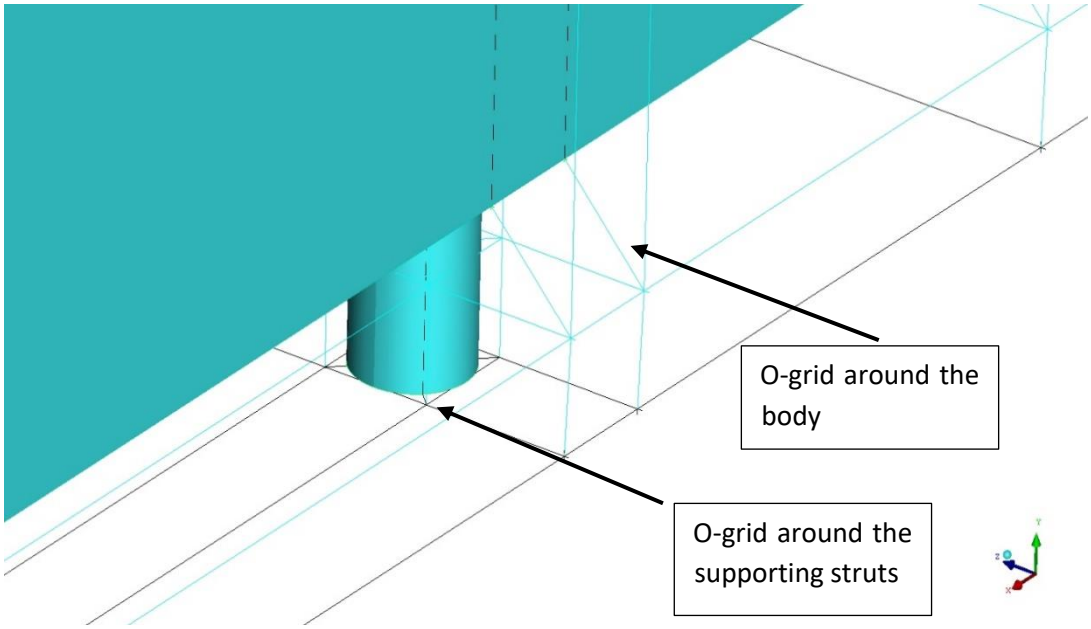

Figure 51: Blocking topology around the back right leg of the Ahmed body.

Once all the blocks have been created, all the geometry constraints, for example, the curves and points, have to be associated with the corresponding edges. In the last step, the number of nodes are distributed along each edge. There is much manual control trying to manipulate the shape of the elements, which can be a very time-consuming process.

In order to achieve accurate results, turbulent flows require some boundary layer consideration during the mesh generation. Turbulence plays a vital role in the transport of mass, momentum and other quantities, so that the near-wall flow behavior has to be resolved accurately. Due to the implementation of the k-ω SST and other wall-resolved turbulence methods, the distance between the walls and the first layer node has to be small to achieve small y^+ values. The procedure for the estimation is shown in section 4.4. Following this calculation a first layer height is estimated as approx. $y = 5 \cdot 10^{-6}$m.

Due to connectivity problems between the legs and the main part of the body the boundary layer height along the body could not be kept constant. The main body frame and the legs possess different first-layer heights. The main problem was to ensure the good quality of the elements at such a small cell size in the y-direction in the near wall zone, therefore the wall distance had to be slightly increased compared to the estimated value done by the procedure in 4.4.3. The wall distance was increased by an order of magnitude to around $1.9 \cdot 10^{-5} m$ in the case of the fine mesh and $5.3 \cdot 10^{-5}$ in the case of the coarse mesh. This still produced satisfactory y^+ values. The fine mesh showed an average y^+=0.5 and the coarse mesh y^+=1.6. The legs have a first-layer height around $3 \cdot 10^{-6}$m. The "Meshing guidelines"[52] suggest that 20 to 30 points in the wall normal direction in the boundary layer produce a useful resolution and ensure a smooth transition between the outer region and the wall region. We use 40 points inside the O-grid blocks in the boundary layer. A similar resolution has been applied by Henry[37], who used 51 points in the near wall mesh. The author in [37] also confirmed that the additional points did not require too much additional computational time and were necessary for a smooth transition.

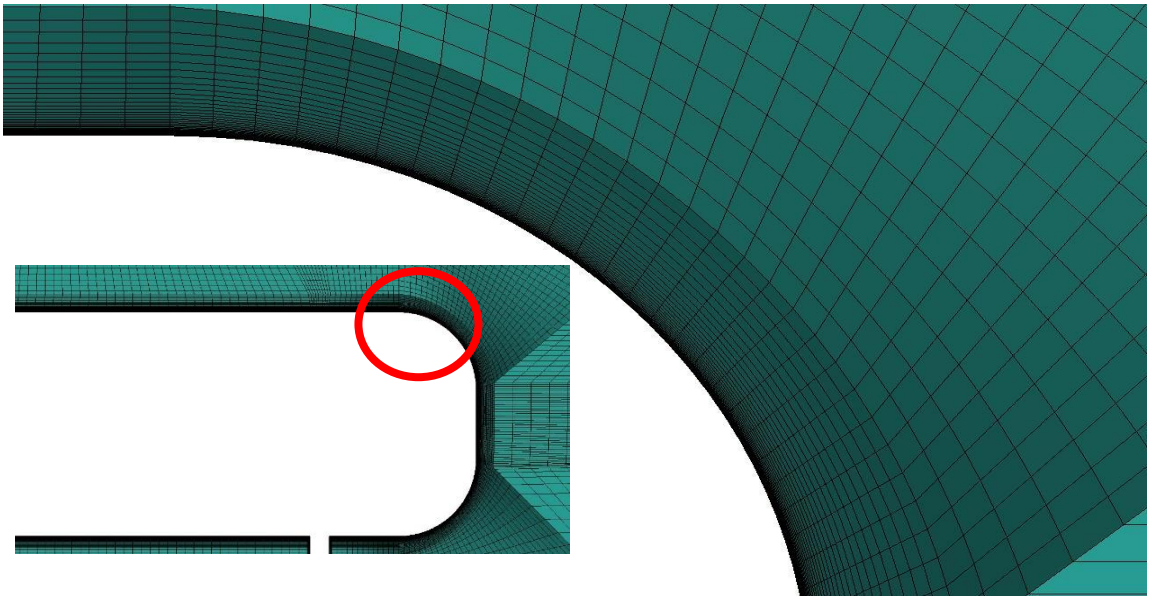

Figure 52: Boundary layer grid around the upper front curved part of the body.

The gap beneath the underbody represents a very turbulent flow region, which is affected by the two walls (underbody and bottom) which causes the creation of the very fine vortical structures in the flow. The flow is even more turbulent due the presence of the four cylindrical legs, which are acting as an additional small bluff bodies disturbing the flow. Such flow conditions require extremely fine meshes in order to capture at least some of the relevant flow features. Even more importantly is the evolution of the flow further downstream because it also affects the wake downstream of the body. A higher density mesh point distribution was therefore also used within this region.

The ground clearance was 50 mm. This gap is meshed with approx. 60 layers in the coarse mesh and even more layers in the fine-mesh configuration. The spacing of the near-wall region on the ground wall has the same first-layer height as the near wall cells on the Ahmed body. The aspect ratios were set to 1.2 and 1.1 to make the transition between the Ahmed body and the ground as smooth as possible.

A local grid refinement is applied to the cells in the wake region and on the slant of the vehicle to capture the small scale turbulence effects. This is an important region where we have to ensure a good mesh resolution and quality, because the wake structure strongly affects the drag and lift of the body. The same applies to region near the slant of the Ahmed body, which also requires a refined mesh in order to predict the correct position where the flow separates.

The far field of the body was not solved to the same extent as the regions near the Ahmed body to reduce the computational costs. In the outer regions, an inviscid wall was prescribed for the boundary conditions to prevent the boundary layer being developed. Coarse grid was used in the wall normal direction in this particular case. The boundary layer starts to grow two body lengths upstream of the generic car model, and is fully developed before interacting with the body [37].

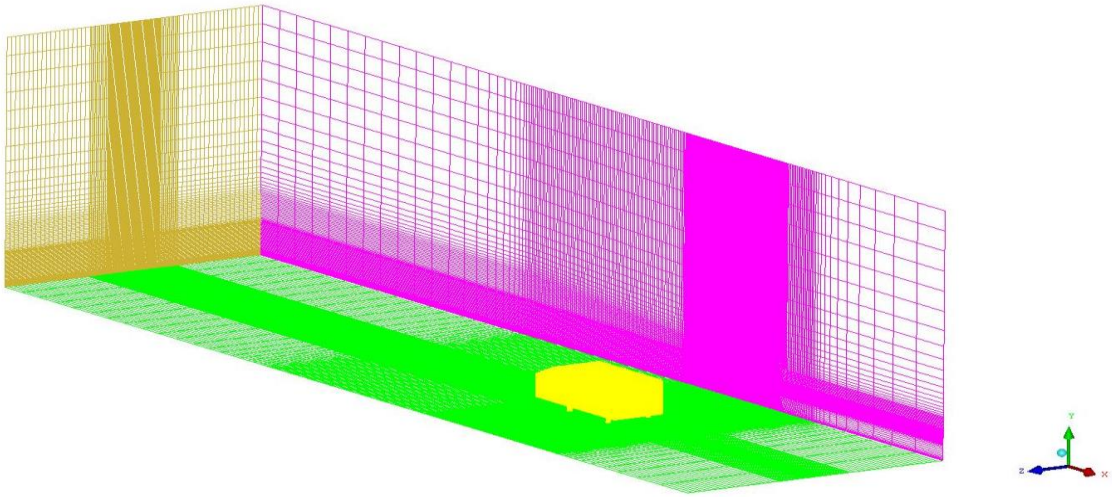

Figure 53: Structured mesh on Domain 2.

6.3 Boundary conditions

For a reliable prediction of the considered flows, the Navier-Stokes equations require the proper boundary and initial conditions. The choice of the boundary condition should reproduce the measurements conditions in the wind tunnel as closely as possible. If available, it is also recommended to check the boundary conditions used on other similar numerical simulations.

The flow velocity and turbulent intensity of the wind tunnel are usually known. The velocity at the inlet was set to 30 m/s and assumed to be uniform. The corresponding Reynolds number is $Re = 2.04 \cdot 10^6$(based on body length L). Velocity magnitude and the flow direction are specified together with turbulence intensity. The latter was provided by the wind tunnel experiment [40] and set to 0.2%. The Airflow is assumed to be incompressible and adiabatic.

A pressure outlet condition was chosen for the outlet. This implies that the pressure and turbulence parameters were prescribed at this boundary. The default values were taken for static (gauge) pressure. Backflow turbulence intensity was set to 0.2%.

The bottom surface and the Ahmed body surface were assigned as non-slip stationary walls.

The symmetry boundary condition was specified for the rest of the bounding faces, wind tunnel top and side planes as suggested in the Fluent guidelines [75].

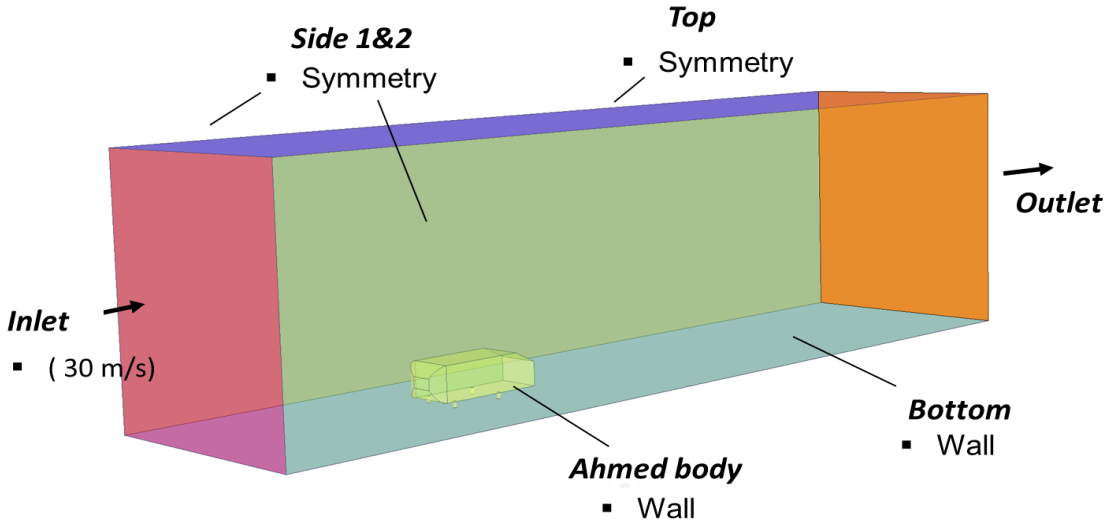

Figure 54: Boundary conditions.

6.4 Evaluation of domain effect on a selected test case

A structured mesh has been created for the domains 1−3 to evaluate the domain effect in a selected test case. All the tested domains have the same near-wall spacing, which ensures the $y^+ \sim 1$. The simulation was done using steady k-ω SST. All material properties and solver settings were kept the same in all cases. The prediction of the drag coefficient was chosen as the criterion for the evaluation. The results are shown in the table below.

Table 3: Drag coefficient comparison for different domain sizes

	Experiment [40]	Domain 1	Domain 2	Domain 3
c_D	0.3077	0.3094	0.2901	0.2909

We had to choose the most appropriate domain size at this point. Domain 1 has a high blockage ratio (4.27%) and risks the effect of artificial acceleration above the body, which causes an overpredicted acceleration of the flow along the roof of the vehicle. However, the prediction of drag coefficient was good (the best among all the tested domains). Domain 2 has a good blockage ratio (2.57%). It predicted good values for the drag coefficient as well. It is smaller than Domain 1 or 3, which translates into a small number of elements and shorter computational time.

Domain 3 was tested to eliminate the danger of artificial acceleration possibly present in Domain 2. There was no significant effect observed in the comparison with Domain 2. Domains 2 and 3 predicted similar c_D values, regardless of the different dimensions in the vertical direction. Domain 3 contains a much higher number of elements, which would lead to longer computational time. This makes it unfavorable for the considered configuration.

Domain 2 was primarily chosen as the best option based on the applied criteria, accuracy and computational cost. It is also very often used as computational domain in previous CFD simulations of the Ahmed body test case in the literature(see section 4.3).

6.5 Considered meshes and quality metrics

Grid types from coarse to dense were generated to perform a grid convergence study. This involved the creation of six different mesh resolutions on Domain 2. They contain from 3.5 M up to 15.8 M elements. The configurations were wall-resolved (y^+=1) and wall-modeled (y^+>>1). In total six meshes were presently used, as listed in Table 4.

Mesh quality plays a significant role in the stability and accuracy of the numerical calculation. Mesh quality has been checked for different parameters during the pre-mesh generation. ICEM defines the determinant (3x3x3 stencil) as the default quality parameter for the hex/quad elements. The measure is based on the computation of the Jacobian matrix (see section 4.4.4), which determines how close the elements are to a perfect shape (cube). In the case of the hex element, a cube element has a determinant equal to 1. Values greater than 0.3 are sufficient for most solvers [64]. The minimal value achieved in the Ahmed body was around 0.8 for all mesh configurations [51].

Angle is another critical parameter. Distorted elements could impact the accuracy of the numerical solution. The program checks the internal angles of the elements and their deviations from 90 degrees. Fluent usually accepts angles higher than 18° [64]. All the grids in the present study have angles greater than 27° [51].

Low orthogonal quality (for hex element orthogonal quality this is equal to the orthogonality) or skewness is not recommended for Fluent solvers. Fluent uses a different categorization than ICEM for some parameters. The classification from bad to worse is generally on opposite sides. In ICEM the worst cells will have an orthogonal quality close to 0, while the best cells will have an orthogonal quality of 1. The scale is the same in both cases. [51] suggested having the orthogonal quality greater than 0.01 for all cell types. The criterion was satisfied in almost all cases except in meshes M2 and M4 (see table 3 below). However, the value was very close to the desired 0.01.

In the case of skewness, zero is ideal and one is the worst possible value in Fluent. It is desirable to have skewness smaller than around 0.8, but values up to 0.95 are also acceptable. Higher values might destabilize the solution and causes convergence problems. In ICEM the skew is defined on different scales: one is ideal, a 0 the worst possible value. Values greater than 0.38 have been achieved in all the considered meshes.[64,51]

Every element type has a different definition of the aspect ratio. The general definition of the ratio is the quotient between the minimum and maximum element size in a particular direction (see subsection 4.4.4). Elements with an aspect ratio of one correspond to a perfectly natural element, while an aspect ratio of 0 indicates a total degenerate element. Fluent scales them from 1 to ∞ [51]. It is

advisable to avoid any sudden changes, especially in the areas with large gradient changes (e.g. the boundary layer). This is important in the wall normal direction. On the other hand, the cells are usually larger in the stream and spanwise direction, which results in poor aspect ratios. This is permissible since the gradients in these two directions are less sharp. Aspect ratios in our case were high near the wall. Small near-wall spacing results in thin and long cells; however, a further reduction of the cells in the z and x-direction to improve the aspect ratio was not possible due to a significant increase in the number of elements.

Table 4: Mesh Quality metric on meshes M1-M6

	M1		***M2***		***M3***		***M4***		***M5***		***M6***	
Type(structured or unstructured)	Struc.		Struc.		Struc.		Struc.		Struc.		Struc.	
Domain size (mm)	(8352x2088x 2088)		(8352x2088x 2088)		(8352x2088x 2088)		(8352x2088x 2088)		(8352x2088x2088)		(8352x2088x2088)	
First-layer height on Ahmed body (m)	5.3e-5		1.9e-5		5.3e-5		1.9e-5		2e-3		2e-3	
Mesh-quality metrics												
	Min.	Max.	Min.	Max.	Min.	Max.	Min.	Max.	Min.	Max	Min.	Max.
Determinant 3x3x3 ***(Unstructured: Jacobian ratio – corner nodes)***	0.8	1	0.8	1	0.8	1	0.8	1	0.8	1	0.8	1
Orthogonal quality	0.02	1	0.009	1	0.02	1	0.009	1	0.4	1	0.4	1
Skew	0.4	1	0.39	1	0.40	1	0.38	1	0.40	1	0.40	1
Aspect ratio	0.0003	1	0.0004	1	0.0004	1	0.0004	1	0.003	1	0.01	1
Number of blocks	231		231		231		231		231		231	
Total cell count	4,461,938		6,937,893		7,520,795		15,876,023		3,481,367		5,883,982	

6.5.1 Resolution requirements for hybrid and LES approach

A majority of the RANS/URANS meshes are not suitable for Hybrid RANS/LES or pure LES simulations [49]. Such meshes are usually too coarse to resolve fine turbulent structures. In the case of the LES-based approach, the mesh has to be fine enough to resolve energy-containing eddies as well as smaller eddies, the length scale of which already lies in the inertial subrange (where the LES filters are usually employed). The mesh resolution directly determines the resolved part of TKE. A coarser mesh resolves a smaller part of the energy spectrum compared to the fine mesh, as illustrated in Figure 55.

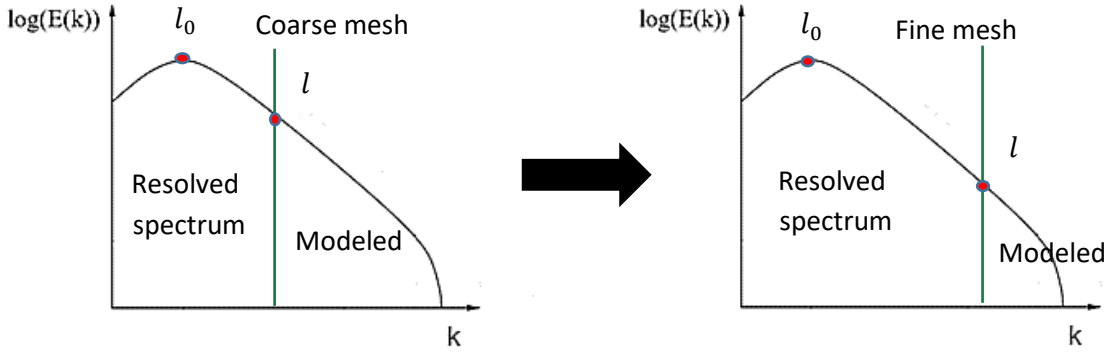

Figure 55: Resolved spectrum in LES on coarse and fine mesh (adapted from[68]).

LES should directly resolve 80% of TKE to be considered as well resolved. The grid density should ideally increase in all three directions in the near-wall as well as other regions of interest, for example, the wake region. There are different techniques to estimate the mesh resolution for LES. Some of them are [69]:

- Comparison between modeled to resolved stresses or turbulence (a smaller ratio means a better resolution)
- Comparison between modelled and resolved turbulent kinetic energy
- Two-point correlations (ratio of the integral length scale to the cell size)
- Comparison between the modeled and resolved dissipation

After testing all of the different methods for a fully developed channel flow, Davidson [69] recommends using two-point correlations as the best option. This provides information on how many cells are needed across the largest scales of motion to be properly resolved. However, at the end, it is up to the user to decide on the level of resolution needed in a particular application. At least four cells are needed for the coarse LES simulation. It is better to use eight or even more cells.[69]

Practical use of this method has been demonstrated by Gerasimov [67]. The integral length scale l_0 can be estimated from a previous RANS simulation using RKE or the SST turbulence model as [67],

$$l_0 = \frac{k^{1.5}}{\epsilon} \quad \text{,or } l_0 = \frac{k^{0.5}}{(C_\mu\, \omega)},\ C_\mu = 0.09 \qquad 6.1$$

If we now define the smallest resolved-length scale in the turbulent spectrum as l, then we need cells that have around half the size of this scale $\Delta=\frac{l}{2}$. This would resolve approx. 80% of TKE of the eddies. The estimation can be done using Table 5. K stands for the resolved turbulent kinetic energy as a function of the turbulent length scale l. The second column represents the ratio between the turbulent length scale and integral turbulent length scale. The smaller the ratio the better the resolution. This

then directly effects the ratio $\frac{l_0}{\Delta}$. Δ represents the cell size. Five cells across the integral length scale are need for the LES simulation to be properly resolved Twelve or more cells would ensure a 90% resolution of the energy spectrum [67].

Table 5: TKE in % for different length scale l and corresponding cell size [67]

Resolved part of TKE in %	$\frac{l}{l_0}$	$\frac{l_0}{\Delta}$
$k_{resolved}(\mathrm{l}) = 0.1 \cdot \mathrm{k_{total}}(\mathrm{l})$; (10%)	6.10	0.33
$k_{resolved}(\mathrm{l}) = 0.5 \cdot \mathrm{k_{total}}\ (\mathrm{l})$; (50%)	1.6	1.25
$k_{resolved}(\mathrm{l}) = 0.8 \cdot \mathrm{k_{total}}\ (\mathrm{l})$; (80%)	0.42	4.8
$k_{resolved}(\mathrm{l}) = 0.9 \cdot \mathrm{k_{total}}\ (\mathrm{l})$; (90%)	0.16	12.5

Contours of the l_0/Δ ratio on the symmetry plane (z=0 mm) for the test case Ahmed body are shown in Figures 56 and 57. The two considerd meshes were M4 and M6 (see section 6.5 for more mesh-related details). The M4 configuration was the finest mesh, with approx. 15 M elements. It was the primary candiate for the LES. The calculation was based on the RKE model (also used for the initializaton of LES). On the other hand, the mesh M6 using the steady SST model produced fairly accurate drag and lift coefficient. It is much coarser than M4 and is used here for the comparision. The areas that are well resolved (where the mesh contains more then 5 cells per integral length scale) are not coloured or are white, respectively. Colored regions show areas with insufficient resolution. Critical regions are indicated in the near-wall region, underbody and the wake.

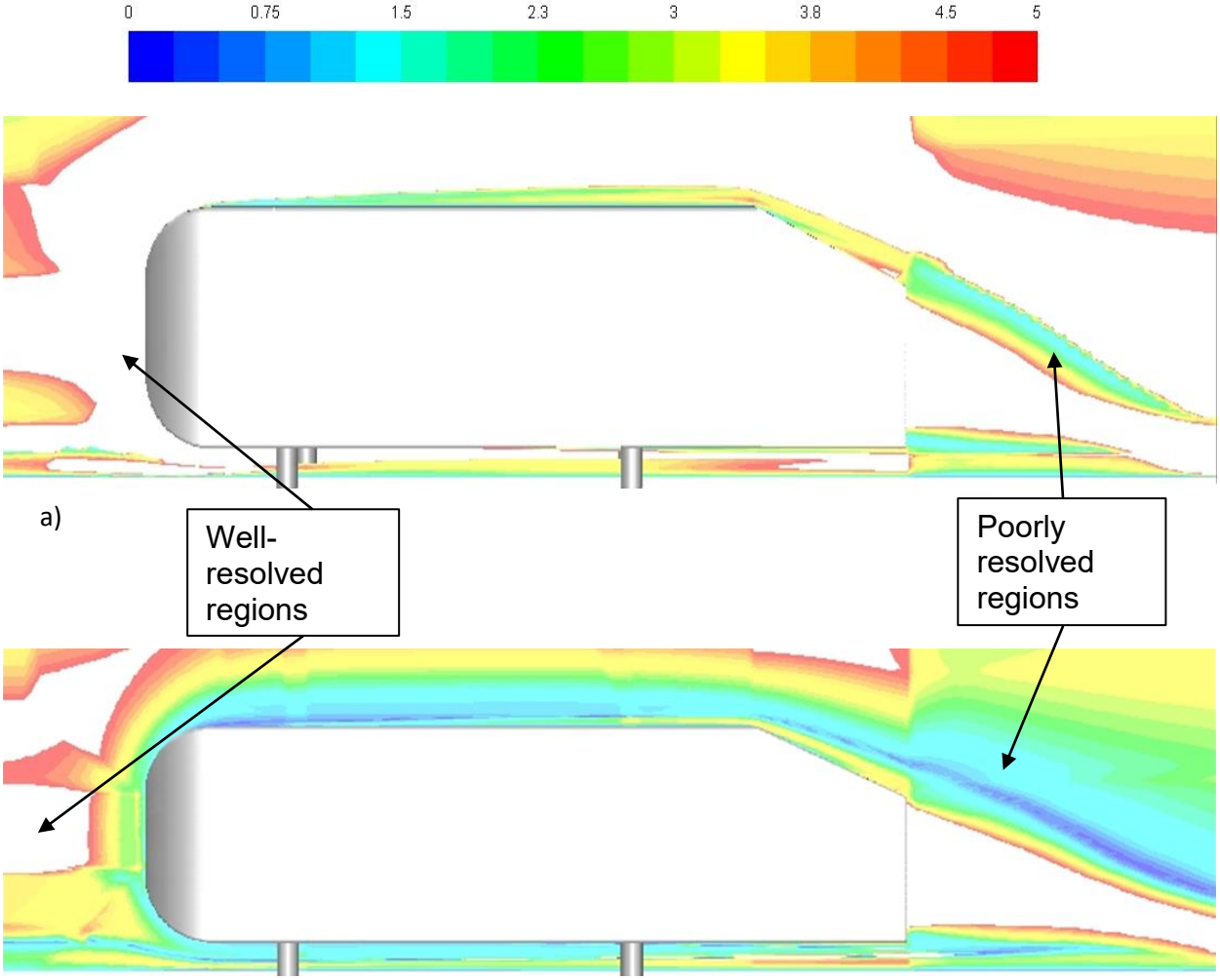

Figure 56: Contours of l_0/Δ ratio on the symmetry plane(z=0 mm): a) M4 (RKE turbulence model); b) M6 (SST turbulence model).

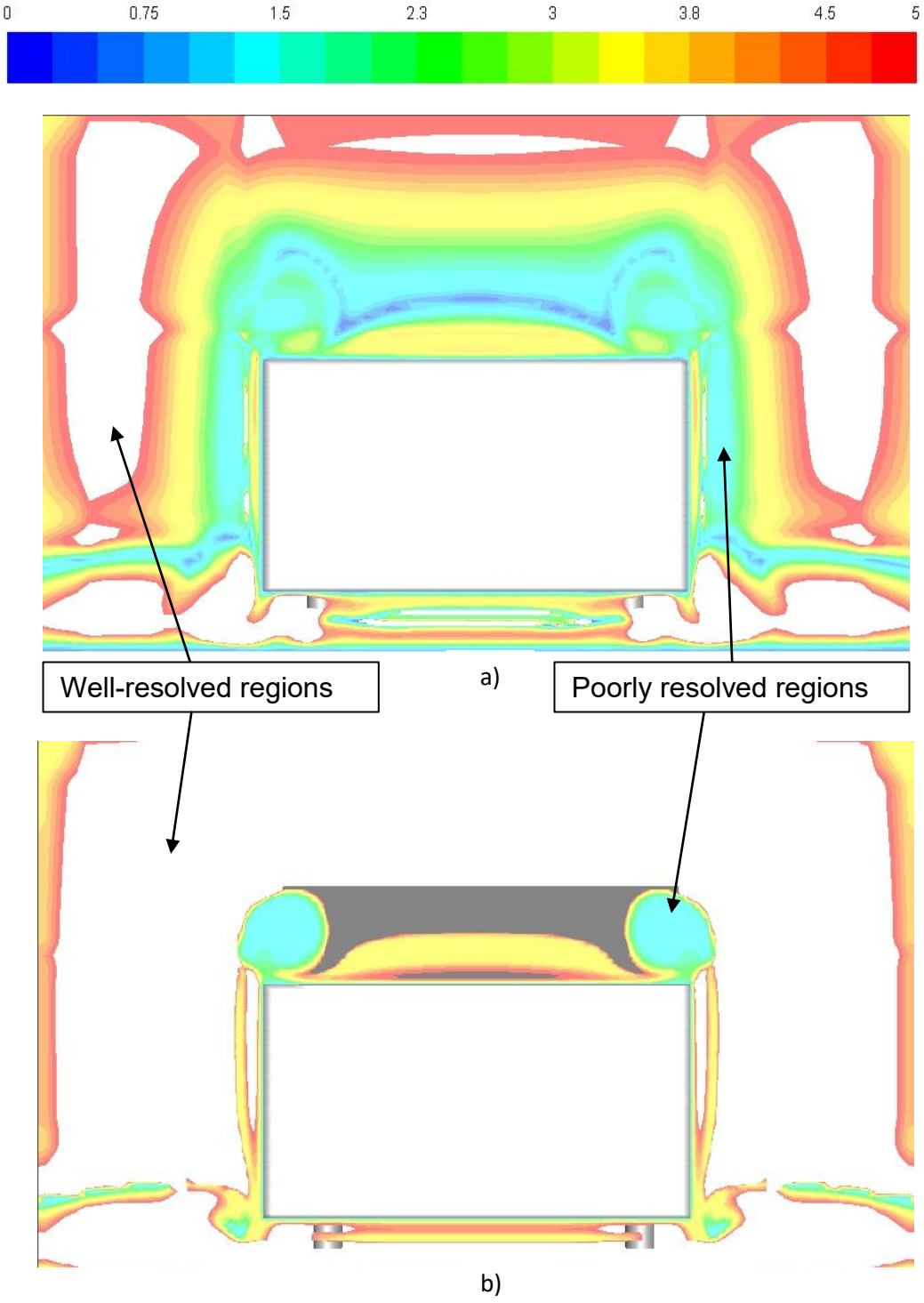

Figure 57: Contours of l_0/Δ ratio on the x=0 mm vertical plane (on the back end of the vehicle): a) M6 (SST); b) M4 (RKE).

The near-wall treatment is even more critical in LES- compared to the RANS-based computations. In typical engineering applications, the length scale linearly decreases as it approaches the wall [72]. Turbulent length scale l_t can be expressed as a product of the wall distance y and constant κ.

$$l_t = \kappa y \qquad 6.2$$

The above formulation suggests that turbulence length approaches zero as we are approaching the wall. This means infinitely small grid spacing in theory. This is not necessary in praxis, since we know that none of the turbulence structure is bigger than the Kolmogorov length scale. Furthermore, the viscous forces (molecular viscosity) in the laminar sublayer dampen the turbulence[72]. As the Reynolds number increases, the viscous sublayer gets thinner and allows the formation of ever-smaller eddies, which need to be resolved. The mesh resolution, and consequently also the computational cost, drastically increases, which makes this method less attractive for engineering applications. In our case, we ensure the average $y^+$of around 0.5 on the mesh M4, which makes the mesh fine enough in the wall normal direction. The second important aspect of the LES grid is the aspect ratios near the wall. Ideal elements would have an aspect ratio of 1. The local aspect ratios must not be too high. Higher values can give good results for simple shear flows or where the near-wall behavior is not so dominant. Span - and streamwise values should be around Δx=40, Δz=20 [67,73]. It is better to switch to a hybrid RANS/LES or SAS approach, which are less sensitive, when higher aspect ratios are unavoidable.

Figure 52 shows the contours of the aspect ratio on the symmetry plane inside the wake and over the slant. The mesh shows values of around 4 in the wake region and over the slant. The problem is the high aspect ratio occurring in the near-wall region, which makes M4 not ideal, but it appears to be sufficient for coarse LES simulation. Similar or even coarser LES meshes for the flow around the Ahmed body can be found in the literature in the study of Aljure et al. [70].

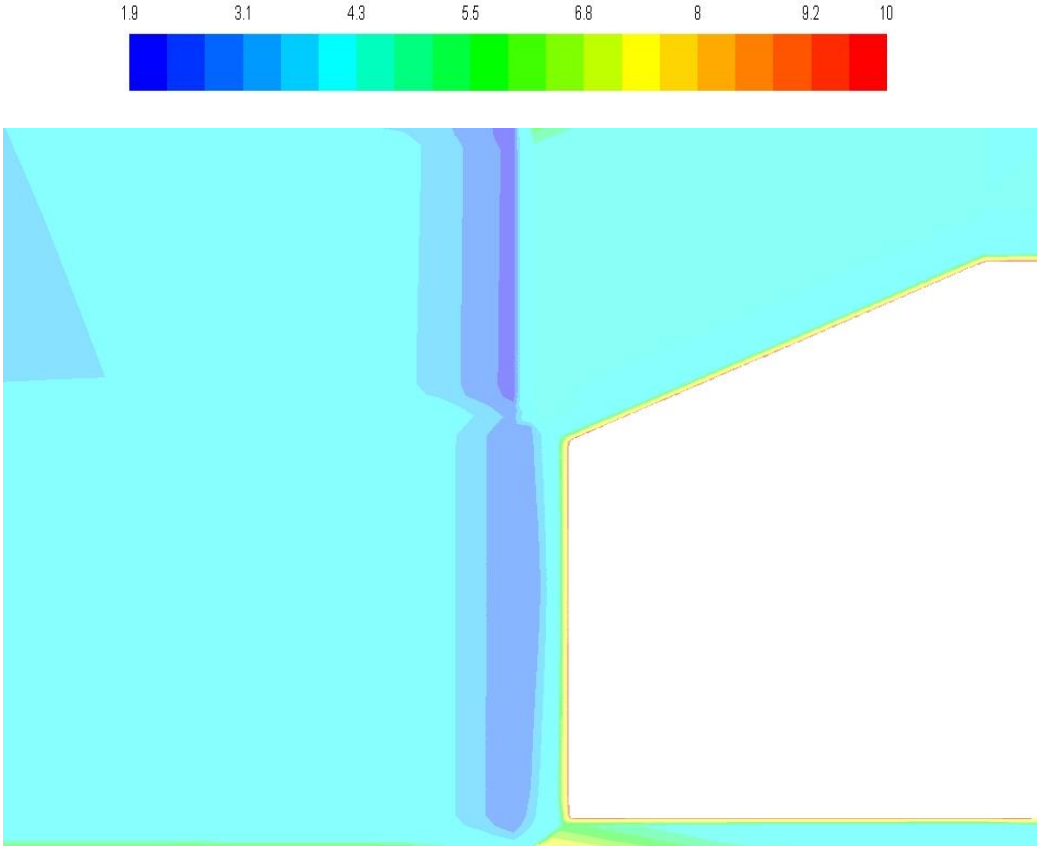

Figure 58: Aspect ratio (clip range 1.9–10) on the symmetry plane (z=0 mm) over the slant and in the region of primary interest (the wake region) for Mesh (M4).

6.6 Solver settings

The calculation was performed using a pressure-based coupled algorithm. The momentum and continuity equation is resolved in a coupled manner. The user can set various under-relaxation factors and the Courant number, which is used to stabilize the solution. The default value is 200. Larger values speed up the convergence, and smaller values improve the stability. For the complex flow, it is advisable to reduce the number. It was presently set to 50 [65].

The fluid was air. The default values for density and viscosity were set to $\rho = 1.1965 \frac{kg}{m^3}$, $\mu = 1.8301 \text{ x } 10^{-5} Pas$. This corresponds to the $Re = 20.4 \cdot 10^5$. To compute the force coefficients (drag and lift) some reference values need to be added. The reference area $0.112 m^2$ is the cross-sectional area of the vehicle perpendicular to the longitudinal X-axis. The value was taken from the publication by Meile et al. [40].

The k- ω SST turbulent model with automatic wall function and RKE with enhanced wall treatment is employed for a steady calculation. After the residuals and other flow equations had reached the convergence criterion (all observed residuals (continuity, momentum and turbulence parameters) reached at least value of around 10^{-4} together with stable behavior of the drag and lift coefficient), the simulation switched to the transient computations. SAS, IDDES, and LES were the tested unsteady models.

The numerical discretization errors (numerical diffusion) are more significant for the first-order scheme. Therefore the higher order schemes were used (third-order MUSCL) for pressure, momentum and turbulence quantities. The Green-Gauss node-base option is turned on. SAS was the first model of choice in the transient case. The gradient node-based option was changed to the least squares cell-based, which is the recommended option by Fluent theory manual[51]. The same applies to the momentum and time discretization, which were switched to the bounded central differencing and bounded second-order implicit. The same settings were applied to the transient calculations.

The turbulent intensity on the inlet and outlet was set to 0.2%. Backflow turbulent intensity ratio on the pressure outlet was set to 10, which was the default value.

The time step size needs to be determined before performing the unsteady simulation. It has to be small enough to resolve the relevant time-dependent features. The estimation (in approx. an order of magnitude) can be done using the Courant−Friedrichs−Lewy (CFL) condition [43],

$$\Delta t < \frac{\Delta x}{u} = \frac{Typical\ cell\ size}{Flow\ velocity} \qquad 6.3$$

The initial estimated time step size was 3.7e-5s. In praxis, the setting is mostly dependent on the stability behavior of the integral values and the residuals. The initialized time step size was reduced to 1e-5s. A maximum number of iterative subcycles within each time step Δt should be chosen, high enough to reach the convergence limits. This is crucial for the total computational time. Max. number of iterations was set to 20.

Each case needs to be initialized, after setting all the simulation parameters. It is essential to provide adequate initial data that are close to the final results in the steady as well as in the transient case. This can reduce the work of the solver to reach the converged solution. Keating [58] recommends using a hybrid initialization when using pressure based coupled solver (PBCS). The initialization is based on

solving the Laplace equation, which provides the initial velocity and pressure flow field. The velocity field is calculated as[51],

$$\nabla^2 \varphi = 0 \tag{6.4}$$

where φ represents the velocity potential($\vec{V} = \nabla\varphi$). The wall, inlet, farfield and outlet boundary condtion are calcualted as,

$$\text{Wall:} \quad \left.\frac{\partial\varphi}{\partial\vec{n}}\right|_{wall} = 0 \tag{6.5}$$

$$\text{Velocity inlet and far field:} \quad \left.\frac{\partial\varphi}{\partial\vec{n}}\right|_{inlet} = V_{\perp}\text{(= seleected normal inlet velocity e.g. in present case 30 m/s)} \tag{6.6}$$

$$\text{Outlet:} \quad \varphi = 0 \tag{6.7}$$

And similar for the pressure field, which is also based on solving the Laplace equation to produce the initial pressure field in the computational domain. The pressure value has to be provided at one of the domain boundary[51].

$$\nabla^2 p = 0 \tag{6.8}$$

p is defined on the outlet and wall boundary as,

$$\text{Wall:} \quad \left.\frac{\partial p}{\partial\vec{n}}\right|_{wall} = 0 \tag{6.9}$$

Outlet: The value for p is 1% bigger than the specified gauge pressure at this boundary

All the turbulent properties are initialized by the constant values over the domain.

Transient cases were initialized with the converged steady solution. The solver settings used for the tested turbulence modelling approaches are listed in Tables 6-10.

Table 6: k-ω SST solver settings

Solution method – k-ω SST − steady	
Pressure−Velocity Coupling	Coupled
Gradient	Green−Gauss Node-Based
Pressure	Second Order
Momentum	Third-Order MUSCL
Turbulent Kinetic Energy	Third-Order MUSCL
Specific Dissipation Rate	Third-Order MUSCL
Solution controls	
Flow Courant Number	50
Velocity inlet	
Turbulent Intensity(%)	0.2
Turbulent Viscosity Ratio	10
Pressure outlet	
Backflow Turbulent Intensity (%)	0.2
Backflow Turbulent Viscosity Ratio	10

Table 7: k-ε(RKE) solver settings

Solution method - k-ε(RKE) – steady	
Pressure−Velocity Coupling	Coupled
Gradient	Green−Gauss Node-Based
Pressure	Second Order
Momentum	Third-Order MUSCL
Turbulent Kinetic Energy	Third-Order MUSCL
Turbulent Dissipation Rate	Third-Order MUSCL
Solution controls	
Flow Courant Number	50
Velocity inlet	
Turbulent Intensity(%)	0.2
Turbulent Viscosity Ratio	10
Pressure outlet	
Backflow Turbulent Intensity (%)	0.2
Backflow Turbulent Viscosity Ratio	10

Table 8: SAS solver settings

Solution methods – SAS − transient	
Pressure−Velocity Coupling	Coupled
Gradient	Least Squares Cell-Based
Pressure	Second Order
Momentum	Bounded Central Differencing
Turbulent Kinetic Energy	Third-Order MUSCL
Specific Dissipation Rate	Third-Order MUSCL
Transient Formulation	Bounded Second-Order Implicit
Solution controls	
Flow Courant Number	50
Velocity inlet	
Turbulent Intensity(%)	0.2
Turbulent Viscosity Ratio	10
Pressure outlet	
Backflow Turbulent Intensity (%)	0.2
Backflow Turbulent Viscosity Ratio	10
Time step(s)	1e-5

Table 9: IDDES solver settings

Solution methods – IDDES − transient	
Pressure-Velocity Coupling	Coupled
Gradient	Least Squares Cell-Based
Pressure	Second Order
Momentum	Bounded Central Differencing
Turbulent Kinetic Energy	Third-Order MUSCL
Specific Dissipation Rate	Third-Order MUSCL
Transient Formulation	Bounded Second-Order Implicit
Solution controls	
Flow Courant Number	50
Velocity inlet	
Turbulent Intensity(%)	0.2
Turbulent Viscosity Ratio	10
Pressure outlet	
Backflow Turbulent Intensity (%)	0.2
Backflow Turbulent Viscosity Ratio	10
Time step(s)	1e-5

Table 10: LES solver settings

Solution methods – LES − transient	
Pressure−Velocity Coupling	Coupled
Gradient	Least Squares Cell-Based
Pressure	Second Order
Momentum	Bounded Central Differencing
Transient Formulation	Bounded Second-Order Implicit
Solution controls	
Flow Courant Number	50
Velocity inlet	
Turbulent Intensity(%)	0.2
Turbulent Viscosity Ratio	10
Pressure outlet	
Backflow Turbulent Intensity (%)	0.2
Backflow Turbulent Viscosity Ratio	10
Time step(s)	1e-5

7 Numerical results

Several different turbulence models are used for simulating the flow over the test case Ahmed body in this subsection. They are all listed in the Table 11 together with the corresponding meshes. The ticks mark, which turbulence model has been calculated on which particular mesh. For example, the nomenclature SST-M2 corresponds to the turbulence model k-$\boldsymbol{\omega}$ SST calculated on the mesh M2. Meshes M1-M6 are described in the subsection 6.5.

Table 11: Considered meshes and turbulence models

Grids	M1	M2	M3	M4	M5	M6
Applied turbulence models						
RANS:k-$\boldsymbol{\varepsilon}$ realizable(**RKE**) (steady)	✓	✓	✓	✓	✓	✓
RANS k-$\boldsymbol{\omega}$ **SST** (steady)	✓	✓	✓	✓	✓	✓
*URANS-**SAS** (trans.)*			✓			✓
***IDDES**(trans.)*			✓	✓		
***LES**(trans.)*			✓	✓		

7.1 Grid convergence study

Steady simulations using both considered steady RANS turbulence models (k-ω SST, k-ε(RKE)) have been performed for all considered mesh configurations (M1−M6). This was reasonable. The computational effort was much smaller compared to the unsteady case. In transient simulations, we consider only the finest grids M3 and M4. In the case of SAS we also considered M6, because it produced good results with the steady k-ω SST on the same mesh, especially regarding the predicted lift coefficient. From this point, it makes sense to assess consequently the transient behavior on the same mesh to see the possible benefits or limitations. All the drag and lift coefficient convergence plots (Figures 59-60) have drag and lift coefficient coming from the supporting struts ($c_{*,ST}$) included in the c_D ($c_D = c_{*,U} + c_{*,S} + c_{*,B} + c_{*,R} + c_{*,SI} + c_{*,F} + c_{*,ST}$). Where the subscript * denots D (drag) or L (Lift). The subscript U, S, R, SI, B refers to the subsurfaces defined in the subsection 7.3.3.2.

Residuals of continuity, momentum and turbulence properties were monitored during the calculations. All the variables achieved the convergence criteria of 10^{-4} or lower. Additionally observed were the drag and lift coefficients. The computational runs were executed dependant on their behavior. After the stabilization of both coefficients, the simulations were run for an additional couple of 100 iterations, to make sure that no more oscillations occurred in the solution. This was done for all steady simulations. Transient simulations were run up to 25,000 on mesh M3 and 15,000 time steps on mesh M4 for the unsteady models, because more time steps were affordable on a coarser mesh with still

shorter computational time while fewer time steps were made on the finer mesh. With the exception of SAS-M6, which showed stable behavior of the drag and lift coefficient after around 5000 time steps. This particular simulation (SAS-M6) was therefore run just up to 15,000 steps in total. All the considered transient simulations were run for long enough, to asses the statistically stationary behavior.

Looking at the drag coefficient convergence plot in Figures 59 and 60, it can be noticed that the values for all models stabilize after around 500 iterations, where the calculation produces a pretty much constant value with some minor oscillations. Unsteady cases produce higher amplitudes in the initial time steps, particularly in the IDDES approach, which in the end significantly overpredicts the drag coefficient. Both LES show very similar behavior at the beginning with a decrease and increase of the coefficient, but later on, M3 produces slightly higher values. Of interest is the comparison between the well-modeled (M6) and the well-resolved (M3) meshes. M6 configurations show smaller mean values but higher amplitudes.

As seen from Figures 61 and 62, the lift coefficient in the steady case evolves very similar to the drag coefficient. After the initial oscillations, the lift stabilizes and reaches a nearly constant value of around 0.364 in case of the RKE-M5, which is in the best agreement with the experimental data by Meile et al. [40]. Amplitudes are significantly higher in the transient cases, especially in SAS-M6, where the lift oscillates between 0.25 and 0.45. On the other hand, SAS with wall-resolved mesh underpredicts the lift. Oscillations are much smaller compared to M6.

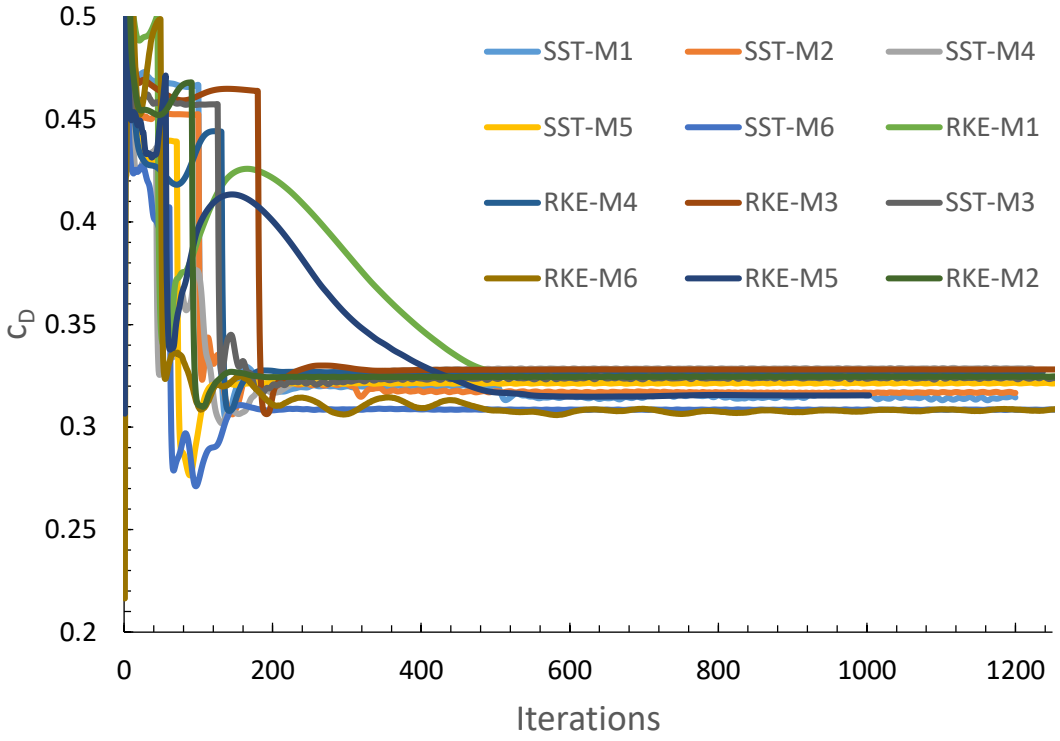

Figure 59: Drag variations for the steady RANS-models using different mesh resolutions M1–M6.

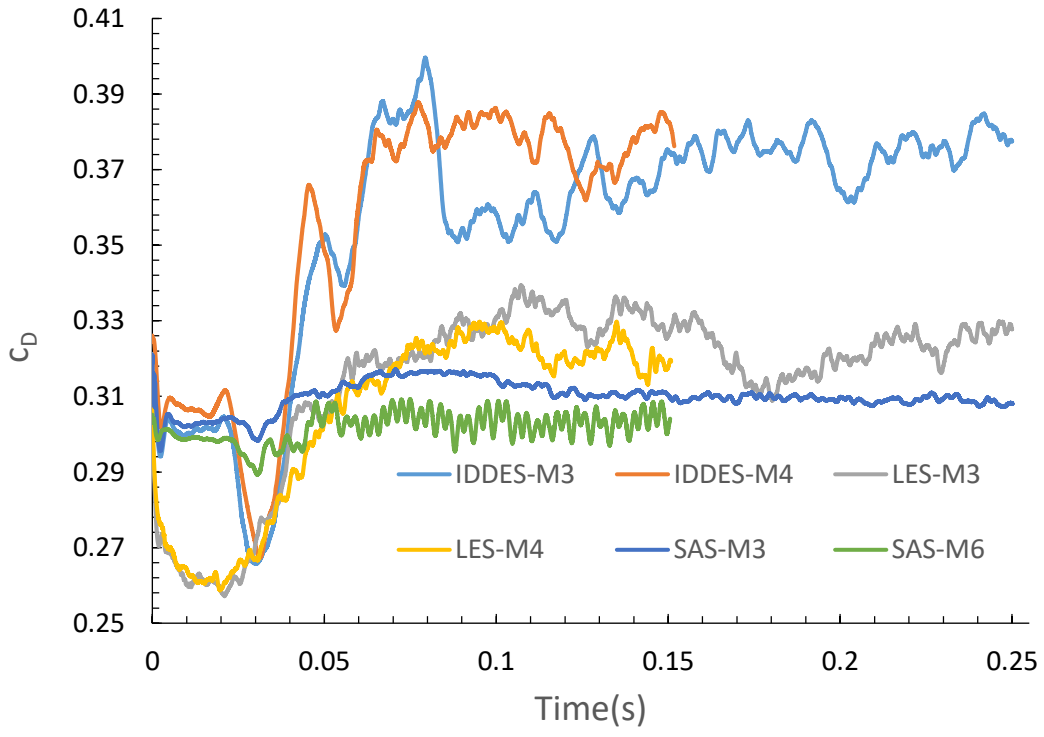

Figure 60: Drag variations for the transient models using different mesh resolutions M3,M4 and M6.

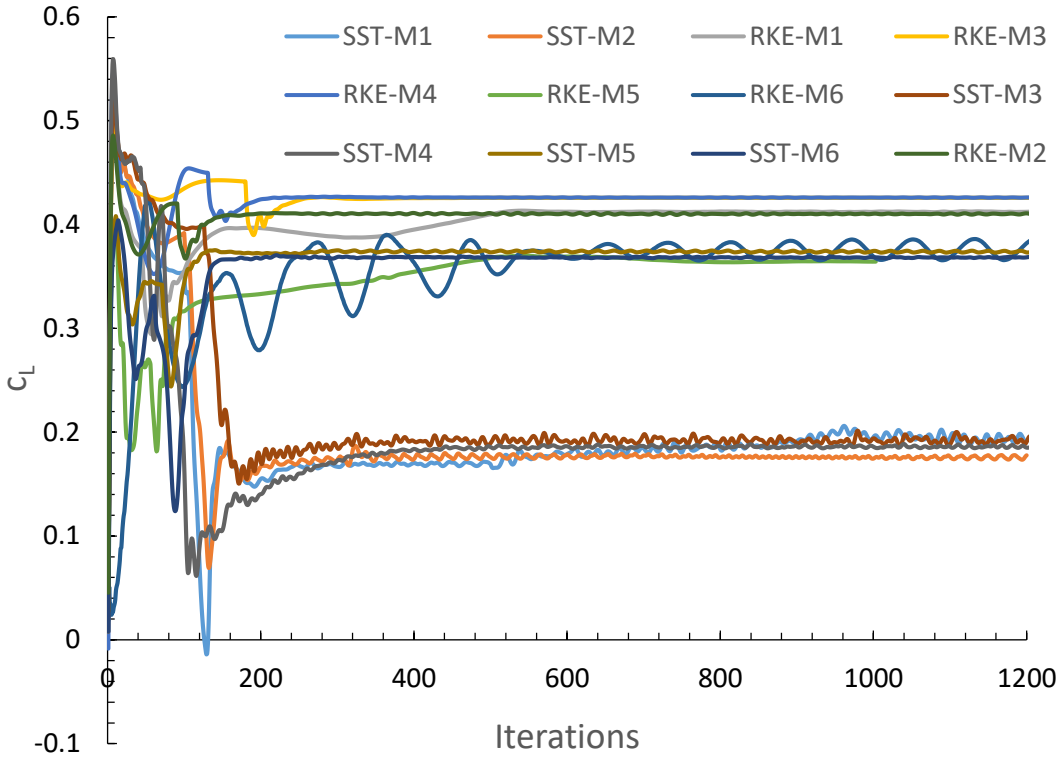

Figure 61: Lift variations for the steady RANS-models using different mesh resolutions M1−M6.

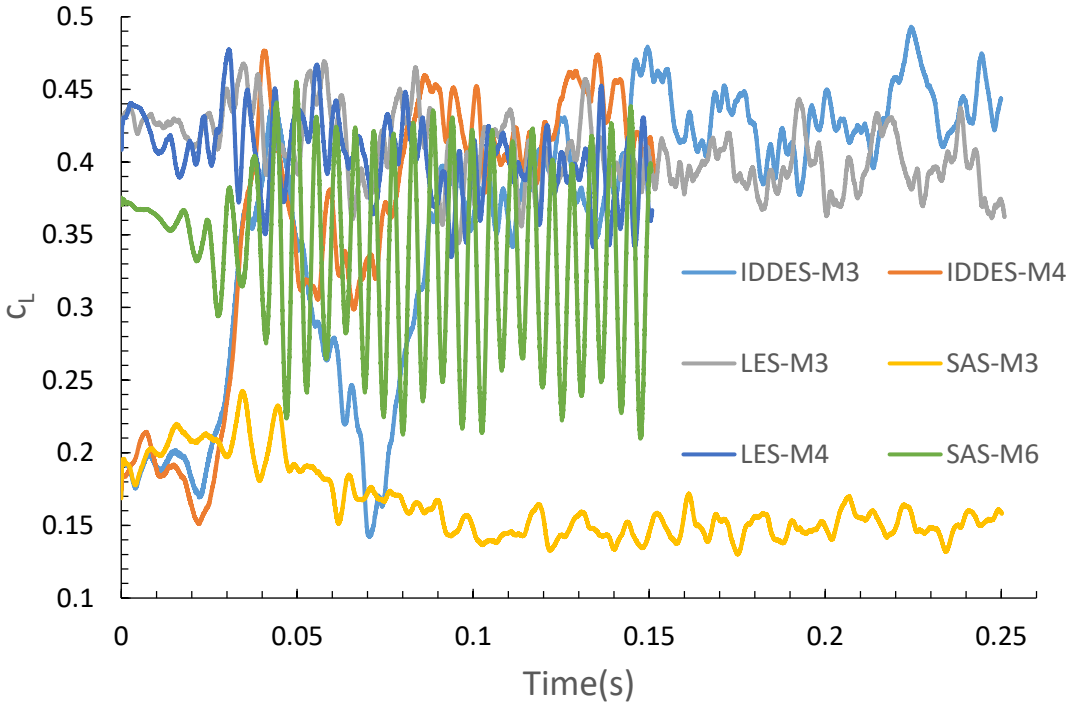

Figure 62: Lift variations for the transient models using different mesh resolutions M3,M4 and M6.

7.2 Near-wall resolution y^+ values

The non-dimensionalized distance of the first grid point from the wall in the y^+-units was checked in order to ensure the required near-wall resolution for different near-wall treatments used in this study. The meshes have been created using three different wall cell-layer heights. Two of them ensure an average of $y^+ \approx 1$ or below (required for wall-resolved simulation). The third was designed to avoid a fine wall-resolved near-wall spacing while using wall functions the Fluent guidelines[51,75] suggest having $y^+ > 30$ at the wall, when applying a wall function. The y^+ for steady RANS and transient approaches can be seen in Tables 12, 13 and 14.

The y^+ is not constant over the surface of the body. It reaches values close to zero on the front surface (stagnation point) and back end of the vehicle (base and slant surface), where the velocity is low. The values are higher along the curved parts of the front surfaces and in underbody region around the legs. Figure 63 exemplarily illustrates the contours of the y^+ on the surface of the Ahmed body for the case SST-M4.

Table 12: average, min, and max y^+ values for steady RANS *k-ω SST*

Simulation	Average y^+	Maximum y^+	Minimum y^+
SST-M1	1.2368	4.0682	0.0123
SST-M2	0.4657	1.3748	0.0098
SST-M3	1.3418	4.1622	0.0047
SST-M4	0.5038	1.3747	0.0077
SST-M5	54.524	118.93	2.9459
SST-M6	56.212	118.50	2.7995

Table 13: average, min, and max y^+ values for steady RANS k-ε realizable(RKE)

Simulation	Average y^+	Maximum y^+	Minimum y^+
RKE-M1	1.2754	4.8430	0.0155
RKE-M2	0.4856	1.6343	0.0119
RKE-M3	1.4041	5.4123	0.0133
RKE-M4	0.5292	1.6524	0.0125
RKE-M5	56.252	128.75	3.9482
RKE-M6	58.171	128.89	4.0041

Table 14: average, min, and max y^+ values for transient SAS, IDDES and LES

Simulation	Average y^+	Maximum y^+	Minimum y^+
SAS-M3	1.3488	5.0637	0.0122
SAS-M6	55.693	142.45	4.2873
IDDES-M3	1.3480	4.9332	0.0122
IDDES-M4	0.5034	1.5548	0.0083
LES-M3	0.9051	4.5181	0.0191
LES-M4	0.3434	1.6220	0.0128

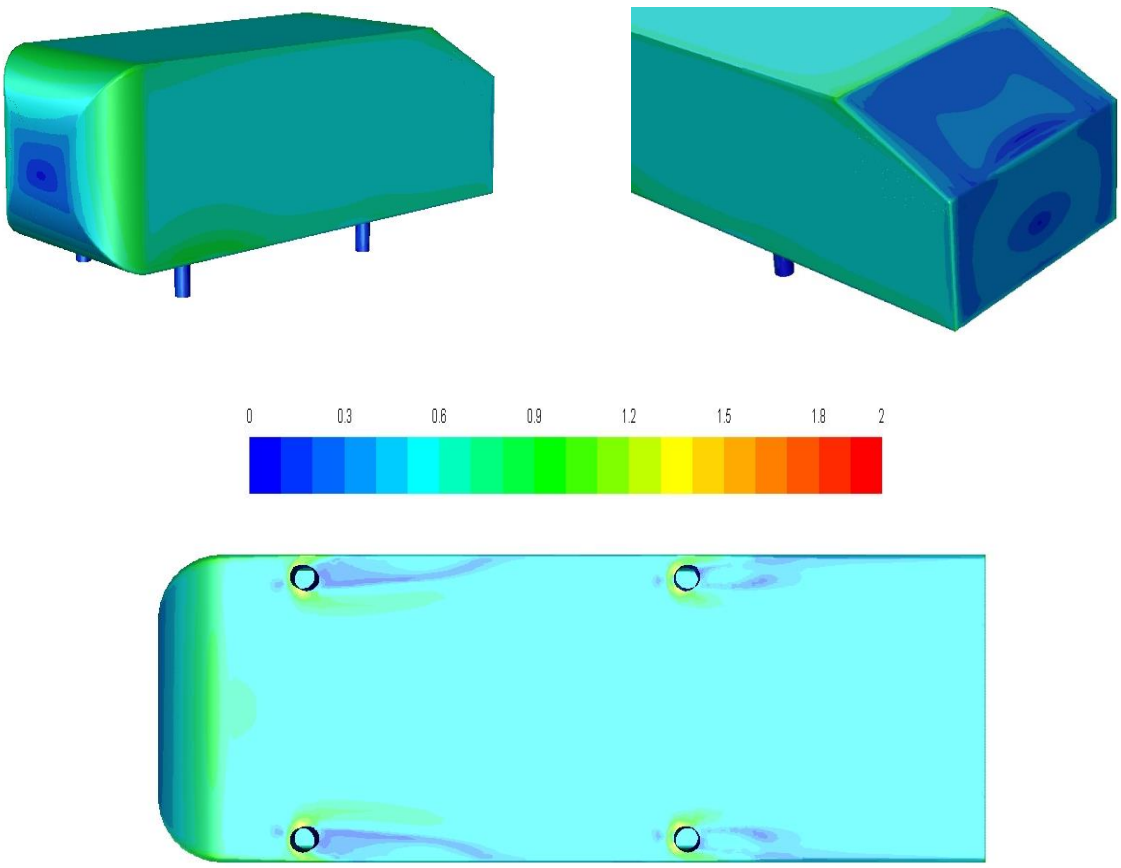

Figure 63: y^+variation on the front, back and underbody surfaces for SST-M4

7.3 Aerodynamic force validation

7.3.1 Drag and lift coefficients

Figure 63 presents relative variations of the drag coefficient predicted by the assessed turbulence models from the experimental value measured by Meile et al. [40] c_D=0.3077. The best agreement has been achieved with the RKE turbulence model using the M3 mesh. This produced a relative error -0.71%. Steady RKE-M4 takes the second place with an error of approximately -1%. RKE-M2 was third with an error of -1.79%. Following is another RKE model with an error of around 1.85%. They all underpredicted the drag coefficient. Steady SST-M4 took fourth place followed by the same turbulence model using the coarser mesh M3. The best transient results were achieved with the LES-M3 with an error of around 3.68%. Steady SST-M6, RKE-M5, SST-M1, and SST-M2 apper in 8th−12th place, respectively. The most computationally expensive transient simulation LES-M4 produced an error of around 5.91%. Next there followed the SAS-M3 and SST, RKE both on M6. The unsteady cases SAS-M6, IDDES-M3, and IDDES-M4 give significantly higher error around 15% .

Analogously to Figure 64, Figure 65 summarizes the relative errors of the predicted lift coefficient. The overall agreement of the lift coefficient with the experimental data was worse in comparison to the drag coefficient. The best value was achieved by RKE-M5, which represents the coarsest mesh with around 3.5 M elements. It produced an error of around 1.68%. SST-M6 was placed second with an error of around 4.18%. Next followed the SST-M5 and RKE-M6. SAS in the M6 configuration was fifth. It underpredicted the lift coefficient by approx. -9%. SAS-M3 and all SST-based models show a similar trend of underpredicting the lift. They underpredicted the lift coefficient by more than 45%. Even though the SAS-M3 gave good results regarding the predicted drag coefficient, it was placed last for the predicted lift. The wall-resolved RKE model showed smaller errors. The best value was achieved with the RKE-M2, followed by the RKE-M1, RKE-M3, and RKE-M4. The errors varied between 14% and 18%. Both LES simulations overestimated lift by about 10%. LES-M4 was may be attributed to mesh refinement. The error of both IDDES-cases was markedly bigger.

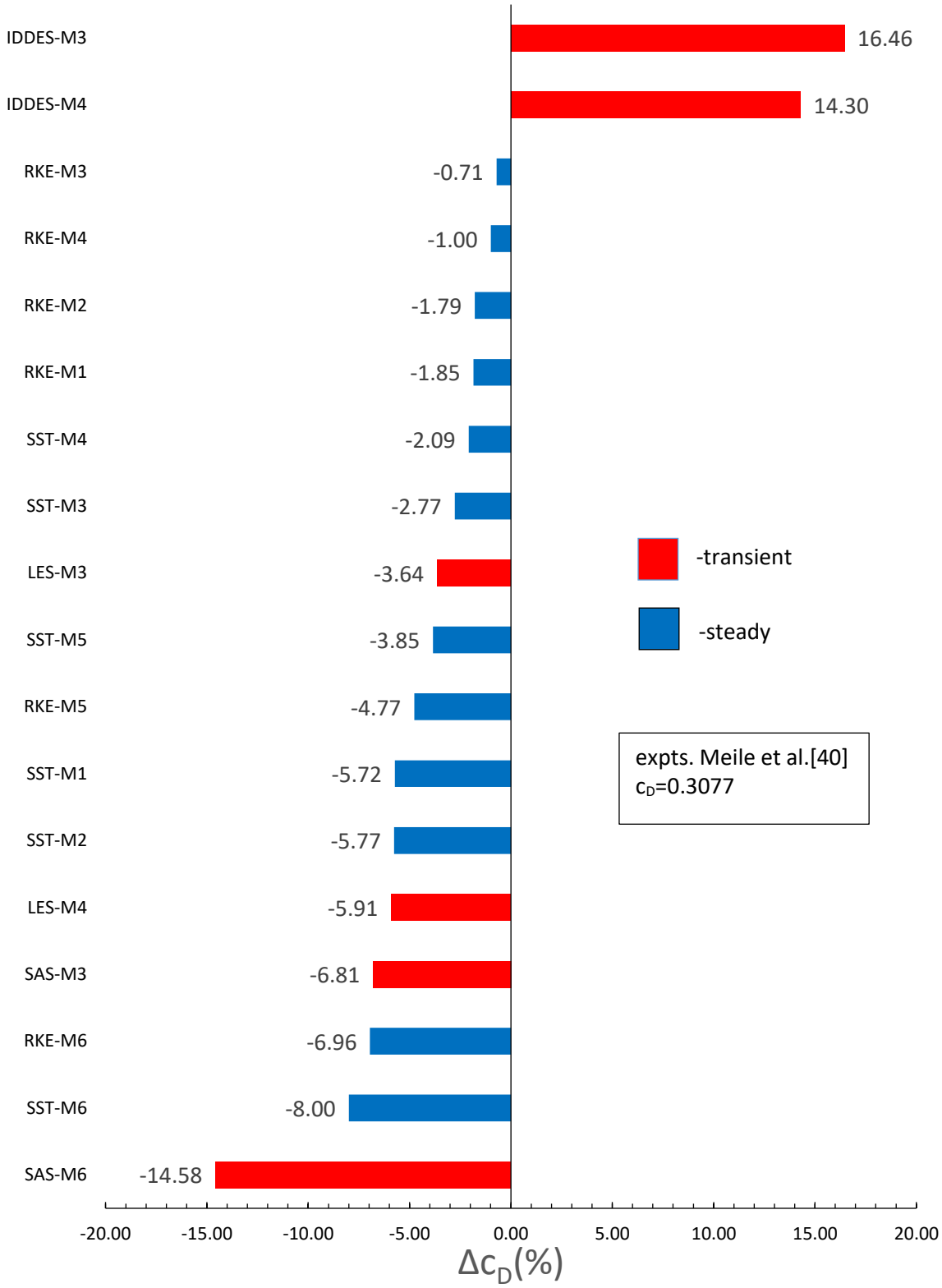

Figure 64: Error of predicted drag coefficient relative to experimental value.

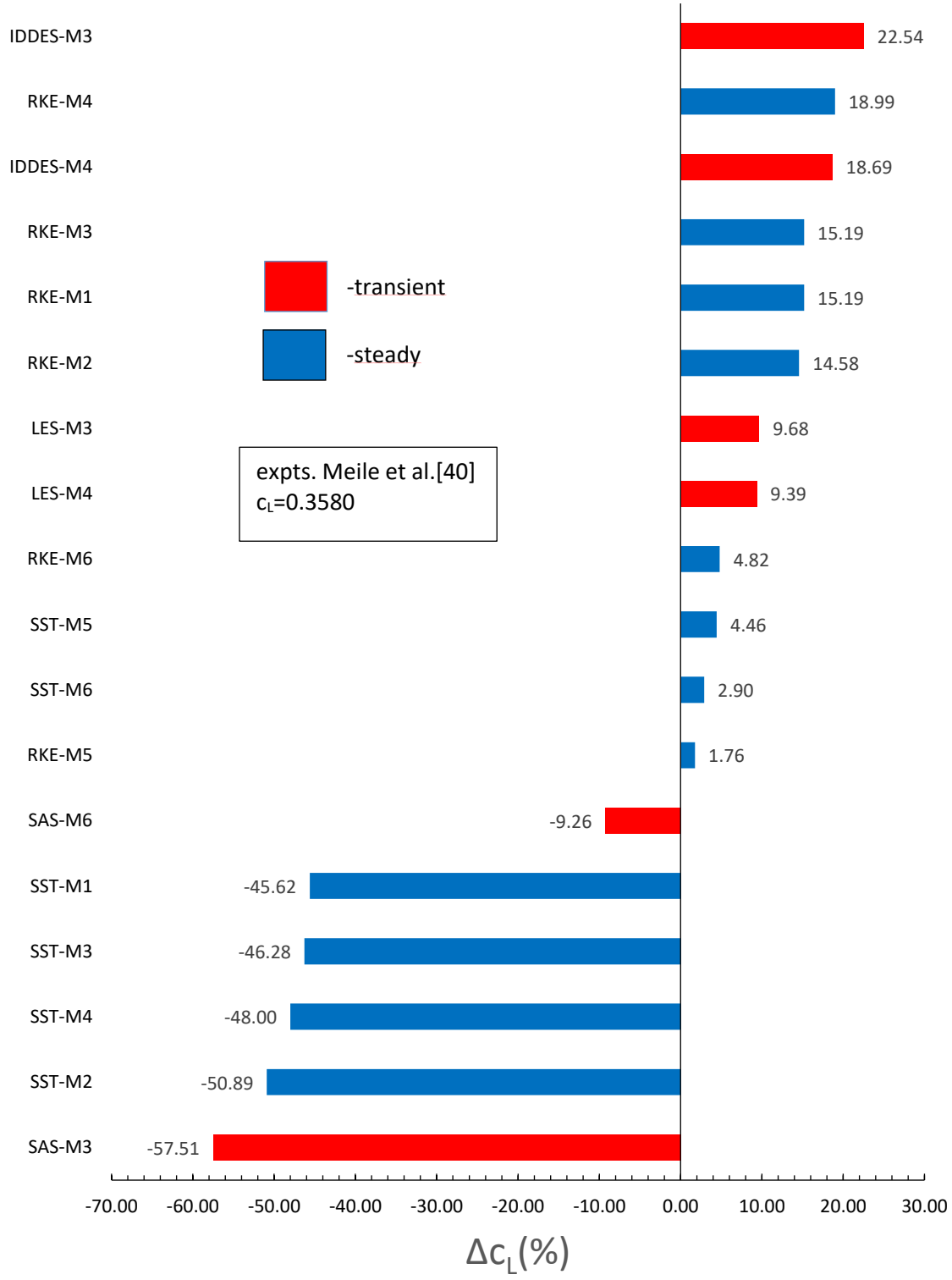

Figure 65: Error of predicted lift coefficient relative to experimental value.

7.3.2 Comparison with the literature

Bordei and Popescu [17] also noticed the inconsistency of the mesh refinement with the accuracy of results obtained for the same Ahmed body configuration, where, for example, an unsteady RKE with 23.5 M elements produced worse results than a steady RKE with 500 k elements, or a k-ω SST with 500 k elements performed better than the same model with 13.8 M elements in Fluent. Similar results have been noticed for both the drag and lift coefficient.

The present IDDES results exhibit significant overpredictions for c_D. Similar overpredictions of the IDDES model for c_D are also observed in the literature [35], where the mesh was wall-resolved ($y^+<1$).

LES results for c_D are available in [20]. The authors of this study [20] tested the following subgrid-scale models for LES (and DES) approaches: LES with Smagorinsky model and wall function (LES-NWM); wall-resolving LES with dynamic Smagorinsky model (LES-NWR); LES with spectral vanishing viscosity (LES-SVV); and detached-eddy simulation (DES-SST).

The presently discussed results from literature [17,20,35] are summarized in Table 15. All of them have been obtained for a roughly 30% higher free-stream velocity and Re number, U (40m/s), Re=2.768x10^6. They considered the same Ahmed body geometry with the same ground clearance (50 mm) as in the present test case. The grids were wall-resolved and wall-modeled.

Table 15: Errors of predicted drag and lift coefficient relative to experiments, from the previous computations in the literature

Literature		c_D	c_L	y^+ wall resolution
Meile [40]	Experiment(Re=2.768x10^6)	0.2967	0.3581	-
	Turbulence model (mesh size M-million, k- thousands)	Δc_D(%)	Δc_L(%)	
Bordei & Popescu [17]	RKE steady (500 k)	1.79	-5.33	248.5
	RKE unsteady (500 k)	2.46	-7.57	248.0
	RKE steady (polyhedra 1.3 M)	-0.57	-14.83	193.2
	RKE unsteady (1.9 M)	26.05	-0.31	112.0
	RKE unsteady (13.8 M)	17.63	1.65	14.0
	RKE unsteady (hexa 23.5 M)	5.16	7.51	90.42
	k-ω SST Fluent (500 k)	-9.00	-15.67	227.2
	k-ω SST Fluent (1.9 M)	-9.67	6.67	102.7
	k-ω SST Fluent (1.68 M)	-3.94	-10.64	84.83
	k-ω SST Fluent (13.8 M)	22.35	-19.02	13.5
Krastev & Bella [19]	RKE steady (1.53 M)	-5.29	-	30-120
	RKE unsteady (3.06 M)	-4.62	-	30-120
Guilmineau et al. [35]	IDDES (23.6 M)	28.14	-7.68	y^+<1
	DES (23.6 M)	47.32	4.64	y^+<1
	K-ω SST (23.6 M)	8.46	-51.86	y^+<1
Serre et al. [20]	LES-NWM (18.5 M)	15.60	-	y^+~40
	LES-NWR (40 M)	16.62	-	y^+<1
	LES-SVV (21.3 M)	6.84	-	y^+~400
	DES-SST (23 M)	45.26	-	y^+~40

7.3.3 Force breakdown

The detailed force analysis was made for all assessed turbulence models using k-ω SST, k-ε (RKE) in the steady case and SAS, IDDES and LES in the transient. The steady RANS, RKE-M5 and SST-M6 simulations were used for the comparison. They were chosen based on the predicted results for the drag and lift coefficient in the subsection 7.3.1, where they produced the best agreement regarding the combined drag and lift coefficient among all steady RANS simulations. M5-RKE was placed first, followed by the SST-M6. All the transient cases were included in the force evaluation within this subsection. This means SAS-M6, SAS-M3, IDDES-M3, IDDES-M4, LES-M3, and LES-M4.

7.3.3.1 Total drag and lift force: pressure and viscous force contributions

Figure 66 shows the comparison between the pressure and viscous force contributions to the drag coefficient. All the steady RANS and hybrid computations predicted a higher viscous part than LES. The values vary between 0.0468 and 0.0580. This is approx. 3.5 times higher than in LES. The pressure contribution was dominant in all the considered models. Both IDDES methods produced the highest values for the pressure drag. In this case the pressure contribution alone made up already the total experimental value obtained by Meile et al.[40]. SAS-M6 produced the smallest pressure contribution, which resulted in a significant underprediction of the drag coefficient.

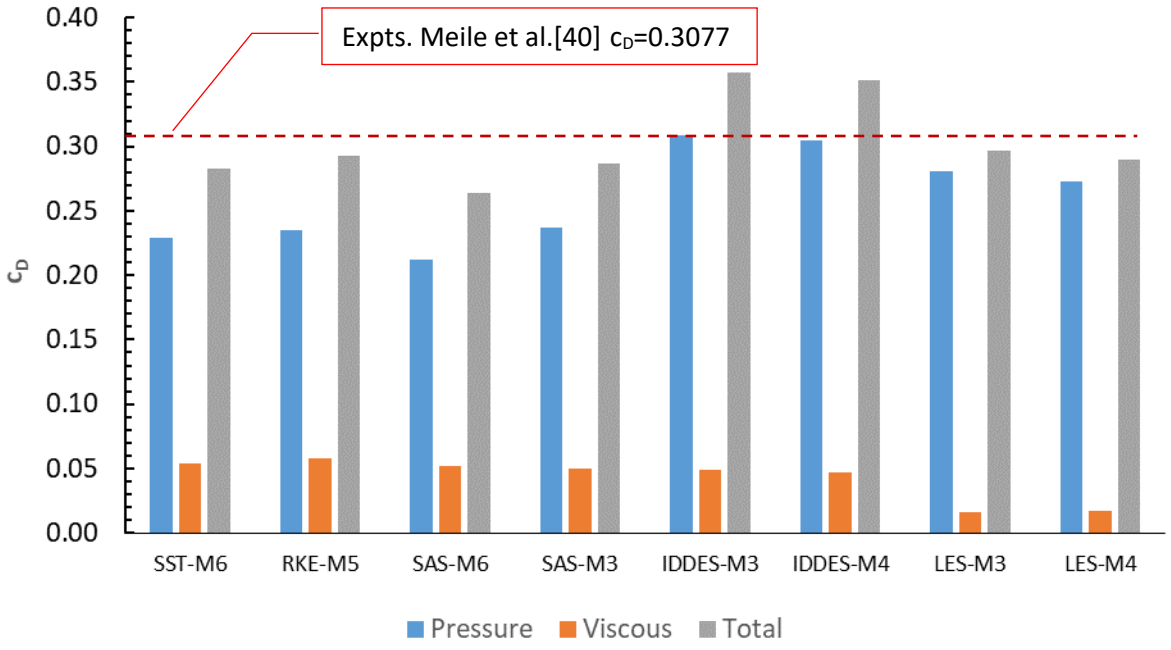

Figure 66: Total drag force coefficient: pressure and viscous force contributions.

Figure 67 shows the pressure and viscous contributions to the total lift coefficients. The viscous force contributions are evidently always negligibly small so that the lift coefficient is essentially only determined by the pressure force. The cross comparison of the individual simulation results shows a significant underprediction of the lift coefficient by the SAS-M3 and a marked overprediction by the IDDES. The best agreement was obtained by the RKE-M5 and SST-M5. The LES overpredicted the lift coefficient by about 10%.

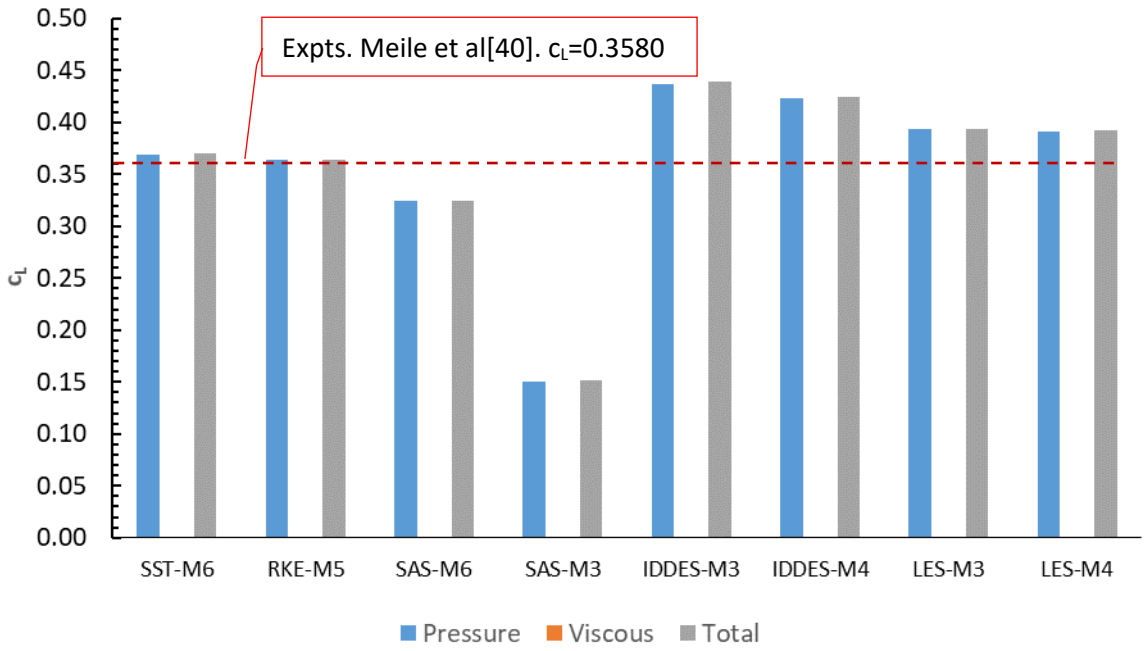

Figure 67: Total lift force coefficient: pressure and viscous force contributions.

7.3.3.2 The breakdown into subsurfaces of the Ahmed body

The surface of the body has to be broken down into different parts to assess the contribution of each one to the overall drag and lift coefficients. The surface of the Ahmed body was divided into five subsurfaces: underbody, base, slant, roof, sides, and front. The forces acting on each subsurface were additionally distinguished into a pressure and viscous component to see which of them is dominant. Since no empirical data were available here for experimental validation, the analysis of the contributions from the subsurfaces only shows a cross-comparison between different turbulence models.

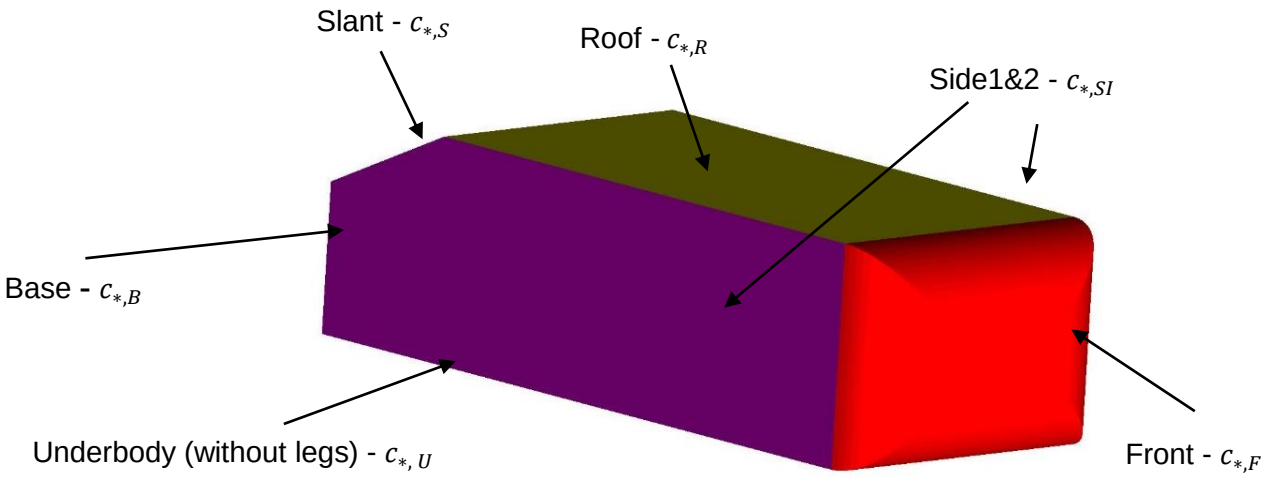

*Figure 68: Definition of the subsurfaces of the Ahmed body. Subscript *: D (drag) or L (lift.*

The contribution from a given subsurface i to the drag and lift coefficient is always computed as

$$c_{D,i} = \frac{1}{A_{ref}\rho W_\infty^2/2}\int_{A_i}\{[-(p-p_\infty)+\tau_{xx}]n_x + \tau_{xy}n_y\}dA \quad 7.1$$

$$c_{L,i} = \frac{1}{A_{ref}\rho W_\infty^2/2}\int_{A_i}\{[-(p-p_\infty)+\tau_{yy}]n_y + \tau_{xy}n_x\}dA \ , \quad 7.2$$

respectively. n_x and n_y denote the components of the unit surface orthogonal vector into streamwise and vertical direction, respectively. The pressure contribution is measured in terms of the local static pressure difference to the free-stream value, being $p - p_\infty$.

7.3.3.2.1 The drag coefficient of subsurface – Front

The drag coefficient at the front part is dominated by the pressure force in all cases, with the exception of LES, where the viscous part shows higher values. This transient simulation predicted the smallest contribution to the total drag from the front part. The highest total value was predicted by the steady SST-M6. Except for LES, all models predicted similar values for the viscous contribution, probably due to the use of a RANS model in the near wall layer, but they differ for pressure drag.

Table 16: Drag coefficient of subsurface – Front.

$c_{D,F}$ *Drag Coefficient – Front*			
	Pressure force	Viscous force	Total
SST-M6	0.0241	0,0109	0,0350
RKE-M5	0.0190	0.0105	0.0294
SAS-M6	0.0191	0.0098	0.0289
SAS-M3	0.0089	0.0098	0.0187
IDDES-M3	0.0101	0.0098	0.0199
IDDES-M4	0.0116	0.0096	0.0212
LES-M3	0.000001	0.0051	0.0051
LES-M4	0.0012	0.0052	0.0065

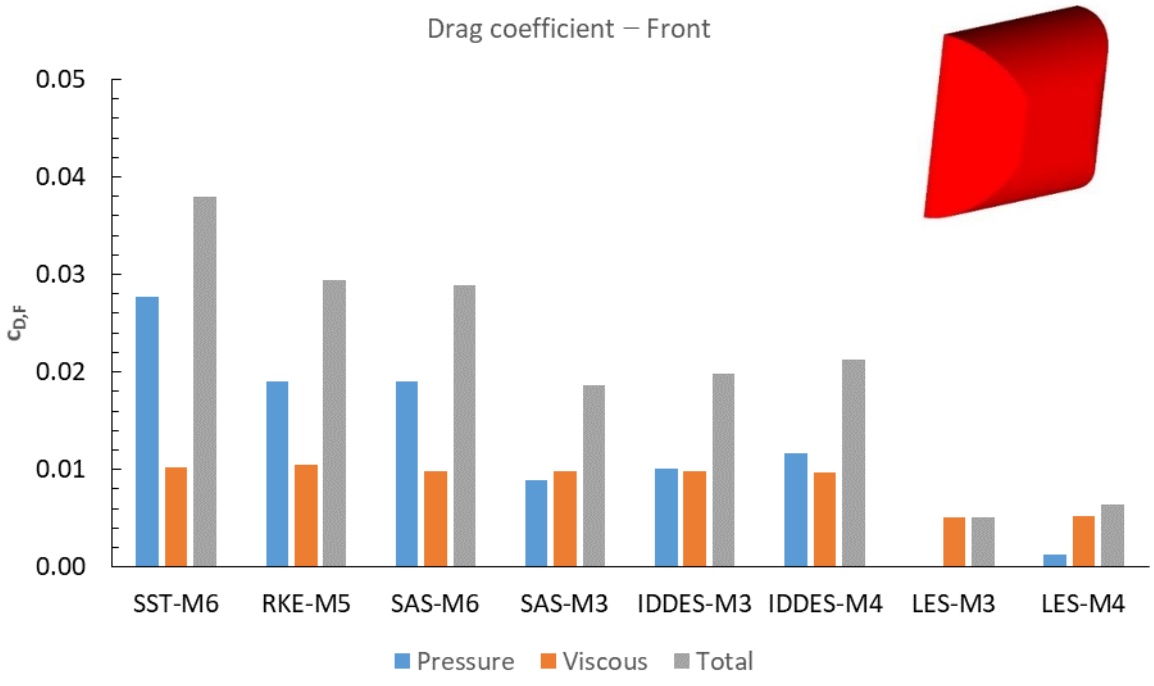

Figure 69: Drag coefficient of subsurface Front.

7.3.3.2.2 The drag coefficient of subsurface – Side 1 & 2

The total contribution of both sides is smaller compared to that of the front. The pressure force was practically negligible in all cases. This was expected due to the orientation of this subsurface, resembling parallel flow along the flat plate, where only a viscous forces are relevant. LES calculations produced here again the smallest contributions with the values below 0.005.

Table 17: Drag coefficient of subsurface – Sides 1 & 2.

$c_{D,SI}$ Drag Coefficient Sides 1 & 2			
	Pressure force	Viscous force	Total
SST-M6	1.95E-09	0.0185	0.0185
RKE-M5	2.09E-09	0.0195	0.0195
SAS-M6	3.55E-09	0.0146	0.0146
SAS-M3	3.18E-09	0.0180	0.0180
IDDES-M3	3.07E-09	0.0170	0.0170
IDDES-M4	3.14E-09	0.0158	0.0158
LES-M3	3.48E-09	0.0042	0.0042
LES-M4	3.32E-09	0.0046	0.0046

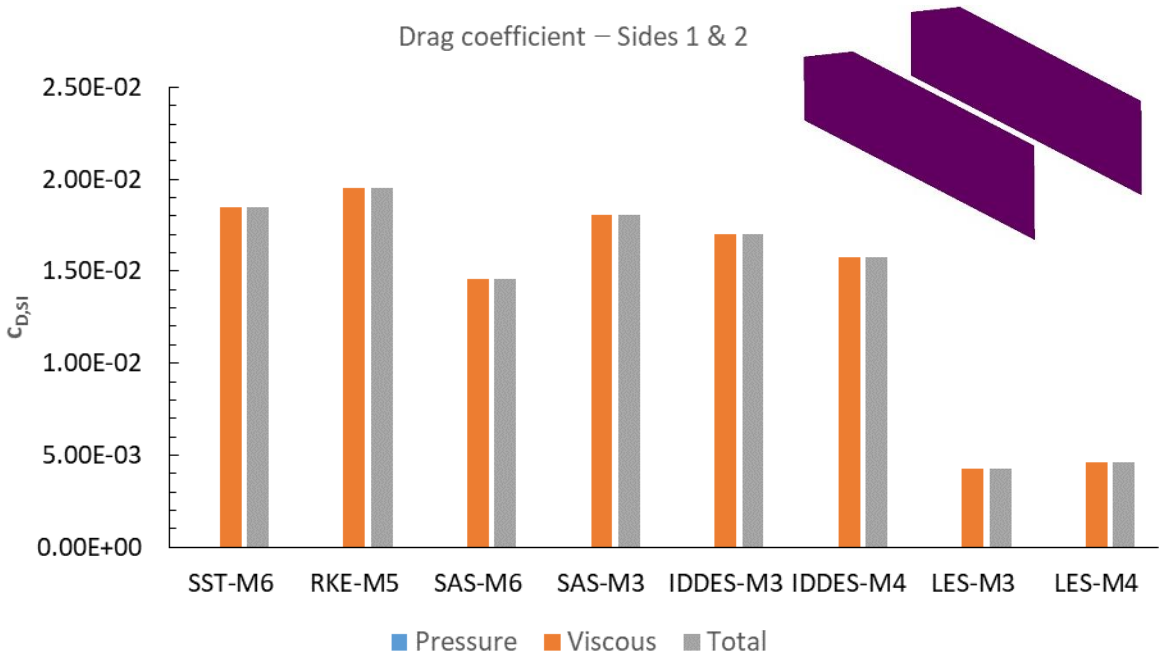

Figure 70: Drag coefficient of subsurface - Sides 1 & 2.

7.3.3.2.3 Drag coefficient of subsurface – Base

As expected, the contribution to total drag increases as we move towards the rear part of the body. The contribution from the subsurface base reaches values of around 0.07 for SST-M6, RKE-M5, SAS-M6 and 0.12 in all other cases, with a slight decrease in the LES cases. As the flow separates it creates a vast separation region with lower pressure. This strongly contributes to the drag.

Table 18: Drag coefficient of subsurface – Base.

$c_{D,B}$ Drag Coefficient –Base			
	Pressure force	Viscous force	Total
SST-M6	0.0687	1.07E-19	0.0687
RKE-M5	0.0734	1.73E-19	0.0734
SAS-M6	0.0665	2.66E-20	0.0665
SAS-M3	0.1255	-1.41E-19	0.1255
IDDES-M3	0.1205	8.52E-20	0.1205
IDDES-M4	0.1189	1.04E-19	0.1189
LES-M3	0.1175	8.37E-20	0.1175
LES-M4	0.1120	4.21E-20	0.1120

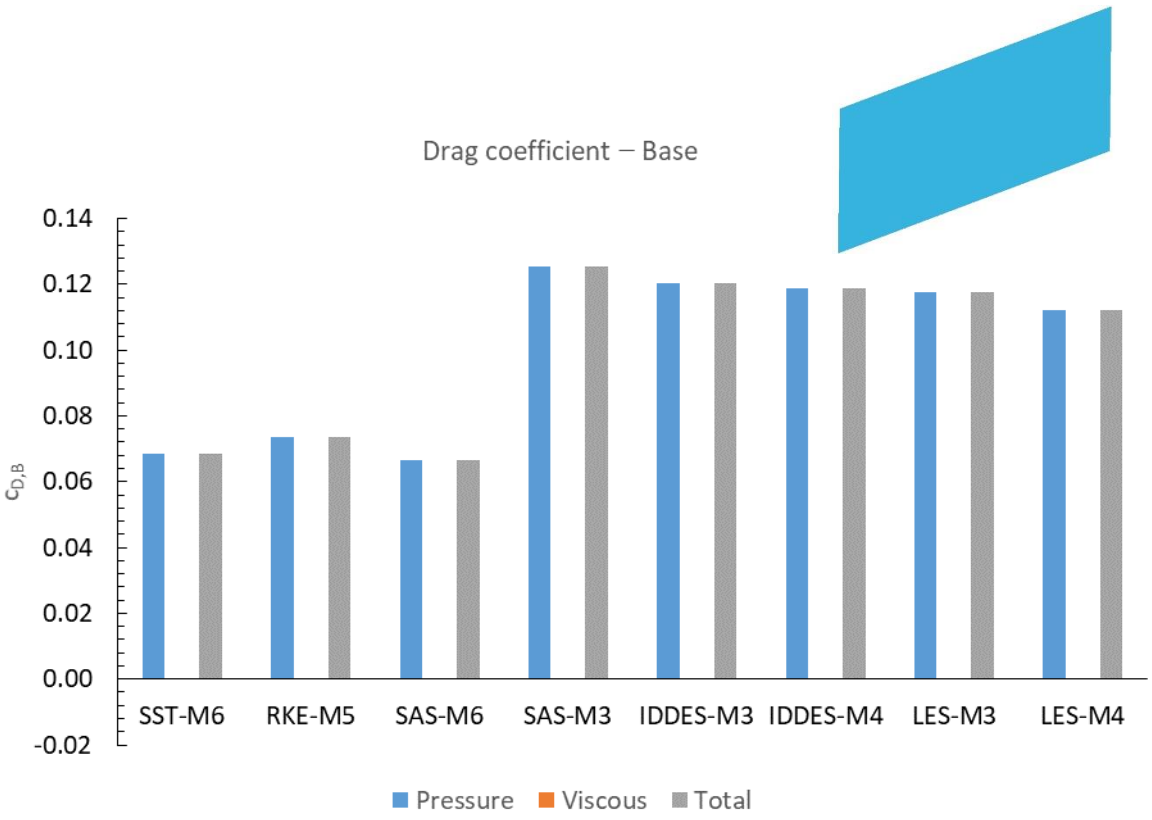

Figure 71: Drag coefficient of subsurface – Base.

7.3.3.2.4 Drag coefficient of subsurface – Slant

The contributions of the subsurface slant to the drag coefficient are even higher than those obtained for the subsurface base in the previous section. The turbulence models predicted here at maximum more than 0.17. Together with the base, the slant evidently produce the most significant contribution to the drag. The SAS-M3 predicted the smallest value for the slant, while the IDDES and LES predicted the highest values.

Table 19: Drag coefficient of subsurface – Slant.

$c_{D,S}$ Drag Coefficient – Slant			
	Pressure force	Viscous force	Total
SST-M6	0.1355	0.0020	0.1376
RKE-M5	0.1425	0.0026	0.1451
SAS-M6	0.1285	0.0018	0.1304
SAS-M3	0.1019	-0.0003	0.1016
IDDES-M3	0.1776	0.0005	0.1781
IDDES-M4	0.1737	0.0005	0.1742
LES-M3	0.1631	0.0005	0.1636
LES-M4	0.1588	0.0004	0.1592

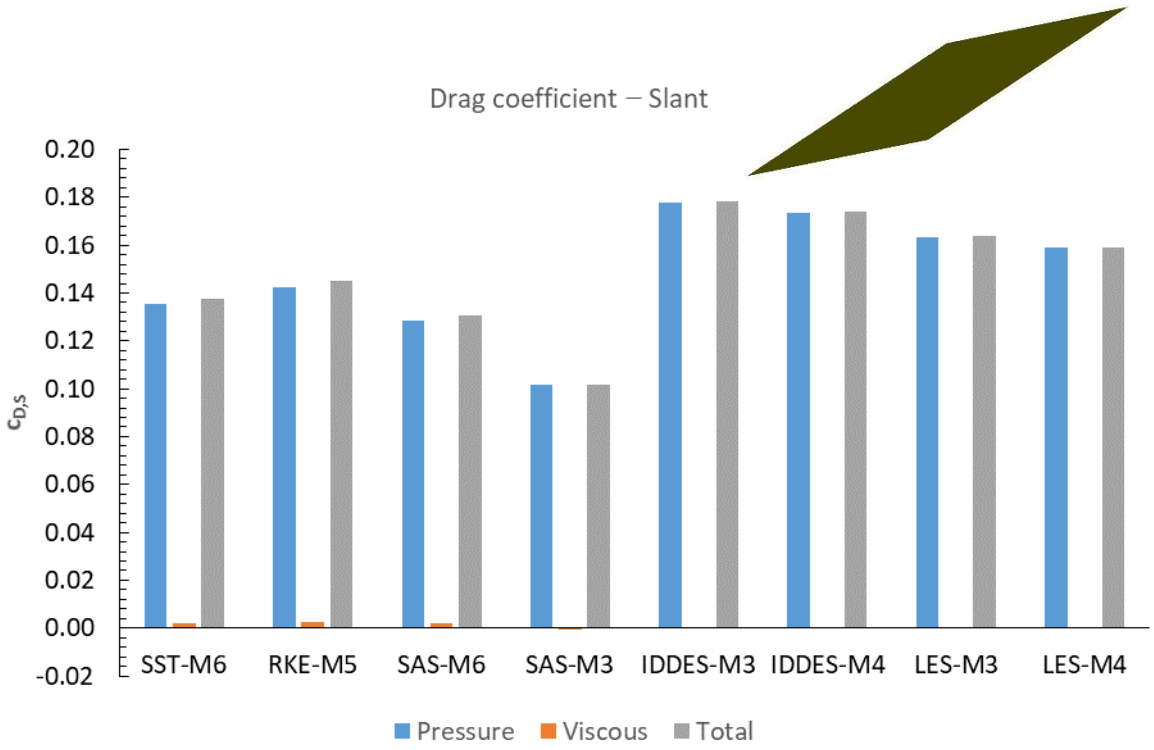

Figure 72: Drag coefficient of subsurface – Slant.

7.3.3.2.5 Drag coefficient of subsurface – Underbody

The drag coefficient for the underbody did not include the legs, which is in accordance with the experimental work done by Meile et al. [40]. The highest values were achieved with RKE-M5 and SAS-M6. LES calculations predicted a more than 70% smaller contribution, compared to all the other simulations.

Table 20: Drag coefficient of subsurface – Underbody.

$c_{D,U}$ Drag Coefficient – Underbody			
	Pressure force	Viscous force	Total
SST-M6	2.21E-12	0.0131	0.0131
RKE-M5	9.17E-11	0.0144	0.0144
SAS-M6	1.21E-10	0.0133	0.0133
SAS-M3	8.02E-11	0.0125	0.0125
IDDES-M3	6.14E-11	0.0122	0.0122
IDDES-M4	3.07E-11	0.0117	0.0117
LES-M3	2.21E-12	0.0037	0.0037
LES-M4	8.02E-11	0.0041	0.0041

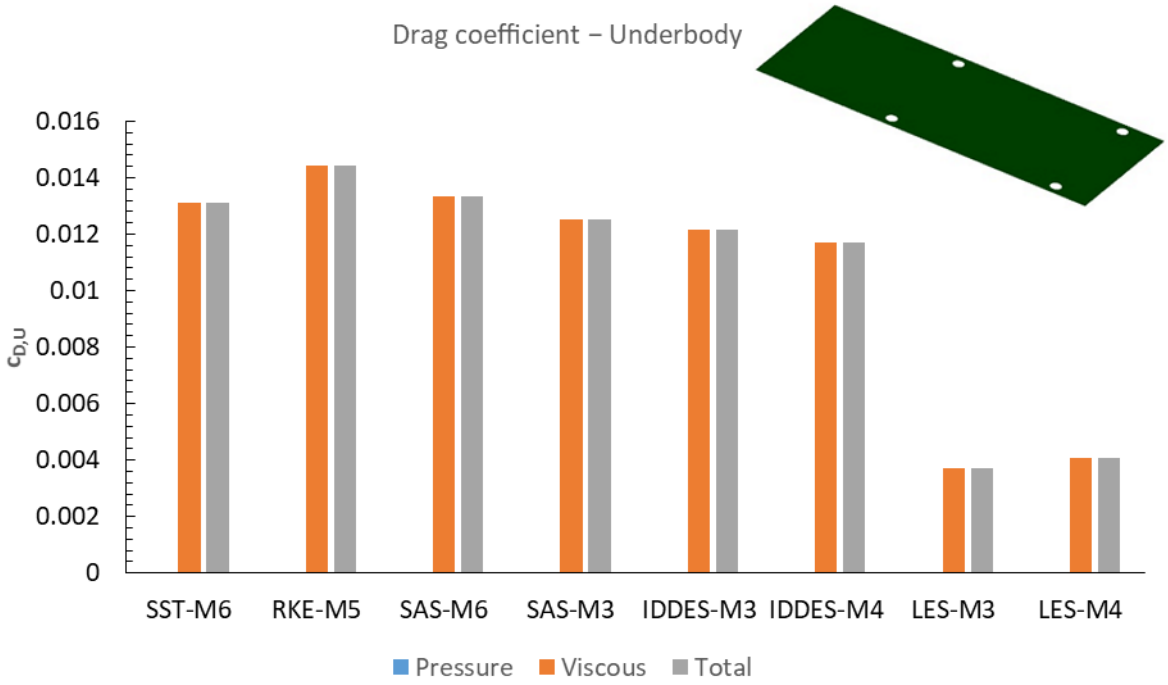

Figure 73: Drag coefficient of subsurface underbody.

7.3.3.2.6 Drag coefficient of subsurface – Roof

Similar to the subsurfaces sides and underbody the subsurface roof only produces a viscous contribution to the drag. The pressure contribution is negligible. All the computations that used a RANS approach (RKE, SST, SAS, IDDES) for the calculation of the boundary layer show higher values compared to LES. The latter produces values of around 0.002, while the RANS-based near-wall models exhibit values around 0.01.

Table 21: Drag coefficient of subsurface – Roof.

$c_{D,R}$ Drag Coefficient – Roof			
	Pressure force	Viscous force	Total
SST-M6	-6.56E-10	0.0103	0.0103
RKE-M5	-2.15E-10	0.0111	0.0111
SAS-M6	-8.96E-10	0.0098	0.0098
SAS-M3	6.60E-10	0.0099	0.0099
IDDES-M3	1.36E-10	0.0101	0.0101
IDDES-M4	-2.5E-11	0.0096	0.0096
LES-M3	-3.10E-10	0.0029	0.0029
LES-M4	-5.87E-10	0.0031	0.0031

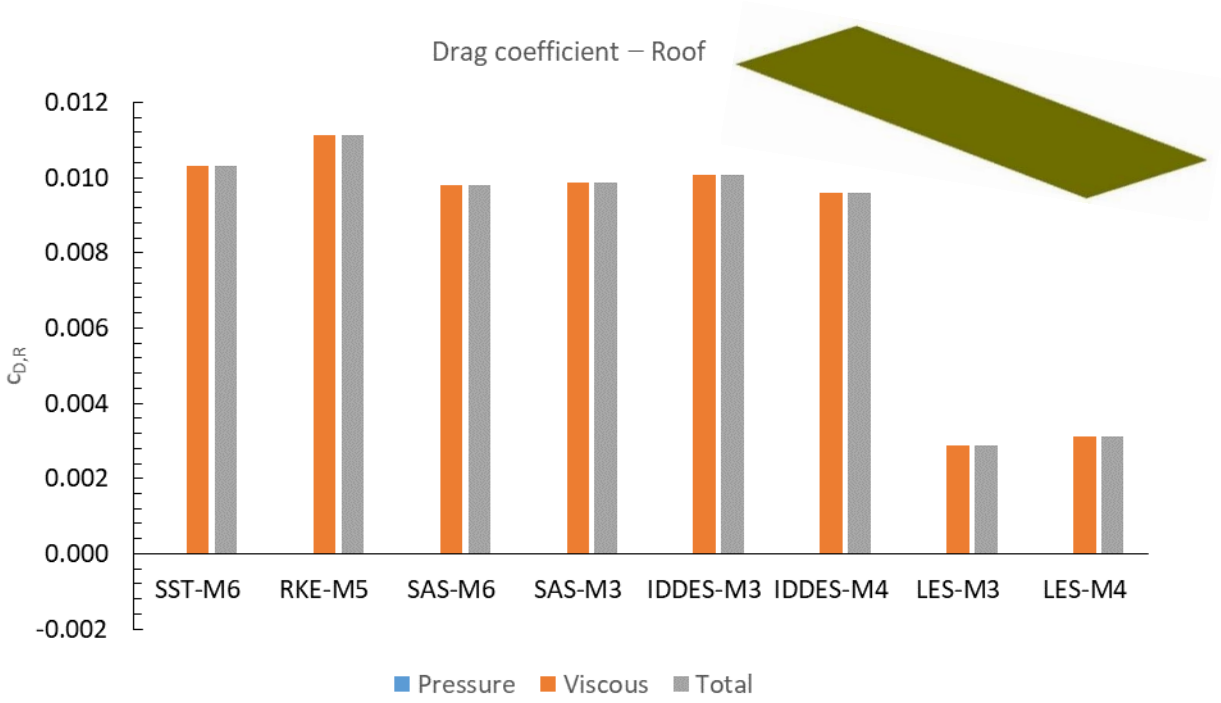

Figure 74: Drag coefficient of subsurface – Roof.

7.3.3.2.7 Relative contributions of subsurfaces to the total drag

The diagrams in the Figures 75-81 below show the total (pressure+viscous) contribution from each subsurface to the total drag acting on the body. This gives a very comprehensive overview, which subsurfaces relatively contribute most. The subsurfaces are successively listed from the front to the rear part, adding up the contributions from the front, underbody, roof, sides 1 & 2, slant, and base. According to the original work of Ahmed[40] experiment, the contribution of the slant and base significantly varies as the slant angle changes. An increase in the slant angle increases the slant contribution and decreases the contribution from the base.

Steady SST-M6 and RKE-M5 predicted the highest contributions from the front (approx 10−13%). The roof and underbody contributions are much smaller and remain between 3% and 4% which is similar to the subsurface sides. The slant contributes approx. 48% in the case of SST-M6 and 49% in the RKE-M5 to the total drag. This is followed by the contribution from the base, with 24−25%.

Among the transient models the IDDES and LES approaches predict very similar relative contributions of the slant and the base. For the other subsurfaces LES always yields significantly smaller relative contributions, indicating again the possibly insufficient resolution of the near-wall regions provided by the grids used for the LES.

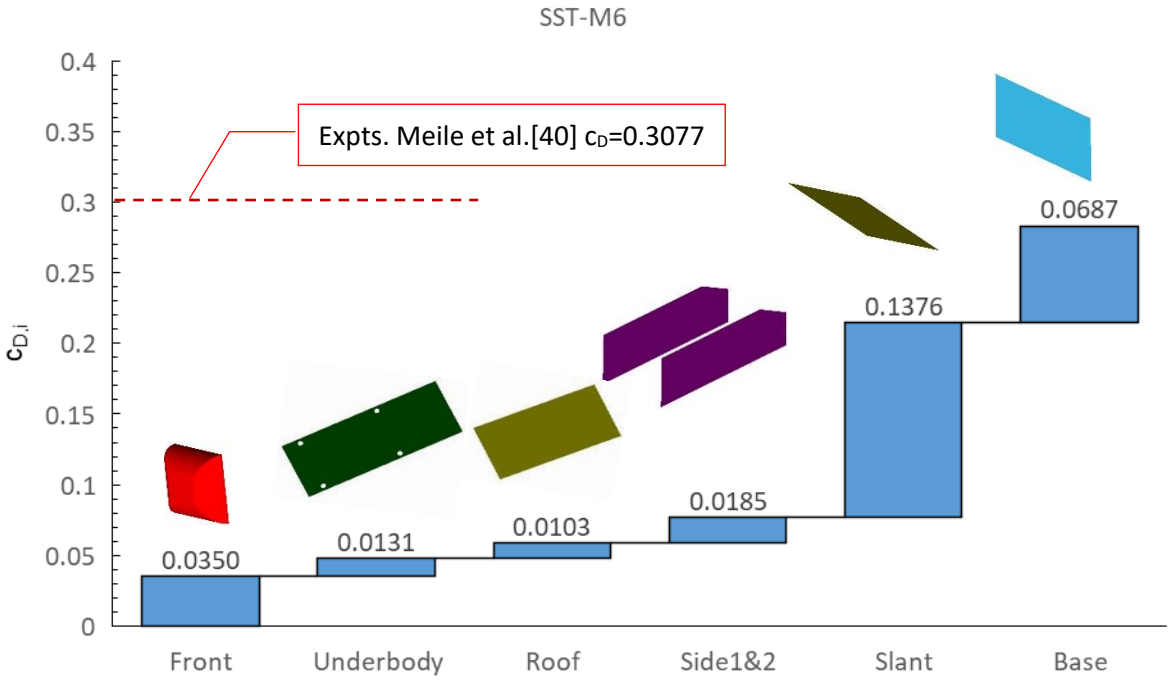

Figure 75: Subsurface contributions to total drag for SST-M6.

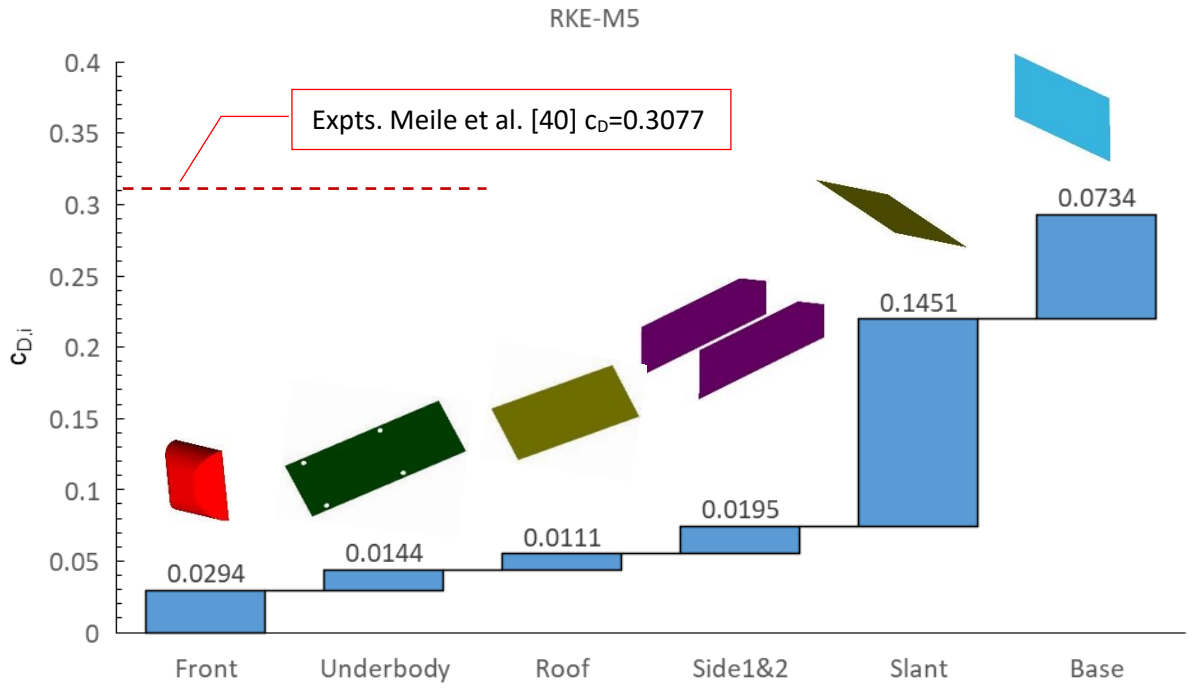

Figure 76: Subsurface contributions to total drag for RKE-M5.

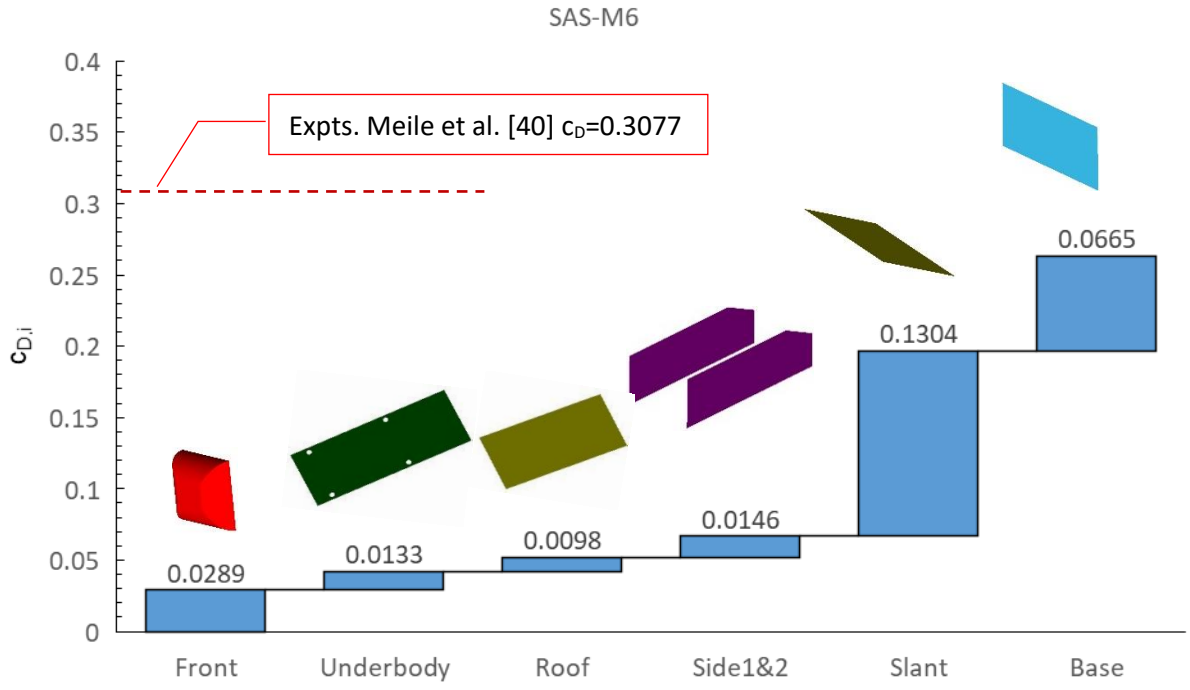

Figure 77: Subsurface contributions to total drag for SAS-M6.

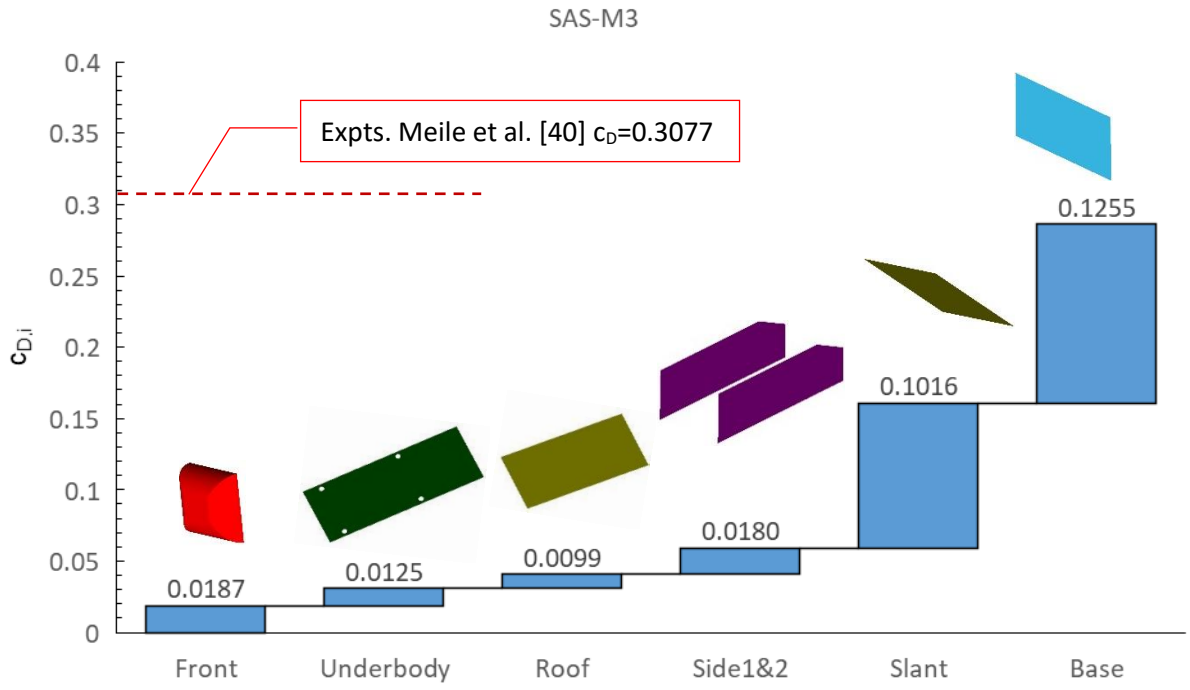

Figure 78: Subsurface contributions to total drag for SAS-M3.

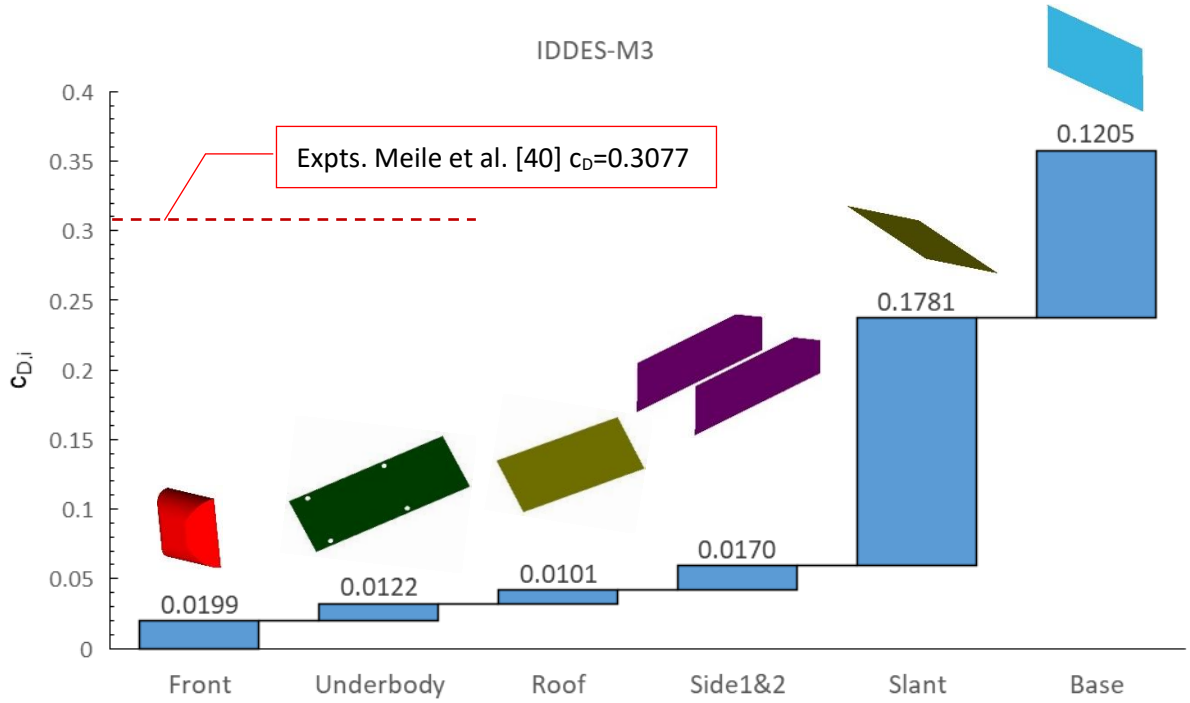

Figure 79: Subsurface contributions to total drag for IDDES-M3.

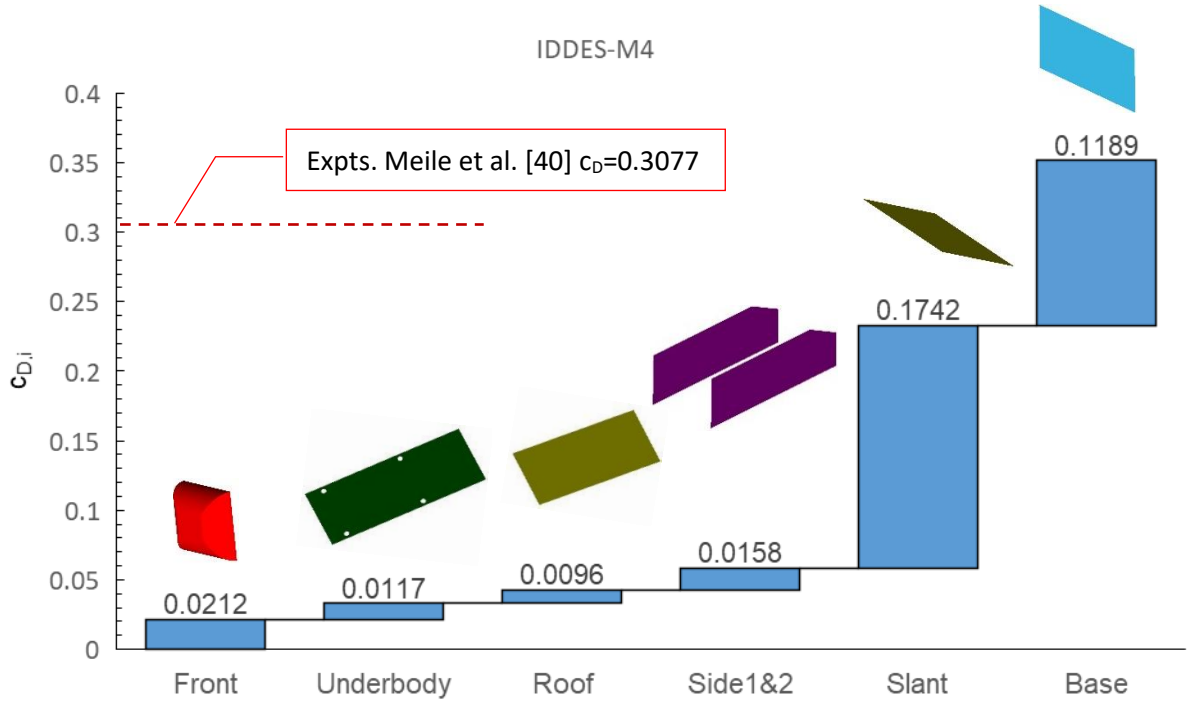

Figure 80: Subsurface contributions to total drag for IDDES-M4.

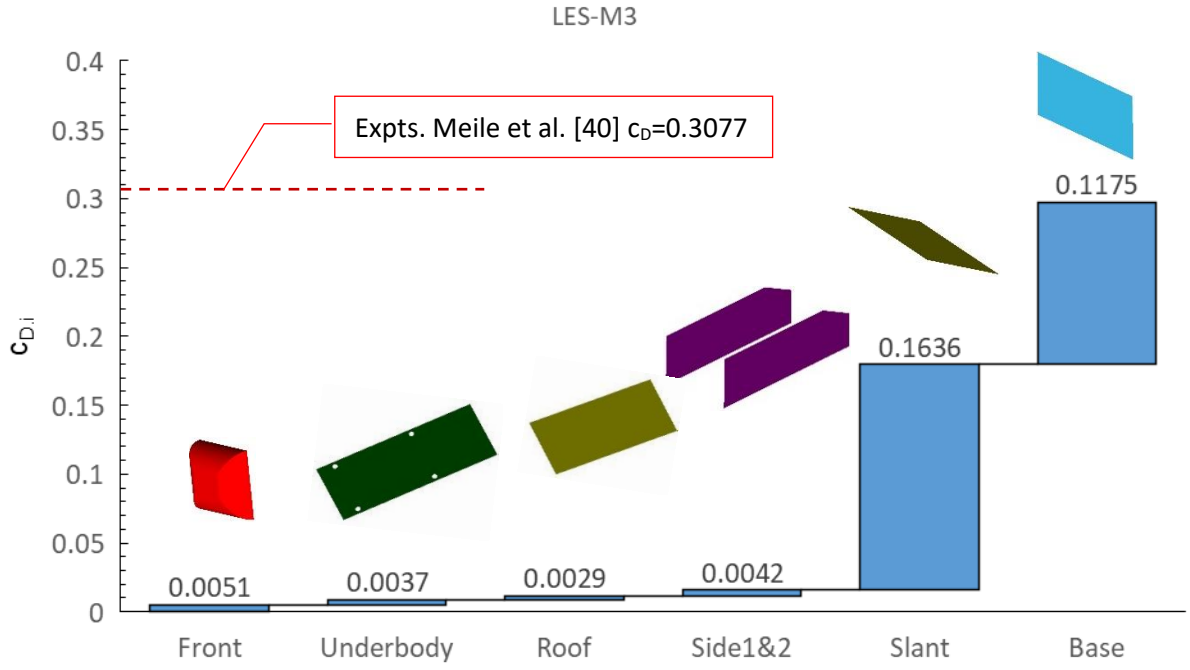

Figure 81: Subsurface contributions to total drag for LES-M3.

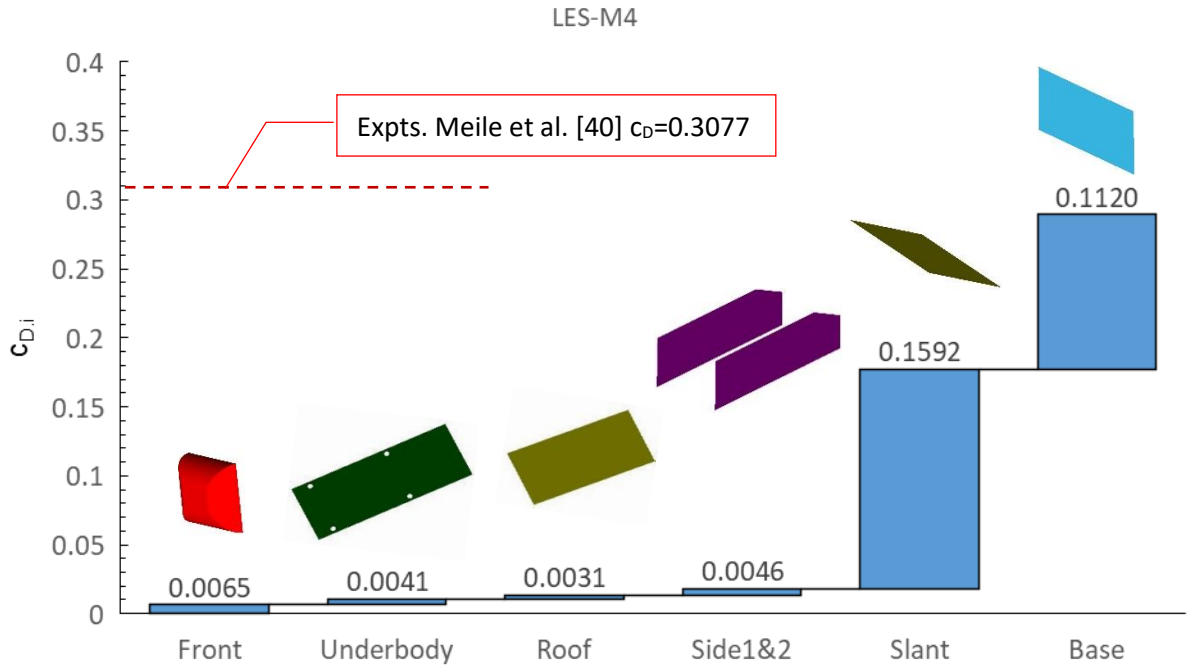

Figure 82: Subsurface contributions to total drag for LES-M4.

7.3.3.2.8 Lift coefficient of subsurface – Front

The variations for the predicted lift coefficient are much smaller here, as compared to the drag coefficient. All methods predicted a force contribution to the total lift coefficient between 0.12 and 0.14. The pressure force clearly dominates the viscous force. The viscous contribution remains negligibly small.

Table 22: Lift coefficient of subsurface – Front

$c_{L,F}$ Lift Coefficient – Front			
	Pressure force	Viscous force	Total
SST-M6	0.1432	0.0011	0.1443
RKE-M5	0.1303	0.0010	0.1313
SAS-M6	0.1279	0.0010	0.1289
SAS-M3	0.1299	0.0009	0.1308
IDDES-M3	0.1306	0.0009	0.1315
IDDES-M4	0.1330	0.0009	0.1339
LES-M3	0.1296	0.0005	0.1301
LES-M4	0.1334	0.0005	0.1339

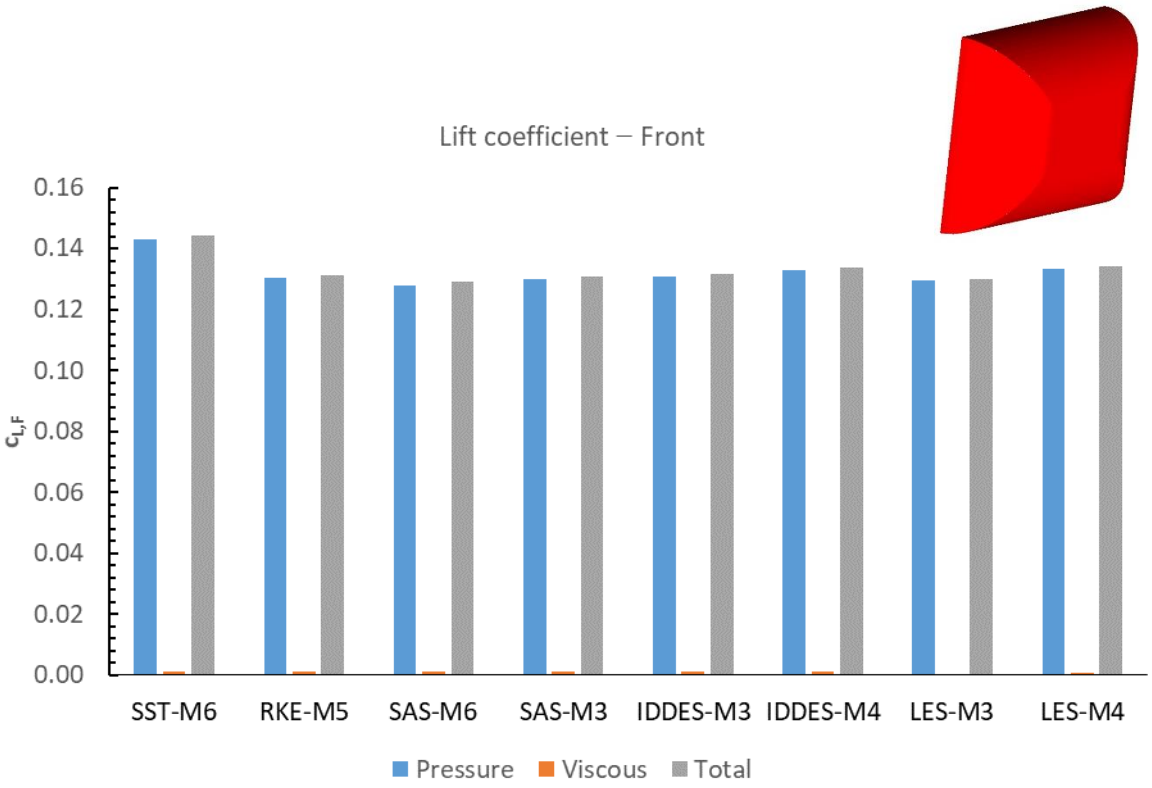

Figure 83: Lift coefficient of subsurface– Front.

7.3.3.2.9 Lift coefficient of subsurface – Sides 1 & 2

The contribution of this subsurface is expectedly negligible, due to the orientation of this surface. The results are included here for completeness. The same applies to the lift force contribution of the subsurface base shown next.

Table 23: Lift coefficient of subsurface – Sides 1 & 2

$c_{L,SI}$ Lift Coefficient – Sides 1 & 2			
	Pressure force	Viscous force	Total
SST-M6	-5.28E-08	1.72E-04	1.72E-04
RKE-M5	-1.26E-10	3.59E-04	3.59E-04
SAS-M6	-3.60E-08	1.96E-04	1.96E-04
SAS-M3	8.76E-10	-9.67E-05	-9.67E-05
IDDES-M3	6.01E-10	3.36E-04	3.36E-04
IDDES-M4	5.72E-10	2.95E-04	2.95E-04
LES-M3	7.37E-10	9.79E-05	9.79E-05
LES-M4	7.44E-10	4.12E-05	4.12E-05

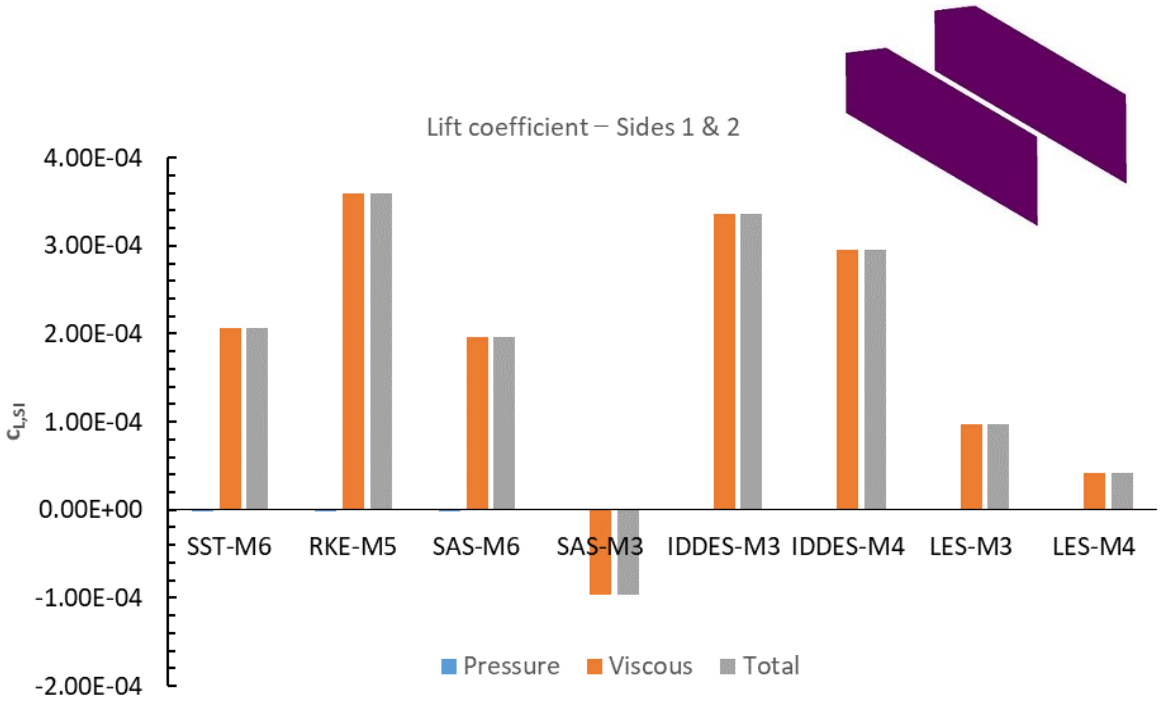

Figure 84: Lift coefficient of subsurface – Sides 1 & 2

7.3.3.2.10 Lift coefficient of subsurface – Base

Table 24: Lift coefficient of subsurface – Base

$c_{L,B}$ Lift Coefficient – Base			
	Pressure force	Viscous force	Total
SST-M6	1.93E-17	1.76E-05	1.76E-05
RKE-M5	3.54E-17	-1.27E-05	-1.27E-05
SAS-M6	5.58E-18	6.34E-05	6.34E-05
SAS-M3	2.56E-18	3.85E-04	3.85E-04
IDDES-M3	8.79E-18	2.49E-04	2.49E-04
IDDES-M4	1.19E-17	2.77E-04	2.77E-04
LES-M3	1.52E-17	8.42E-05	8.42E-05
LES-M4	1.36E-17	1.01E-04	1.01E-04

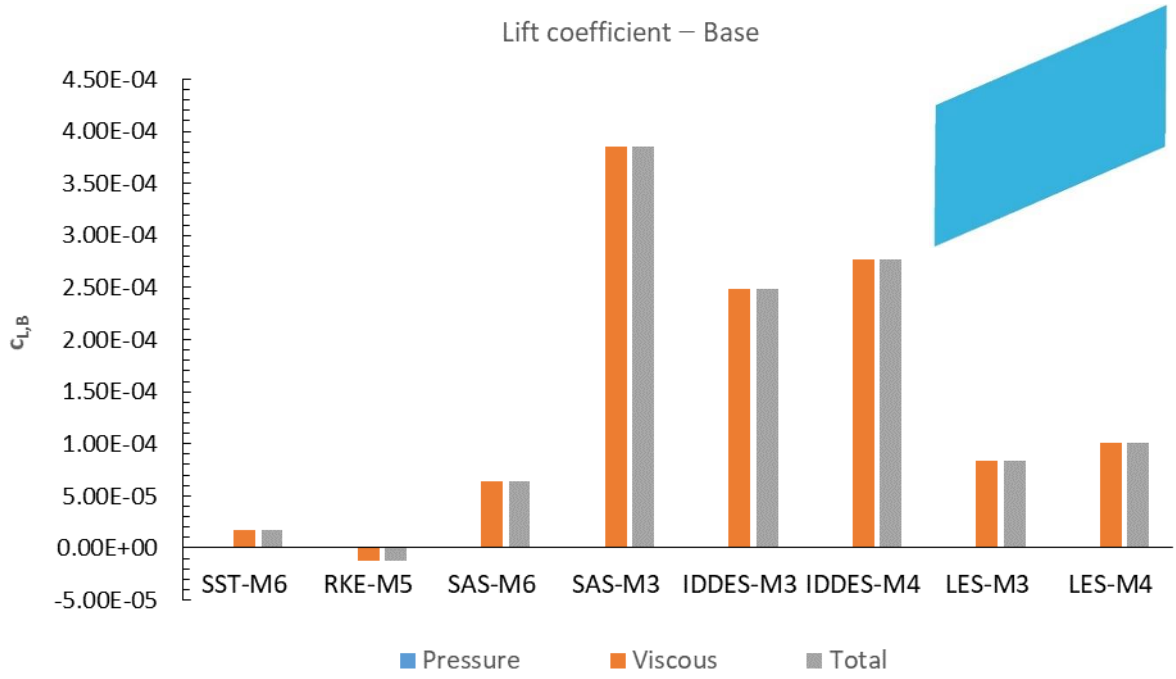

Figure 85: Lift coefficient of subsurface – Base.

7.3.3.2.11 Lift coefficient of subsurface – Underbody

As the flow reaches the front part of the body, it is redirected towards the underbody on the lower side. The open cross-section gets smaller and the velocity increases and as a result, the static pressure drops inside the gap between the underbody and the ground. Due to this significant pressure drop all turbulence models predicted considerably high negative contributions around -0.70 with a negligible viscous force component. The IDDES show the lowest values and the LES the highest.

Table 25: Lift coefficient of subsurface – Underbody

$c_{L,U}$ Lift Coefficient – Underbody			
	Pressure force	Viscous force	Total
SST-M6	-0.7454	5.15E-06	-0.7454
RKE-M5	-0.7454	5.39E-06	-0.7454
SAS-M6	-0.7616	8.42E-06	-0.7616
SAS-M3	-0.7192	-4.75E-06	-0.7192
IDDES-M3	-0.6791	-5.18E-06	-0.6791
IDDES-M4	-0.6942	-4.62E-06	-0.6942
LES-M3	-0.7683	-4.13E-06	-0.7683
LES-M4	-0.7650	-4.21E-06	-0.7649

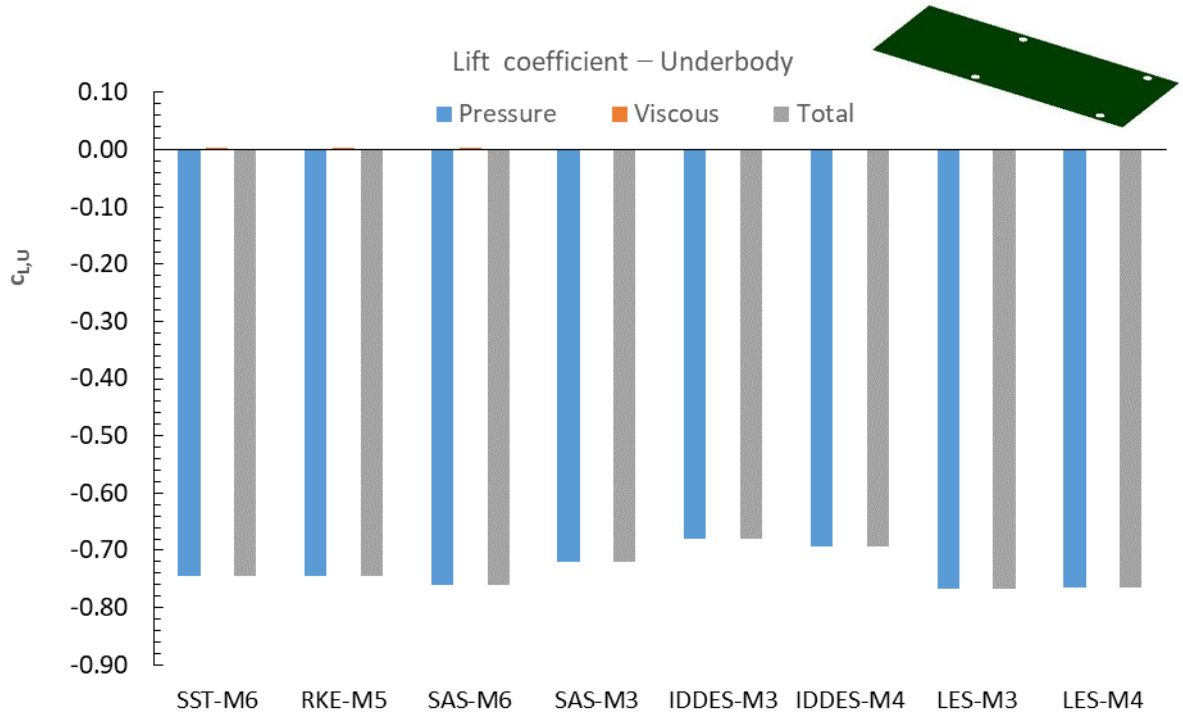

Figure 86: Lift coefficient of subsurface – Underbody.

7.3.3.2.12 Lift coefficient of subsurface – Roof

For similar reason (flow is accelerated and the static pressure drops) as in the case of subsurface underbody, the subsurface roof also yields a very high quantitative contribution to the total lift coefficient. Due to the different orientation of the surface, the values are positive here. The different models predict positive values between 0.6 and 0.68. A little bit higher deviations are obtained by the SAS-M3, which produces values of around 0.5. The viscous force contribution is again vanishingly small in all cases.

Table 25: Lift coefficient of subsurface – Roof

$c_{L,R}$ Lift Coefficient – Roof			
	Pressure force	Viscous force	Total
SST-M6	0.6798	3.18E-12	0.6798
RKE-M5	0.6737	-1.53E-12	0.6737
SAS-M6	0.6823	3.97E-12	0.6823
SAS-M3	0.5215	2.53E-12	0.5215
IDDES-M3	0.6094	7.69E-12	0.6094
IDDES-M4	0.6149	9.24E-12	0.6149
LES-M3	0.6861	2.18E-11	0.6861
LES-M4	0.6810	2.61E-11	0.6810

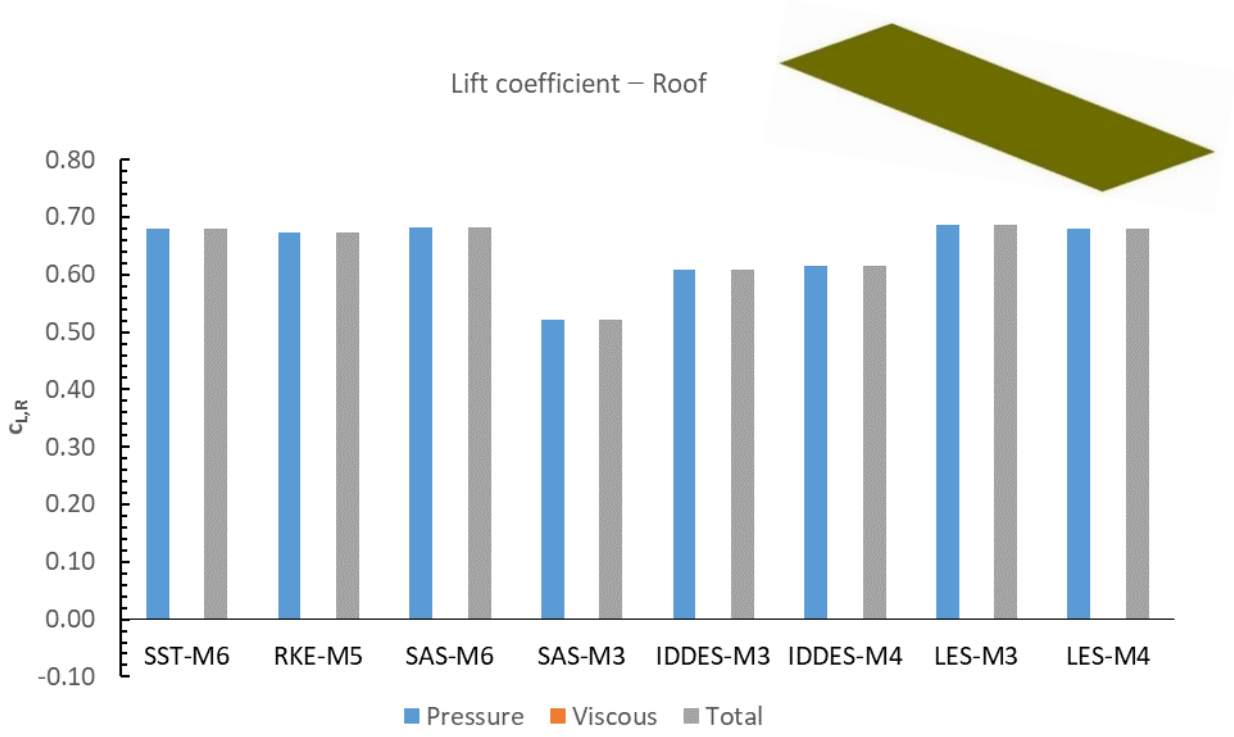

Figure 87: Lift coefficient of subsurface – Roof.

7.3.3.2.13 Lift coefficient of subsurface – Slant

Together with the roof, the subsurface slant represents another surface of the Ahmed body that provides a significant positive contribution to the lift coefficient. Compared to other turbulence models, the SAS-M3 predicted the smallest contribution with a value around 0.21. The IDDES achieved the highest value. The viscous contribution is small.

Table 26: Lift coefficient of subsurface – Slant

$c_{L,S}$ Lift Coefficient – Slant			
	Pressure force	Viscous force	Total
SST-M6	0.2906	-0.0010	0.2897
RKE-M5	0.3056	-0.0012	0.3044
SAS-M6	0.2756	-0.0009	0.2747
SAS-M3	0.2185	0.0001	0.2187
IDDES-M3	0.3765	-0.0002	0.3763
IDDES-M4	0.3697	-0.0003	0.3694
LES-M3	0.3457	-0.0002	0.3455
LES-M4	0.3418	-0.0002	0.3416

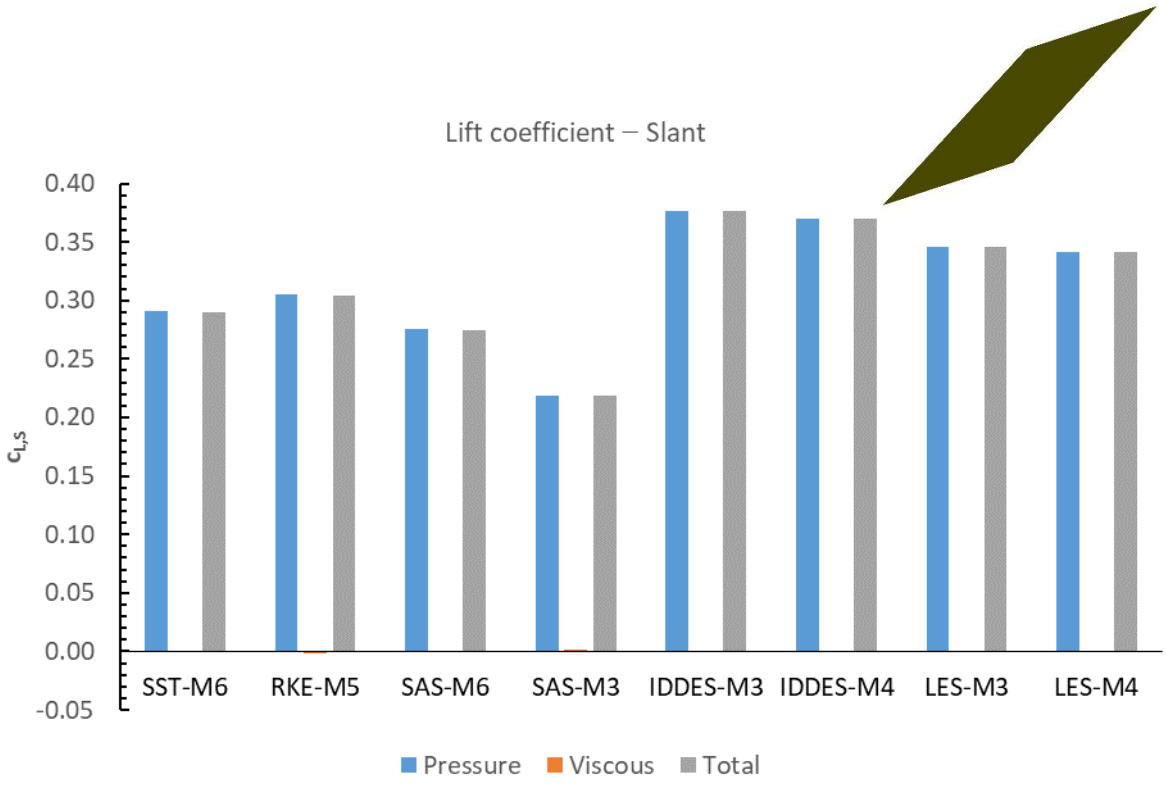

Figure 88: Lift coefficient of subsurface – Slant.

7.3.3.2.14 Relative contributions of the subsurfaces to the total lift

No experimental or numerical data are available that would describe in detail the lift force contributions from different subsurfaces of the Ahmed body. Therefore, the breakdown of the relative contributions to the values for the lift coefficient are shown in Figures 89−96 include only the present computational results. While the absolute contribution of the front is approximately the same for all models, notable difference apper in the predicted contributions from the subsurfaces underbody, roof and slant. As a common feature the slant always markedly overcompensates the net suction (negative lift) induced by the subsurfaces roof and underbody. As such, the slant significantly determines the finally reached total values c_L.

Steady RKE-M5 and SST-M6 predicted the best overall values for the lift coefficient. The relative net contribution from the subsurfaces underbody and roof predicted by these models are -17% and -19%, respectively. The slant contributes another approx. 80% of the positive total value for c_L in both cases.

Similar tendencies are observed for the transient models. The downforce on the underbody is again considerably higher compared to the upwind force acting on the roof. The SAS-M3 shows the highest downforce as well as the lowest lift force action on the roof. This results in the highest net downforce suction generated by these two surfaces and is not compensated neither by the positive lift on the slant nor the front part. This translates into a significant underprediction of the total lift coefficient. For the SAS-M6 the underprediction is smaller, where the wall-function based near-wall treatment evidently provides better prediction of the pressure difference between the upper and lower body part.

The negative net force between the roof and the underbody in LES and IDDES varies between 16% and 21%. Values of the slant and front are higher compared to those obtained by the steady calculation. This finally translates into the overprediction of the lift coefficient.

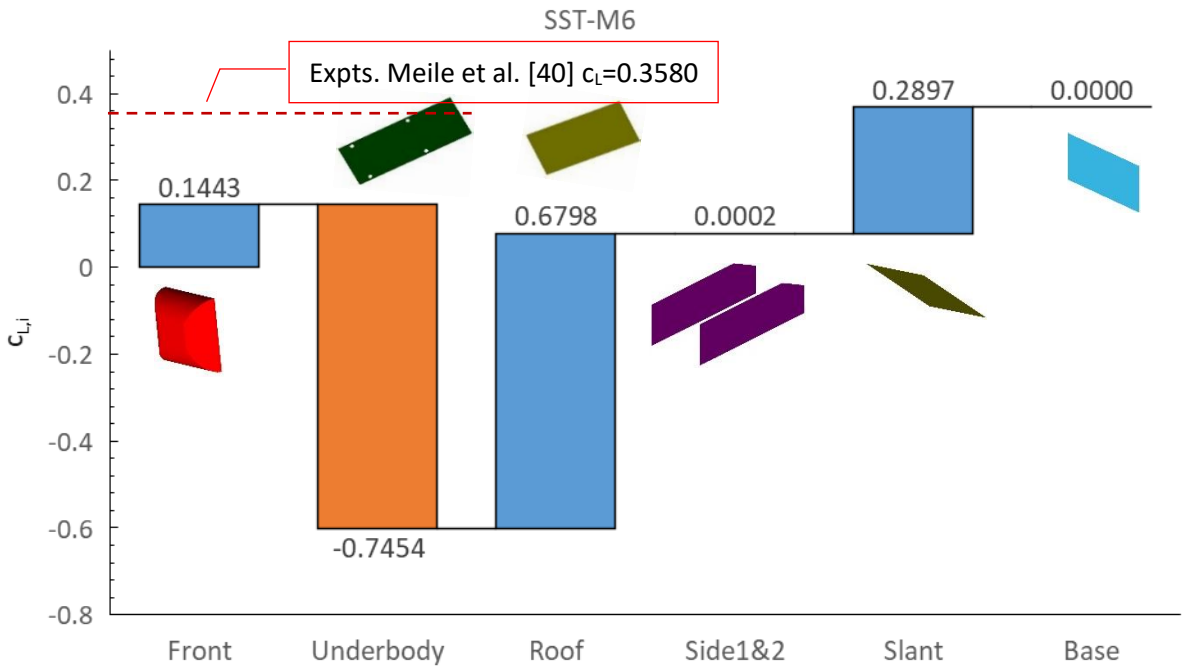

Figure 89: Subsurface contributions to total lift for SST-M6.

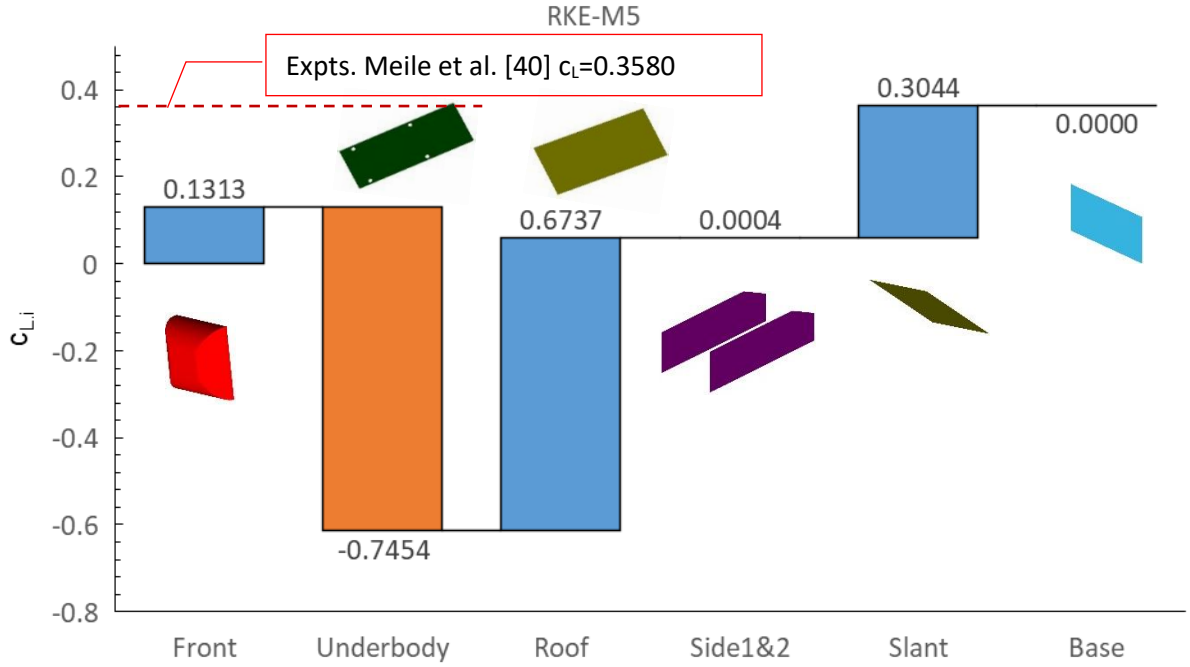

Figure 90: Subsurface contributions to total lift for RKE-M5.

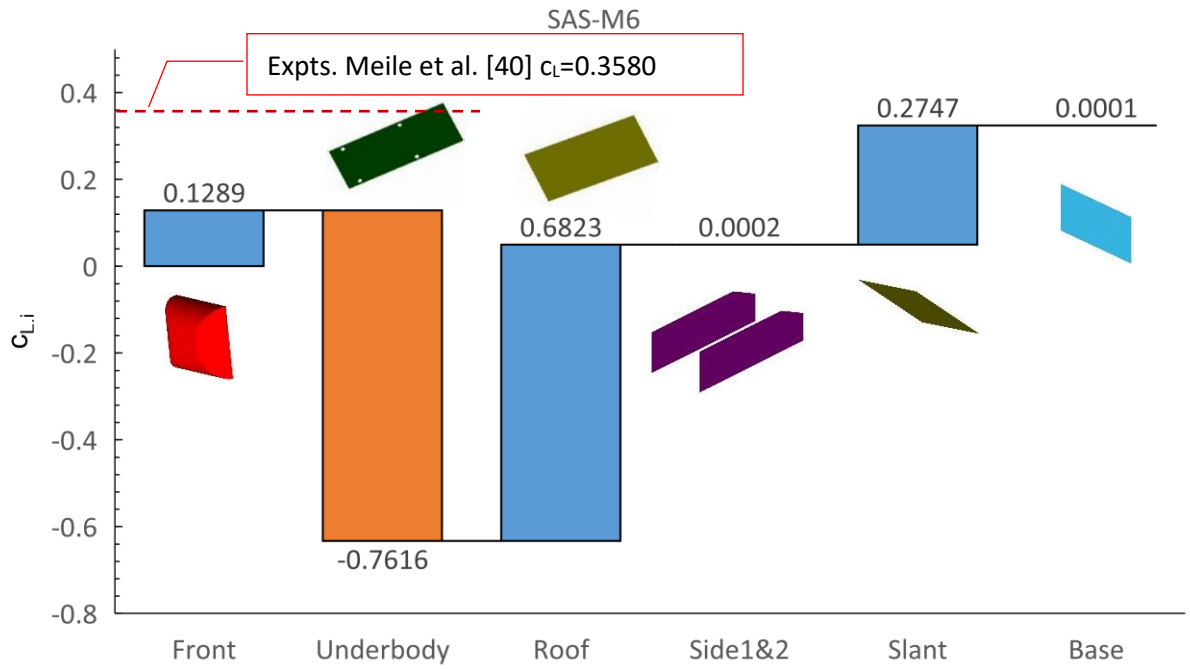

Figure 91: Subsurface contributions to total lift for SAS-M6.

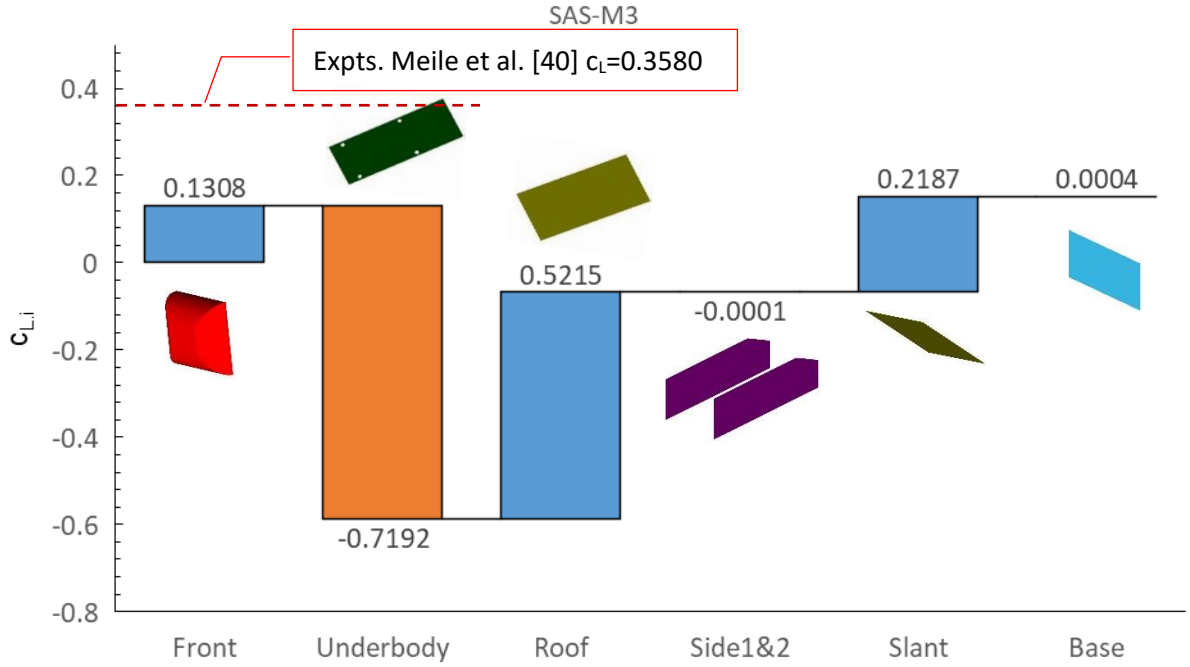

Figure 92: Subsurface contributions to total lift for SAS-M3.

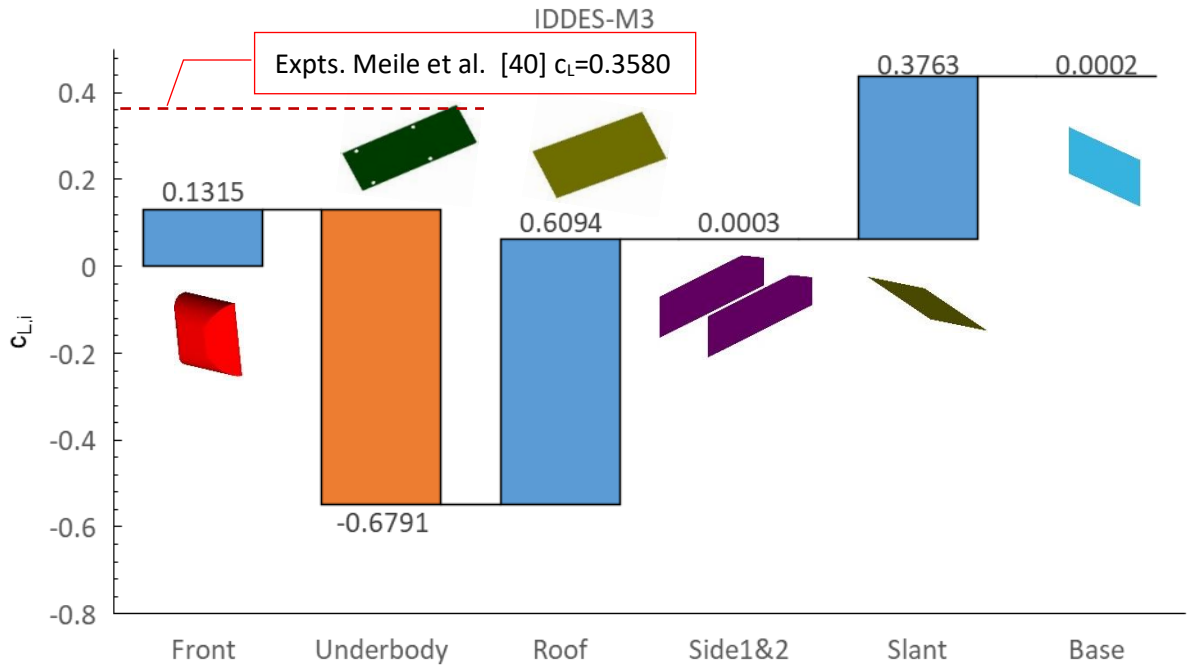

Figure 93: Subsurface contributions to total lift for IDDES-M3.

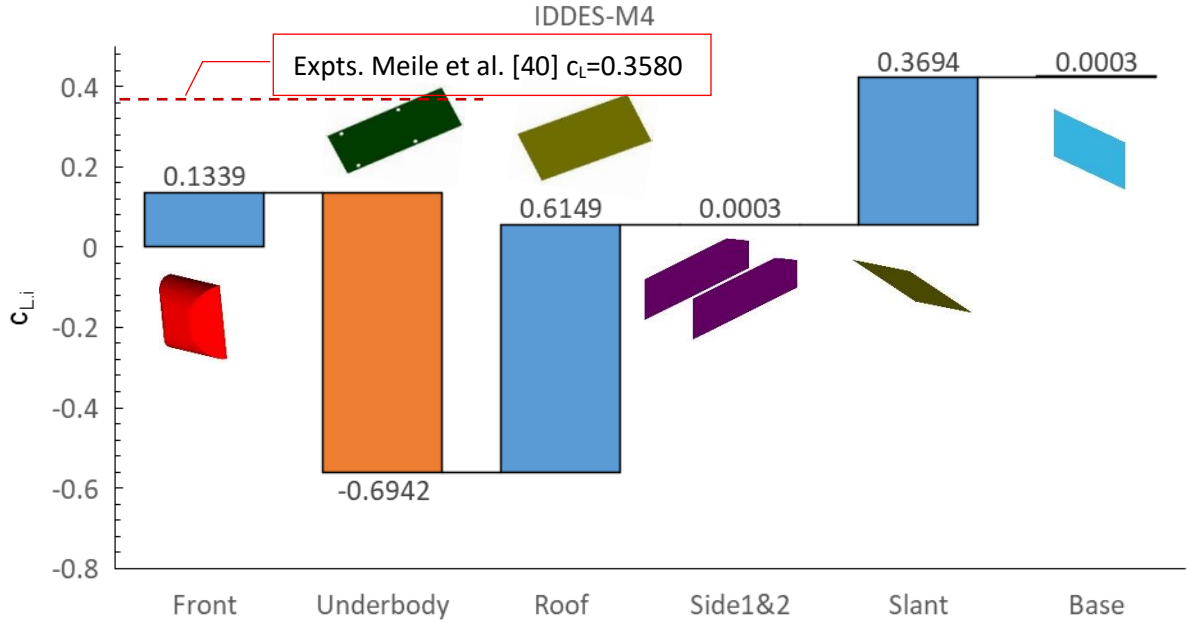

Figure 94: Subsurface contributions to total lift for IDDES-M4.

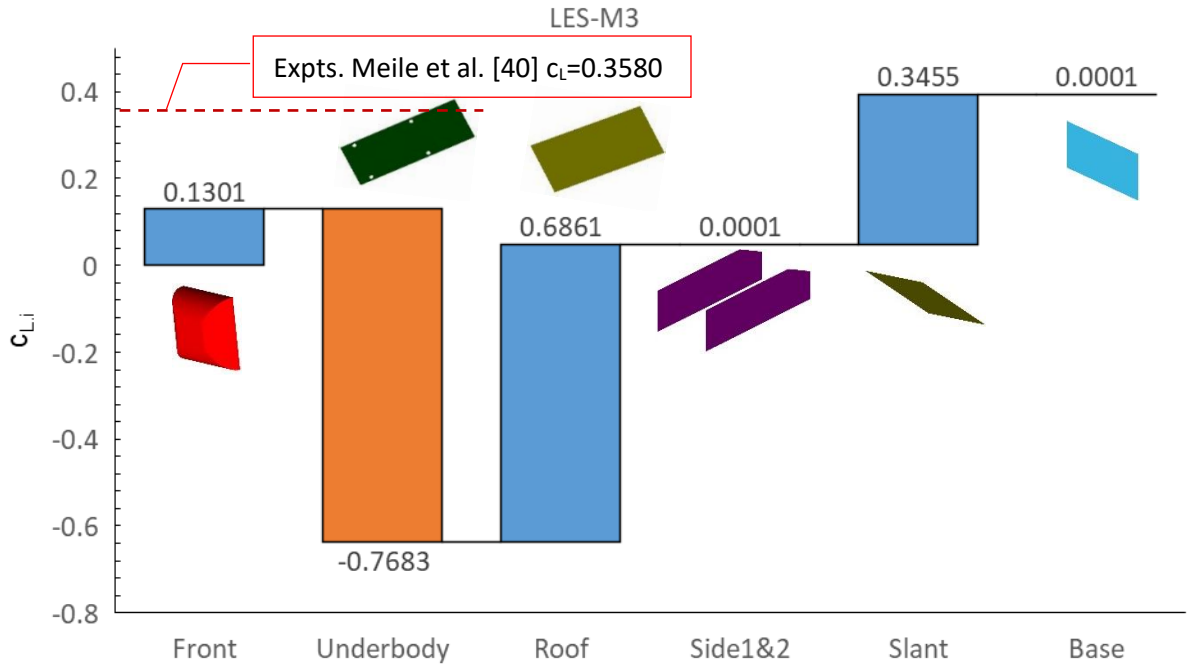

Figure 95: Subsurface contributions to total lift for LES-M3.

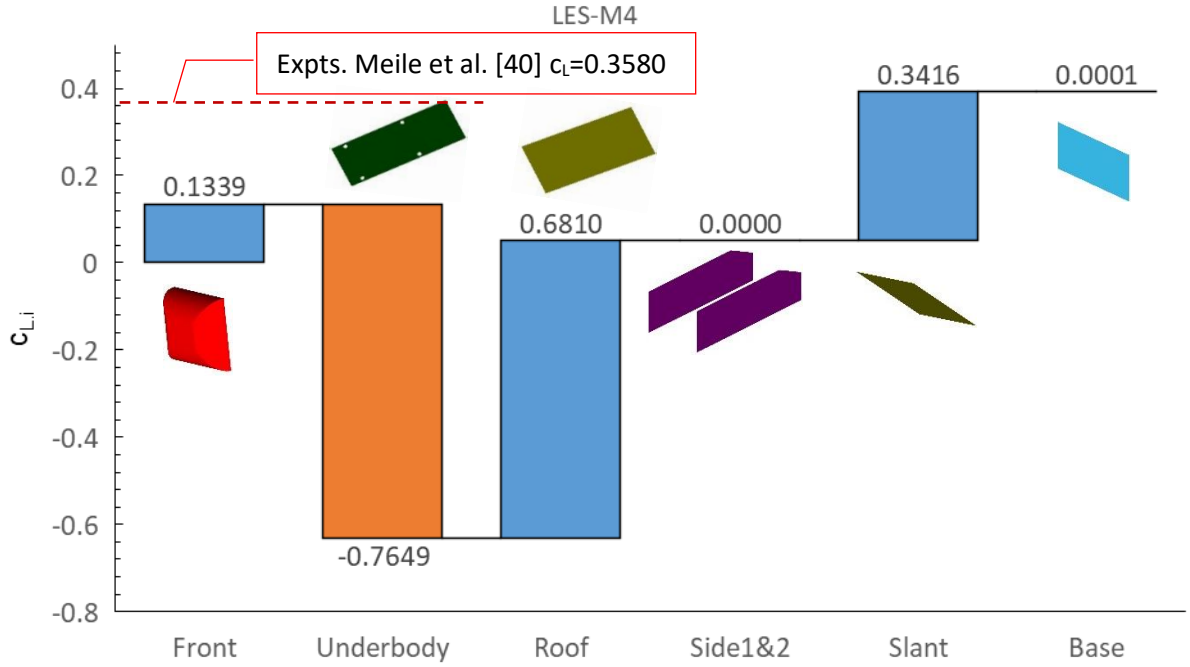

Figure 96: Subsurface contributions to total lift for LES-M4.

7.4 Predicted velocity profiles

The experimental data from Meile et al. [40] provided the flow field measurements in the wake and the slant of the Ahmed body. The measurements were made using the PIV method. Meile et al.[40] compared the measurements with available experimental data from the literature on symmetric flow conditions to get an idea of the quality of the results obtained with the PIV method. In this comparison normalized velocity profiles showed excellent agreement in a wide area of the wake with the velocity profiles obtained by Lienhart and Becker[39], who performed an extensive LDA investigation. Some deviation was observed in the near-wall region for a 25° angle.

In the experiment of Meile et al.[40] the velocity profiles were measured at streamwise positions from x=191 mm (on the slant) to x=-442 mm (in the wake region). As seen from Figure 97 seven velocity profiles from this region were chosen for the validation of the numerical results. Four of them are located at the slant, at x=191 mm, x=138 mm, x=80 mm, and x=3 mm. Three of them are in the wake region at x=-17 mm, x=-145 mm, and x=-440 mm. Two additional positions were chosen in front of the body (x=1244 mm) and on the roof just before the slant (x=191 mm) in order to assess the profiles produced by the different turbulence models before the flow reaches the nose of the body and the slant. No experimental data were available for the validation of the profiles predicted at these two additional positions.

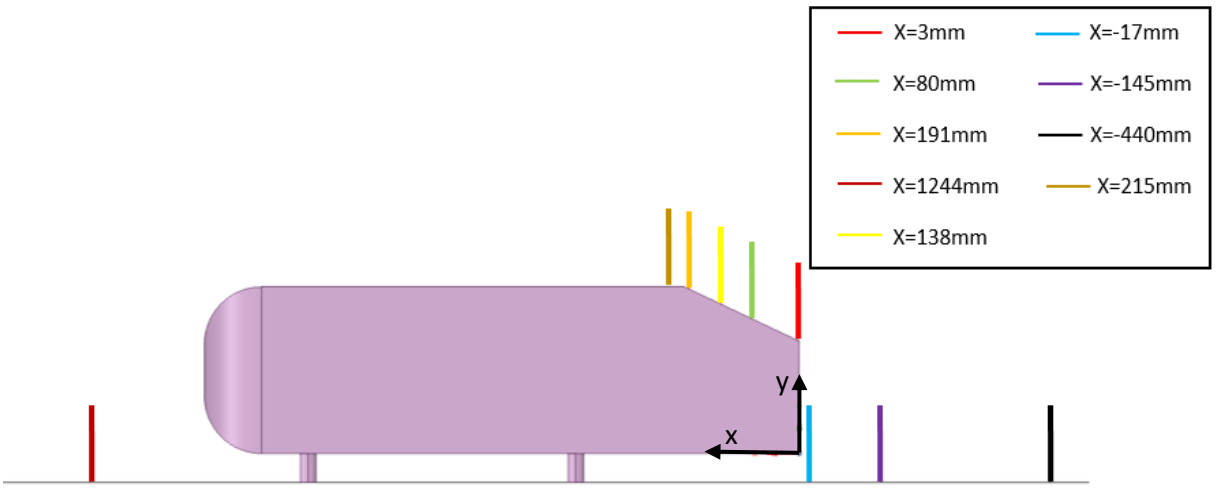

Figure 97: Positions of the velocity profiles for validation of the CFD results against experiments.

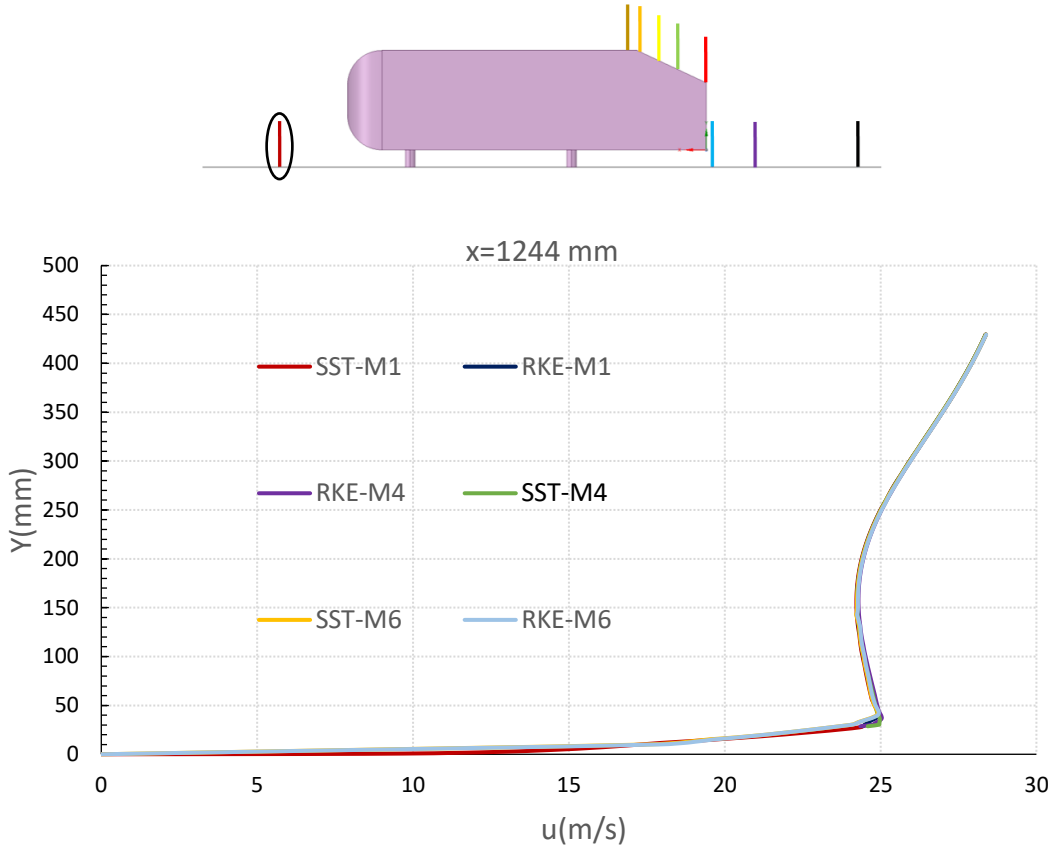

Figure 98: Velocity profiles (x=1244 mm) from steady RANS models.

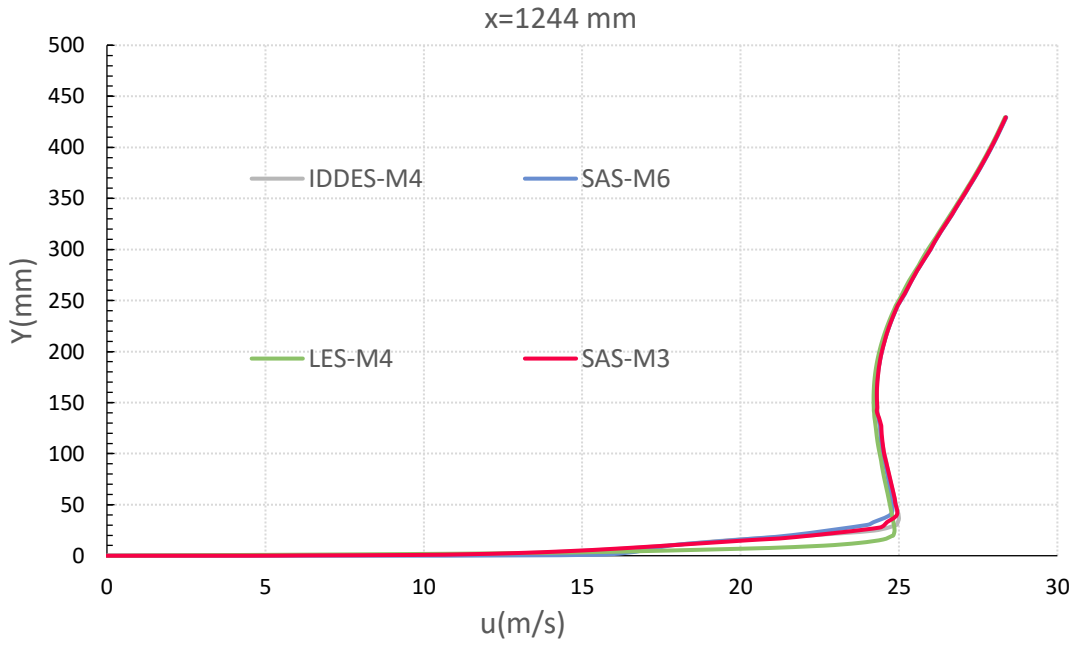

Figure 99: Time-averaged Velocity profiles (x=1244 mm) from unsteady turbulence models.

Figure 98 and 99 show the velocity profiles predicted at the x position 1244 mm. There is no major difference between the different turbulence models using different meshes. A slightly bigger deviation was obtained just with the LES-M4.

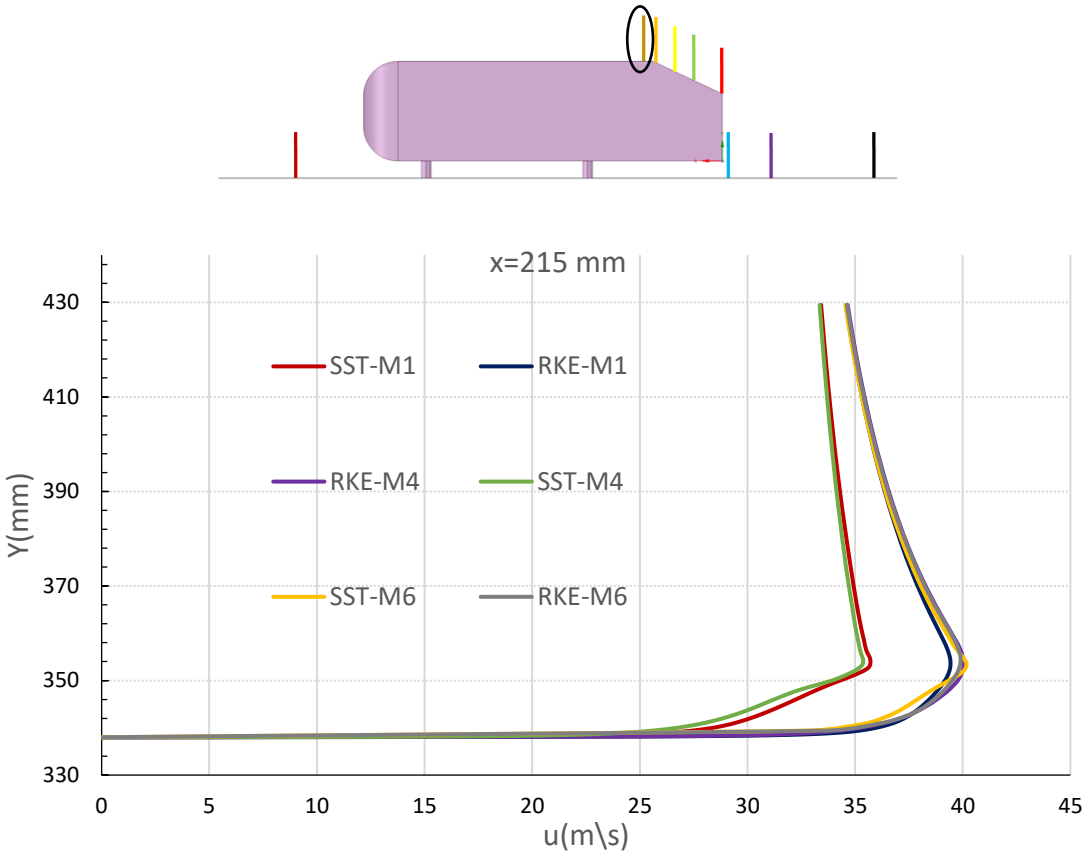

Figure 100: Velocity profiles (x=215 mm) from steady RANS models.

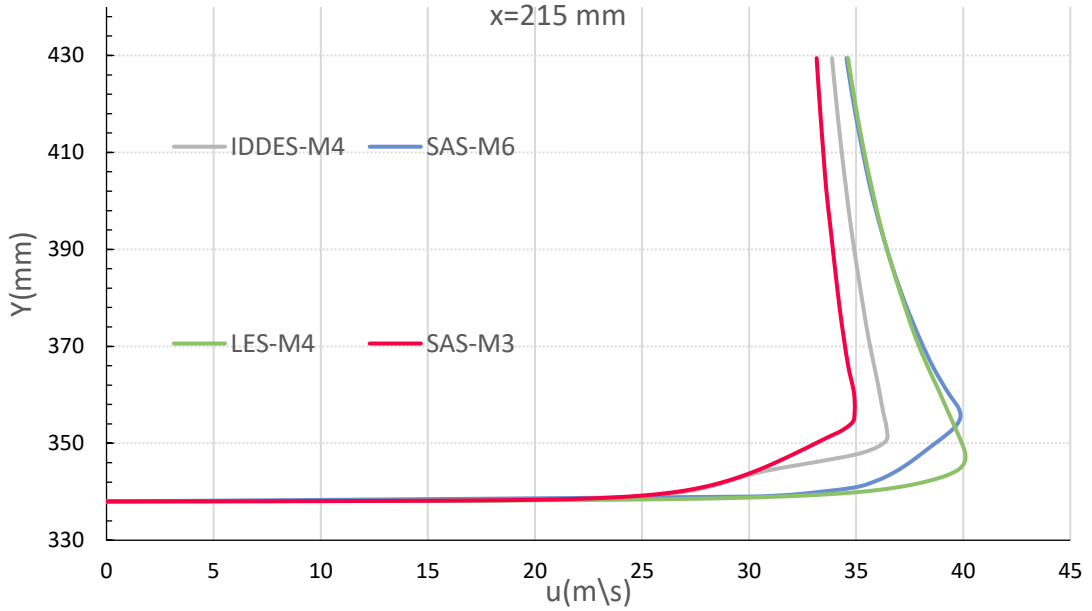

Figure 101: Time-averaged Velocity profiles (x=215 mm) from unsteady turbulence models.

The next profiles shown in Figures 100-101 are located on the roof of the body, just before the start of the slant. Among the steady RANS models the k-ω SST model applying the fine wall-resolving grid, for example, the meshes M1 and M4, show a lower velocity (approx. 35 m/s) compared to the RKE, which always shows a faster flow (peak at around 40 m/s). A similar behavior is observed for the transient model exhibiting smaller velocities for IDDES-M4 and SAS-M3 on one hand for while higher velocities for LES-M4 and SAS-M6 on the other.

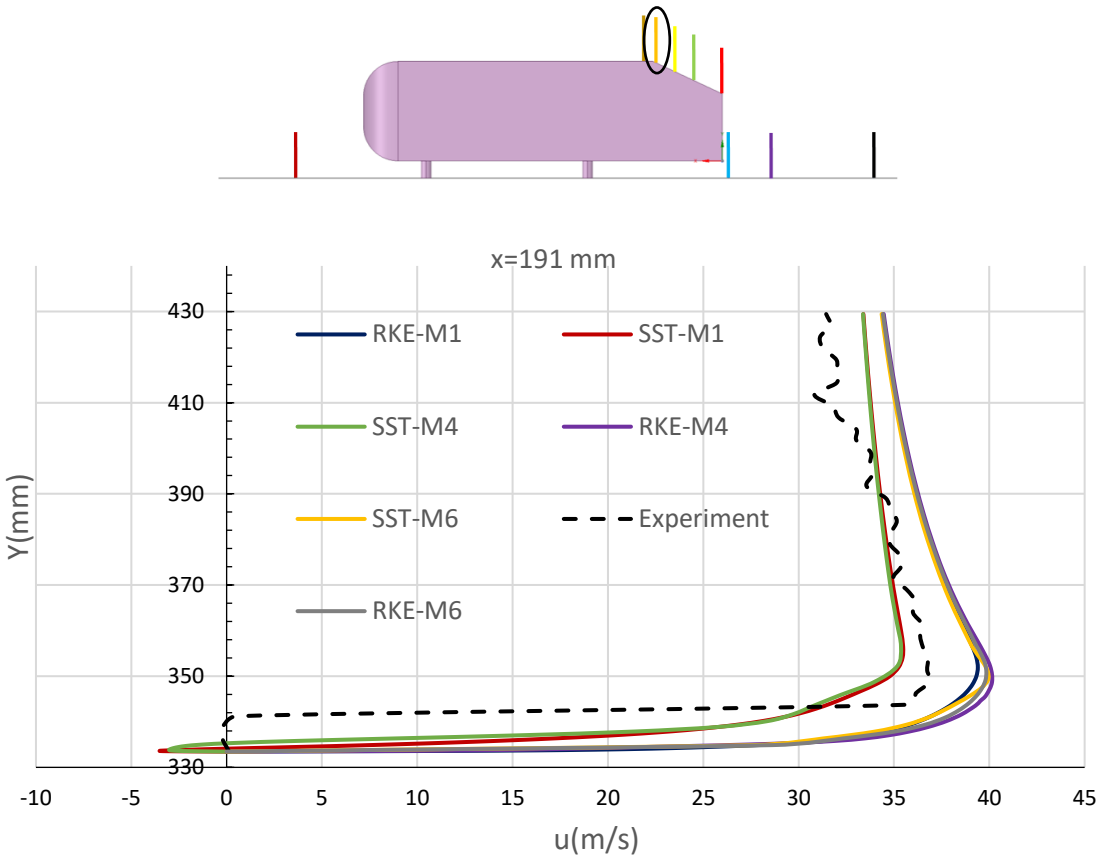

Figure 102: Velocity profiles (x=191 mm) from steady RANS models.

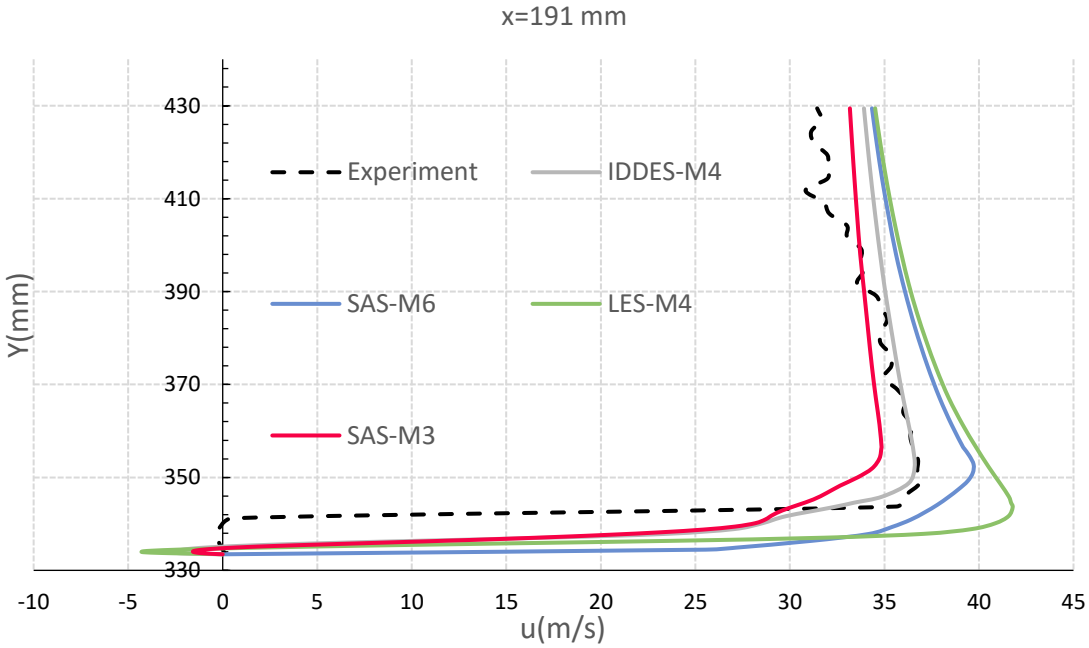

Figure 103: Time-averaged Velocity profiles (x=191 mm) from unsteady turbulence models.

The experimental data at the x=191 mm already indicate some flow separation. The CFD results generally do not capture this near-wall behavior accurately. They do not show any separation, e.g. RKE-M1 and RKE-M4 in the steady and SAS-M6 in the transient case, or they show a separation with a too strong backflow, such as SST-M1 and SST-M4 in the steady and LES-M4 in the transient case. IDDES-M4 shows good agreement in the middle section of the wall distance.

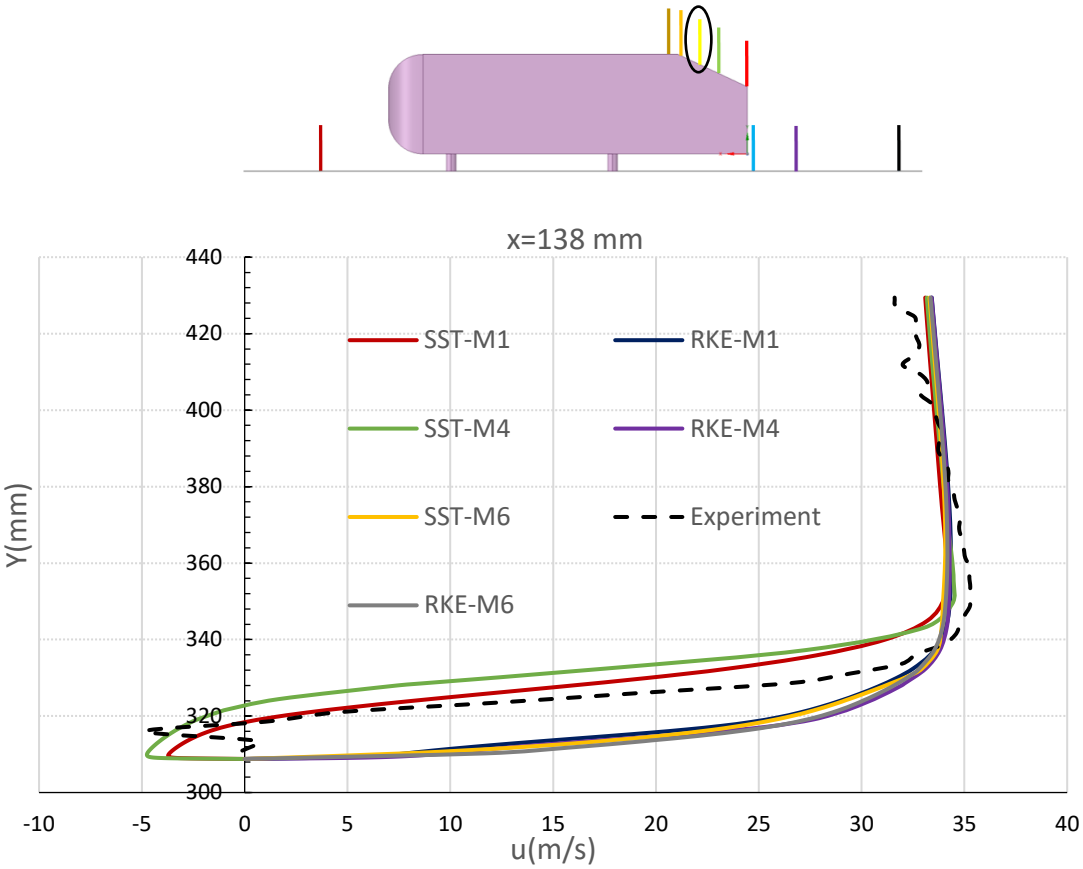

Figure 104: Velocity profiles (x=138 mm) from steady RANS models.

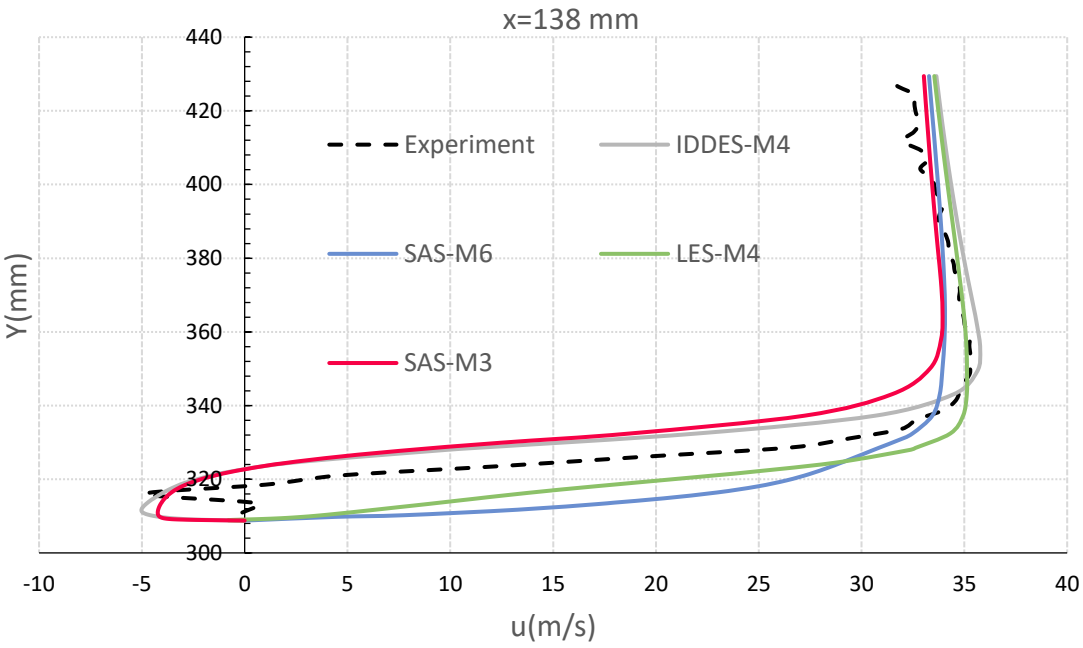

Figure 105: Time-averaged Velocity profiles (x=138 mm) from unsteady turbulence models.

The experimental data at 138 mm clearly show detached flow. Wall-resolved steady k-ω SST models this detached flow fairly well (SST-M1 and SST-M4), while all the other steady-case simulations show attached flow. The IDDES and SAS approach were the only two that predicted the flow separation in the transient case. In the region high above the wall, the simulations generally show better agreement with the experiment.

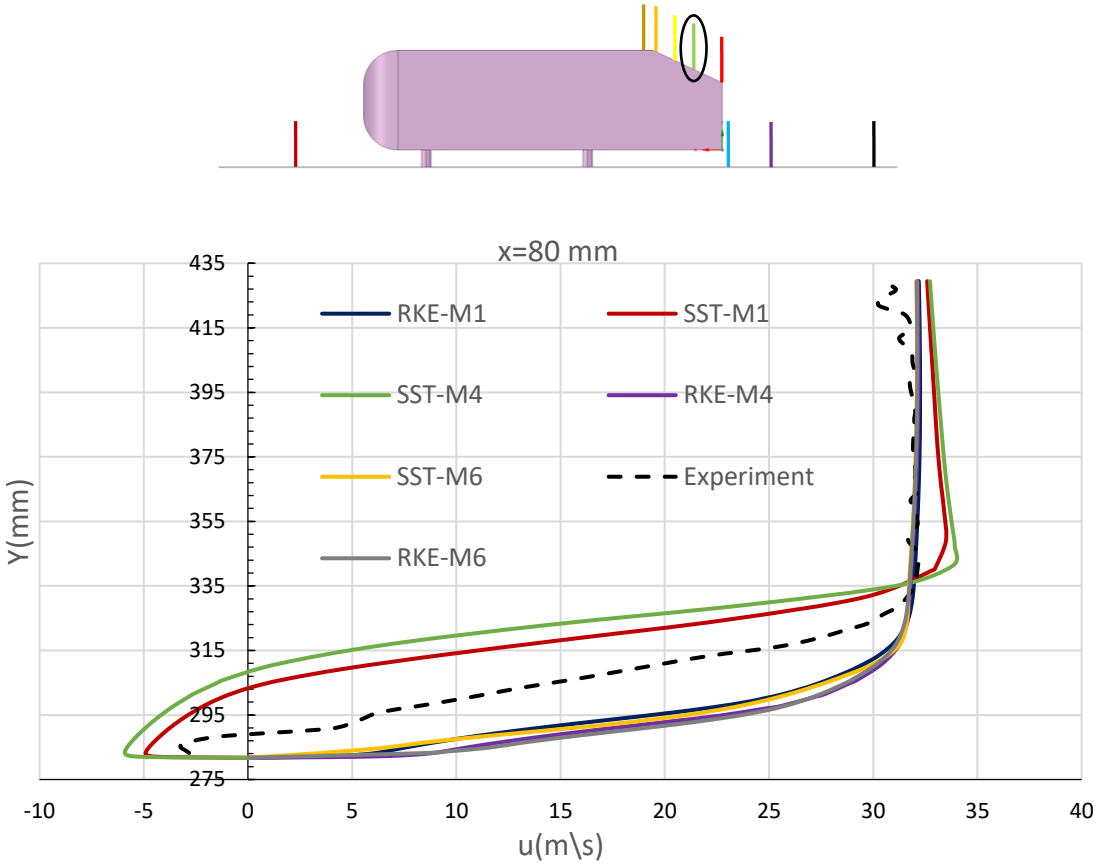

Figure 106: Velocity profiles (x=80 mm) from steady RANS models.

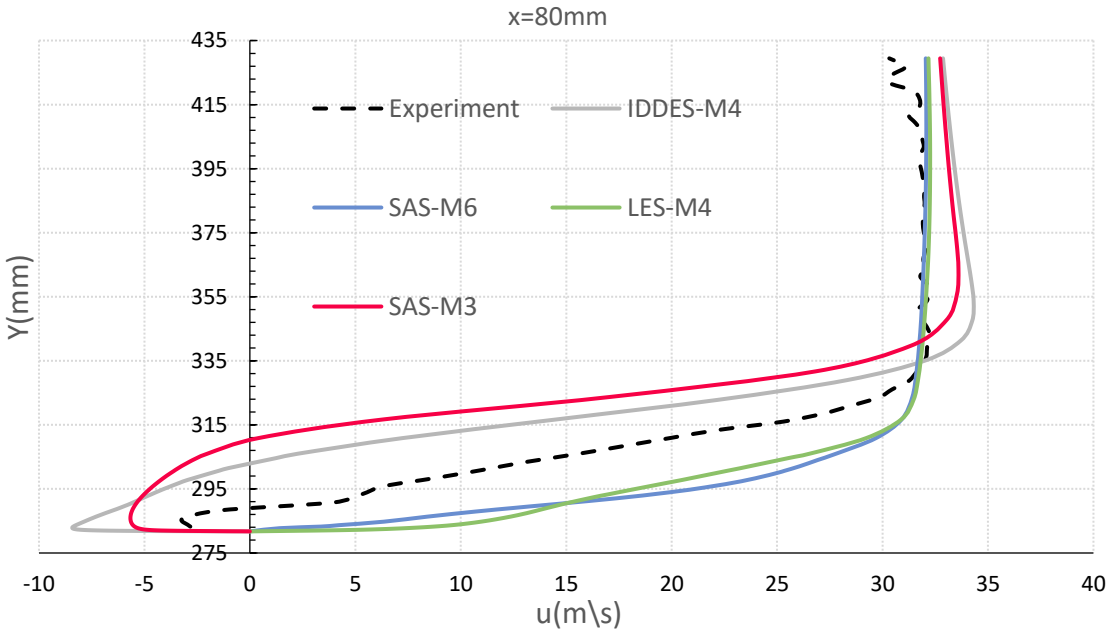

Figure 107: Time-averaged Velocity profiles (x=80 mm) from unsteady turbulence models.

The profile at x=80 mm still shows detached flow in the experiment. The wall-resolved k-ω SST, SST-M1 and SST-M4 and the unsteady approaches, IDDES and SAS show a similar velocity distribution in the near-wall region, but only qualitatively and not quantitatively correct. On the other hand, all other models, which completely miss this weak near-wall separation, produce a much better agreement with the experiments in the outer flow region.

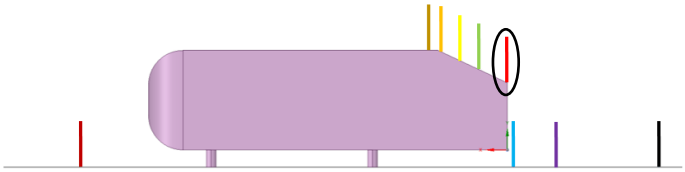

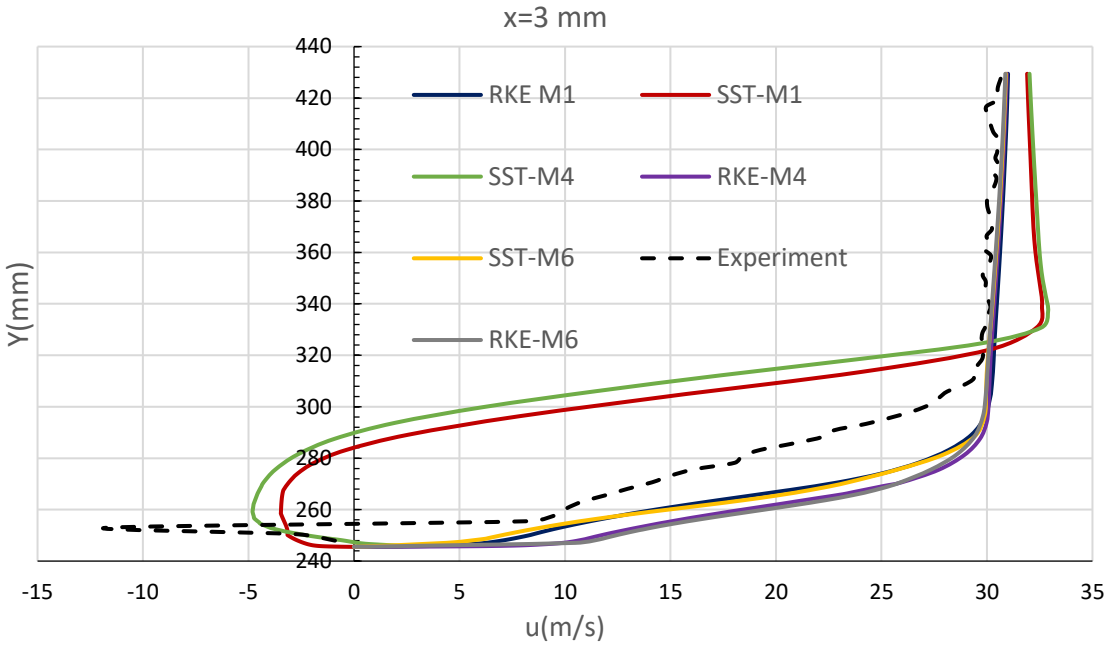

Figure 108: Velocity profiles (x=3 mm) from steady RANS models.

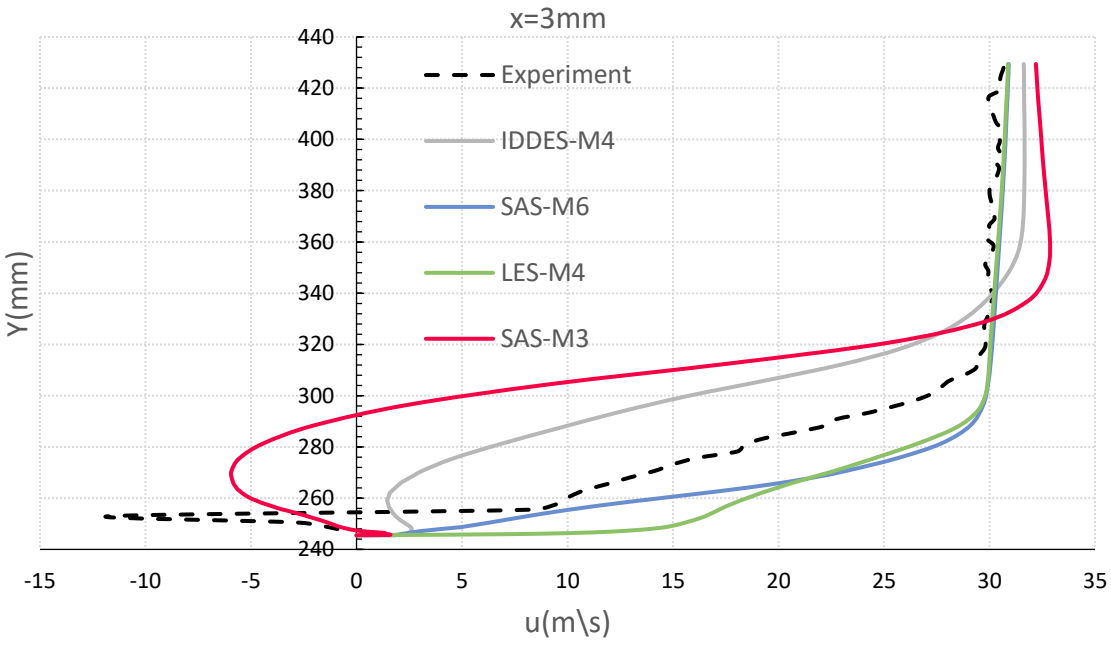

Figure 109: Time-averaged Velocity profiles (x=3 mm) from unsteady turbulence models.

At the last position over the slant, at x=3 mm, just before the slant ends, the experiments indicate again some separation, which is present in the near-wall region, where the high magnitude of the backflow velocity appears questionable, though. All wall-resolved k-ω SST models as well the SAS-M3 show a large region of detached flow. All other turbulence models predicted no flow separation. None of the models is able to predict quantitatively well the intermediate region with $260 \leq y \leq 300$ mm.

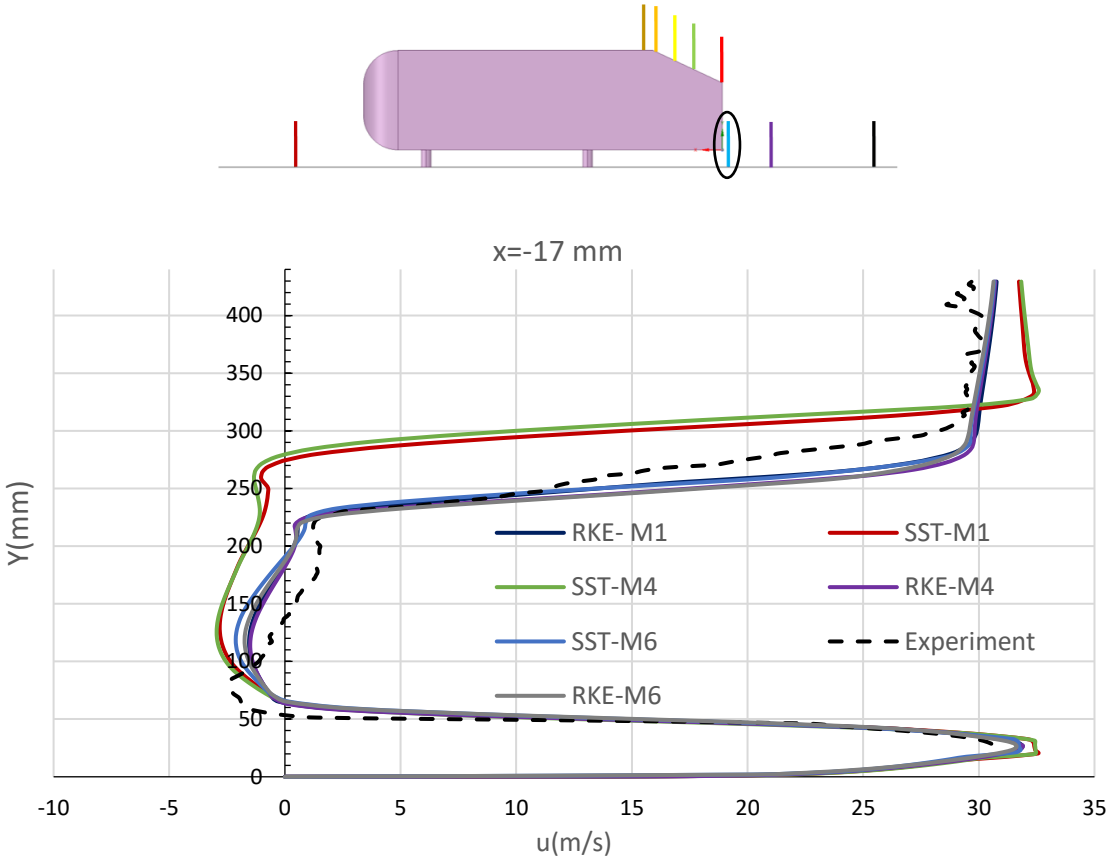

Figure 110: Velocity profiles (x=-17 mm) from steady RANS models.

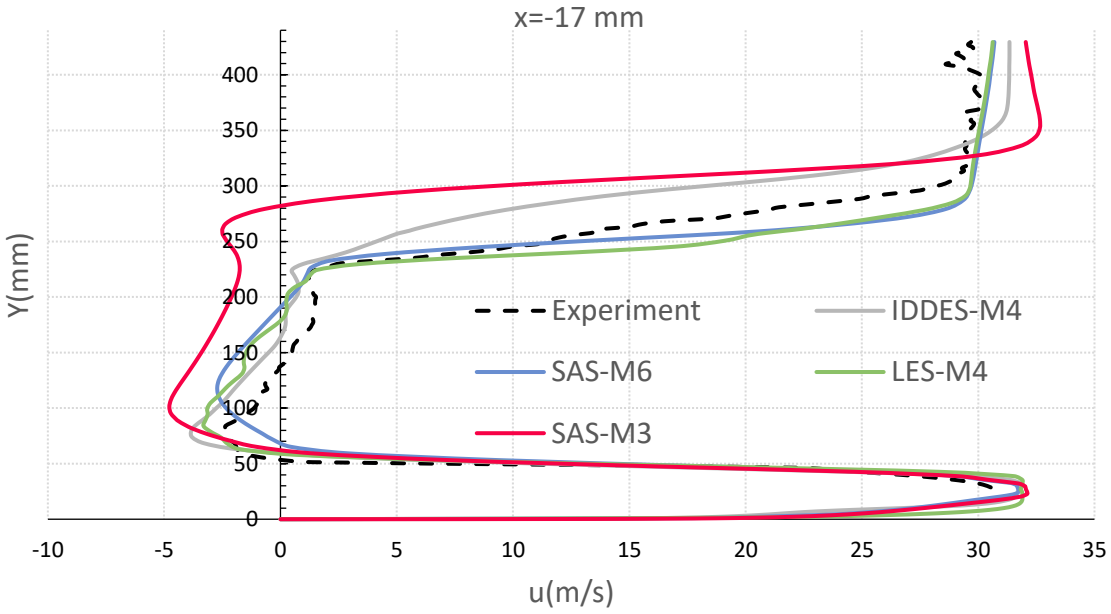

Figure 111: Time-averaged Velocity profiles (x=-17 mm) from unsteady turbulence models.

The next evaluated profile is already in the wake region. The wall-resolved k-ω SST models, SST-M1 and SST-M4, and SAS-M3 show highest deviations from the experiments, especially in the upper region, where they strongly overpredict the backflow. All other simulations performed better. LES-M4 showed the best agreement. SAS-M6 shows similar results as LES-M4, except around Y=100 mm.

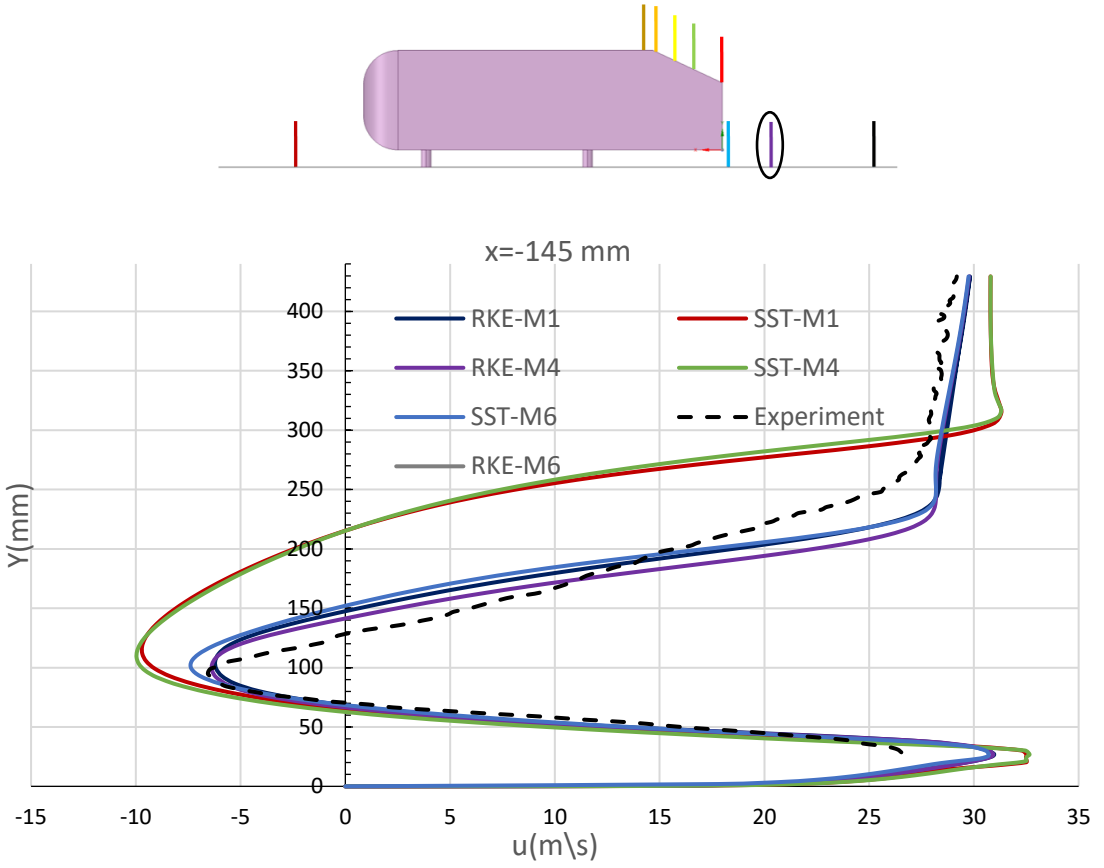

Figure 112: Velocity profiles (x=-145 mm) from steady RANS models.

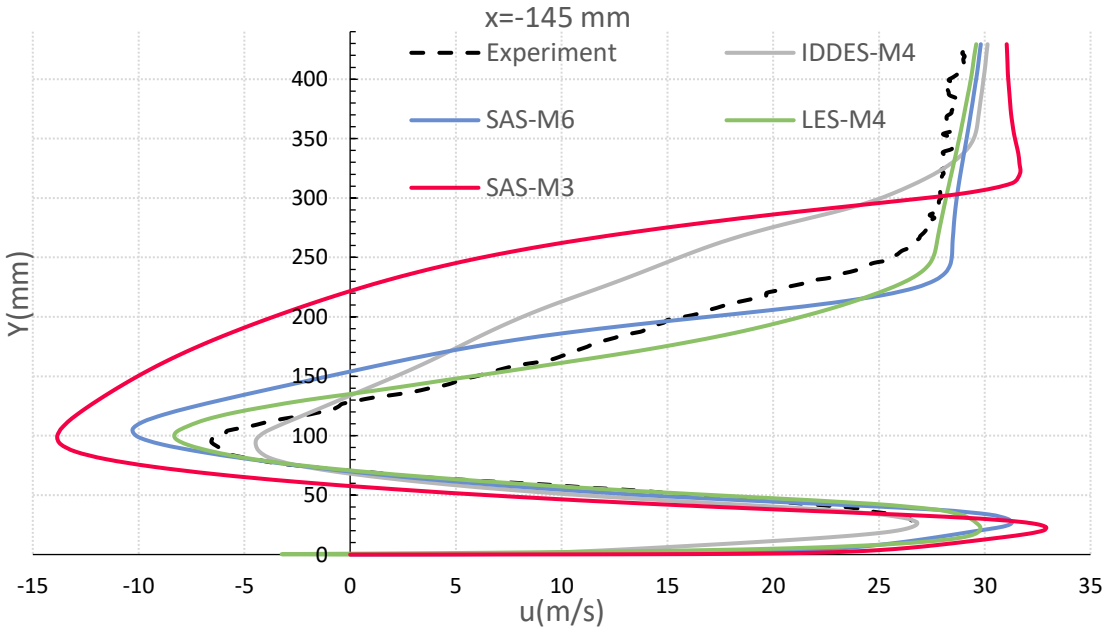

Figure 113: Time-averaged Velocity profiles (x=-145 mm) from unsteady turbulence models.

The next considered profile is positioned further downstream in the wake region at the x=-145 mm. The best agreement was obtained with RKE-M6, RKE-M1 and SST-M6 in the steady case. The wall-resolved SST-M1 and SST-M4 show the worst agreement with the large separation region. The SAS-M3 shows a similar disagreement in the transient case. On the other hand, the wall-function based version SAS-M6 showed reasonable agreement. Still, none of the turbulence models outperform LES.

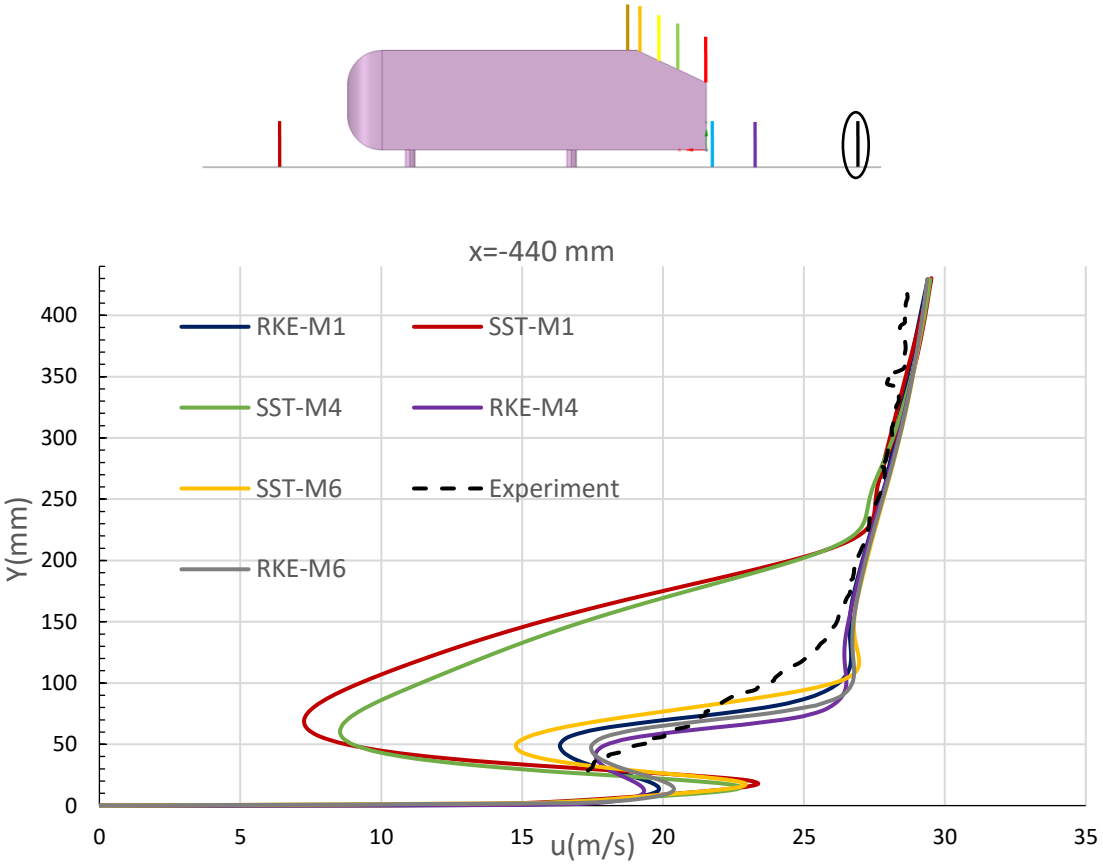

Figure 114: Velocity profiles (x=-440 mm) from steady RANS models.

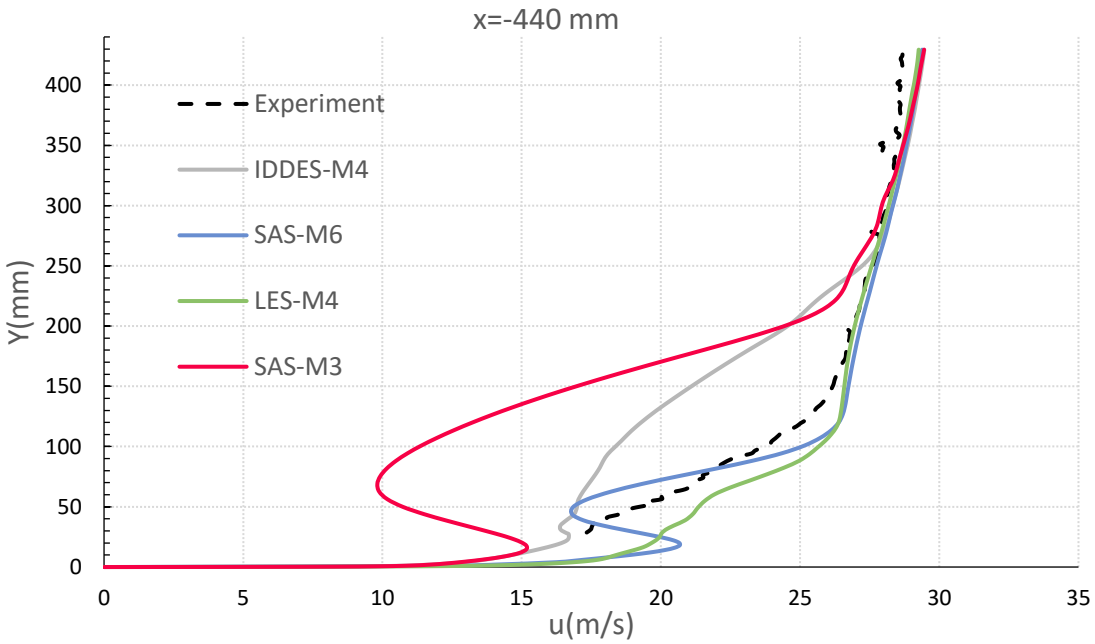

Figure 115: Time-averaged Velocity profiles (x=-145 mm) from unsteady turbulence models.

The experiment profile at the last considered position at x=-440 mm does not exhibit the typical features of wake flow anymore. The profile shows no backflow region. In contrast, all steady turbulence models predict a pronounced minimum in the local velocity around Y=50mm, indicating a still prevalent

influence of the wake. The SST-based models seem to produce this feature more pronouncedly than the RKE models. Among the transient models SAS-M3 yields the strongest deviation from the experiments. IDDES performed better, while LES-M4 achieved again the best agreement.

7.4.1 The sensitivity to the grid

Mesh resolution plays an important role in numerical simulations. The ultimate goal in all engineering application is to satisfy the need for accuracy with a computationally affordable grid. To assess the grid sensitivity in transient simulations for the meshes M3 and M4, we selected the velocity profiles on three different locations for evaluation. As seen from Table 4, the mesh M4 provides a finer resolution near the wall, which translates into a double total number of grid points as compared to the mesh M3.

Figures 116−118 show the comparison between the predictions of the transient models IDDES and LES using the meshes M3 and M4. At x=191 mm, the IDDES profiles show minimal differences between M3 and M4. A notable difference is observed with the LES in the near-wall region, where M4 shows a higher positive peak than M3. On the other hand, LES-M3 shows a slightly more pronounced negative peak in the near wall region at the next position (x=138 mm). The IDDES-profiles show again no notable effect of the grid resolution.

At the furthest downstream position x=-145mm, the finer mesh leads a slightly longer positive peak close to the wall (at around y≈ 25 mm wall distance) for both IDDES and LES.

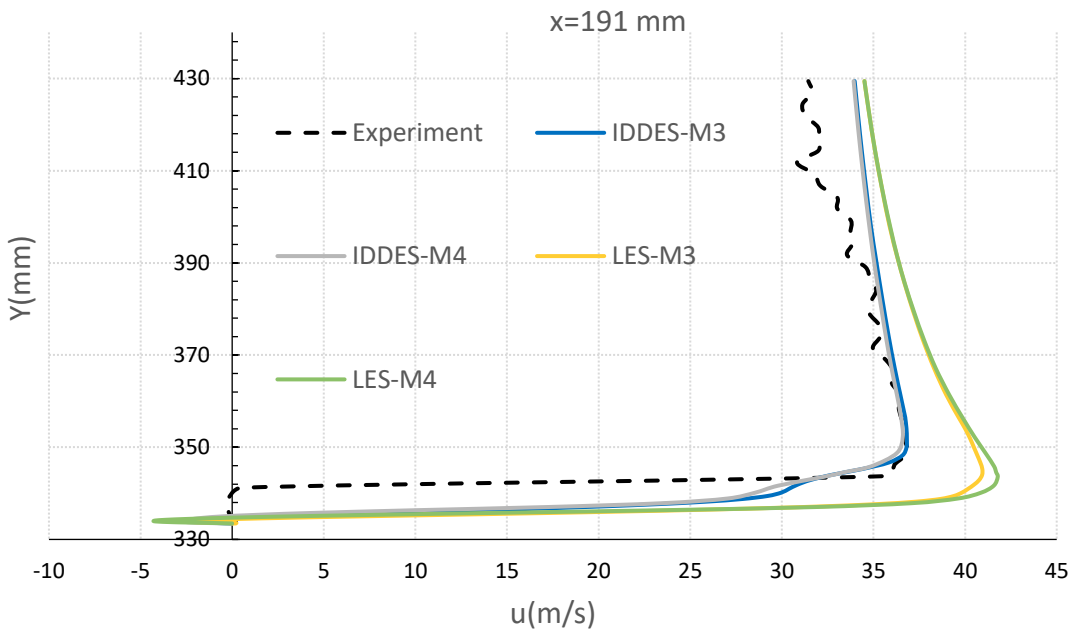

Figure 116: Time-averaged velocity profile (x=191 mm) from IDDES and LES with meshes M3 and M4.

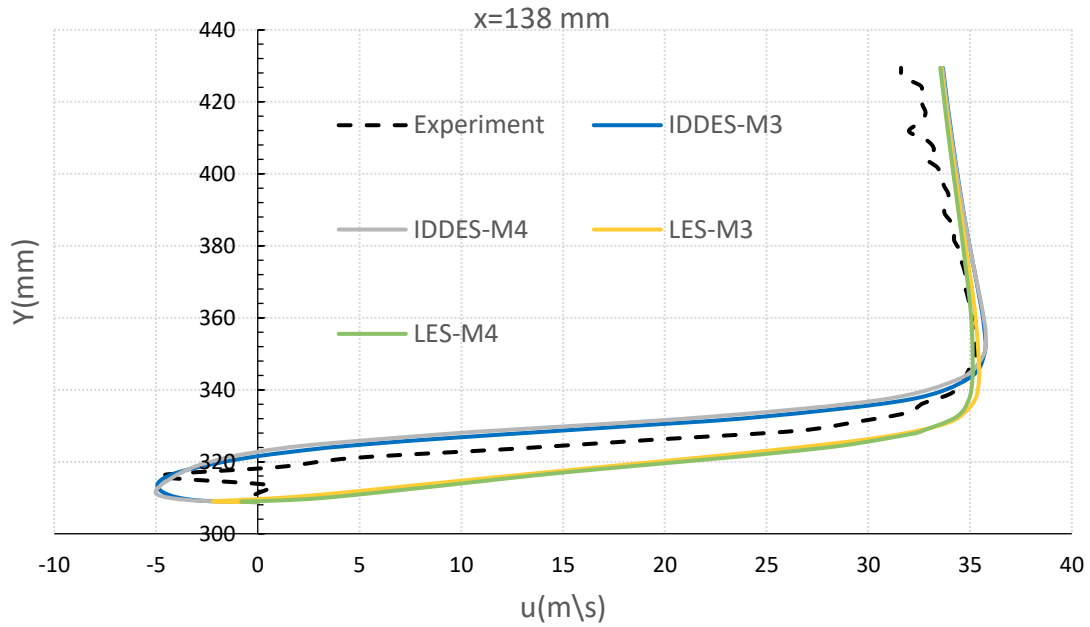

Figure 117: Time-averaged velocity profile (x=138 mm) from IDDES and LES with meshes M3 and M4.

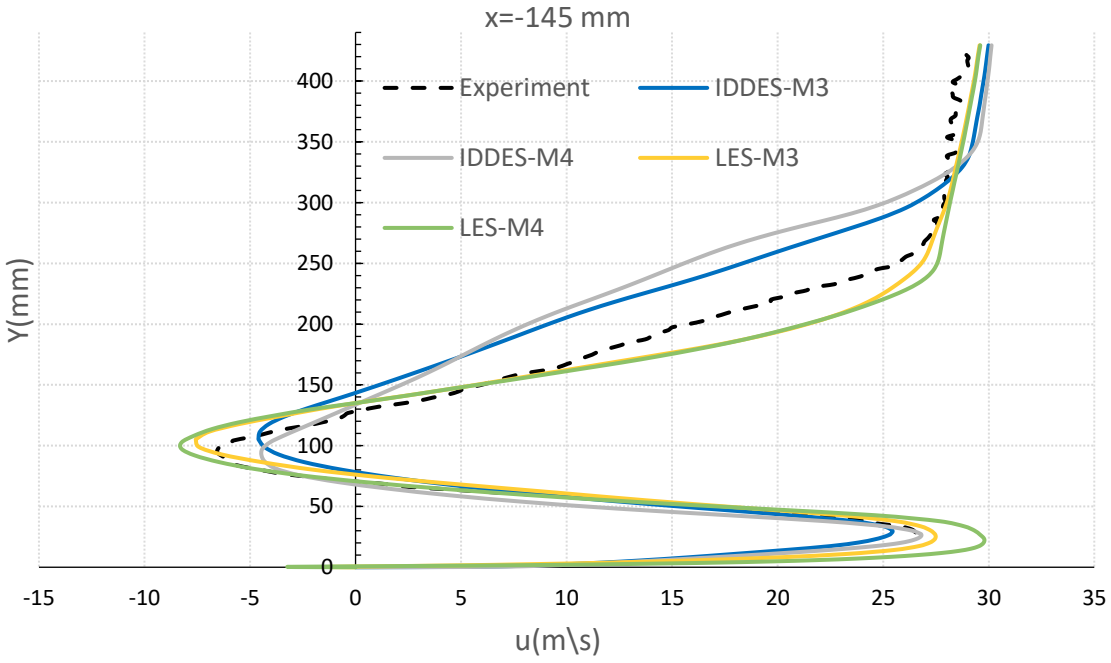

Figure 118: Time-averaged velocity profile (x=-145 mm) from IDDES and LES with meshes M3 and M4.

Summing up, it can be stated that LES appears as more sensitive to the special resolution than IDDES. This outcome is expected, because the present LES does not apply any near-wall modelling, unlike the IDDES approach.

7.5 Predicted static pressure

Additionally to the velocity profiles, Meile et al.[40] measured the static pressure distribution on the slant, base, and underbody. The pressure distribution was measured using a pattern of pressure taps with a width of 0.5 mm, which were connected via plastic tubes to the pressure sensors. The positions of the pressure taps are illustrated in Figure 119 together with their exact coordinates in mm in the table on the left. The metering points (MPs) are located on three different vertical planes:

- MP 1−10: z=0 mm (symmetry plane)
- MP 11−17: z=-90 mm
- MP 18−24: z=-180 mm

Ahmed body 25°		
Point MP	X(mm)	Y(mm)
1, 11, 18	215	338
2, 12, 19	181.01	328.59
3, 13, 20	101.26	291.40
4, 14, 21	21.50	254.20
5, 15, 22	0	214
6, 16, 23	0	125
7, 17, 24	0	65
8	21	50
9	128.45	50
10	215	50

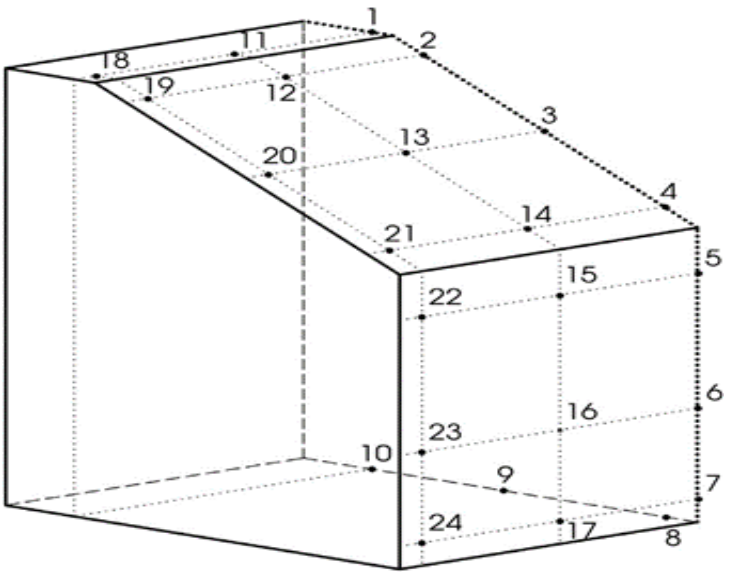

Figure 119: Pressure tap positions on Ahmed body [40].

Looking at the plots for the symmetry plane z=0 mm in Figures 120 −121, the experiment shows a decrease in pressure from point 1 to 2. A minimum of around 0.82 is reached at measuring point (MP) 2, then followed by an increase in pressure as indicated at MP 3 and 4. At the last couple of points, the pressure stabilizes and reaches a constant value of around -0.1. None of the steady RANS simulations was able to predict the pressure drop at point 2 correctly. They either predicted no or a minimal drop. The predicted pressure variations commonly differ from a minimum level at point 1 and then further increase towards a roughly constant level from point 5 onwards, where they agree fairly well with the experiment. A similar trend was noticed in the transient case of SAS-M6. The IDDES shows better results but worse compared to LES-M4, which is superior. The latter is the only one able to correctly predict the pressure drop at MP 2. There is still a lack of agreement with the experiment in the qualitative values.

MPs 11−17 are positioned somewhere in the middle between the symmetry plane and the horizontal side surface of the body. The experiment shows a very similar pressure variation to the measurements on the plane z=0. There is a pressure drop at point 12, followed by a monotonous increase as the flow reaches the rear part of the body. The turbulence models performance is very similar to the previous plane for both steady and models configurations (see Figures 122−123).

The outermost vertical plane at z=-180 mm contains the measuring points MP 18−24. The pressure minimum is moved further downstream and reaches its minimum at point 20. The reason for that is the formation of the C-pillar vortex along the side edges of the slant. The pressure then increases and reaches a constant value at around - 0.1. Again, none of the simulations were able to predict the pressure drop correctly. SST-M1, SST−M4 and SAS-M3 always predict a too high pressure up to MP 21. LES yields again the best agreement (see Figures 124−125).

Figures 126-127 present the pressure coefficient along the bottom surface for the steady and transient models at the center-line position (on the symmetry plane z=0 mm) of the Ahmed body. The pressure coefficient takes the value of around one at the front part of the body and then decreases over the curved lower edge. This is followed by the smooth pressure increase to the rear part of the vehicle. There is no significant difference between the steady and transient model predictions. Some deviations are observed near the back end of the vehicle.

Figures 128-129 show the pressure coefficient over the top surface on the symmetry plane of the Ahmed body. It takes the value of around one at the front part of the body and then decreases over the curved upper edge. All calculations show pretty much the same results in this region. As the flow continues to move over the top surface, the SAS-M6 model shows smaller distortion. Velocity decreases but there is no flow separation. Beyond around 0.5 m the coefficient begins to drop towards a distinct minimum right at the beginning of the slant. None of the calculations correctly predicted the pressure minimum on the flow over the slant. All simulations predicted the minimum more upstream than in the experiment. There is also a big difference in the minimum value predicted by the different turbulence models. The wall-resolved SST (also SAS, IDDES) using the M1−M4 mesh configurations predicted a much lower pressure drop compared to the other simulations. For all other models the predicted minimum value slightly varies, but, the minimum is predicted at the same streamwise position.

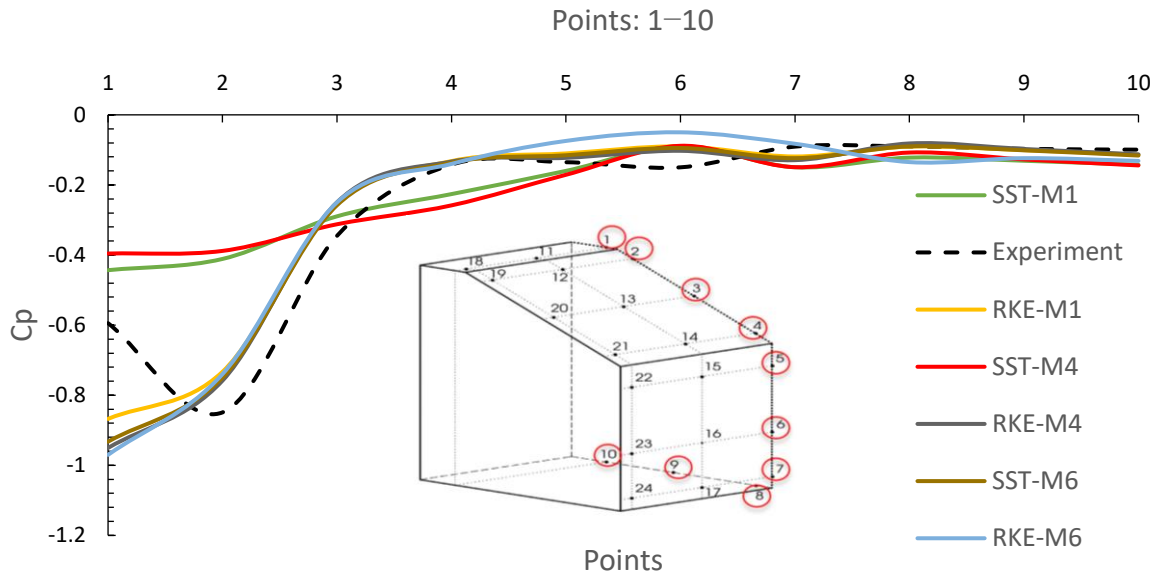

Figure 120: Pressure coefficient distribution from steady RANS simulations along the line with MP1 - MP10.

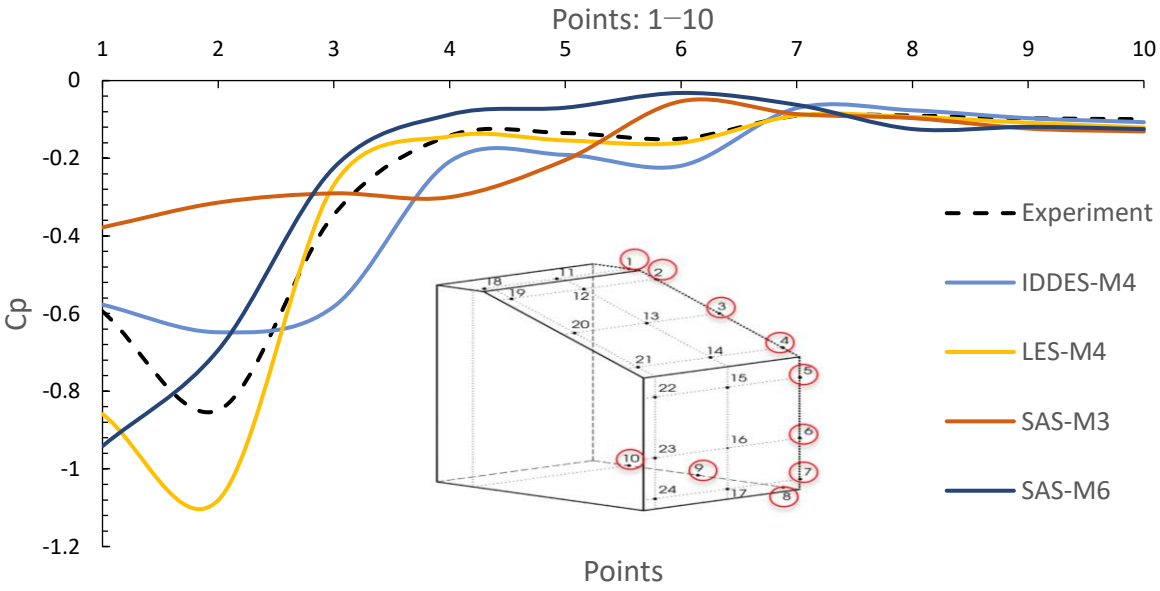

Figure 121: Time-averaged pressure coefficient distribution from the transient model simulations along line with MP 1 – MP 10.

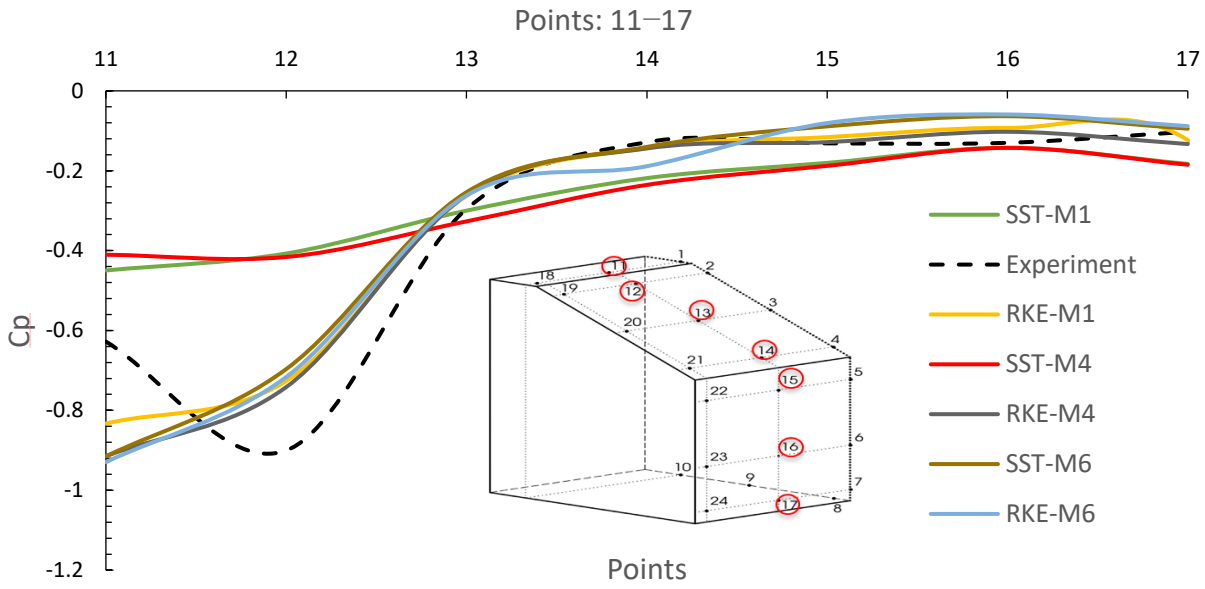

Figure 122: Pressure coefficient distribution from steady RANS simulations along the line with MP 11 – MP 17.

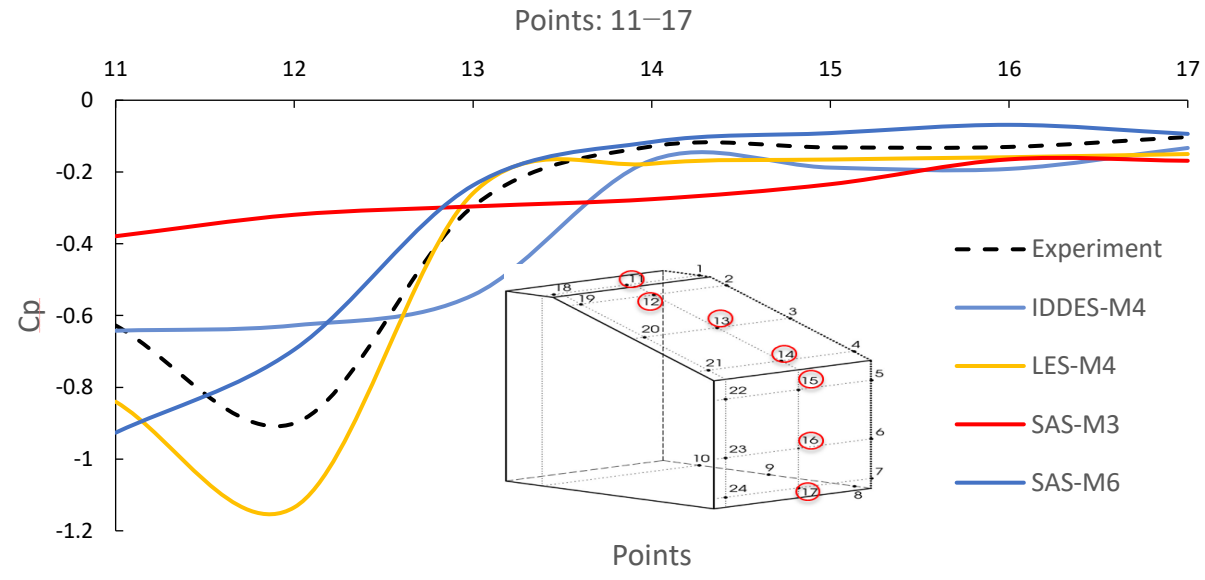

Figure 123: Time-averaged pressure coefficient distribution from the transient model simulations along line with MP 11 – MP 17.

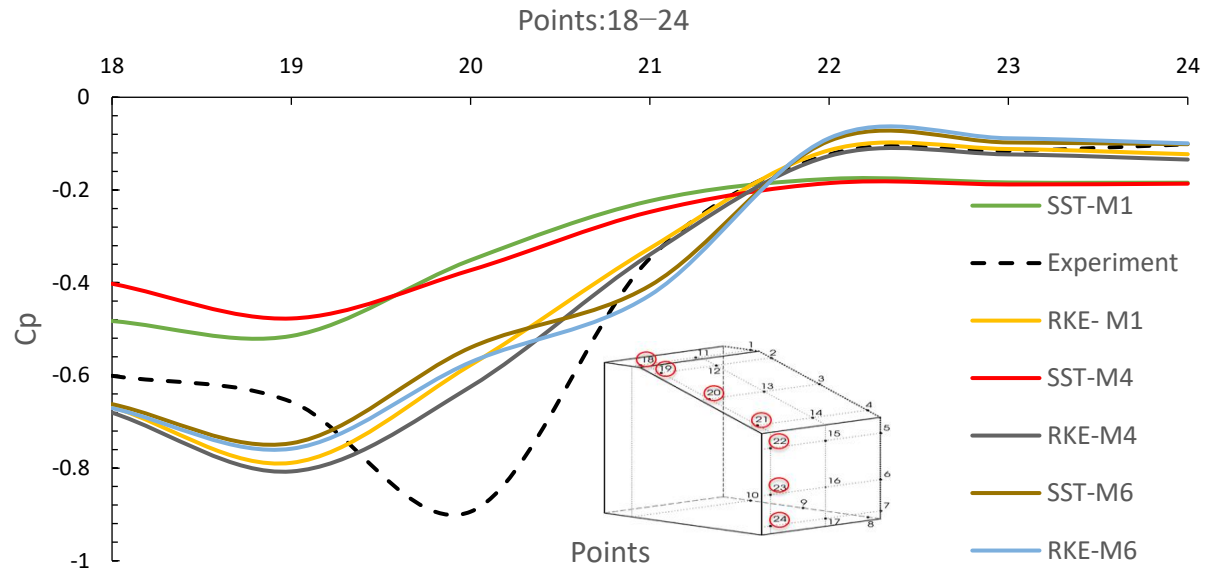

Figure 124: Pressure coefficient distribution from steady RANS simulations along the line with MP 18 – MP 24.

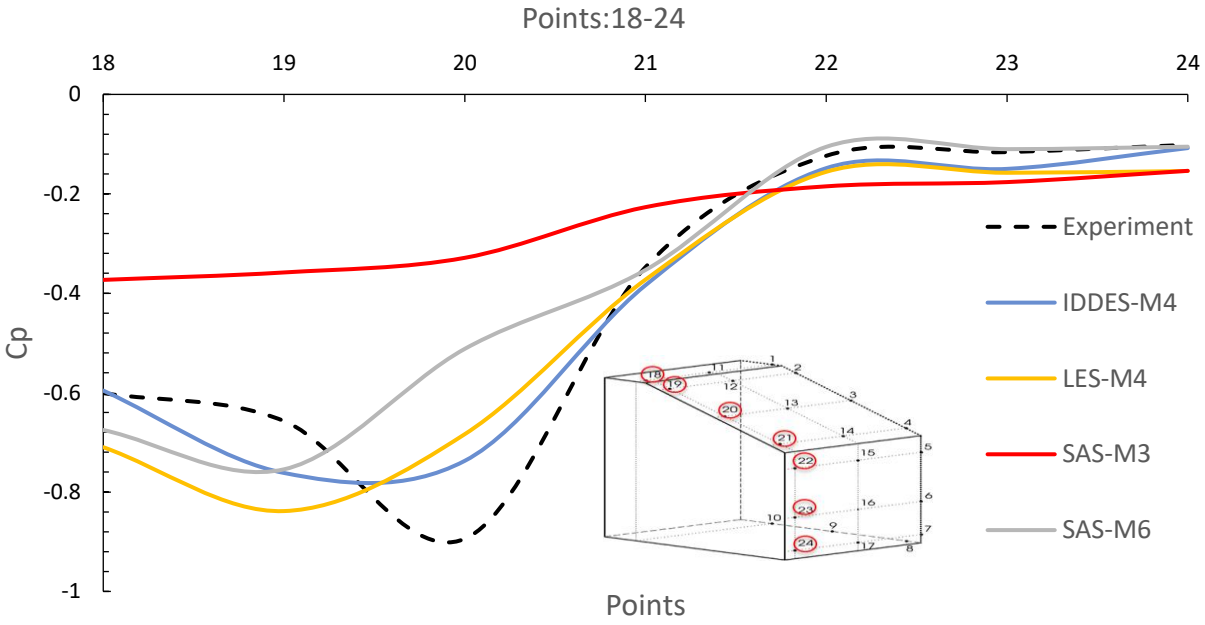

Figure 125: Time-averaged pressure coefficient distribution from the transient model simulations along line with MP 18 – MP 24.

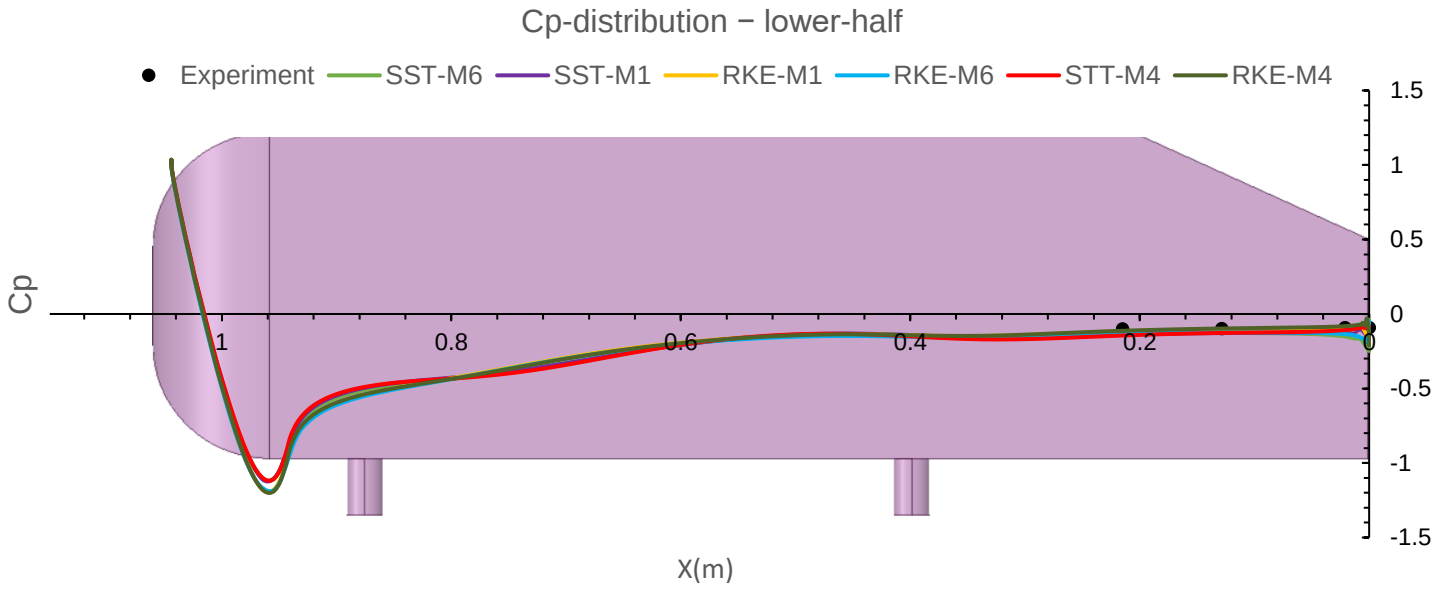

Figure 126: Pressure coefficient distribution along the bottom surface from RANS steady simulations on symmetry plane z=0.

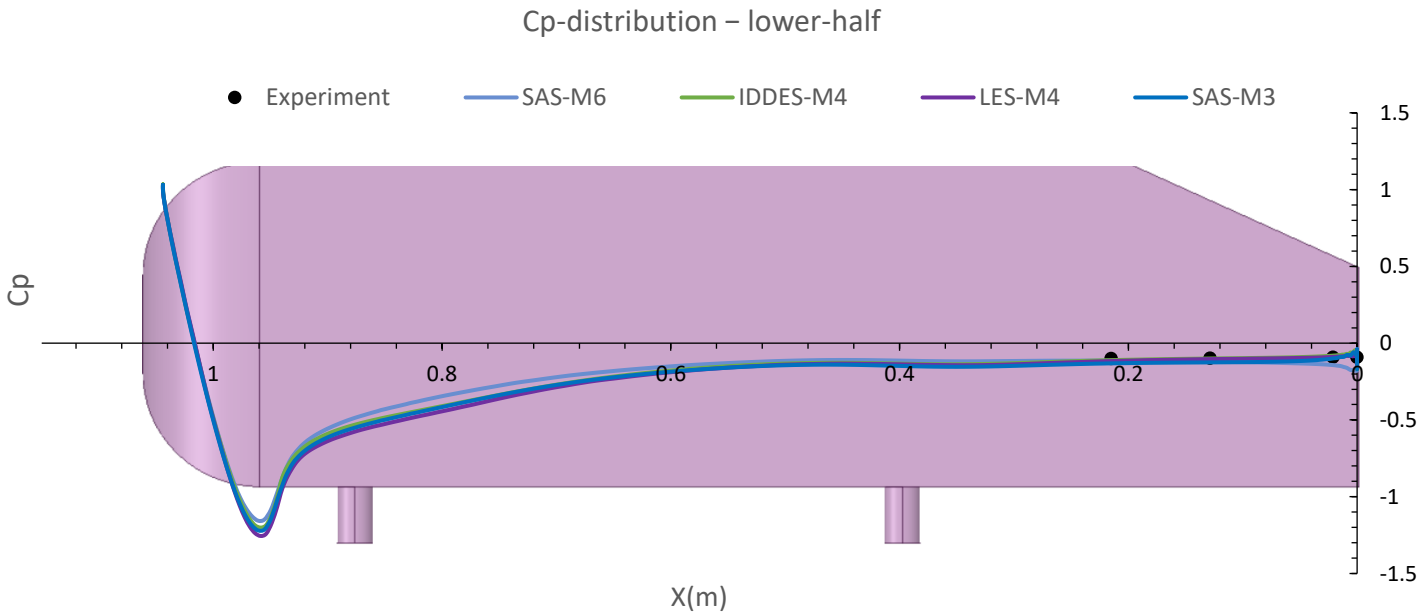

Figure 127: Time-averaged pressure coefficient distribution along the bottom surface from transient model simulations on symmetry plane z=0.

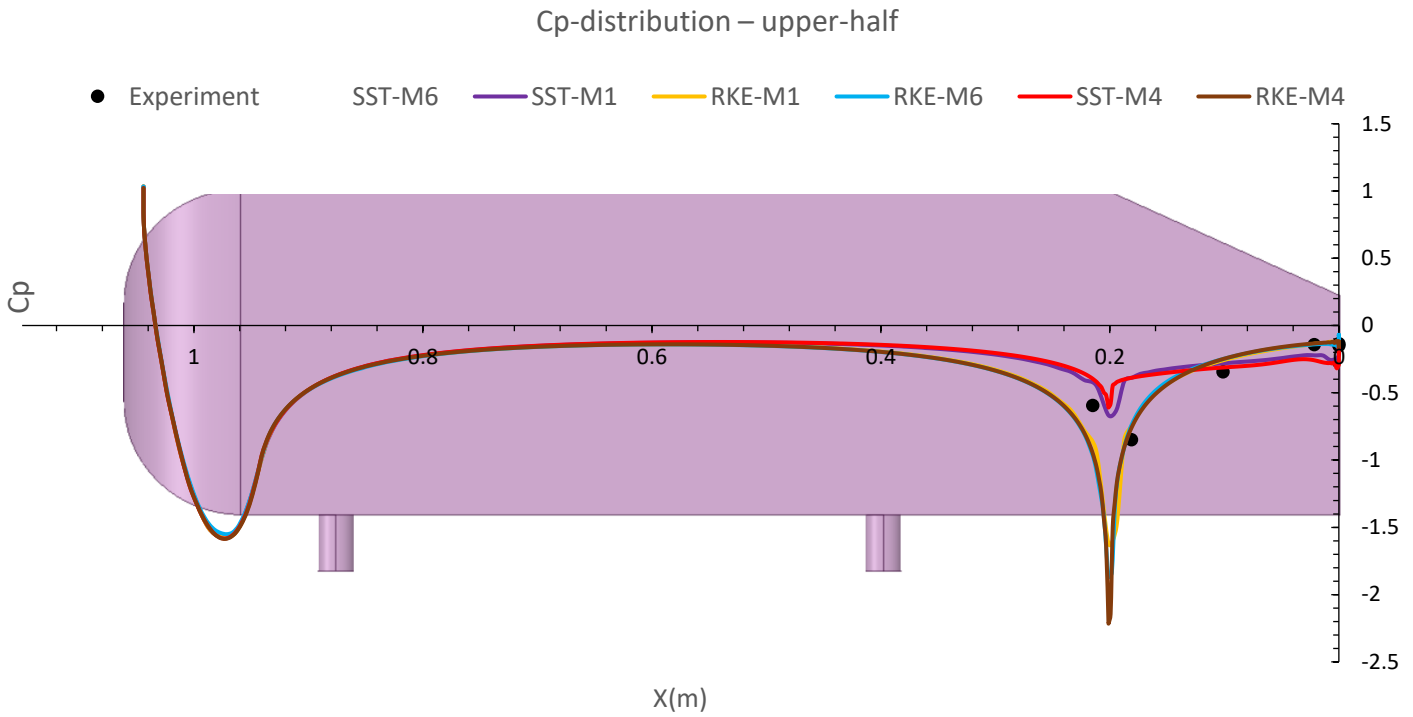

Figure 128: Pressure coefficient distribution along the upper surface from RANS steady simulations on symmetry plane z=0.

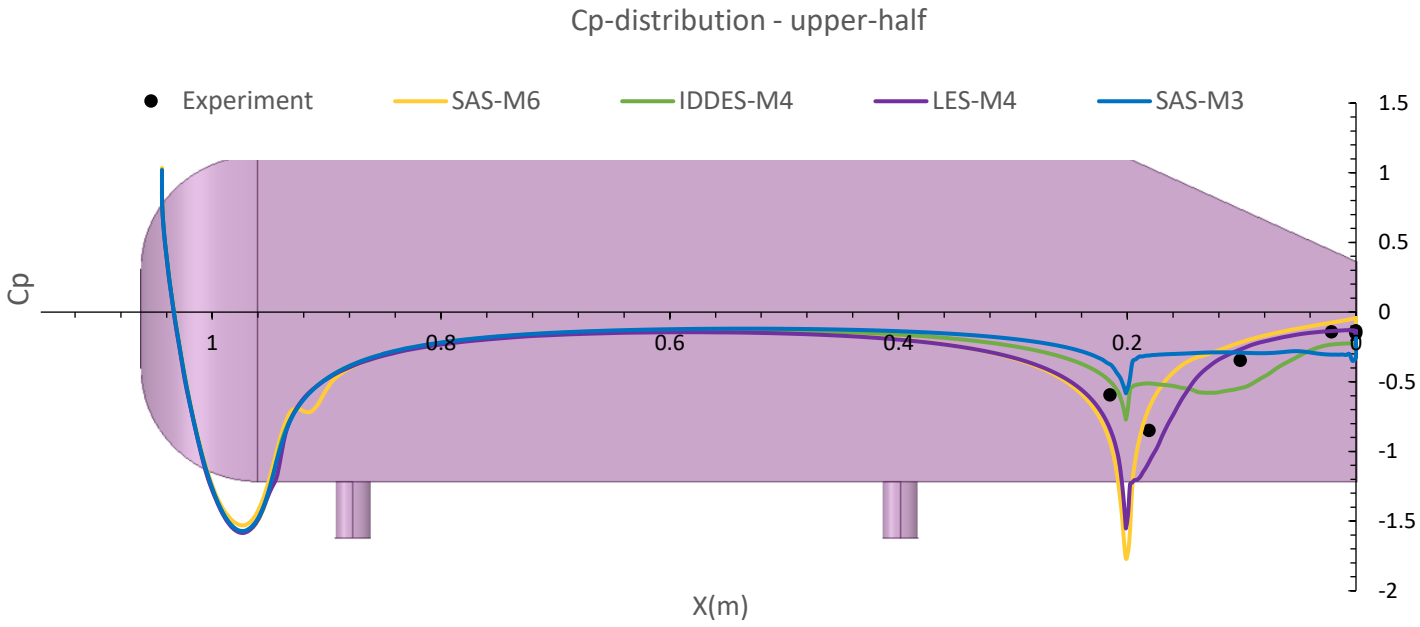

Figure 129: Time-averaged pressure coefficient distribution along the upper surface from transient model simulations on symmetry plane z=0.

7.6 Predicted wake region

Many of the different experiments found in literature also describe the flow patterns observed in the wake at a sub-critical slant angle of the body. The flow generally separates at the upper slant edge, and then reattaches on the same surface. This results in a relatively small recirculation region, which has a semi-elliptical shape. The shape is determined by the two counter-rotating C-pillar vortices, which form on each side edge of the slant. These lateral parts are areas with the high negative relative pressure, which results in higher lift values compared to, for example, the 35° configurations of the Ahmed body. The second separation occurs at the lower slant edge, forming a wake with two horseshoe vortices. According to Meile et al.[40], the wake closes, further downstream after approx. 200 mm.

In the present analysis of the results the streamlines obtained for each turbulence models on the symmetry plane (z=0 mm) are shown. As seen from Figures 130-131, the steady RANS model k-ω SST predicted the fully separated flow over the entire slant surface. The model completely failed to predict the flow reattachment. The vortex cores in the wake region have their centers practically on the same vertical line at around x=-140 mm in the M1 both and M4 mesh configurations.

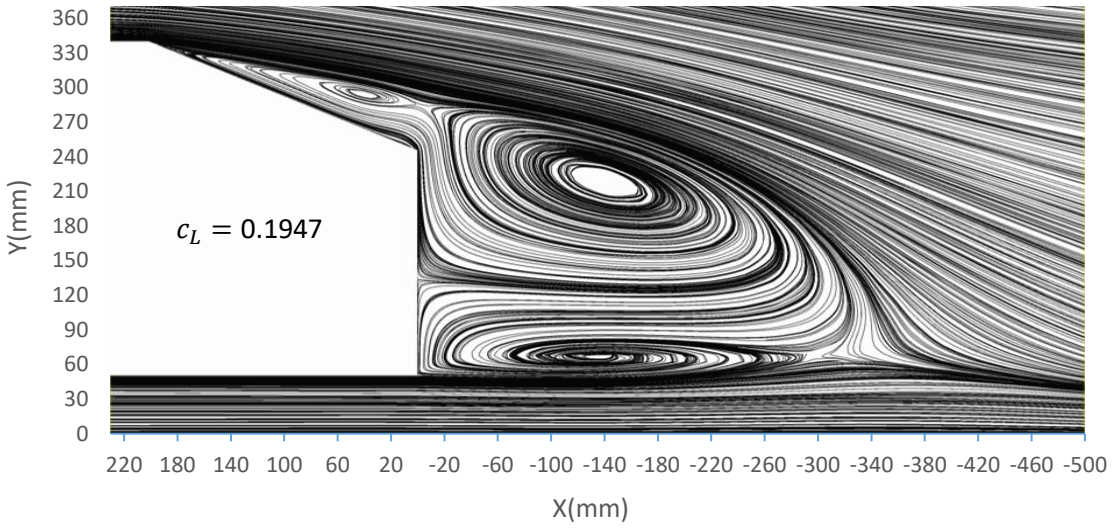

Figure 130: Streamlines from steady RANS model SST-M1.

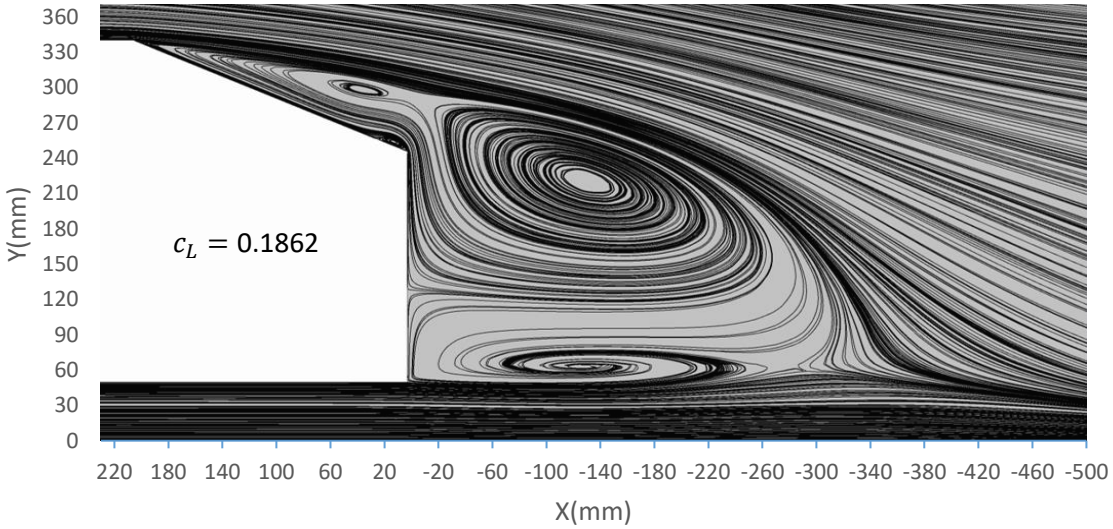

Figure 131: Streamlines from steady RANS model SST-M4.

The separation is even more pronounced for the fine mesh when looking at the upper edge of the slant. The flow starts to detach earlier compared to SST-M1. The wake closes after 340 mm, which is longer compared to the measurements. The present massive overprediction of the flow separation over the slant is in agreement with the numerical results from Guilmineau [35] as shown in Figure 132.

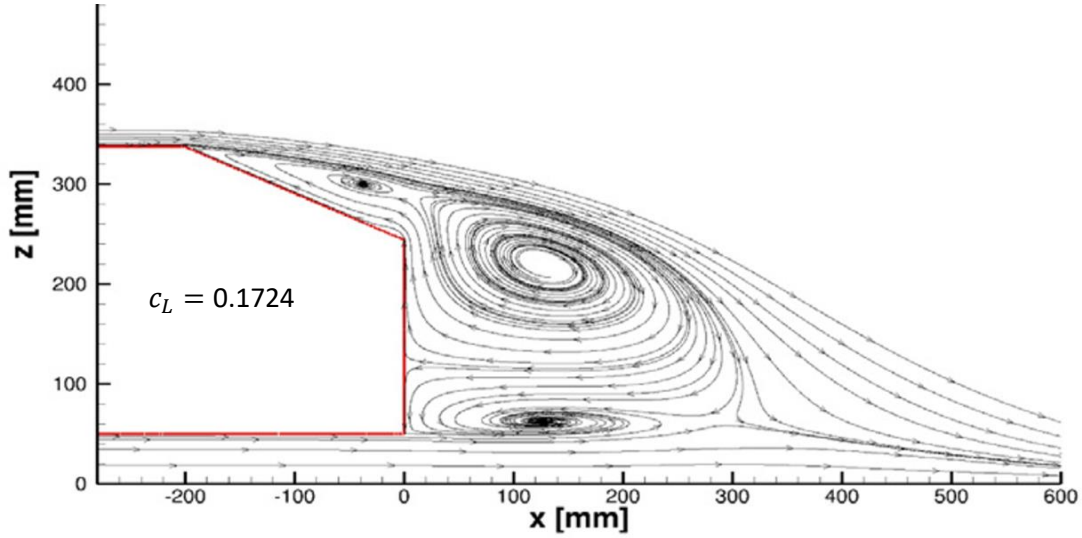

Figure 132: Streamlines from steady RANS model k-ω SST at Re= 7.68x10^5shown in[35].

Contrary to the k-ω SST model, the RKE predicted a fully attached flow over the entire slant region. The models predicts the formation of two vortices in the wake region, one above the other. Their center point is moved more to the left side, towards the base of the body. The cores are located at approx. x=-100 mm in the vertical direction. The wake closes after -260 mm. The results in the coarse and fine grid configuration are similar. The SST on the non-wall-resolved (wall-function based) grid (SST-M6) gives RKE-like results, as seen from Figure 135.

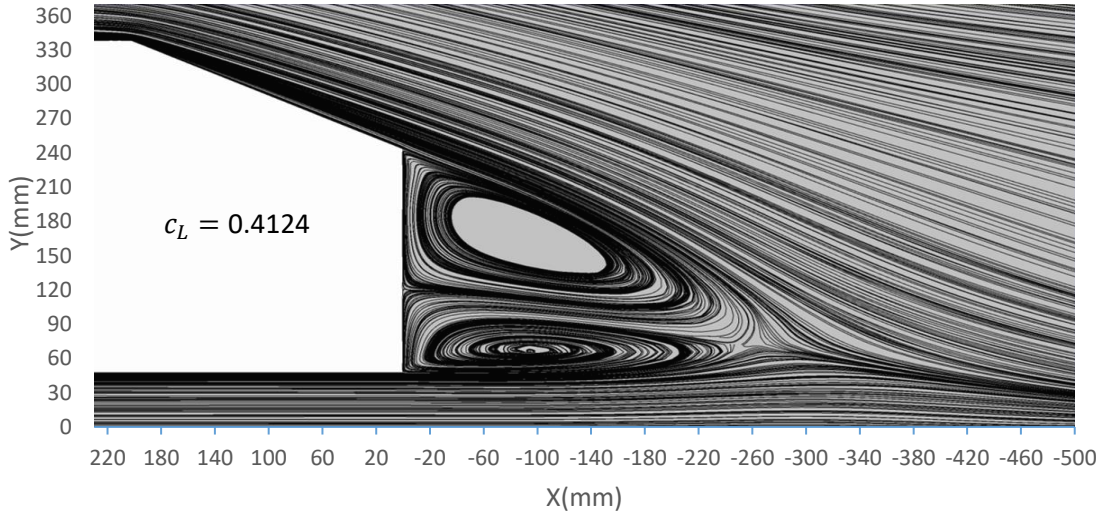

Figure 133 Streamlines from steady RANS model RKE-M1.

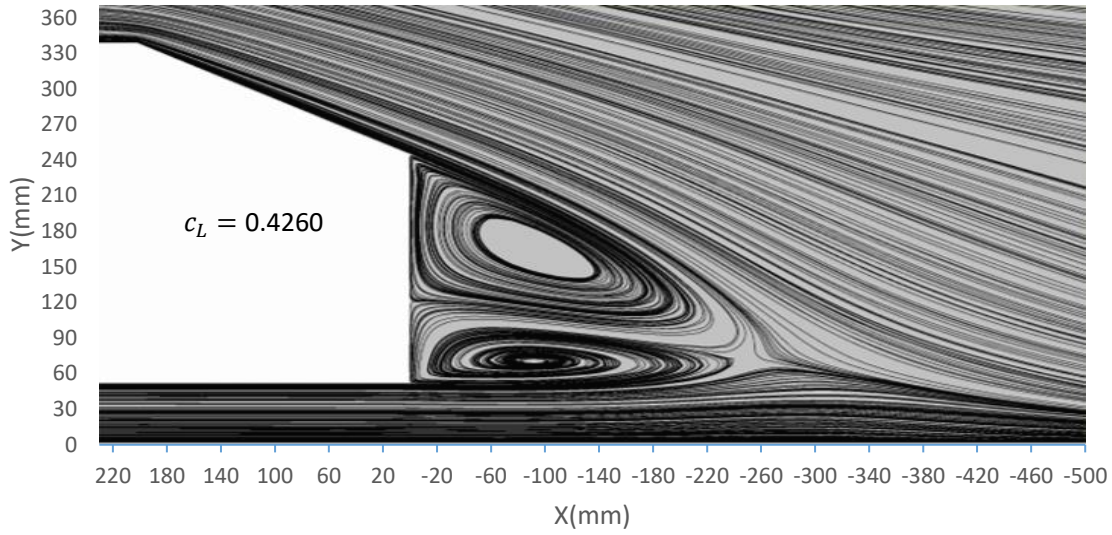

Figure 134 Streamlines from steady RANS model RKE-M4.

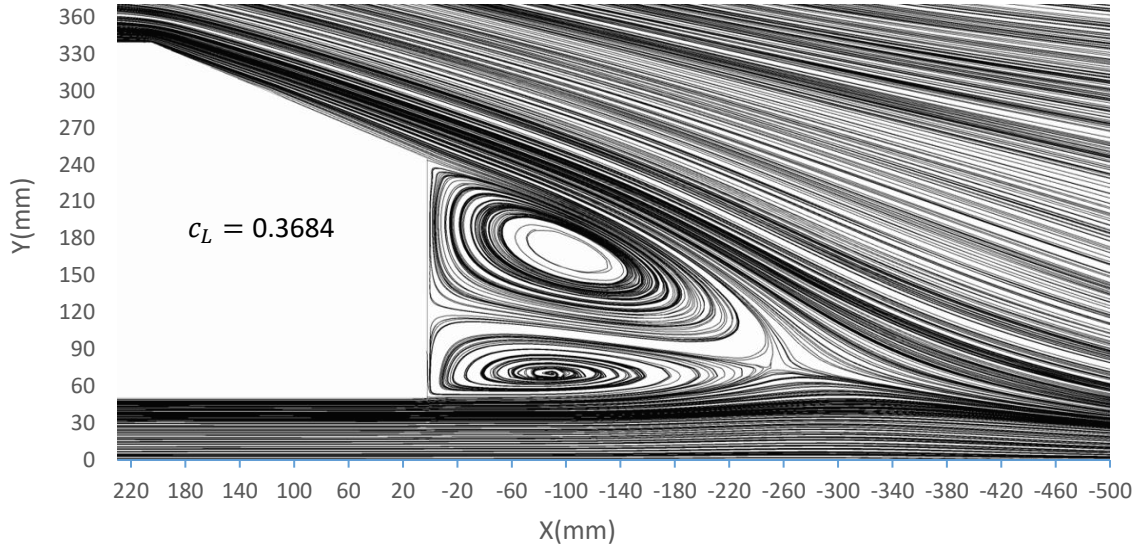

Figure 135: Streamlines from steady RANS model SST-M6.

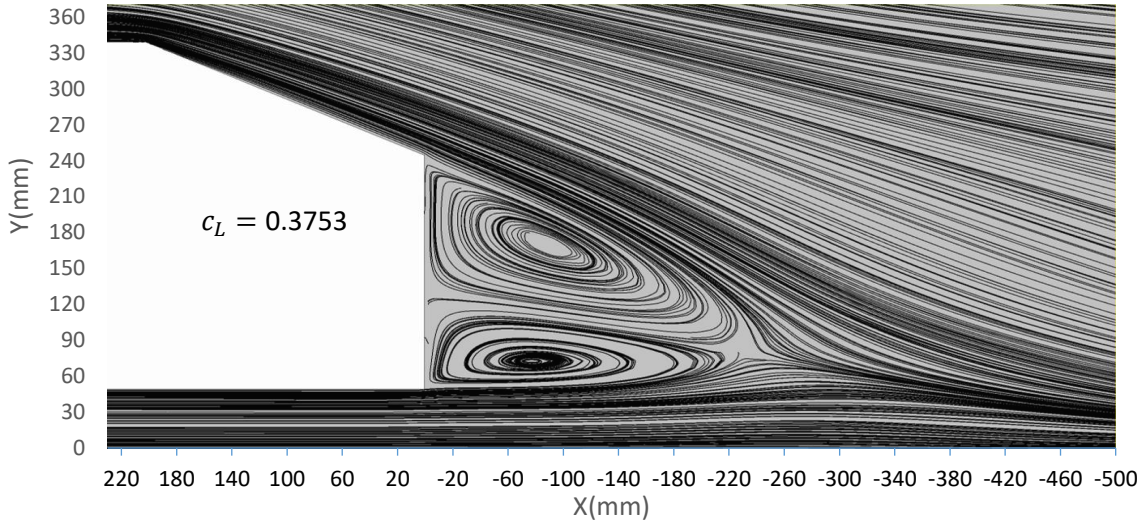

Figure 136: Streamlines from steady RANS model RKE-M6.

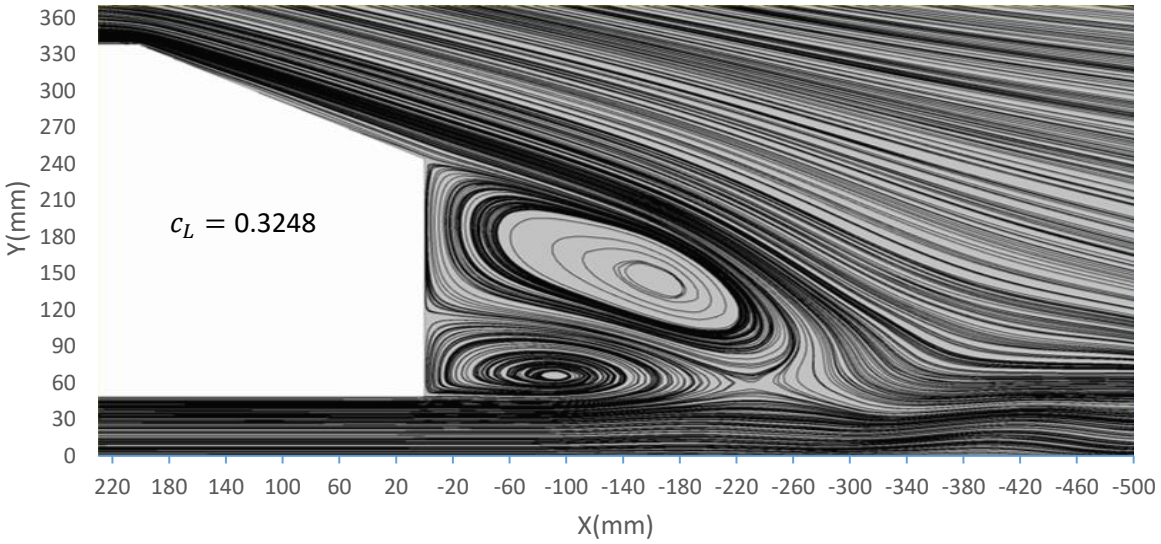

Figure 137: Streamlines from transient model simulation SAS-M6.

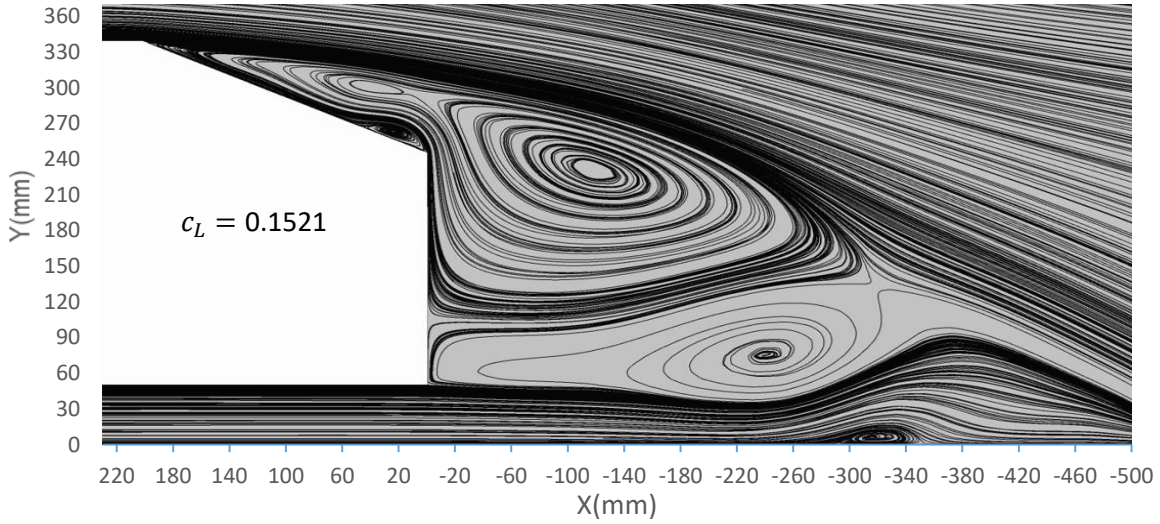

Figure 138: Streamlines from transient model simulation SAS-M3.

Results of the transient model SAS are illustrated in Figures 137−138. The wall-function modeled version of the SAS-M6 predicted reasonably accurate results for the lift coefficient, with an error around 9%. The streamlines plot is similar to that of the RKE-M1 and RKE-M4 or the SST-M6, with the attached flow over the entire slant. The SAS-M3 shows a completely different picture, the flow is entirely separated, which is similar to the SST-M1 and SST-M4 configurations, which results in the significant underprediction for the lift.

According to our literature review, the the study of Guilmineau et al.[35] suggests IDDES as the only hybrid RANS/LES method able to predict the flow reattachment on the slant, describing accurately the size of the separated region as well. In the present case, the method predicts the flow reattachment on the slant, but it does not predict the same size of the separated region. The separation bubble is longer and thicker compared to [35] as seen from the Figures 139 and 140. The wake region is shorter compared to both steady RANS calculations discussed above.

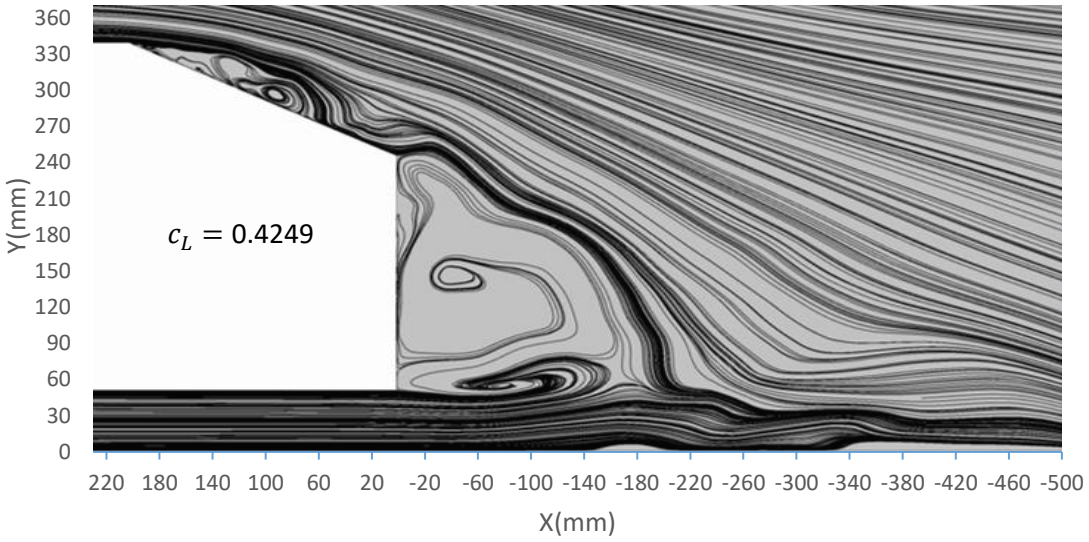

Figure 139: Streamlines from transient model simulation IDDES-M4.

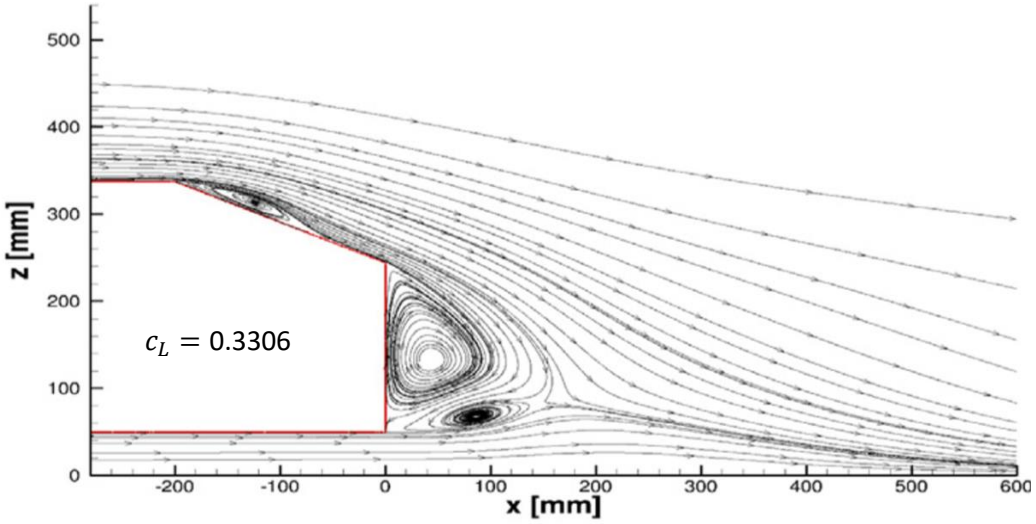

Figure 140: : Streamlines from transient-hybrid model IDDES from literature[35].

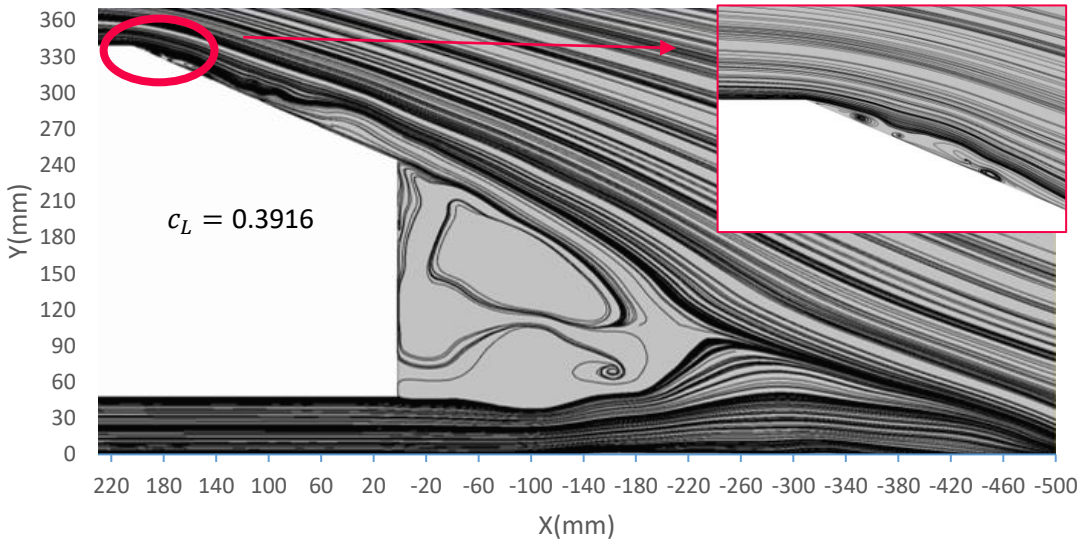

Figure 141: Streamlines from transient model simulation LES-M4.

Finally, we discuss the LES results, as the most sophisticated among the tested turbulence modeling methods (see Fig. 141). The literature review [20] reveals that not all subgrid-scale models are able to predict the flow reattachment on the slant, e.g. the dynamic Smagorinsky, which yields no separation over the slant (see Figure 142). In [20] the LES-SSV was the only method capable of capturing the flow reattachment (see Figure 143). According to the authors, this method provided the most accurate description of the wake region. The size and locations of the two recirculation regions show good agreement with the experiment. The present LES-M4 was able to predict the flow separation over the slant, but the bubble was shorter and thinner as seen from Figure 141 compared against Figure 143. The wake region behind the base is a bit longer. The position of both counter-rotating vortices slightly differs. This may be due to coarser meshes used in the present study.

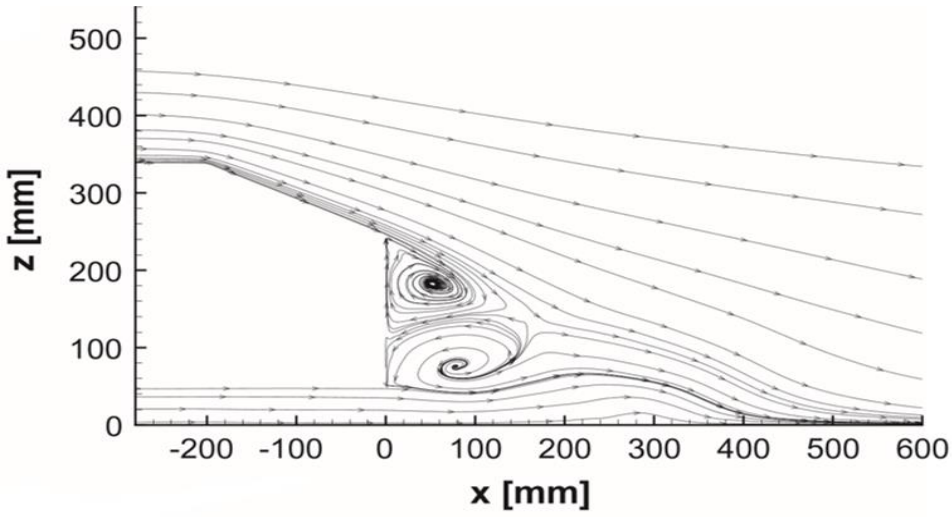

Figure 142: Streamlines from LES-NWR with dynamic Smagorinsky subgrid-scale model from literature[20].

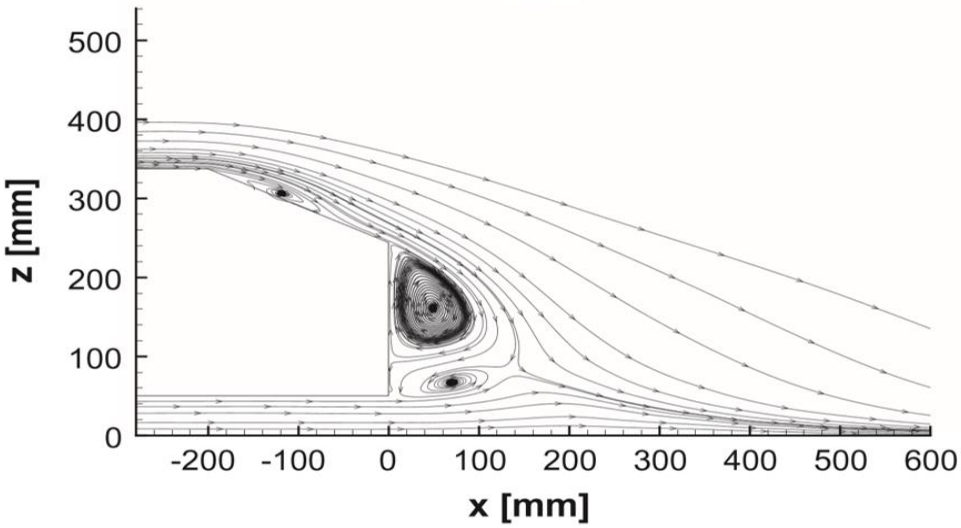

Figure 143: Streamlines from LES-SVV with spectral vanishing method from literature[20].

The flow does not just separate at the back of the body but also at the front, over the rounded part of the body, as already discussed in section 3.2. This has been confirmed experimentally by Spohn and Gilliéron [41] as well as numerically by Kranjović et al. [15,16]. The phenomenon is captured only by

the present LES-M4, as shown in Figure 144. All other simulations show the fully attached flow over the front upper-curved part.

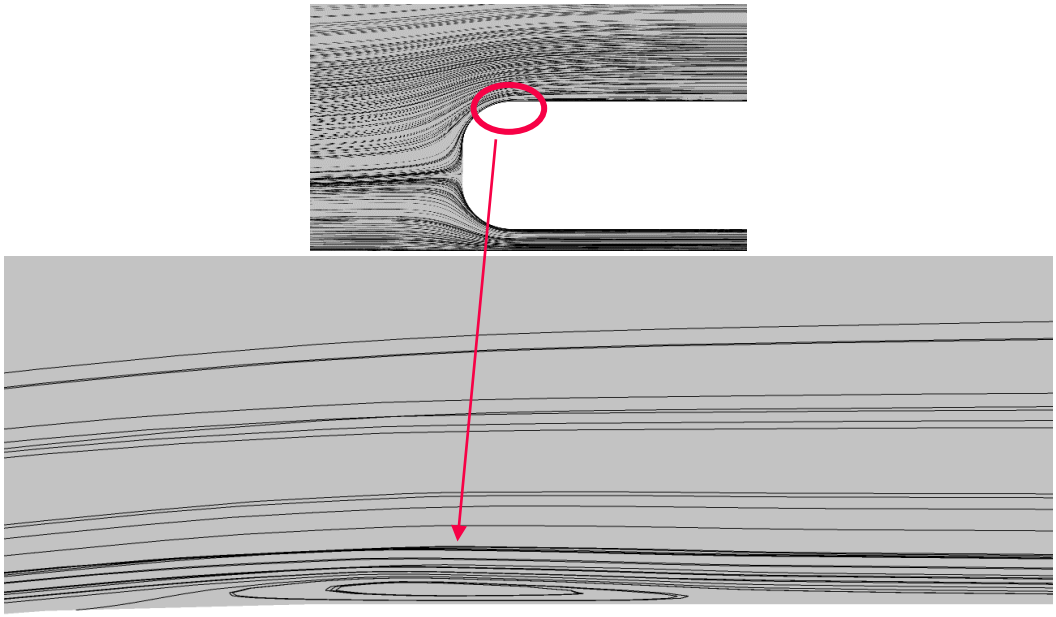

Figure 144: Streamlines (over the front part in symmetry plane z =0 mm): LES-M4.

7.7 Predicted turbulent kinetic energy

Turbulent kinetic energy (TKE) describes the mechanical energy of the eddies in turbulent flow, and it is a measure of turbulence intensity. It can be calculated by the mean of the turbulence normal stresses. written as [42]:

$$k = \frac{1}{2}\overline{u_i' u_i'} \tag{7.3}$$

Contours of the TKE plotted on the symmetry plane are discussed in the following figures. For the steady RANS models, SST-M1 and SST−M4 shown in Figures 145 and 146, the maximum value is reached in the lower part in the wake region at around x=-210 mm. SST-M4 predicts higher turbulence intensity compared to SST-M1. SST-M4 shows a second peak above the slant. Conversely, the SST-M6 shows markedly lower turbulence levels, similar to the RKE-M1 and RKE-M4, presented in Figures 148 and 149 respectively. The wall-resolved transient model SAS-M3 produces a very similar TKE field as observed for the steady wall-resolved approaches SST-M1 and SST-M4 (see Figures 145,146 and 152).

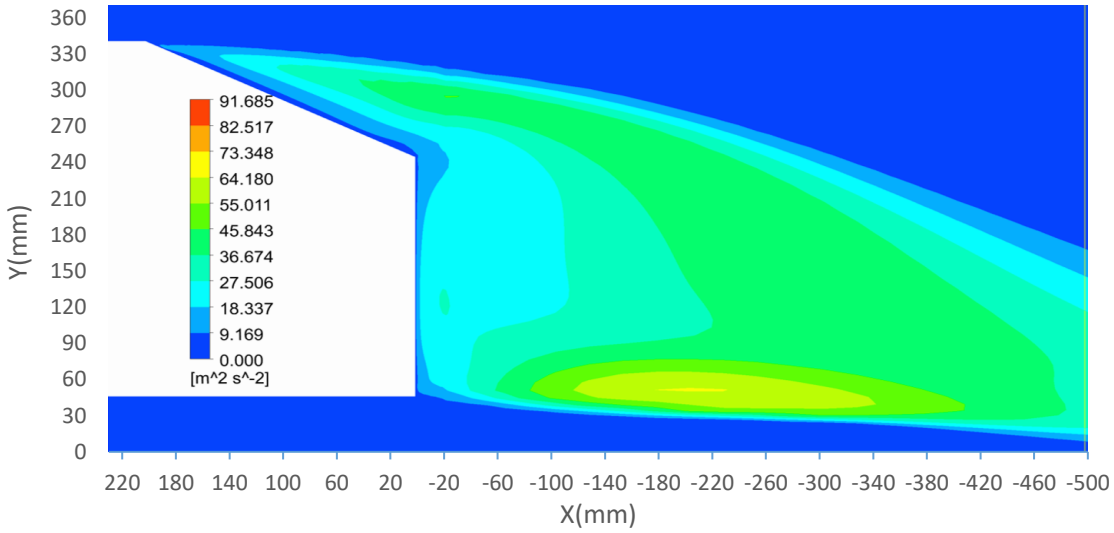

Figure 145: Contours of TKE from the steady RANS model SST-M1.

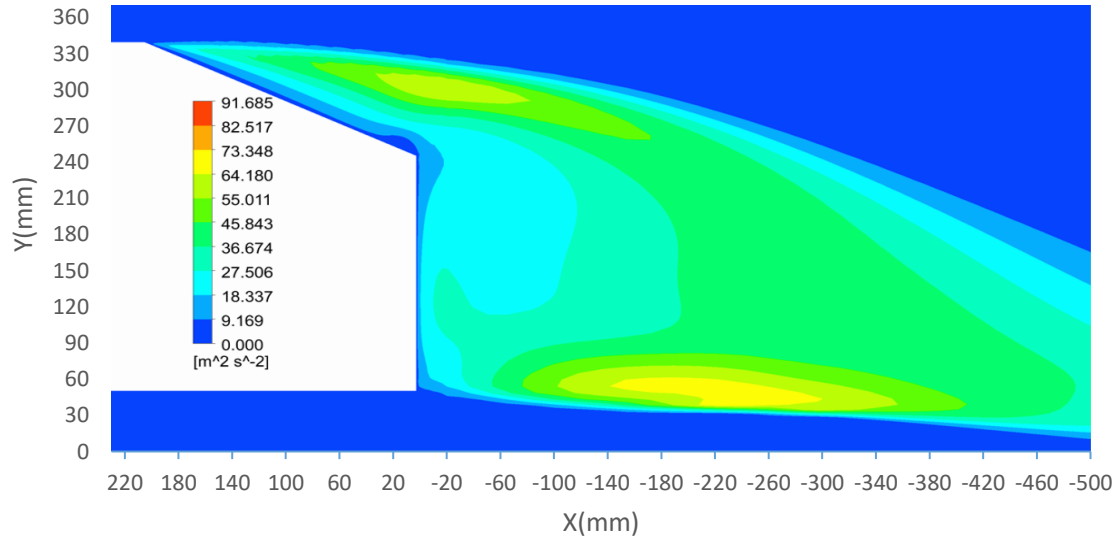

Figure 146: Contours of TKE from the steady RANS model SST-M4.

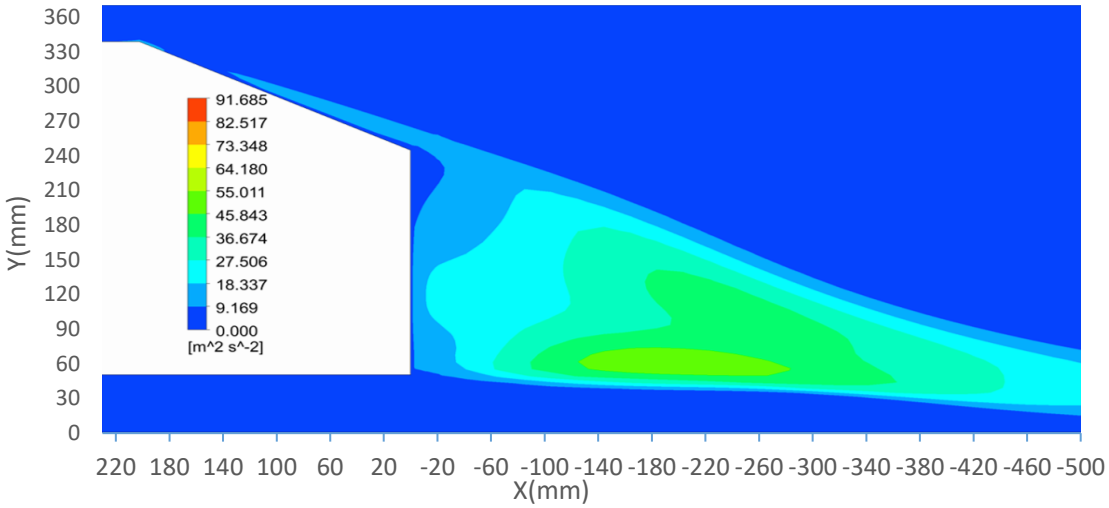

Figure 147: Contours of TKE from the steady RANS model SST-M6.

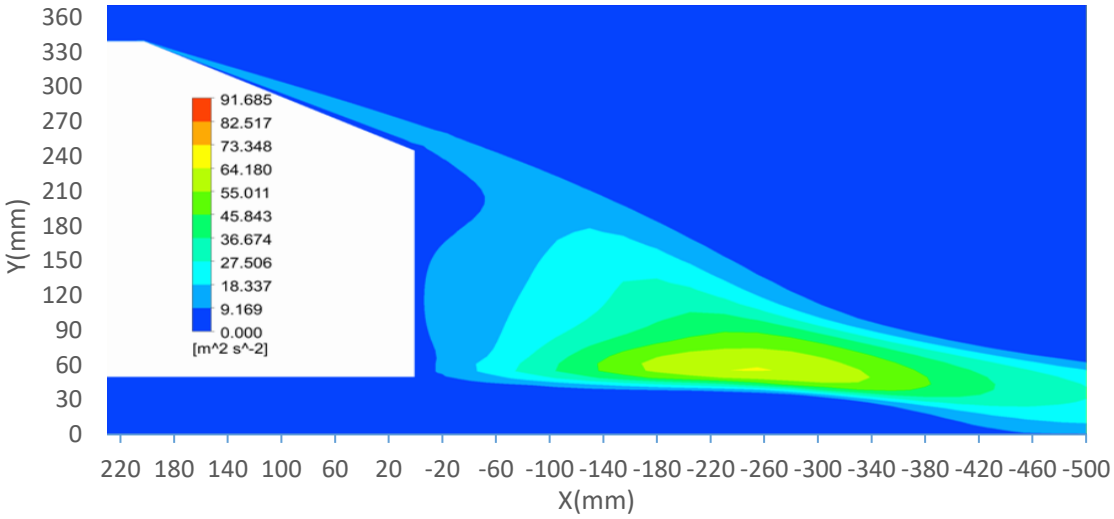

Figure 148: Contours of TKE from the steady RANS model RKE-M1

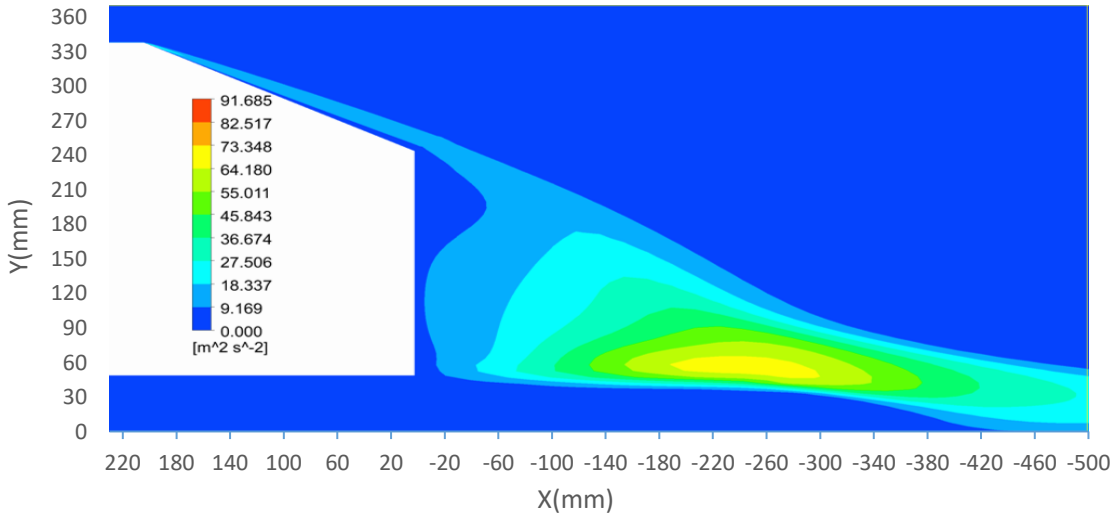

Figure 149: Contours of TKE from the steady RANS model RKE-M4.

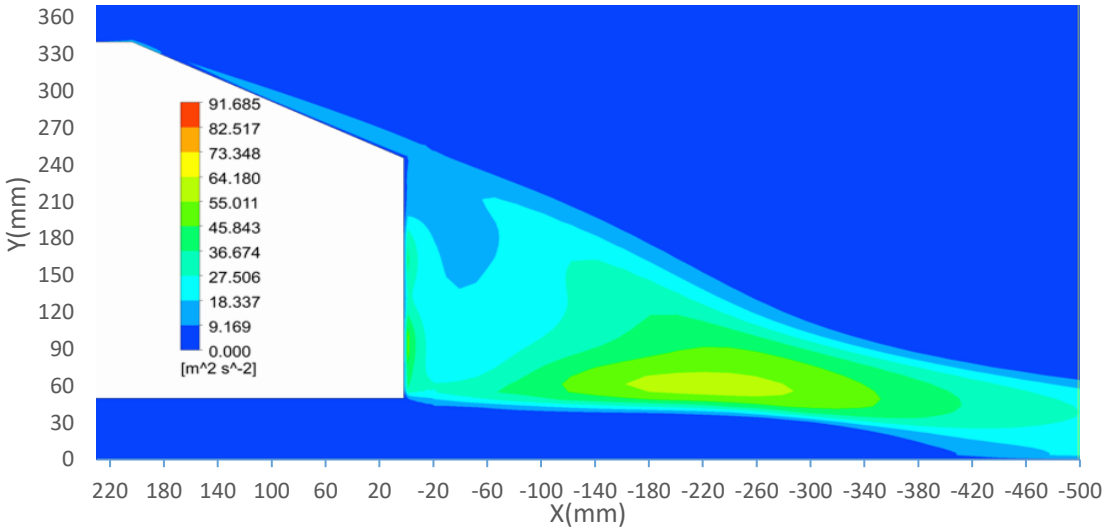

Figure 150: Contours of TKE from the steady RANS model RKE-M6.

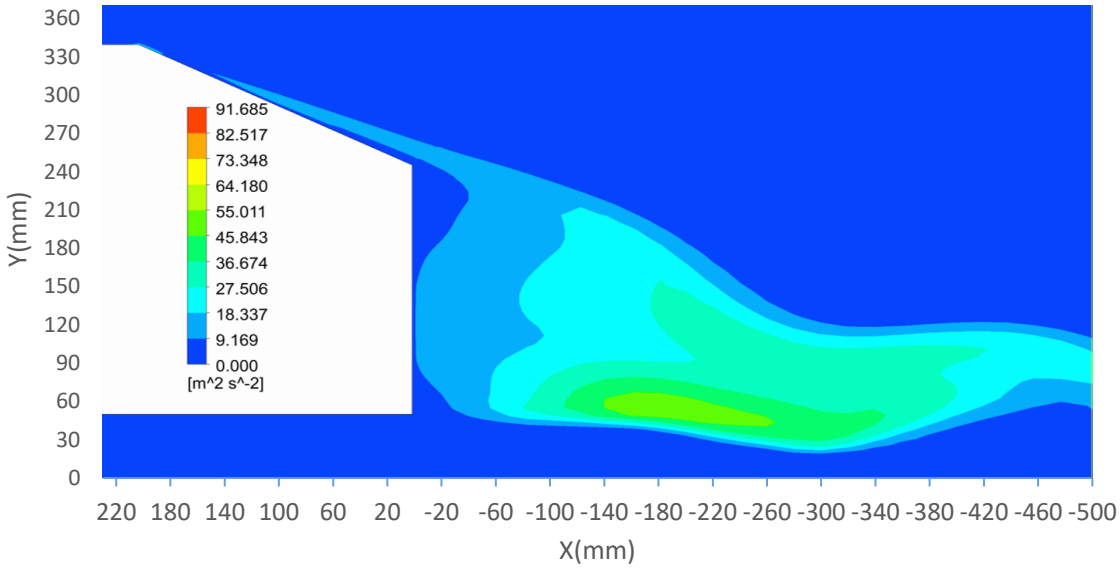

Figure 151: Contours of TKE from the transient model SAS-M6

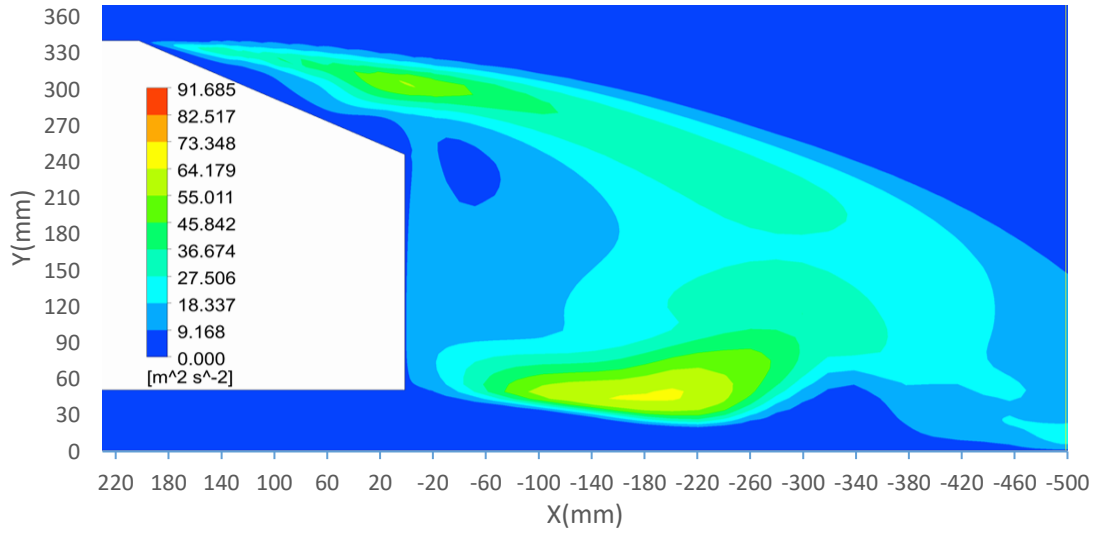

Figure 152: Contours of TKE from the transient model SAS-M3.

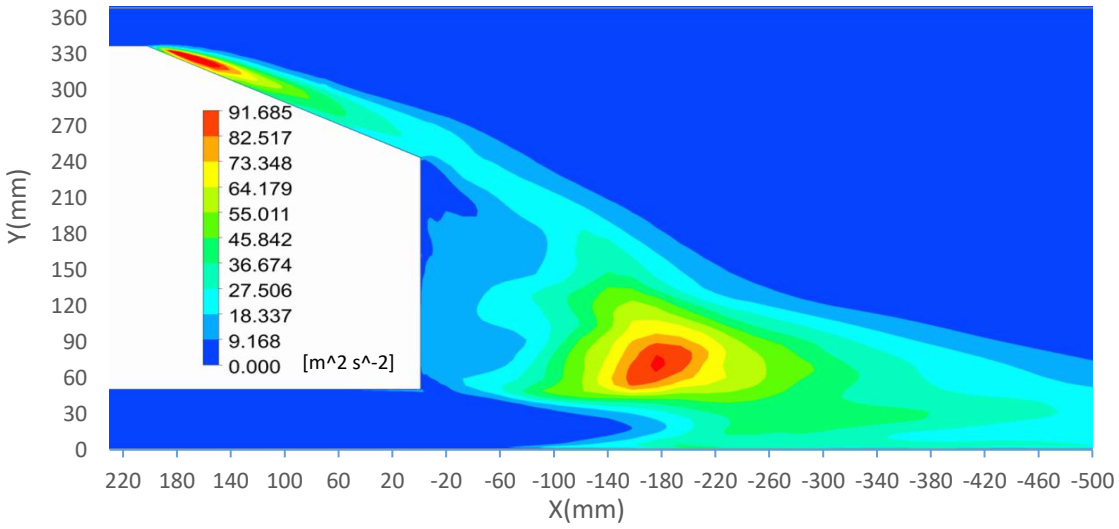

Figure 153: Contours of TKE ($k_{total} = k_{resolved}$+k_{sgs}) from the transient model LES-M4.

LES is basically the only approach able to resolve some part of the TKE spectrum directly. It is convenient to distinguish the TKE from the resolved and modeled part and then compare it to the RANS predictions. This can also serve as a rough estimation of the quality of LES simulation in order to see how much energy is being modeled and how much resolved. The resolved part of the TKE can be calculated from the instantaneous velocities predicted by LES as [67],

$$\mathrm{k_{resolved}} = \sum_{i=1}^{3} \frac{1}{2} < \boldsymbol{u_i} - < \boldsymbol{u_i} >>^2 \qquad 7.4$$

where the angle brackets here stand for the statistical averages (e.g. in time, or in statistically homogenous directions, if available). The modeled part of the TKE in LES can be approximated using subgrid-scale viscosity and length scale [67],

$$\mathrm{k_{sgs}} = \left(\frac{\mu_{sgs}}{\rho l_{sgs}}\right)^2 = \left(\frac{\mu_{sgs}}{\rho \min[\kappa y, C_S \Delta]}\right)^2 \qquad 7.5$$

In the case of the WALE sgs-model, C_S changes to C_W(=0.325). As seen from the LES, it produces a significantly more intense peak of the total TKE in the vortical wake region as compared to the other models discussed above. The contribution $\mathrm{k_{sgs}}$ appears to be minor, as seen from the Figures 154 and 155.

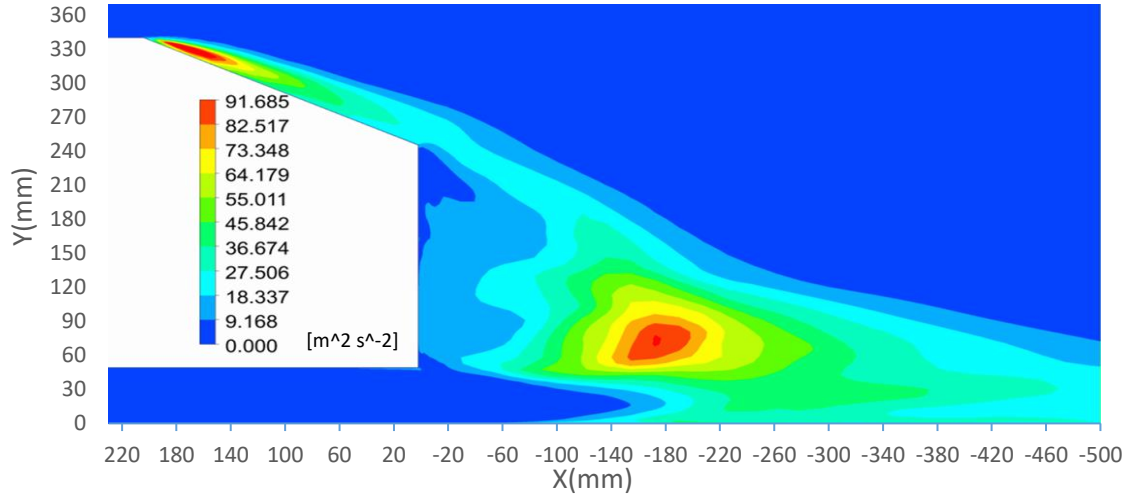

Figure 154: Contours of $k_{resolved}$ from the transient model LES-M4.

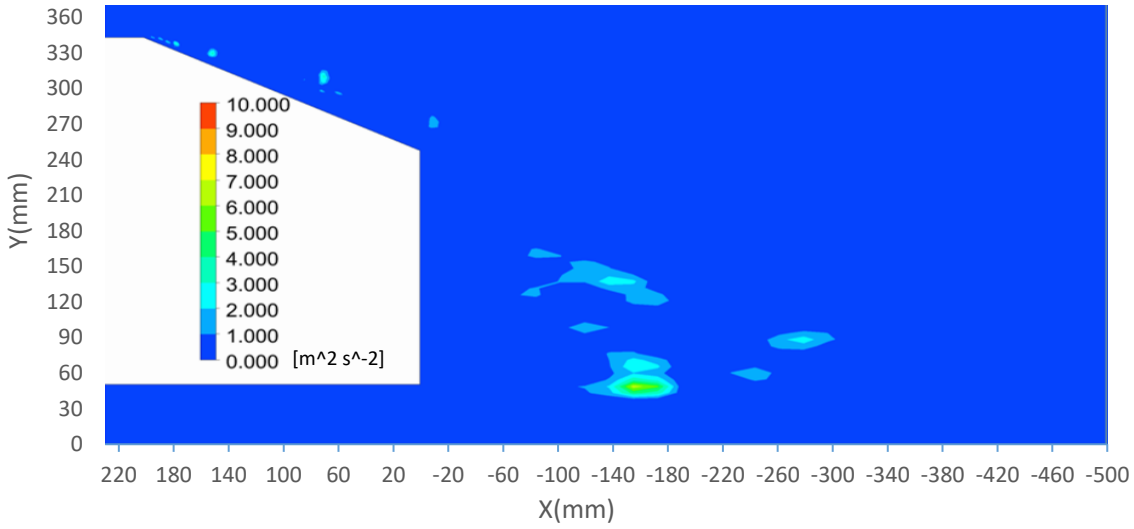

Figure 155: Contours of k_{sgs} from the transient model LES-M4.

In LES, the subgrid-scale model and the numerical discretization error depend on the mesh resolution. Therefore, it is difficult to establish a general quality measurement. Celik et al. [71] proposed the LESIQ factor for the evaluation of the numerical results, which is based on the Richardson extrapolation. The method has been validated against many experimental and DNS results to estimate the quality of the resolution and has shown promising results. It is defined using the subgrid-scale viscosity ratio [67],

$$\mathrm{LESIQ_v} = \frac{1}{1 + 0.05\left[\frac{(\mu + \mu_{sgs})}{\mu}\right]^{0.53}} \qquad 7.6$$

The index varies between 0 and 1 (the higher the value, the better the resolution). Values between 0.75 and 0.85 can be considered sufficient for most engineering applications. Caution is advised, particularly for highly turbulent and anisotropic flows; the method could produce inaccurate results in such cases. The symmetry plane in Figure 156 presents the contours of $\mathrm{LESIQ_v}$ in the symmetry plane for the present LES-M4. There are some poor-quality areas in the wake region and in the slant. Ideally, the grid resolution should be increased here for further LES simulations.

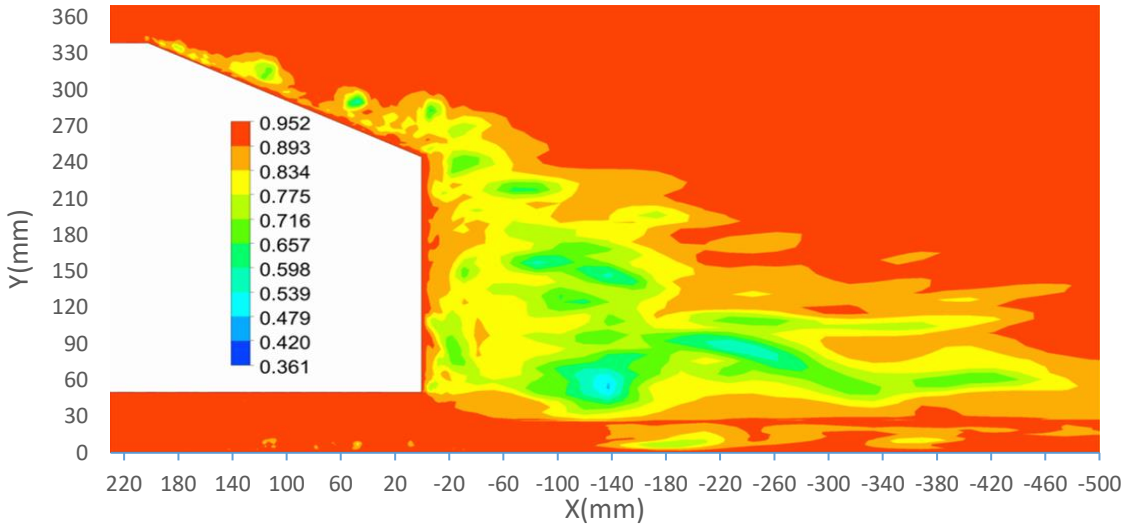

Figure 156: Contours of $LESIQ_v$ for LES - M4 on the symmetry plane (z=0 mm).

7.8 Vortical structures – Q-criterion

The Q-criterion is an excellent indicator for visualizing the vortical flow structures. It is defined as the second invariant of the velocity gradient tensor. The structures have been visualized in CFD-Post, which defines the Q-criterion as in equation 7.7 [72]:

$$Q_{Dim} = C_Q(\Omega^2 - S^2) \qquad 7.7$$

C_Q is a constant, ANSYS Fluent uses $C_Q = 0.5$ and CFD-Post $C_Q = 0.25$, but the value of the constant size does not have any significant relevance. S is the Frobenius norm of the strain tensor, being $S = \sqrt{S_{ij}S_{ij}}$, and $\Omega = \sqrt{\omega_{ij}\omega_{ij}}$, represents the Frobenius of the vorticity tensor. The Q can be defined in non-dimensional or dimensional form (the present case is in non-dimensional) [72]. The qualitative value depends on the Reynolds number and varies inside the domain. A suitable picture usually demands some experimenting in the selecting of the iso-surface value before obtaining useful results[72]. The present cases were plotted using an iso-surface value $5000s^{-2}$. The results are shown in Figures 157-161.

The flow along the front part of the body hardly shows any vortical structures in the steady RANS calculation. The same applies to the SAS and IDDES models. They all use RANS models for the near-wall treatment. The IDDES shows more turbulent structures, in particular, along the side walls, however, still less compared to LES, where the whole surface is covered by fine structures. Since all the RANS approaches use statistically, basically steady, turbulence models to model the turbulence structures, none of them predicted these fine vortices occurring in the statistically stationary flow regions (like the ground floor region), which happens to be the case with the LES simulation.

As the flow continues to move towards the back, it curls over the side edges and forms two counter-rotation C-pillar vortices on each side. They are clearly seen also in the steady RANS model SST-M6 as a very smooth structure, which propagates far downstream towards the domain exit. All the transient models predict much more unsteadiness here, but we can still discern the formation of the C–pillars vortices on each side of the slant.

The SAS-M3, which predicted high turbulent levels on top of the large separation bubble over the slant, consistently shows high turbulent activity in this region. The whole slant is covered with the single iso-surface. In contrast SAS-M6 exhibits in some subareas of the slant clear from vortical structures.This indicates a low level of turbulence. The formation of the small recirculation region can be identified by the small-scale vertical structures appearing near the upper-slant edge in the IDDES and LES results.

Two longitudinal vortices form between the underbody and the stationary ground wall, one on each side, which can be clearly seen in the results of the steady model SST-M6. According to Kranjović et al [16], this happens as the consequence of both boundary layers, which grow along the underbody and floor. The accompanying displacement of fluid redirects the flow towards the sides, where it mixes with the outer flow and forms coherent turbulent structures in the form of longitudinal vortices on each side of the body, along its longitudinal lower edge. Due to to unsteady description of the instantaneous vortical structures of the flow, this particular flow appears as well as more corrugated in the present results for the transient approaches SAS, IDDES, and LES.

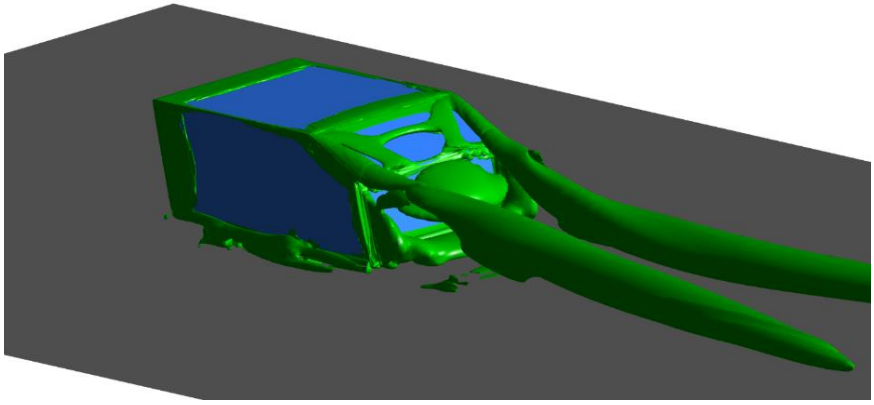

Figure 157: Vortical structures based on Q-criterion for steady RANS model SST-M6

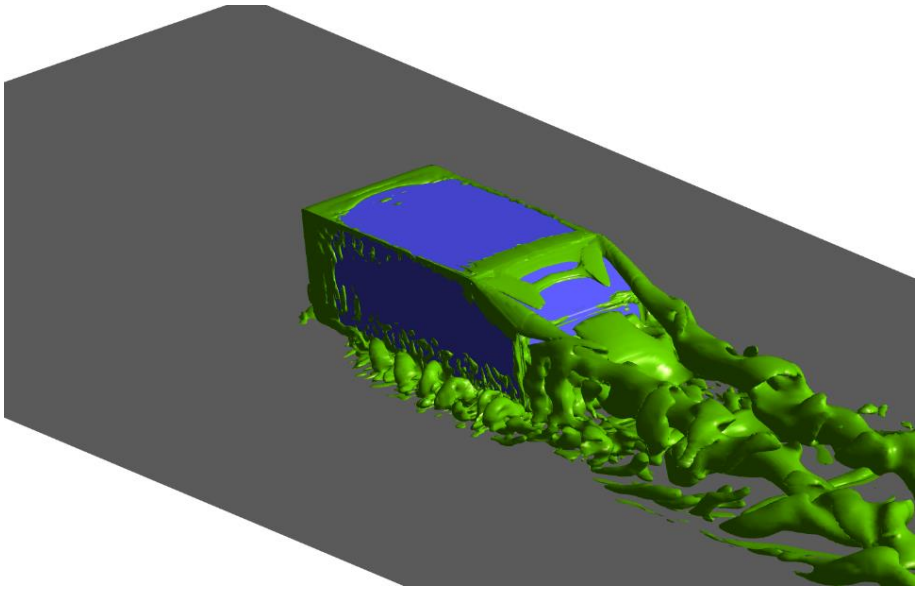

Figure 158: Vortical structures based on Q-criterion for transient model SAS-M6

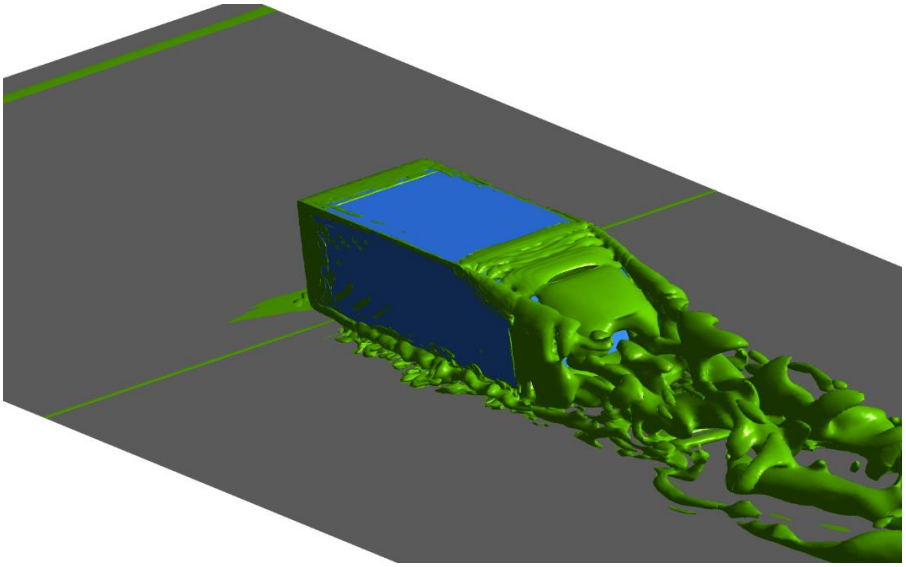

Figure 159: Vortical structures based on Q-criterion for transient model SAS-M3.

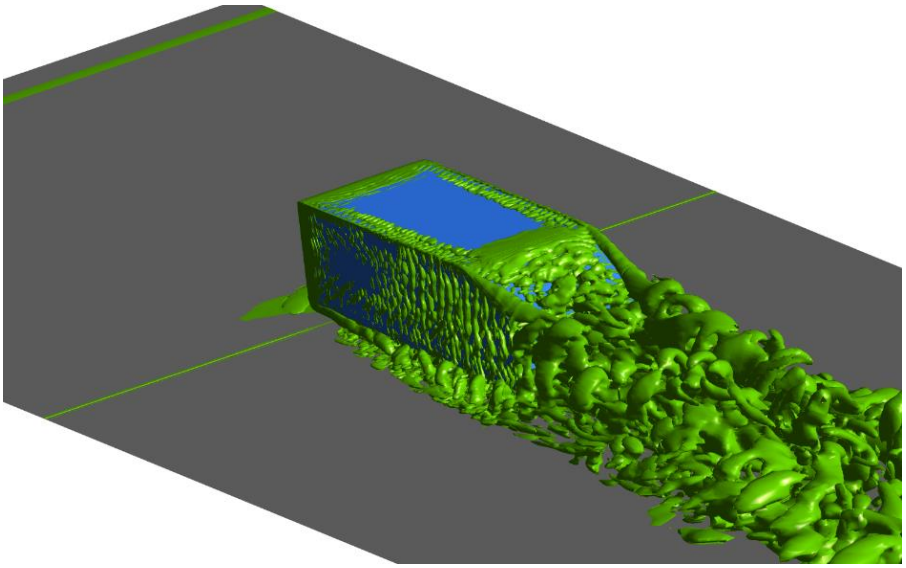

Figure 160: Vortical structures based on Q-criterion for transient model IDDES-M4.

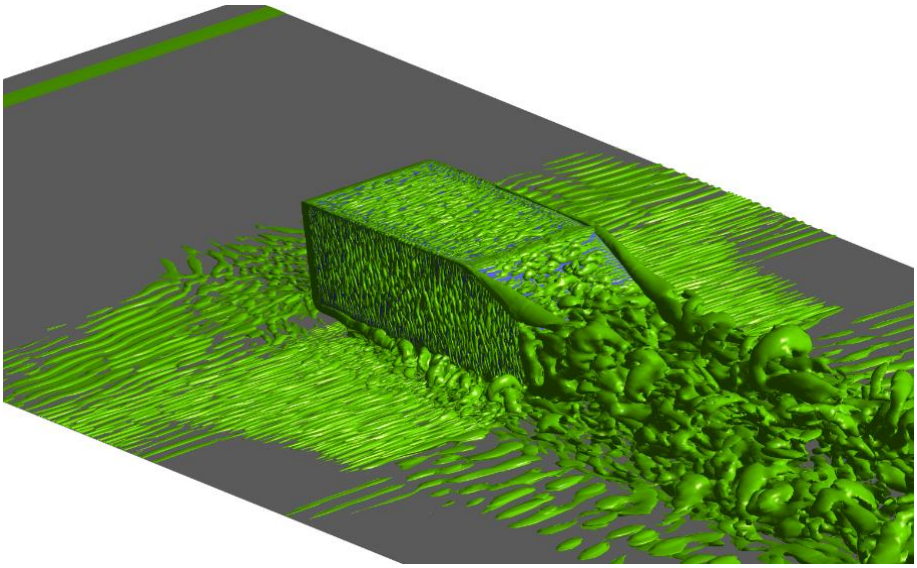

Figure 161: Vortical structures based on Q-criterion for transient model LES-M4.

7.9 Computational time

Not only the accuracy of the obtained simulation but also the computational time plays an important role when using CFD in industrial application. Many simulations often need to be run, before finding an optimal setup. It is desirable to provide a turnaround time as short as possible. Steady calculations are computationally cheap and produce results in a matter of hours. Transient simulations are more time-consuming and can stretch the calculation time to several weeks. However, they may be necessary in some cases − for example, when considering some transient information as an essential design parameter in a particular application. High-performance computers (HPCs) are becoming more and more available for industrial use. A large number of cores together with efficient software allow fast parallelization. This distributes the problem over several computational cores, enabling a much faster calculation, which makes the unsteady calculation more amenable for everyday use.

Table 27: Reported time statistics used for the calculation of the computational time

		SST	***RKE***	***SAS***	***IDDES***	***LES***
		steady		transient		
Average elapsed time per iteration/time step(s)	Mesh(M5)	10.5	9.2	-	-	-
	Mesh(M6)	19.3	18.9	13.6	-	-
	Mesh(M3)	25.5	24.8	18.9	36.1	29.1
	Mesh(M4)	45.1	46.5	-	73.6	84.2
	Number of iterations to convergence	500	500	-	-	-
	Number of time steps until statistical convergence (M6, M3 and M4 mesh configurations)	-	-	10000(M6)	20000(M3)	20000(M3)
				20000(M3)	10000(M4)	10000(M4)
	Time steps for sampling statistics (M6, M3 and M4 mesh configurations)	-	-	5000(M6)	5000 (M3)	5000 (M3)
				5000(M3)	5000(M4)	5000(M4)

The present case was run in the Linux operating system using Intel Xenon X5690 processors. The processors have six dual cores, which provides 12 logical units. All simulations were run parallel. The reported time statistics for steady and transient cases for different mesh configurations and turbulence models can be seen in Table 27. RANS computations were run until the state of convergence was reached. This happened once the drag and lift coefficient values had stabilized**,** after approx. 500 iterations in the steady RANS simulation. In the unsteady simulations a statistically converged solution was reached after 10,000 or 20,000 time steps depending, on the mesh resolution. The coarse grid simulations were run longer and the fine grid simulation shorter, less so, to save a computational expense. After reaching a statistically stationary behavior, the unsteady simulations were run for an additional 5000 time steps to gather the data for sampling statistics.

Table 28: CPU(central processing unit) hours

	SST	***RKE***	***SAS***	***IDDES***	***LES***
	steady		transient		
CPU hours (h)					
Time until statistical convergence (h)					
Mesh(M5)	17.0	15.3	-	-	-
Mesh(M6)	32.2	31.5	453.3	-	-
Mesh(M3)	42.5	41.3	1260.0	2406.7	1940.0
Mesh(M4)	75.2	77.5	-	2453.3	2806.7
Time for sampling statistics (h)					
Mesh(M6)	-	-	226.7	-	-
Mesh(M3)	-	-	315.0	601.7	485.0
Mesh(M4)	-	-	-	1226.7	1403.3
Total computational time, CPU hours (h)					
Mesh(M5)	17.0	15.3	-		
Mesh(M6)	32.2	31.5	680.0	-	-
Mesh(M3)	42.5	41.3	1575.0	3008.3	2425.0
Mesh(M4)	75.2	77.5		3680.0	4210.0

Table 28 shows the computational cost expressed in terms of CPU-hours. Figures 162 gives a cross-comparison of the total CPU hours consumed by the different models. The total calculation time for steady RANS simulations varies from 17 to 77 CPU hours. There is no significant difference between the SST and RKE turbulence models. Differences are small even for the different considered grid configurations. As we turn to the transient simulations, the CPU time drastically increases. Among the transient models, the SAS seems to be least time-consuming, but it still requires in total almost 40 times

more CPU – hours then steady RANS model on mesh M3. As expected, the LES needs the most computational time followed by the IDDES, which is placed second. It should be taken into account that all transient simulations require adequate data for the initialization. This data is usually provided by a precursor steady RANS calculations. Precisely speaking, this should be included into total computational time, which would increase the computational cost even further.

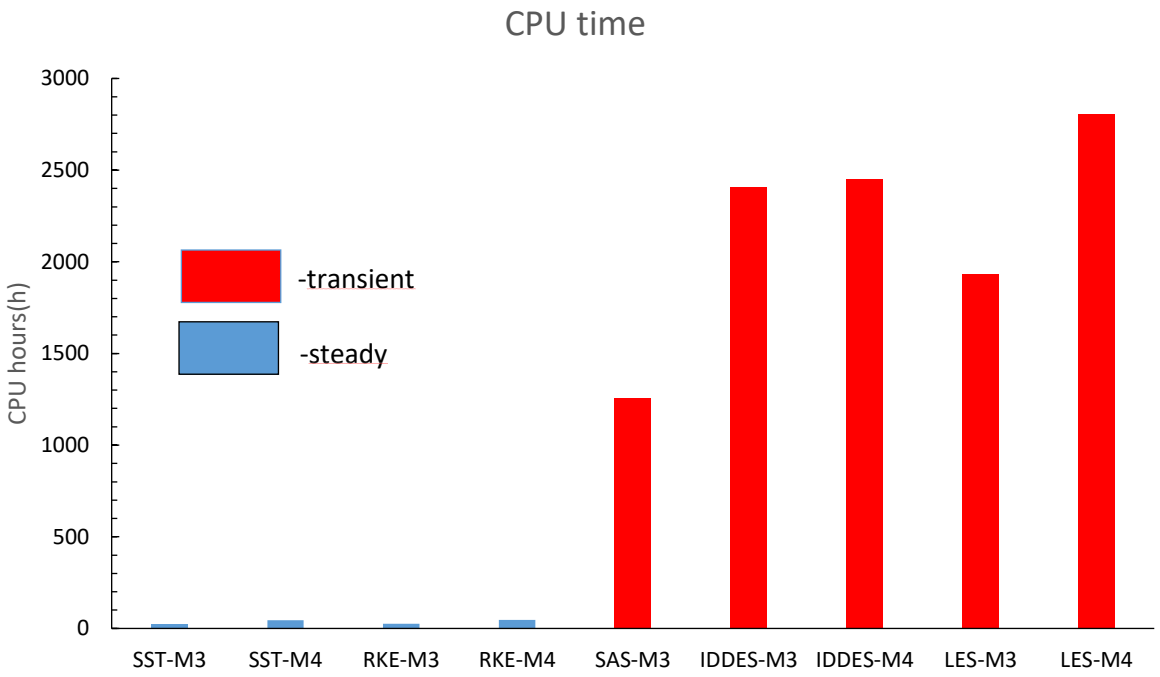

Figure 162: CPU time comparison.

8 Summary and conclusions

The present study investigated the possible benefits by switching from steady to transient turbulence model simulations for use in the development process of the automotive industry. The relevant literature was reviewed at first in order to assess the present state of art in simulating aerodynamic flow around car-like bodies or simplified but representative geometries. The steady RANS approach was suggested here as a still reliable choice for the attached boundary layer flows, but in generally hits its limits as the flow gets more complicated and includes mild to high separation, in predicting accurately the occurring flow patterns. The Ahmed body with a 25° subcritical slant angle was chosen as a well suited and challenging test case, mainly due to the partial reattachment of the separated flow near the downstream end of the slant, which is particularly hard to predict by any turbulence model. Several different turbulence models were tested on a structured grid configuration, which was found to be the best option for the applied meshing.

The steady RANS models outperformed the transient approaches regarding predicted drag and lift coefficients. The predictions turned out to be particularly sensitive to the actually applied near-wall modelling, using alternatively wall-resolved or wall-function based boundary conditions. This was specially in the case for the k- ω SST model. The best predictions were achieved with the k-$\boldsymbol{\varepsilon}$ realizable RKE-M3 (drag coefficient) and the RKE-M5 (lift coefficient) on two of the coarsest meshes, one of which was not wall-resolved (M5). The fundamental advantage of the k- ω SST turbulence model over the k-ε model, in that it provides a continuous description of k and ω inside buffer and viscous sublayers down to the wall, effectively rather decreased than increased the accuracy. As expected, a beneficial effect of mesh refinement was noticed only for the LES and IDDES. The results were improved when comparing the M3 and M4 mesh configuration (although not significantly). The reason for this improvement lies in the enhanced mesh resolution, which implies a larger directly resolved part of the turbulent kinetic energy spectrum, and hence less model uncertainty. An increased resolution should further improve LES results. However, this would mean an excessive increase in computational costs.

The surface of the Ahmed body was divided into five different subsurfaces (front, sides, underbody, roof and slant) in order to exam the partial contribution (drag and lift) from each surface to the total value. The front part contributes approx. 2−12% (depending on the model) to the overall drag coefficient. The contribution to the total lift coefficient is very similar for all models (approx. 30% of total c_L). The side walls have very small impact on the total drag or lift (viscous forces are clearly dominant over pressure force here). The difference between positive lift (roof) and negative lift (underbody suction) contributes notably to the total lift (up to ≈20%). SST-M6, SAS-M6, LES-M4 predict very similar underbody suction and positive lift along the roof, while SAS-M3 and IDDES-M4 predict notably less for both. The wall-resolved SAS-M3 markedly under-compensates the net suction (negative lift) induced by the subsurfaces roof and underbody exhibiting a very low positive contribution from the slant, where it strongly overpredicts the separation without reattachment. Therefore, the SAS-M3 finally predicts the lowest total coefficients of c_D and c_L. Wall-modeled k- ω SST, IDDES and LES predicted no or only partial separation with reattachment along the slant and produced higher values for lift and drag. The base represents the second highest contribution to the overall drag (from aprox. 22% to 36%). Lift force on the base is practically negligible. The numerical results confirm the experimental measurements from Ahmed, which show that for drag for 25 ° slant angle configurations the contribution from slant significantly determines the finally reached total levels of c_D and c_L.

The predicted velocity profiles at selected streamwise positions on the slant helped to explain the strongly different predicted separation behavior, especially when comparing the wall-resolved with the wall-function based results. The wall-resolved models SST M1, SST-M4 and SAS-M3 show much slower flow along the roof of the body compared to all other turbulence models. This velocity deficit results in a strongly separated flow over the slant, which finally translates into an underpredicted lift coefficient. The wall-resolved LES, as well as IDDES, partly give a more accurate description of local flow conditions, especially in the wake region. LES is the only approach able to predict the closing of the wake correctly.

Variations of the static pressure predicted from LES, IDDES, and SAS show no significant difference except close to the upstream edge of the slant. LES predictions for the static pressure come closest to the experiments. None of the steady calculations were able to correctly predict the pressure drop observed in the experiment at the very beginning of the slant, on all three considered vertical planes, although the RKE-M5 finally still predicted the most accurate value for the lift coefficient. All models predict a sharp pressure drop occurring a little bit further upstream from the slant, as compared to the experiments.

The wall-resolved k- ω SST model appears to be highly sensitive to the adverse pressure gradients producing strong separation along the slant. It predicts large wake regions with a separated flow associated with very high turbulence levels as compared to the RKE model. These shortcomings of the wall-resolved k- ωSST model in describing the slant and wake region translate into a significantly underpredicted lift coefficient. IDDES and SAS-M3 also strongly overpredict separation, and they do not predict reattachment as well (as seen in the experiments). LES predicts some separation (weaker than in the experiments), and reproduces reattachment reasonably well. Moreover, only LES predicts a very small flow separation bubble at the beginning of the roof.

The unsteady RANS model SAS can resolve more of the unsteady flow structures compared to its steady counterpart k- ω SST. However, this did not yield notable improvements over the steady k- ω SST model in terms of more accurately predicted integral values (drag coefficient, lift coefficient). The comparatively much higher computational costs of SAS do not pay off. An accurately prepared steady RANS modeling approach still appears as preferable to unsteady RANS approaches, such as SAS, regarding computational costs and reliability of the results.

The high computational costs strongly limit the use of LES. Under-resolved LES can capture force-relevant features like separation, reattachment, laminar/turbulence transition, but only qualitatively. The more comprehensive description of the flow field does not automatically translate into highly accurate predictions of c_D and c_L. In the end, it could be concluded that LES represents the most appropriate candidate when considering transient (time-resolved) simulations, whose quantative accuracy strongly depends on the applied resolution though.

A road map at the first stage of aerodynamic optimization based on the present study is shown in Figure 163. At first, it is on the user to decide how detailed flow information would be necessary for a particular aerodynamic optimization. If the vortical flow patterns are not considered as an essential design parameter and accurately predicted c_D, c_L satisfy the requirements, then it is recommended to perform the wall-function-based steady RANS computation. It turned out that k- ω SST (steady) and RKE produced the best results on this types of meshes. Drag and lift coefficient predictions were very close to the experimental value, although the models could not predict any flow separation at the upper edge of the slant. The alternative RANS approach were to perform a wall-resolved computation. This requires meshes with a fine near-wall resolution, which ensure the y^+ value of around 1 or below.

Steady RKE models produced the best result on this types of meshes. The use of the k- ω SST model would be inappropriate, beacuse this model completely failed to predict the wake region and the lift coefficient. Therefore, the results from the wall-resolved RKE model are used as initial conditions for the successive transient simulation using LES. After setting the solver settings and boundary conditions for the transient simulations, it is desirable to check the mesh quality. This can be done by using the integral length scale ratio. The majority of the RANS grids are not suitable for the LES. The procedure reveals the poor mesh resolution regions of the grid. The mesh should be modified or completely reconstructed if the condition is not satisifed. LES together with the WALE subgrid-scale model was chosen as the best transient model. The quality of the obtained solution should be checked once more after the simulation has been completed. The parameter LESIQv, or the resolved part of TKE are good candidates for evaluating the achieved resolution. The procedure is finished if the calculation meets all the criteria. If not, the mesh should be refined and the LES recalculated.

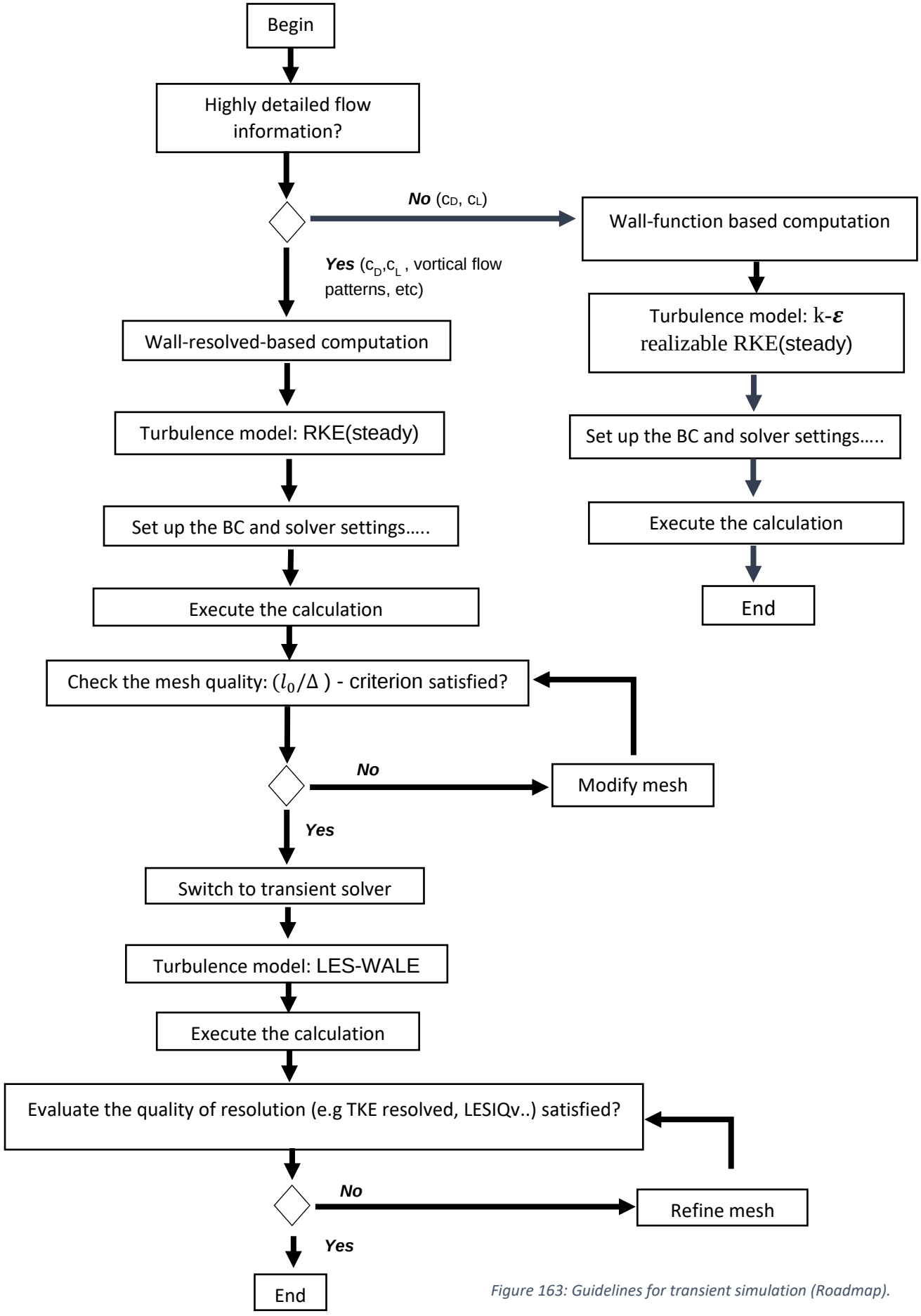

Figure 163: Guidelines for transient simulation (Roadmap).

9 Future recommendations

Further investigation should focus primarily on the use of the LES approach. A recommended first step would be to further optimize the mesh resolution. The number of elements should be increased by a factor of at least 2 or 3, as suggested in [20,47]. This would give a good indication to what extent this substantial but still affordable increase in mesh resolution improves the results. This should finally help to determine the minimum mesh resolution that provides reasonable results for the considered test case, being sufficiently accurate for the industry. The next step would be to optimize the solver settings as well as the mesh generation procedure in order to decrease the computational costs. Thereafter, it is suggested sense to switch to more complex geometries like the DriveAer model, and evaluate the turbulence model performance on such, a more comprehensive test case. This would give more representative results for a car geometry as compared to the Ahmed body, which misses many of the typical geometrical elements of the car, such as wheels, mirrors and an underbody.

10 Bibliography

[1] Wong JY. Theory of ground vehicles (3rd Edition.). New York, John Wiley & Sons, 2001.

[2] Agathangelou B. and Gascoyne M. Aerodynamic Design Considerations of a Formula 1 Racing Car. Proceedings of the SAE International Congress and Exposition, Detroit, MI, Feb. 23–26 1998, SAE Paper No. 980399.

[3] Spalart Philippe R. Philosophies and fallacies in turbulence modeling. Progress in Aerospace Sciences, 2015, Vol.74, pp.1−15.

[4] Corson D., Jaiman R., Shakib F. Industrial application of RANS modeling: capabilities and needs. International Journal of Computational Fluid Dynamics, 2009, Vol. 23; pp.337−347.

[5]Perzon S. and Davidson L. On the transient modeling of the flow around vehicles using the Reynolds equation. In: International Conference on Applied Computational Fluid Dynamics (ACFD) Beijing China. 2000. pp. 720−727.

[6] Hanjalic K. Will RANS survive LES? A view of perspectives. Journal of Fluids Engineering, 2005, Vol. 127; pp.831−839.

[7] Durbin P.A. and Reif Pettersson B.P. Statistical theory and modeling for turbulent flows. United Kingdom, John Wiley & Sons, 2011,

[8] Iaccarino G , Ooi A., Durbin P. A., & Behnia M . Reynolds averaged simulation of unsteady separated flow. International Journal of Heat and Fluid Flow, 2003, Vol.24; pp.147−156.

[9] Palkin E., Mullyadzhanov R., Hadžiabdić M. & Hanjalić K. Scrutinizing URANS in shedding flows: the case of cylinder in cross-flow in the subcritical regime. Flow, Turbulence and Combustion, 2016, Vol. 97; pp.1017−1046.

[10] Fröhlich J. and Von Terzi D. Hybrid LES/RANS methods for the simulation of turbulent flows. Progress in Aerospace Sciences, 2008, Vol. 44; pp.349−377.

[11] Menter F.R. and Egorov Y. The scale-adaptive simulation method for unsteady turbulent flow predictions. Part 1: theory and model description. Flow, Turbulence and Combustion, 2010, Vol. 85; pp.113−138.

[12] Egorov Y., Menter F. R., Lechner R. & Cokljat D. The scale-adaptive simulation method for unsteady turbulent flow predictions. Part 2: Application to complex flows. Flow, Turbulence and Combustion, 2010, Vol. 85; pp.139−165.

[13] Spalart Philippe R. Detached-eddy simulation. Annual Review of Fluid Mechanics, 2009, Vol.41; pp.181−202.

[14] Krajnović S., Minelli G., Basara B. Partially-averaged Navier–Stokes simulations of two bluff body flows. Applied Mathematics and Computation, 2016, Vol. 272; pp.692−706.

[15] Krajnović S. and Davidson L. Flow around a simplified car, part 1: large eddy simulation. Journal of Fluids Engineering, 2005, Vol.127; pp.907−918.

[16] Krajnović S. and Davidson L. Flow around a simplified car, part 2: understanding the flow. Journal of Fluids Engineering, 2005, Vol.127; pp. 919−928.

[17] Bordei S. and Popescu F. Aerodynamic results for a notchback race car. University of Galati, Galati, ISSN, 2011, 1221−4566.

[18] Guilimineau E. Computational study of flow around a simplified car body. Journal of Wind Engineering and Industrial Aerodynamics, 2008, Vol. 96; pp. 207−1217.

[19] Krastev V.K. and Bella G. On the steady and unsteady turbulence modeling in ground vehicle aerodynamic design and optimization. SAE Technical Paper, September 2011.

[20] Serre E., Minguez M., Pasquetti R., Guilmineau E., Deng G. B., Kornhaas M. & Rodi W. On simulating the turbulent flow around the Ahmed body: a French−German collaborative evaluation of LES and DES. Computers & Fluids, 2013, Vol. 78; pp.10−23.

[21] Forbes D., Page G., Passmore M., Gaylard A. A study of computational methods for wake structure and base pressure prediction of a generic SUV model with fixed and rotating wheels. Proceedings of the Institution of Mechanical Engineers Part D. Journal of Automobile Engineering, 2017; Vol. 231; pp.1222−1238.

[22] Ashton N. and Revell A. Comparison of RANS and DES methods for the DrivAer automotive body. SAE Technical Paper, 2015, No. 2015-01-1538, University of Manchester.

[23] Jakirlić S. et al. Eddy-resolving simulations of the notchback 'DrivAer' model: influence of underbody geometry and wheels rotation on aerodynamic behaviour. SAE Technical Paper No. 2016-01-1062, 2016.

[24] Katz J., Race car aerodynamics. Bentley Publishers,USA, 1995.

[25] Hucho W.H., Aerodynamics of road vehicles: from fluid mechanics to vehicle engineering. Great Britain, Butterworth-Heinemann , 1987.

[26] Blacha T and Islam M. The aerodynamic development of the new Audi Q5. SAE International Journal of Passenger Cars-Mechanical Systems, 2017, Vol.10; pp.638−648.

[27] Samples M., Gaylard A.P. and Windsor S. The aerodynamics development of the Range Rover Evoque. In: 8th MIRA International Conference on Vehicle Aerodynamics. 2010. pp. 13−14.

[28] Islam M., Decker F., De Villiers E., Jackson A., Gines J., Grahs T. & Font J. C. Application of detached-eddy simulation for automotive aerodynamics development. SAE Technical Paper, 2009, No. 2009-01-0333

[29]Jakirlic S et al. Critical assessment of some popular scale-resolving turbulence models for vehicle aerodynamics. SAE International Journal of Passenger Cars − Mechanical Systems, 2017, Vol.10; pp.235−250.

[30] Stevenson TJ. Simulation of ground vehicle aerodynamics applied to a generic Le Mans prototype. 2013. PhD Thesis. University of the Witwatersrand

[31] T.H. Shih, W. W. Liou, A. Shabbir, Z. Yang, and J. Zhu. A New k-ε - Eddy-Viscosity Model for High Reynolds Number Turbulent Flows - Model Development and Validation". Computers Fluids. 1995 Vol. 24; pp. 227–238.

[32] Khare A., Singh A., Nokam K. Best practices in grid generation for CFD applications using HyperMesh. HyperWorks Technology Conference, 2009, pp. 1–10.

[33] ANSYS Meshing User's Guide, Release 18.2

[34] Ahmed S.R., Ramm G., Faltin G. Some salient features of the time-averaged ground vehicle wake. SAE Technical Paper, 1984, No. 840300

[35] GUILMINEAU, E., et al. Assessment of hybrid RANS-LES formulations for flow simulation around the Ahmed body. Computers & Fluids, 2018, Vol.176; pp. 302-319.

[36] Le Good G.M. and Garry K.P. On the use of reference models in automotive aerodynamics. SAE Technical Paper, 2004, No. 2004-01-1308

[37] Henry ML. Insight derived from high order structured finite difference CFD simulations of flow past generic simplified car models. 2016. PhD Thesis. The University of North Carolina at Charlotte.

[38] Heft A.I., Indinger T. and Adams N.A. Introduction of a new realistic generic car model for aerodynamic investigations. SAE Technical Paper, 2012, No. 2012-01-0168.

[39] Lienhart H. and Becker S. Flow and turbulence structure in the wake of a simplified car model. SAE transactions, 2003, pp. 785-796.

[40] Meile W., Ladinek, T., Brenn G., Reppenhagen A. & Fuchs A. Non-symmetric bi-stable flow around the Ahmed body. International Journal of Heat and Fluid Flow, 2016, Vol.57; pp.34−47.

[41] Spohn A., Gilliéron P. Flow separations generated by a simplified geometry of an automotive vehicle. In: IUTAM Symposium: unsteady separated flows. 2002. pp. 8−12.

[42] URL: https://www.sharcnet.ca/Software/Fluent6/html/ug/node496.htm

[43] ANSYS CFX User's Guide, Release 18.2

[44] Girimaji S.S., Srinivasan R, Jeong E. PANS turbulence model for seamless transition between RANS and LES: fixed-point analysis and preliminary results. In: ASME/JSME 2003 4th Joint Fluids Summer Engineering Conference. American Society of Mechanical Engineers, 2003. pp. 1901−1909.

[45] Vino G., Watkins S., Mousley P., Watmuff J. & Prasad S. The unsteady near-wake of a simplified passenger car. In: 15th Australasian Fluid Mechanics Conference The University of Sydney, Sydney, Australia. 2004. pp. 13-17.

[46] Menter F. R., Egorov Y. Revisiting the turbulent scale equation. In: IUTAM Symposium on One Hundred Years of Boundary Layer Research. Springer, Dordrecht, 2006. pp. 279-290.

[47] Hinterberger C., Garcia-Villalba M., Rodi W. Large eddy simulation of flow around the Ahmed body. In: The aerodynamics of heavy vehicles: trucks, buses, and trains. Springer, Berlin, Heidelberg, 2004. pp. 77−87.

[48] Ferziger J. H. and Peric M. Computational methods for fluid dynamics. Springer Science & Business Media, 2012,

[49] Hirsch C. Numerical computation of internal and external flows: the fundamentals of computational fluid dynamics. Elsevier, 2007.

[50] Wilcox David.C. Turbulence Modeling for CFD. DCW Industries, Inc., La Canada, CA, 1993.

[51] ANSYS Fluent Theory Guide, Release 18.2

[52] Chan W., Gomez R., Rogers S. & Buning P. Best practices in overset grid generation. In: 32nd AIAA Fluid Dynamics Conference and Exhibit. 2002. pp. 3191.

[53] ANSYS ICEM CFD User's Manual, Release 18.2

[54] Davidson L. Fluid mechanics, turbulent flow and turbulence modeling, 2015, course material, Chalmers University of Technology. URL: http://www.tfd.chalmers.se/~lada/postscript_files/solids-and-fluids_turbulent-flow_turbulence-modelling.pdf

[55] Shur M. L., Spalart P. R., Strelets M. K. & Travin A. K. A hybrid RANS-LES approach with delayed-DES and wall-modelled LES capabilities. International Journal of Heat and Fluid Flow, 2008, Vol.29; pp.1638−1649.

[56] Gritskevich M. S., Garbaruk A. V., Schütze J. & Menter F. R. Development of DDES and IDDES formulations for the k-ω shear stress transport model. Flow, Turbulence and Combustion, 2012, Vol. 88; pp. 431−449.

[57] Nicoud F. and Ducros F. Subgrid-scale stress modelling based on the square of the velocity gradient tensor. Flow, Turbulence and Combustion, 1999, Vol.62; pp.183−200.

[58] Keating M. Accelerating CFD Solutions, ANSYS Advantage: Excellence in Engineering Simulation, vol. V, no. 1, pp. 48-49, 2011.

[59] Menter F. and Esch T. Elements of industrial heat transfer predictions. In: 16th Brazilian Congress of Mechanical Engineering (COBEM), 2001 Vol.109; pp.650.

[60] Menter F., Carregal Ferreira J., Esch T., Konno B. The SST turbulence model with improved wall treatment for heat transfer predictions in gas turbines. Proceedings of the International Gas Turbine Congress 2003 Tokyo November 2−7, 2003.

[61] Menter F. Two-equation eddy-viscosity turbulence models for engineering applications. AIAA Journal, 1994, Vol.32; pp.1598−1605.

[62] Meile W., Brenn G., Reppenhagen A. & Fuchs A. Experiments and numerical simulations on the aerodynamics of the Ahmed body.CFD Letters, 2011, Vol.3; pp.32−39.

[63] Schlichting H. and Gersten K. Boundary-layer theory. Springer, 2016.

[64] URL: https://www.cfd-online.com/Forums/ansys-meshing/82122-mesh-quality-criteria-icem.html

[65] Franklyn J.K., Applications Specialist, ANSYS, Inc: Coupling momentum and continuity increases CFD robustness. URL : http://www.enginsoft.it/software/ansys/cfd/fluent/fluent-solver.pdf

[66] Launder B. E. and Spalding D.B. The numerical computation of turbulent flows. In: Numerical prediction of flow, heat transfer, turbulence and combustion. Pergamon, 1983. pp. 96-116.

[67] Gerasimov Aleksey, ANSYS Sweden, Quick guide to setting up LES-type simulations, Version 1.4, May 2016 . URL:
http://www.tfd.chalmers.se/~lada/comp_turb_model/postscript_files/Quick_Guide_to_Setting_Up_LES_version_1.4_for_Lars.pdf

[68] Steiner H. Numerical methods in fluid mechanics and heat transfer, Lecture Notes − Part 2, WS 2016

[69] Davidson L. Large eddy simulations: how to evaluate resolution. International Journal of Heat and Fluid Flow, 2009, Vol. 30; pp.1016−1025.

[70] Aljure D.E., Lehmkuhl O., Rodríguez I., Oliva A. Flow and turbulent structures around simplified car models,Computers & Fluids, 2014, Vol. 96: pp.122−135

[71] Celik I.B., Cehreli Z.N., Yavuz I. Index of resolution quality for large eddy simulations. Journal of Fluids Engineering, 2005, Vol.127; pp.949−958.

[72] ANSYS CFX 17 Reference guide. URL: https://www.sharcnet.ca/Software/Ansys/17.0/en-us/help/cfx_ref/bp_turbu_s_7.html

[73] ANSYS Fluent Users guide, Release 18.2

[74] Perzon S. On blockage effects in wind tunnels – a CFD study. SAE Technical Paper, 2001.

[75] Lanfrit M. Best practice guidelines for handling automotive external aerodynamics with FLUENT. 2005., Version 1.2, Fluent Deutschland GmbH

[76] FLUENT 6.3 User's guide − 12.9.2 Filtered Navier−Stokes Equations, URL: https://www.sharcnet.ca/Software/Fluent6/html/ug/node507.htm

[77] Brondolo L. Comparative investigation of large eddy simulation and RANS approaches for external automotive flows. 2011., Msc thesis, Cranfiled University

[78] Umur T. Investigation of turbulence models used in automotive industry. Msc Thesis. The Graduate School of Natural and Applied Sciences of Middle East Technical University, 2011.

[79] ANSYS ICEM CFD Help Manual, Release 18.2

[80] Mockett Charles.A comprehensive study of detached eddy simulation. Ph.D. Thesis, Technical University of Berlin, 2009

[81] Keogh J., Barber T., Diasinos S. & Doig G. The aerodynamic effects on a cornering Ahmed body. Journal of Wind Engineering and Industrial Aerodynamics, 2016, Vol. 154: pp.34−46.